OCEAN COLOUR ANALYSIS USING CZCS DATA

by

David Hawkesford Lawrence

B.Sc. (Hons).

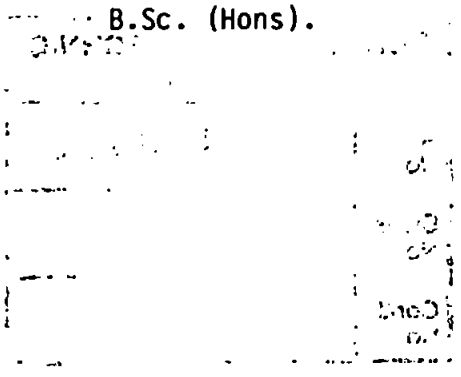

Submitted to the Council for National Academic Awards in partial fulfilment of the requirements for the degree of Doctor of Philosophy

Submitted February 1987

Department of Communication Engineering
Faculty of Technology
Plymouth Polytechnic
Plymouth
Devon
United Kingdom

In collaboration with:
Institute for Marine
Environmental Research
Prospect Place
Plymouth, Devon
United Kingdom

ACKNOWLEDGEMENTS

I gratefully acknowledge the assistance rendered by all those who have contributed to this project, in particular:

My supervisors Dr J G Wade and Dr G E Millward who not only set up this project but also encouraged me to persevere when progress seemed difficult and slow.

I received a great deal of technical and engineering assistance at the outset of the project from the Department of Communication Engineering, but I would like to make a special mention of Michael Rendle and Andy Grantham, without whom the image processor would never have come into existence.

Mr Xihuang Ling implemented the clustering and monocluster blocks algorithms. Mr Ling, from Shanghai in China, was sponsored by the British Council.

John Horne of the Polytechnic Computer Centre advised me on reading CZCS computer tapes on the Prime computer. Betty Fox provided transparencies taken from an aircraft.

I received much advice and all my sea truth from Dr J Aiken (IMER, Plymouth) and Dr P Holligan (MBA, Plymouth).

Dr S M Singh of Reading University (formerly at Dundee University) helped me to get to grips with atmospheric correction and Mr P Baylis of Dundee University advised on reading CCTs.

Jerry Francis of Arrow Computer Systems Ltd. dealt with several computer crises with good humour.

Janet Rayne and Rob Looker of C.A.T.S (Computer Aided Technical Services) in Plymouth typed the thesis with great care and patience.

This project was funded by the Science and Engineering Research Council under grant number GR/B/67247.

OCEAN COLOUR ANALYSIS USING CZCS DATA

by DAVID HAWKESFORD LAWRENCE, B.Sc.(Hons)

ABSTRACT

A low-cost image processor has been designed and built to provide a system suitable for investigating the quantitative mapping of phytoplankton patchiness using Nimbus-7 CZCS satellite images. The processor design was based upon a Motorola 68000 computer linked to a 768x512x8 bit imagestore. High resolution images were input from the CZCS CCT via a 40 Mbyte tape transport. The system had the novel capability for real time linear and non-linear operations upon images on a pixel-by-pixel basis and fast evaluation (< 10 seconds) of retrieval algorithms involving narrow band images. Software was developed to manage the images in the following ways: high emphasis filtering, edge detection, contrast stretch routines, rectification, and pseudo colour routines for grey-level colouring prior to display of the processed image on a double resolution colour monitor.

Initial testing of the instrument was via multiband aerial photographs input through a broadcast quality camera, although the major analysis was carried out on CZCS data. Software was developed to correct the measured radiances at the satellite for atmospheric effects, thus giving values of the water-leaving radiances. In the correlation studies the sea truth was obtained in the form of chlorophyll concentrations determined during UOR surveys of the English Channel. Both high and low chlorophyll concentration scenes were analysed. The algorithm testing involved ratioing the radiances from the various narrow bands and incorporating them in quantitative expressions which were linear, logarithmic and polynomial. Four different images were investigated and the results showed that the observed chlorophyll concentrations were best correlated with water-leaving radiances through a linear expression. The spectral information was also analysed with a clustering technique to identify patches of chlorophyll of varying concentrations. The work shows that digital image processing can be used in conjunction with retrieval algorithms to provide real time detection of phytoplankton fronts in coastal waters.

CONTENTS

Page No.

APPENDICES

LIST OF PLATES

ABBREVIATIONS

ADC	Analogue to Digital Converter
ALU	Arithmetic and Logic Unit
ASCII	American Standard Code for Information Interchange
bpi	bits per inch
CCD	Charge Coupled Device
CCT	Computer Compatible Tape
CLIP	Cellular Logic Image Processor
CMOS	Complementary Metal-Oxide Semiconductor
CPR	Continuous Plankton Recorder
CPU	Central Processing Unit
CRT	Cathode Ray Tube
CZCS	Coastal Zone Color Scanner
DC	Direct Current
DEC	Digital Equipment Corporation
DMA	Direct Memory Access
DN	Digital Number
ERS-1	ESA Remote Sensing (satellite)
ERTS	Earth Resources Technology Satellite (now LANDSAT)
ESA	European Space Agency
FFT	Fast Fourier Transform
FM	Frequency Modulation
FOV	Field Of View
GCP	Ground Control Point
GMT	Greenwich Mean Time
HRV	High Resolution Visible (SPOT sensor)
IEE	Institution of Electrical Engineers
IEEE	Institute of Electrical and Electronics Engineers
IFOV	Instantaneous Field Of View
I^2S	International Imaging Systems
kbyte	1024 (2^{10}) bytes
LIDAR	Laser induced fluorescence system
LSB	Least Significant Bit
LUT	Look-Up Table
Mbyte	1048576 (2^{20}) bytes
MESSR	Multispectral Electronic Self-Scanning Radiometer (MOS sensor)
MOS	Marine Observation Satellite
MPP	Massively Parallel Processor
MSB	Most Significant Bit
MSS	Multi-Spectral Scanner (On Landsat)

NASA	National Aeronautics and Space Administration
NERC	Natural Environment Research Council
NETD	Noise Equivalent Temperature Difference
NOSS	National Oceanic Satellite System
OCS	Ocean Color Scanner
OCM	Ocean Colour Monitor (proposed for ERS-1)
Pixel	Picture element
RAM	Random Access Memory
SPOT	Système Probatoire d'Observation de la Terre (Earth Observation Test System)
TTL	Transistor-Transistor Logic
UOR	Undulating Oceanographic Recorder
VDU	Visual Display Unit
ZIP	Zonal Information Processor (for the CZCS)

CHAPTER 1

INTRODUCTION

1.1 OVERVIEW

1.1.1 Problems of scale in oceanography

The oceans cover some 70% of the Earth's surface (Harvey 1982), corresponding to about 360 million square kilometres (Allan 1983). The dynamics of the ocean are such that order-of-magnitude changes can occur within days and over large areas (Hibbs & Wilson 1983). Consequently, in addition to establishing mean values, it is vital to measure variations in ocean properties in order to arrive at a full understanding of the oceans. The requirement to sample vast areas in a short timeframe represents a daunting prospect for the oceanographer and it has been said that 'the worst place from which to study the sea is the sea surface' (Allan 1983). The data collected by a single research vessel is amassed over a period of days or even weeks, i.e. it is not a simultaneous dataset, and the vessel cannot sample large expanses of sea. In addition to these shortcomings, surveys at sea incur a great expenditure of valuable time and money. This is apparent when one considers the cost of data collection and analysis associated with the CPR (continuous plankton recorder) plankton atlas of the North Atlantic and North Sea (Lucas & Glover 1975). Moving away from the sea surface to a high-altitude vantage point provides a perspective not available from ships. The development of Earth satellites turned this dream into reality and heralded a new approach to oceanography, namely satellite oceanography or marine remote sensing. Remote sensing techniques provide synoptic coverage of huge areas in a single 'snapshot'. To some extent ships and satellites furnish complementary

data and there are definite advantages in using them together (Johnson & Harriss 1980). Remote sensing, when used in conjunction with in-situ measurements, is a powerful technique which relies upon the collaboration of science and technology.

1.1.2 Remote sensing

Remote sensing may be loosely defined as the technique by which information concerning a remote object or region is acquired without making direct physical contact. A corollary of this definition is that only electromagnetic or sound waves may be used in remote sensing as both of these interact with matter but do not constitute 'tactile' contact in the everyday sense. In principle therefore, remote sensing embraces photography, human vision, optical and radio astronomy, radar, sonar etc. However, the term is usually reserved for the observation of the surface of the Earth or other bodies in our solar system and assumes that a two-dimensional image will be generated. Remote sensing developed from aerial photography and the term has only been in use since about 1960 (Bauer 1976).

For terrestrial remote sensing, electromagnetic radiation in the form of microwaves, light or infra-red energy is used. Figure 1.1 illustrates the various types of terrestrial remote sensing in a hierarchical fashion, in order of decreasingly important distinctions. Passive remote sensing measures reflected solar energy or radiation emitted by the object, i.e. blackbody radiation, but the term also includes the measurement of the Earth's magnetic or gravitational field. In contrast, when the illumination source is the sensor itself, such as microwave instruments or LIDAR (laser induced fluorescence system), it is termed active remote sensing. Remote sensing may be

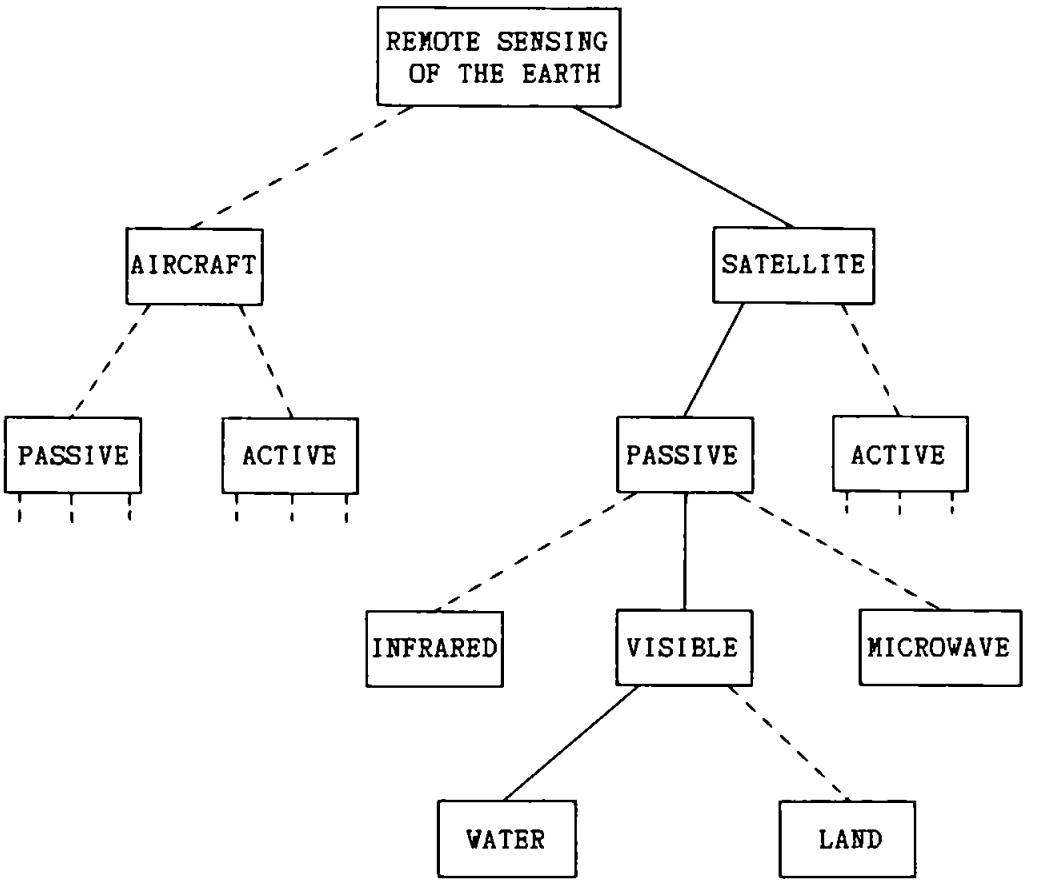

Figure 1.1 Illustration of the different types of remote sensing. The one used in this work is depicted by those rectangles joined with solid lines.

performed from a variety of platforms, including satellites, aircraft, rockets and balloons. Several important distinctions may be drawn between the remote sensing of land and oceans:

(i) Ocean features are less stable than land ones, i.e. the former may change in comparatively short time intervals.

(ii) The signal emerging from within the sea is generally much smaller than that reflected from the land's surface due to the sea's lower albedo. Both the solar elevation and sea-surface roughness influence the sea's albedo.

(iii) Atmospheric correction is necessary for remote sensing of the sea but not for land as a direct consequence of (ii).

The techniques of remote sensing were originally developed for land purposes and their extension to the marine environment is hampered by the above colluding factors. The boxes linked by solid lines in Fig. 1.1 describe the type of remote sensing used in this work. The interactions of light which are involved in marine remote sensing are shown in Fig. 1.2; the scattered and specularly reflected rays represent extraneous signals, whose removal is the task of atmospheric correction. There are many texts available on remote sensing; see for example Colwell (1983), Curran (1985), Holz (1985) and Swain & Davis (1978) for the subject in general and Deepak (1980), Gordon & Morel (1983), Gower (1980, 1981) and Stewart (1985) for satellite oceanography in particular.

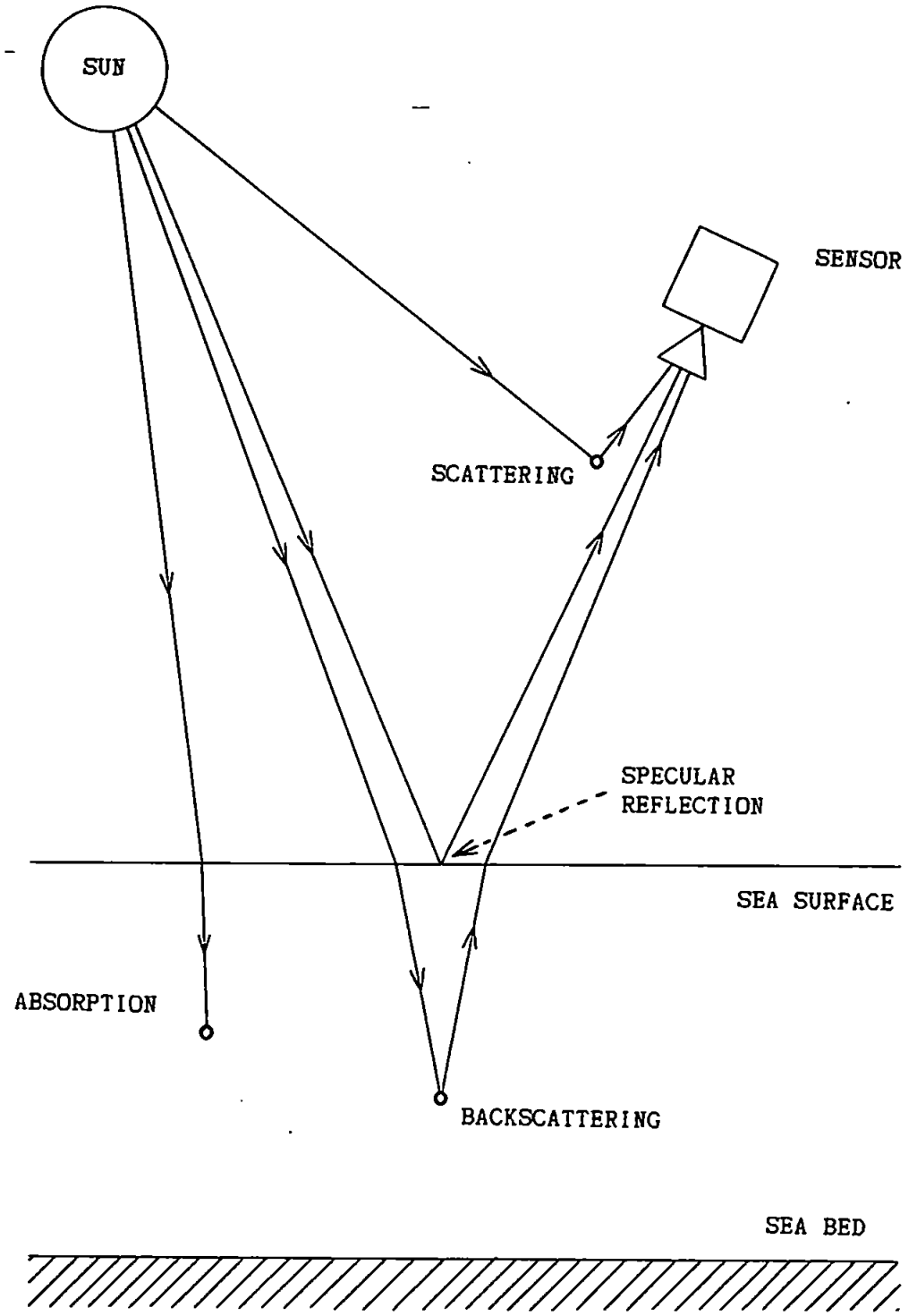

Figure 1.2 Sunlight interacts with the atmosphere and ocean in several ways. The scattered and reflected rays represent unwanted signals.

1.1.3 Ocean colour

The newcomer to remote sensing may be surprised to learn that an ocean's colour is capable of providing detailed quantitative information about the ocean's composition (Bohren 1983). However, one soon realises that for a distant observer the only discernible feature is the variation in colour; in all other respects the sea surface is featureless at large scales. The use of the term 'colour' implies that the visible range of wavelengths is to be considered, being that octave of optical wavelengths which suffers the least atmospheric loss and represents an atmospheric window. It is no accident then that both human vision and photosynthesis exploit this window of maximum energy. Any colour may be defined as a particular combination of the three primary colours (red, green and blue) (Gregory 1979). Since the colour of the oceans is rarely reddish or brown, just two primary colours (green and blue) are needed to define ocean colour (Hojerslev 1980). Measuring the amount of green and blue light emerging from the sea enables a colour index to be defined, from which quantitative information may be inferred. This information may then be used for monitoring marine plants and as an aid to understanding oceanic fertility and fisheries management. The identification of different objects or materials ultimately relies upon the analysis of spectral variations in the measured signals.

1.1.4 Water types

Natural waters exhibit highly variable properties and this is reflected in Jerlov's (1968) optical classification scheme which distinguishes between ten different water types. In the context of remote sensing though, a distinction only needs to be made between two basic water types (Morel & Prieur 1977):

(i) Case 1 waters whose optical properties are determined solely by phytoplankton and their byproducts. Absorption of light by pigments is the dominant process in these waters.

(ii) Case 2 waters whose optical properties are determined by materials other than those in Case 1, i.e. resuspended organic and/or inorganic sediments and terrigenous particles. In this situation, particle scattering is the primary process; pigment absorption is of secondary importance.

The differences are summarised in Fig. 1.3. Components 1, 2 and 3 tend to co-vary and a water body containing one or more of components 4, 5 or 6 is classified as Case 2 (Gordon & Morel 1983). Ocean waters usually belong to Case 1, while coastal waters are usually Case 2; although it is quite possible for coastal waters to be Case 1. Case 2 waters are more difficult to sense remotely due to the unpredictable nature of sediments and particulate material.

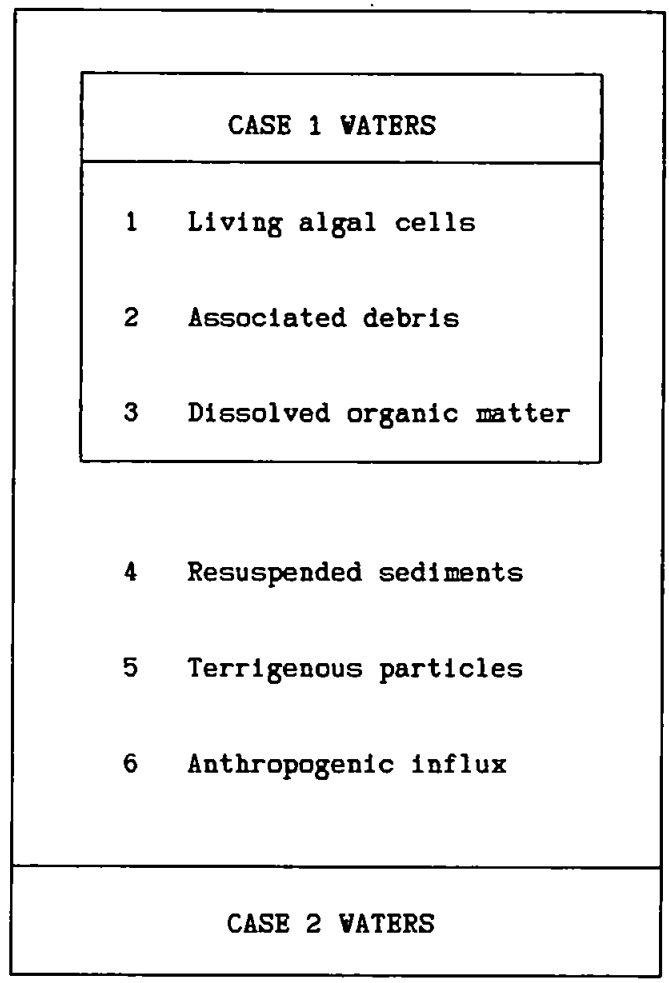

Figure 1.3. Definition of Case 1 and Case 2 waters in terms of constituents. (Taken from Gordon and Morel 1983.)

1.2 MARINE RESOURCES

1.2.1 Photosynthesis and the role of chlorophyll

Without photosynthesis there would be no form of life, as we know it, on Earth. Photosynthesis by all plants traps on average 1% of the solar radiation incident upon the Earth's surface and stores it in carbohydrates, proteins, fats and other energy-yielding compounds (Milgrom 1984). A supply of carbon dioxide, water, light and nutrients (nitrates, phosphates and silicates) is required for photosynthesis. Approximately one half of the annual carbon production by photosynthesis takes place in the sea (Yentsch 1983). Apart from producing energy for the maintenance and growth of life, oceanic photosynthesis is a major source of atmospheric oxygen (Apel 1983). In the sea, photosynthesis is accomplished by phytoplankton - microscopic plant organisms whose sizes range from less than 5μm to 1mm or more. Plankton have no means of propulsion; they merely float and drift under the influence of wind and currents (Boney 1975). Phytoplankton, therefore represent the primary producers of organic matter which support the whole marine food chain and hence their abundance largely determines and reflects the total marine productivity (Stowe 1979). Photosynthesis relies upon certain photosynthetic pigments for its operation, principally chlorophyll 'a', which is regarded as the key indicator of potentially productive waters on account of its characteristic absorption spectrum in the visible range. These photosynthetic pigments, including chlorophyll 'a', are contained within the phytoplankton, of which the most abundant species are diatoms and dinoflagellates. The principle of remote sensing of chlorophyll 'a', and hence phytoplankton, is that chlorophyll absorption influences ocean colour with absorption peaks at 440 and 675 nm in the visible region. Both the standing crop of phytoplankton and

its corresponding primary productivity are related to ocean colour (Hojerslev 1980).

1.2.2 Nutrients and ocean fronts

Except in upwelling regions, nutrient levels limit the growth of phytoplankton. Nutrients are introduced into the euphotic or upper layer of the water column by the upwelling of deeper, cooler water. Photosynthesis does not take place below the euphotic zone due to a shortage of light. Productive regions therefore have well-mixed water columns and no thermocline, whereas stratified regions of low productivity develop thermoclines which inhibit the influx of nutrients. The thermocline is an abrupt temperature transition marking the boundary between two separate layers; the upper one containing warm water of low density, the lower one with cold water of higher density. Water column mixing is produced by tides, wind and currents in conjunction with bottom friction (Yentsch 1983). The likelihood of full vertical mixing depends upon the water depth and tidal velocity (Simpson & Hunter 1974, Yentsch & Garfield 1981).

Ocean fronts are horizontal boundaries between dissimilar water masses (Johnson & Harriss 1980, Le Fèvre et al. 1983, Holligan et al. 1984a, 1984b) and the spatial structure of temperature and ocean colour fronts are similar (Mueller & LaViolette 1981, Yentsch & Garfield 1981, Gordon & Morel 1983) because productive regions contain relatively cold water and vice versa. However, this is not always the case for two reasons. Firstly, remotely-sensed chlorophyll applies to depths of 1 to 20 metres or so, over which there is likely to be considerable vertical structure in chlorophyll concentration while infrared measurements register the temperature of the top 0.05mm of the sea only (Mueller &

LaViolette 1981). Secondly, peak phytoplankton growth occurs after the maximum in nutrient level, producing a time lag between the two types of imagery. In conclusion then, visible and thermal imagery do not necessarily represent a duplication of information.

1.2.3 Fisheries

The total productivity of all plant life on Earth, in terms of fixed carbon, is approximately 100×10^9 metric tons per annum (Boney 1975). A significant proportion of this (20×10^9 tons) is produced in the oceans (Smith & Baker 1983). This reference contains a thought-provoking table of mean and total productivity values for open oceans, coastal zones and upwelling areas. The total weight of fish (or tertiary consumers) is only a tiny fraction of the marine productivity because the number of grazers or consumers in the food chain (Boney 1975) diminishes markedly with each step up the chain and also because of organic matter consumed for respiration purposes. The latter would otherwise be available for tissue formation. It has been estimated that the annual quantity of fish harvested during the 1970s was about 70 million tons (Johnson & Munday 1983). Furthermore, only an additional 30 million tons could have been produced economically. The most productive regions surrounding the UK are the fronts of Ushant, Flamborough and Islay in which dense patches or blooms of phyto-plankton develop in the spring and autumn, making them prime fishing sites (Pingree et al. 1975). These areas are poorly researched and thus not fully exploited. The prediction of phytoplankton distributions (both temporal and spatial) would be of great assistance in the management of the sea and its resources.

1.3 REMOTE SENSING TECHNOLOGY

1.3.1 Preamble

Before the era of satellite oceanography, photographic images taken from aircraft were used to monitor water quality or turbidity in terms of concentrations of chlorophyll and suspended solids (Klooster & Scherz 1973, Lillesand et al. 1975, Deschamps et al. 1977). This form of imagery is still put to good use in the 1980's (Khorram 1981a, Spitzer et al. 1982). The requirement for atmospheric correction is less severe for airborne remote sensing and may even become unnecessary at low altitudes.

Despite its inadequate radiometric sensitivity and inferior spectral resolution, the LANDSAT (formerly ERTS - Earth Resources Technology Satellite) series of satellites has been used extensively for satellite oceanography (Alberotanza & Zandonella 1981, Brooks 1975, Horstmann & Hardtke 1981, Khorram 1981b, Kritikos et al. 1974, Le Fevre et al. 1983). However, the spaceborne instrument used in this work is NASA's Coastal Zone Color Scanner (CZCS) which is an experimental sensor carried on the Nimbus-7 satellite, specially designed for the remote assessment of ocean colour. The Multispectral Electronic Self-Scanning Radiometer (MESSR), aboard Japan's Marine Observation Satellite (MOS-1), represents the only true successor to the CZCS, in the sense that its spectral and radiometric characteristics are suitable for ocean colour measurement. The MOS-1, is due for launch in late 1986 or early 1987 (Moore 1986).

The collection of sea truth for the validation of CZCS data is achieved with the undulating oceanographic recorder (UOR) (Aiken 1980, 1981a, 1981b). The UOR measures chlorophyll fluorescence as an indicator of

chlorophyll concentration in $mg.m^{-3}$. This is in contrast with the CPR which captures plankton on a strip of cloth whilst the ship is underway and provides the number density and species composition of phytoplankton (Boney 1975).

1.3.2 The CZCS

The CZCS is a mechanically-scanning radiometer with six spectral channels, viewing the Earth from an altitude of 955 km in a near-polar Sun-synchronous orbit. Four channels are in the visible range, one in the near infrared and one in the thermal infrared. Each scan of the Earth is 1600 km wide and the ground resolution is nominally 825 metres. The CZCS has a tilt mechanism for the avoidance of Sun glint (specular image of the Sun) and its data is quantised to 256 levels (8 bits). As the diffuse reflectance or albedo of the sea is so small, the CZCS features an unusually high radiometric sensitivity. The specific purpose of the CZCS is to estimate the near-surface concentration of phytoplankton pigments and total seston, being the first satellite-borne instrument of its kind. It can also measure surface temperature and the diffuse attenuation coefficient (Gordon 1981b). The CZCS enables the distribution of phytoplankton chlorophyll to be visualised and changes in time and space, such as phytoplankton blooms, to be observed. It is capable of delineating subtle variations in ocean colour through a turbid atmosphere. Remote sensing with the CZCS is no panacea for the oceanographer though, as it suffers from several difficulties peculiar to satellite oceanography, namely:

(i) Ocean colour imagery can only be acquired in the daytime and under cloudless conditions; these are fundamental restrictions which cannot be avoided in the visible range.

(ii) The CZCS has insufficient spectral resolution to distinguish between chlorophyll and degraded photosynthetic pigments, such as phaeopigments.

(iii) Only the uppermost part of the water column (20 metres or less) is probed by the CZCS, implying that phytoplankton chlorophyll peaks may be too deep for detection; furthermore all information on vertical structure is lost (Platt & Herman 1983).

Although the CZCS only samples the upper layer, the remotely-sensed chlorophyll concentration is still a reliable index of total chlorophyll in the water column because the euphotic and penetration depths are highly correlated (Smith & Baker 1983).

1.3.3 Digital image processing

Spaceborne remote-sensing instruments view great expanses of the Earth with ever-increasing spatial resolution. This results in prodigious quantities of data, which will only increase in the future. For the CZCS, a standard scene consisting of just 2 minutes of data corresponds to an area of approximately 1600 by 800 km (Hovis 1982) and represents about 2×10^6 pixels per channel, thus totalling 12×10^6 pixels in all. Only by using a digital computer can these high volumes of digital data be handled, especially as the data is usually supplied on computer-compatible tapes. There is also the additional and essential requirement to extract a subset of the data and convert it into two-dimensional form for display purposes. This is achieved through the use of an imagestore or framestore coupled to a high-resolution monitor. Collectively a computer and imagestore, in conjunction with

a suitable software package, constitute an image processor which is also used to perform data analysis and extraction of housekeeping and calibration information etc. An image processor has now become indispensable for fast and efficient extraction of salient information from raw data.

1.4 OBJECTIVES

The aims of this project fall into two broad categories. Firstly, the design and construction of an appropriate low-cost image processor for the display and manipulation of images. This involves both hardware and software development and represents the engineering component of the project. Secondly, the creation of a software package for the correction and analysis of remotely-sensed data in order to quantitatively map the distribution of phytoplankton in productive coastal waters. This process relies upon sea truth for the validation of retrieval algorithms. More specifically, the objectives of this work are:

(i) The development of a low-cost 768 by 512 pixel imagestore and its interfacing to a minicomputer. Provision of software for controlling the imagestore and managing the transfer of data between imagestore and computer.

(ii) The development of a pipeline processor and associated software for the real-time evaluation of simple retrieval algorithms.

(iii) The establishment of a monochrome broadcast-quality camera facility for transferring images from photographic prints and transparencies to the imagestore.

(iv) The production of software for routine image processing, such as contrast stretch, histogram equalisation, false and pseudo colour, smoothing and sharpening.

(v) The extraction of housekeeping information and calibration values from raw CZCS data, and the generation of spectral images.

(vi) The radiometric conversion and atmospheric correction of CZCS spectral images, including the calculation of Sun-satellite geometry.

(vii) The rectification of CZCS images in order to locate pixels corresponding to sites sampled by ship.

(viii) The application of linear, power and polynomial regression techniques to develop relationships between CZCS radiances and either CPR sea truth or UOR chlorophyll concentrations.

(xi) The application of novel clustering methods (unsupervised classification) for mapping relative phytoplankton concentration from CZCS data.

CHAPTER 2

PHYSICAL AND TECHNOLOGICAL BASIS OF REMOTE SENSING: OCEAN COLOUR AND THE CZCS

This chapter examines the principles of marine remote sensing in detail, that is the theoretical relationships between ocean colour and the optical properties of sea water, and the characteristics of the Nimbus-7 and CZCS used for measuring ocean colour. Atmospheric effects and the estimation of water-leaving radiances are discussed later in chapter 4. The techniques and instruments used for direct in-situ measurement of chlorophyll concentration are described briefly.

2.1 MARINE OPTICS

2.1.1 Ocean colour

The physics of marine optics and more particularly ocean colour is well understood and developed (Jerlov 1968, 1976). The term 'ocean colour' is not simply the colour of the ocean as perceived by human vision; it has a stricter and far less arbitrary definition in terms of upwelling and downwelling irradiance (Appendix 1). Intrinsic ocean colour is the spectrum of the reflectance $R(\lambda)$ in the visible region with $R(\lambda)$ defined by (Morel and Prieur 1977, Gordon 1980, Morel 1980, Gordon and Morel 1983):

$$R(\lambda) \equiv E_U(\lambda)/E_D(\lambda) \qquad (2.1)$$

where $E_U(\lambda)$ and $E_D(\lambda)$ are the upwelling and downwelling irradiance respectively, measured just beneath the sea surface (Fig. 2.1). Consequently $R(\lambda)$ is not influenced by specular reflection at the

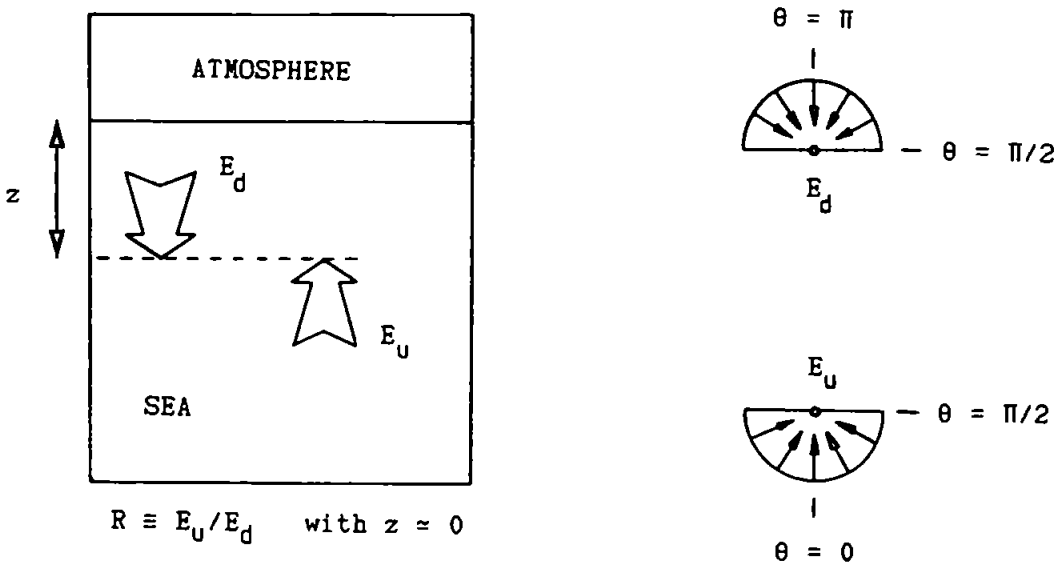

Figure 2.1 Reflectance and irradiance. E_d (E_u) is the total downwelling (upwelling) irradiance over the upper (lower) hemisphere.

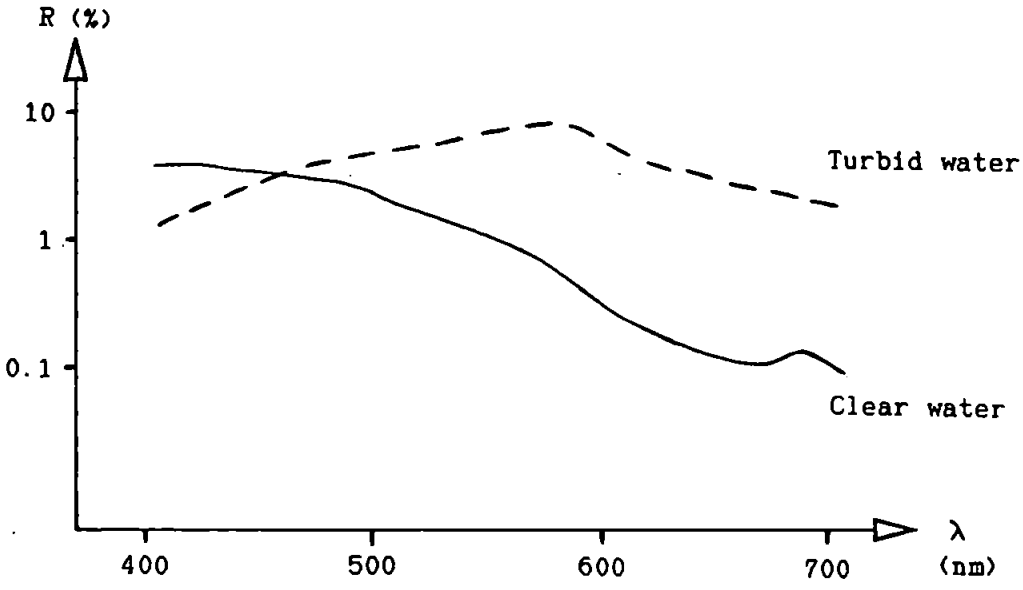

Figure 2.2 Typical ocean colour spectra, R(λ). [After Morel (1980)].

surface. The $R(\lambda)$ is also known as irradiance ratio or irradiance reflectance and represents the fraction of downwelling photons which return towards the surface as upwelling photons. Although the mechanism by which downwelling photons are redirected upwards to the surface is called scattering, the term reflectance is used since reflection is just one manifestation of the scattering phenomenon. The upwelling radiance is approximately diffuse or uniform just below the sea surface (Gordon 1976b), thus enabling the definition of $R(\lambda)$ to be stated in terms of irradiance only. For a given water body and wavelength, $R(\lambda)$ is constant, i.e. it is independent of E_D. Any changes in E_D cause a proportional change in E_U. Therefore E_D may be regarded as a normalisation factor which renders $R(\lambda)$ independent of illumination conditions above the surface. $R(\lambda)$ exhibits little change with variations in solar zenith angle (Kattawar and Humphreys 1976), being less than 15% for angles of 0° to 60° (Gordon 1976b). The solar zenith angle is the angle between the Sun-to-pixel and zenith-to-pixel directions. The water content directly affects $R(\lambda)$ which may therefore be used to discriminate between different water types (Morel 1980). Figure 2.2 shows typical reflectance spectra for clear and turbid waters. R is usually only a few percent, but may reach 10% or fall below 1%, depending upon the wavelength and the water's constituents.

2.1.2 Ocean colour and optical properties

The relationship between ocean colour and the inherent optical properties of sea water is derived from the solution of the equation of radiative transfer (Jerlov 1968, Thomas 1980). As this equation is an integro-differential one (Jerlov 1968), it is solved numerically and usually by incorporating simplifying assumptions. Many workers have

tackled this problem but only two approaches are discussed here. Firstly, Gordon and Brown (1973) identified the single scattering albedo ω_0 (= b/c) and the scattering phase function ($P(\theta)$) as the determinants of R. Then a Monte-Carlo method (Gordon et al. 1975) was used to simulate the passage of photons through water, assuming that all forward scattering occurs at 0° (quasi single scattering approximation). It was found that R could be expressed as a polynomial expansion:

$$R = \sum_{i=1}^{3} r_i X^i \tag{2.2}$$

with X given by:

$$X = \frac{b_b}{a + b_b} \tag{2.3}$$

As the first term is dominant, it is valid to state that R is proportional to X or:

$$R \propto \frac{b_b}{a + b_b} \tag{2.4}$$

The constant of proportionality varies between 0.32 (Sun near the zenith) and 0.37 (totally diffuse illumination). The value a is the absorption coefficient of sea water and b_b is the backscattering coefficient, which is derived from the volume scattering function $\beta(\theta)$ (Appendix 2). At this stage it is useful to distinguish between inherent and apparent optical properties. Inherent ones are invariant with respect to changes in radiance distribution, while apparent ones are not.

The inherent properties are:

i) Absorption coefficient - a.

ii) Volume scattering function - $\beta(\theta)$.

iii) Total scattering coefficient - b (derived from $\beta(\theta)$).

iv) Forward and backscattering coefficients - b_f and b_b (derived from $\beta(\theta)$).

v) Attenuation coefficient - c (c = a + b).

Hence R is directly related to the inherent optical properties a and b_b of sea water, and does not change with variations in the distribution of radiance above and hence below the surface.

The second analysis of the radiative transfer problem is due to Morel and Prieur (1977) who used the successive order scattering method, resulting in the expression:

$$R = 0.33 \left| \frac{b_b}{a} \right| (1+\Delta) \qquad (2.5)$$

The Δ term depends upon the radiance distribution and $\beta(\theta)$ but never falls outside the range $\pm$ 0.05, so for practical use it may be neglected giving:

$$R = 0.33\ b_b/a \qquad (2.6)$$

Moreover Δ is only slightly wavelength-dependent in the visible spectrum. Eq. 2.6 is only valid for small values of b_b/a, i.e. < 0.3 (Sathyendranath and Morel 1983).

In almost all oceanic and coastal waters $b_b \ll a$ in the visible region (Morel and Prieur 1977, Gordon and Morel 1983, Kirk 1983, Sathyendranath and Morel 1983), in which case Eq. 2.4 may be simplified to the same form as Eq. 2.6. These two equations also share almost identical constants and together provide strong theoretical support for a direct link between R and a and b_b. We may conclude then, that R is governed by the ratio of back-scattering to absorption. This may be understood physically by referring to Fig. 2.3. The appearance of b_b in the denominator of Eq. 2.4 accounts for double backscattering which causes upwelling photons to be redirected downwards.

The analysis so far has been solely concerned with diffuse reflectance, i.e. the fraction of downwelling irradiance transformed into diffuse upwelling irradiance. However a remote sensor is only capable of measuring directly the water-leaving radiance L_W (after atmospheric correction if necessary), and not $R(\lambda)$. The relationship between $L_W(\lambda)$ and $R(\lambda)$ is derived here and starts with definitions of E_U and E_D (Fig. 2.1) from which R itself is defined (Gordon and Morel 1983, Sathyendranath and Morel 1983):

$$E_U = \int_0^{2\pi} \left[\int_0^{\pi/2} |\cos\theta| \cdot L_U(\theta,\phi) \sin\theta \, d\theta \right] d\phi \qquad (2.7)$$

E_D is defined in a similar way but with the limits of 0 and $\pi/2$ (integration over θ) replaced by $\pi/2$ and π respectively. $L_U(\theta,\phi)$ is the sub-surface upwelling radiance in the direction (θ, ϕ), where θ is the angle in the vertical plane (Fig. 2.4) and ϕ is the azimuthal angle (horizontal plane). If $L_U(\theta,\phi)$ is independent of θ and ϕ, then

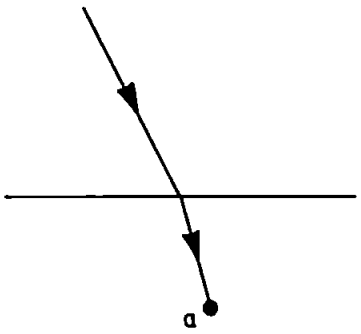

(i) Absorption
- reduces R.

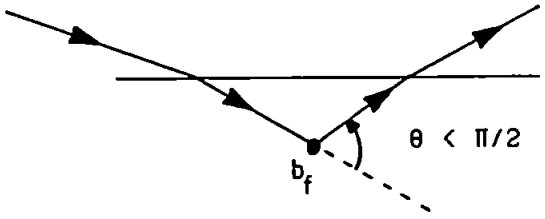

(ii) Forward scattering may increase R, but with a fairly high sun, this is unlikely. Thus, this mechanism may be neglected and b_f does not appear in the expression for R.

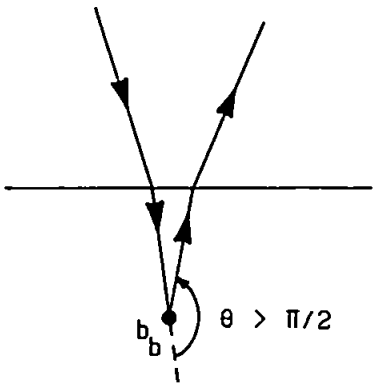

(iii) Backscattering
- increases R.

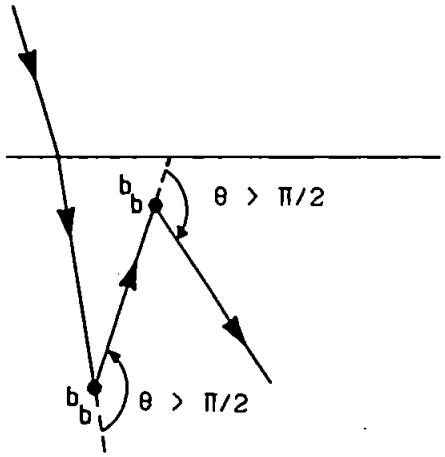

(iv) Double backscattering
- may reduce R.

$$R \propto \frac{b_b}{a + b_b}$$

(iii) → b_b; (i) → a; (iv) → b_b

In most natural waters $b_b << a$, thus $(a+b_b) \simeq a$, in which case:

$$R \propto b_b/a$$

Figure 2.3. Relationship between R, a and b_b.

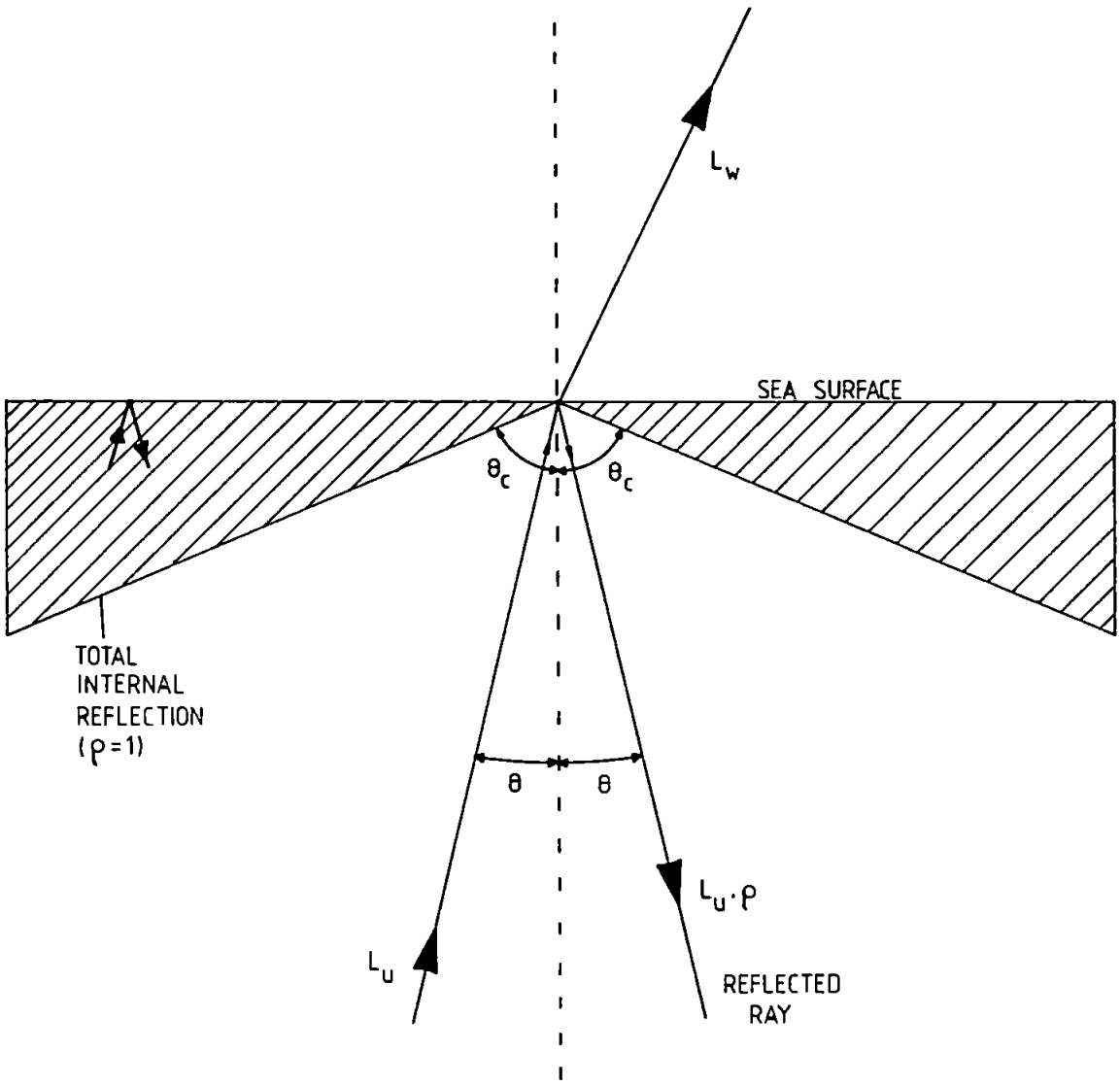

$\rho \approx 0.02$ FOR A SMOOTH SURFACE

ρ - REFLECTANCE

θ_c - CRITICAL ANGLE

$\theta_c = \sin^{-1}(1/1.341)$

$\approx 48^\circ$

[1.341 = REFRACTIVE INDEX OF SEAWATER]

FIGURE 2.4 UPWELLING (L_u) AND WATER-LEAVING (L_w) RADIANCE

Eq. 2.7 becomes:

$$E_U = \pi L_U \tag{2.8}$$

Unfortunately, this is not quite true because for θ greater than the critical angle (48°; Fig. 2.4), total internal reflection occurs at the water-air interface and the radiance for $\theta > 48°$ increases rapidly (Plass et al. 1975). However, for $\theta < 48°$, the radiance is approximately uniform and the relation for L_U becomes:

$$L_U = E_U/Q \tag{2.9}$$

where L_U is the radiance in the zenith direction and Q is approximately 5 (Austin 1980). Theoretically Q displays a small wavelength dependence which is negligible in the visible range. L_U is related to R by:

$$L_U = R.E_D/Q \tag{2.10}$$

The water-leaving radiance L_W may be found from L_U via (Morel 1980):

$$L_W = L_U (1 - \rho)/n^2 \tag{2.11}$$

L_W and L_U exhibit the same spectral behaviour. The $(1 - \rho)$ term accounts for loss due to total internal reflection, with $\rho \approx 0.02$. The reduction in radiance due to change in refractive index is accounted for by the n^2 term, where n is the refractive index of sea water relative to air (1.341). This reduction does not imply an energy loss;

it is merely a consequence of the increase in solid angle which occurs for a sub-surface cone of light emerging above the surface. Substituting for L_U in Eq. 2.11 from Eq. 2.10:

$$L_W = \frac{R.\ E_D}{Q} \cdot \frac{(1 - \rho)}{n^2} \qquad (2.12)$$

Austin (1980) gives $(1 - \rho)/n^2$ as 0.544 and so finally the relationship between L_W and R is:

$$L_W(\lambda) = 0.544\ \frac{R(\lambda).E_D(\lambda)}{Q} \qquad (2.13)$$

where λ has been introduced to identify the wavelength-dependent quantities. E, L and R are always regarded as spectral quantities although this may not be indicated for the sake of brevity. For practical purposes and under favourable conditions (clear sky and high solar altitude), the ratio of L_W at two wavelengths is assumed to be proportional to the corresponding ratio of R (Sathyendranath and Morel 1983).

As far as photosynthesis is concerned, red (λ = 700nm) and blue (λ = 400nm) photons or quanta are equally effective in promoting photosynthesis (Kirk 1983), despite the fact that blue quanta carry almost twice as much energy as red ones. In this context it is more appropriate to express radiant flux in quanta.s^{-1} than in watts. The number of quanta per second corresponding to a radiant flux of Φ watts is given by:

$$\frac{\Phi}{h\nu} = \frac{\Phi}{hc/\lambda} = \frac{\Phi\lambda}{hc} = 5.034 \times 10^{24}\Phi\lambda \qquad (2.14)$$

where ν and λ are the frequency and wavelength respectively of the photons, with λ in metres. h is Planck's constant and c is the velocity of light. This expression assumes that all photons have the same wavelength.

2.1.3 Influence of ocean constituents upon optical properties

It has already been shown that R is determined by the ratio (b_b/a), and Gordon (1977) asserts that the only parameter which may be determined from remote sensing is this combination of inherent optical properties. The next stage in understanding the remote sensing of ocean colour is to investigate how the composition and concentration of ocean constituents influence a and b_b and thus (b_b/a). All inherent optical properties, including a and b_b, are rigorously additive (Gordon 1977, Sathyendranath and Morel 1983), i.e. the total coefficient is simply the sum of coefficients for each constituent. The total absorption and backscattering coefficients are:

$$a = a_W + \sum_{i=1}^{n} a_i \qquad (2.15)$$

$$b_b = b_{bW} + \sum_{i=1}^{n} b_{bi} \qquad (2.16)$$

where a_W and b_{bW} apply to pure water and a_i and b_{bi} apply to constituent i for an ocean with n constituents. As the scattering phase function of pure water is symmetrical, b_{bW} may be replaced by $b_W/2$:

$$b_b = b_w/2 + \sum_{i=1}^{n} b_{bi} \tag{2.17}$$

where b_w is the scattering coefficient of pure water. If each constituent i has concentration C_i, then Eqs. 2.15 and 2.17 may be represented as (Sathyendranath and Morel 1983):

$$a = a_w + \sum_{i=1}^{n} a_i^* C_i \tag{2.18}$$

$$b_b = b_w/2 + \sum_{i=1}^{n} b_{bi}^* C_i \tag{2.19}$$

where the asterisk denotes that the coefficient is 'specific', i.e. per unit concentration of constituent i. Once these specific coefficients are known for each constituent and for all visible wavelengths, R may be expressed in terms of the different concentrations.

It might be thought that Rayleigh's theory (Rayleigh 1871a, b, c) would be adequate for describing the scattering of light by water molecules since the molecular size is much smaller than the wavelength of visible light. Indeed it does reproduce satisfactorily the observed dependence of the scattering coefficient upon wavelength and scattering angle. Unfortunately, the scattering intensity is seriously overestimated as the theory takes no account of the strong molecular interactions which occur in liquids (Sturm 1981), but not in gases for which the theory was developed. A proper solution was provided by Smoluchowski (1908) and Einstein (1910) who proposed that molecular scattering in liquids is due to fluctuations in density at the microscopic level which produce corresponding fluctuations in the local dielectric constant. This in turn causes the refractive index to fluctuate as refractive index is the square root of relative permittivity or dielectric

constant (Yarwood 1973). The changes in refractive index are responsible for this type of scattering which is known as 'density fluctuation scattering' (Jerlov 1968). Density fluctuations are caused by the continuous random motion of molecules. Although the predicted wavelength dependence is λ^{-4} under this regime, the observed dependence is slightly different, namely $\lambda^{-4.3}$ (Morel and Prieur 1977); the discrepancy being due to a small variation in the refractive index of water with wavelength (Kirk 1983).

The Smoluchowski-Einstein theory alone is insufficient for describing scattering in the sea as even the clearest waters contain suspended particles in abundance, which exhibit an approximately hyperbolic size distribution (Bader 1970). Some theoretical studies assume different size distributions, namely normal and log-normal (Morel and Bricaud 1981) or $r^6 \exp(-2r)$ (Kattawar and Humphreys 1976) where r is the particle radius. Despite these different distributions, they all indicate that particles may be present in a wide range of sizes and more importantly that the particle size may be comparable with or greater than the wavelength of visible light. In this case Mie's scattering theory (Mie 1908) must be used instead. Mie and Rayleigh scattering are discussed further in section 4.2.1.

Particle scattering in natural waters is very strongly peaked in the forward direction (Gordon 1973) and the degree of asymmetry is described by the back-scattering ratio r_p, defined as the ratio of the backscattering coefficient b_b to the total scattering coefficient b. For phytoplankton this ratio is of the order of 0.1% whereas for non-chlorophyllian particles it is 1 or 2% (Sathyendranath and Morel 1983). The term 'non-chlorophyllian' refers to particles which are not

derived from phytoplankton or its byproducts. Since r_p is small for phytoplankton and non-chlorophyllian particles $b_b \ll b$, bearing in mind that it is b_b and not b upon which R depends. Scattering and backscattering are depressed at wavelengths corresponding to strong absorption bands (Morel and Bricaud 1981), with the scattering spectrum assuming the inverse form of the absorption spectrum (Sathyendranath and Morel 1983).

Optically pure water exhibits low absorption from 400 to 600nm, with a slight minimum around 430nm; from 600nm onwards the absorption increases rapidly (Fig. 2.5). This increase in the red end of the spectrum is in fact the tail-end of a series of distinct absorption bands in the infra-red (Jerlov 1968). The coefficient of molecular scattering by water $b_W(\lambda)$ is approximated by (Sathyendranath and Morel 1983):

$$b_W(\lambda) = b_W(500)\left(\frac{\lambda}{500}\right)^{-4.3} \qquad (2.20)$$

where $b_W(500)$ is $0.00288m^{-1}$ (at 500nm). Since R is proportional to (b_b/a), the reflectance of pure water is high in the blue region and very small in the red, thus accounting for its blue colour. The variation in R is greater than the variation in b_b or 1/a alone.

Natural waters contain many different constituents (Spitzer et al. 1982), categorised by Fig. 2.6. Dissolved material comprises salts and yellow substances. Salts increase the scattering by 30% compared with pure water (Kirk 1983); however of the dissolved materials only the yellow substances are optically important (Jerlov 1968). Yellow

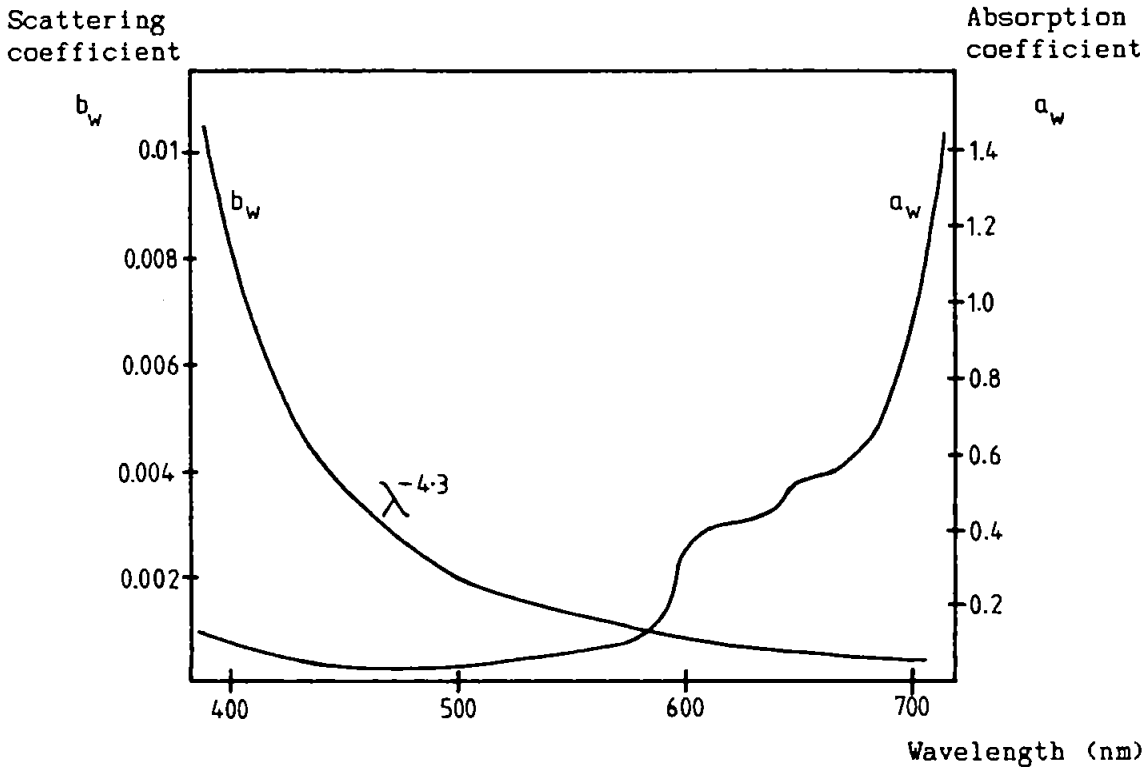

Figure 2.5 Optical characteristics of pure water.

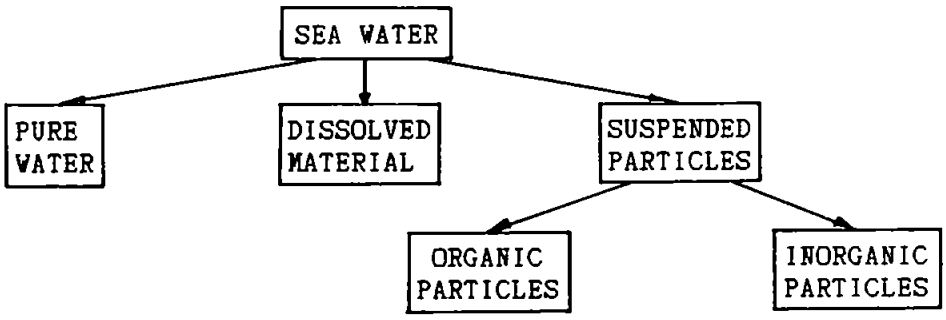

Figure 2.6. Composition of sea water.

substances represent a group of complex organic compounds produced by the decomposition of plant tissue due to microbial action. The major sources of yellow substances are river run-off and land drainage (Hojerslev 1981), although a small amount is released from brown seaweed and phytoplankton (Yentsch 1983). Yellow substances are removed from the oceans by the processes of oxidation and adsorption on sinking particles. The German term 'gelbstoff' is often used as an alternative name for yellow substances. Yellow substances are so named because they shift water colour from blue to yellow as a consequence of their high absorption in the blue region (Fig. 2.7a). This absorption stems from an ultra-violet absorption peak which overlaps the visible spectrum (Yentsch 1983). The absorption spectrum has an approximately exponential form (Deschamps et al. 1977, Johnson and Munday 1983):

$$a_y(\lambda) = a_y\,(500)\,\exp\left[-0.014\,(\lambda - 500)\right] \qquad (2.21)$$

with λ in nm.

The suspended particles or particulates result from wave action, land drainage and rivers and constitute a highly heterogeneous group, which may be divided into two distinct types: organic and inorganic (Brown and Gordon 1974). The organics have a refractive index of 1.01 - 0.01i relative to water; the imaginary part representing absorption. Inorganics or minerals are non-absorbing with refractive index in the range 1.15 to 1.20 relative to water. Consequently, organics may be regarded chiefly as absorbers, while minerals are pure scatterers. Although the bulk of suspended particles is usually organic, scattering is still dominated by the mineral component. The wavelength dependence of mineral scattering (Fig. 2.7b) is typically (Deschamps et al. 1977,

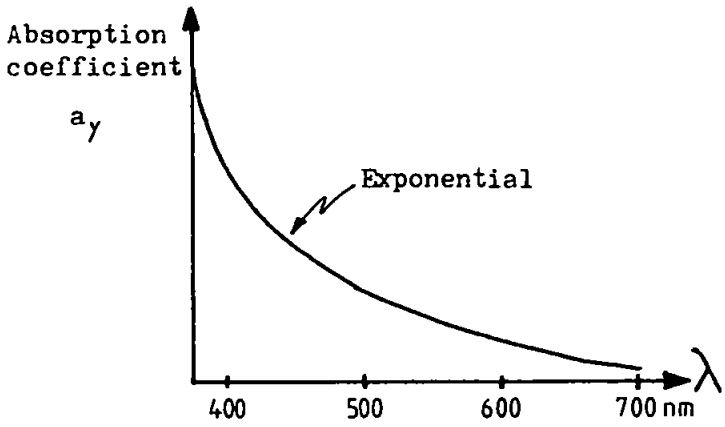

(a) Absorption spectrum of yellow substances.

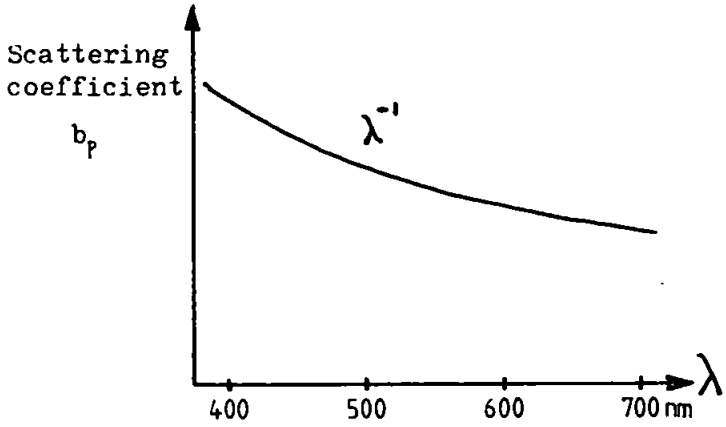

(b) Scattering spectrum of minerals. (Absorption by minerals is small). The scattering dependence may be weaker than λ^{-1}.

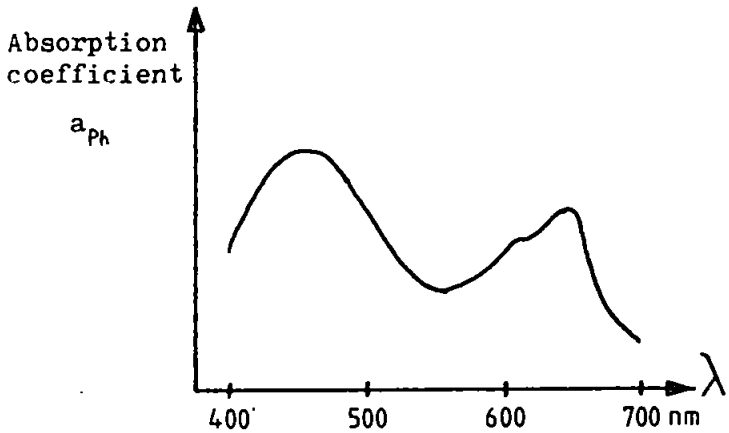

(c) Absorption spectrum of chlorophyll 'a'. (Taken from Clarke et al. 1970).

Figure 2.7 Optical characteristics of ocean constituents. Absolute values are not used as they depend upon the concentration of the constituents.

Morel and Prieur 1977):

$$b_p(\lambda) \approx b_p(\lambda_o)\left(\frac{\lambda}{\lambda_o}\right)^{-1} \qquad (2.22)$$

where $b_p(\lambda)$ and $b_p(\lambda_o)$ are the scattering coefficients at λ and λ_o. The wavelength dependence may be weaker than λ^{-1} in surface waters because the majority of the scattering is by large particles greater than 2μm (Jerlov 1968). Eq. 2.22 is invalid for pigmented or absorbing particles due to the interaction between the scattering and absorption processes in this case (Morel 1980). Although molecular scattering by water only makes a small contribution to total scattering, it may become significant when considering backscattering alone as particle scattering is so strongly peaked in the forward direction (Morel and Prieur 1977).

Phytoplankton and zooplankton constitute suspended organic material and are insignificant as far as scattering is concerned. Phytoplankton though play a significant part in absorption due to the absorption characteristics of the enclosed photosynthetic pigments. Indeed, it is these absorptive features which enable pigment concentrations to be measured remotely. The key photosynthetic pigments are chlorophylls, carotenes and biliproteins (Singh et al. 1983), each of which may exist in slightly different chemical forms; for further details consult Boney (1975). Chlorophylls and carotenes are found in all photosynthetic plants, while only cyanobacteria contain biliproteins as well (Kirk 1983). Chlorophyll 'a' is the dominant chlorophyll and has absorption peaks at 440nm (blue) and 675nm (red) (Fig. 2.7c), although these shift slightly when chlorophyll bonds with proteins or lipids. The blue peak is more intense than the red one. The situation is further complicated

by the presence of chlorophyll 'a' degradation products or phaeopigments, namely phaeophytin 'a' and phaeophorbide 'a' (Singh et al. 1983). The phaeopigments have similar absorption spectra to chlorophyll 'a' with the absorption peaks displaced by 10 or 20 nm towards the blue (Gordon and Clark 1980a). The CZCS only has a few spectral channels and cannot distinguish between chlorophyll 'a' and the phaeopigments and so these are combined to produce a single photosynthetic pigment index. The phaeopigments result from the acidification of chlorophyll 'a' (Gordon et al. 1983b) and are present in small quantities (10 or 20%) compared to chlorophyll 'a' (Gordon et al. 1980a). A particular level of chlorophyll 'a' concentration produces a characteristic reflectance spectrum or spectral signature and over a wide range of concentrations a consistent family of spectra is generated (Fig. 2.8). The mean slope of each spectrum decreases with increasing concentration (Clarke et al. 1970). The apparently anomalous increase in the green region may be explained by the increased phytoplankton backscattering throughout the visible range, emphasised by low chlorophyll 'a' absorption in the green. There is a small region between 500 and 550nm in which the reflectance remains almost constant, irrespective of phytoplankton concentration.

This led to the idea of a 'hinge point' (Hovis et al. 1980, Johnson and Munday 1983) or point of inflection. The response of the CZCS to different chlorophyll concentrations is illustrated in Fig. 2.9 in an idealised form and also shows the hinge point at about 530nm. In addition, the figure provides some justification, albeit abstract, for the use of ratios in chlorophyll retrieval algorithms; the approach being to use CZCS channel 3 (near the hinge point) as a quasi-

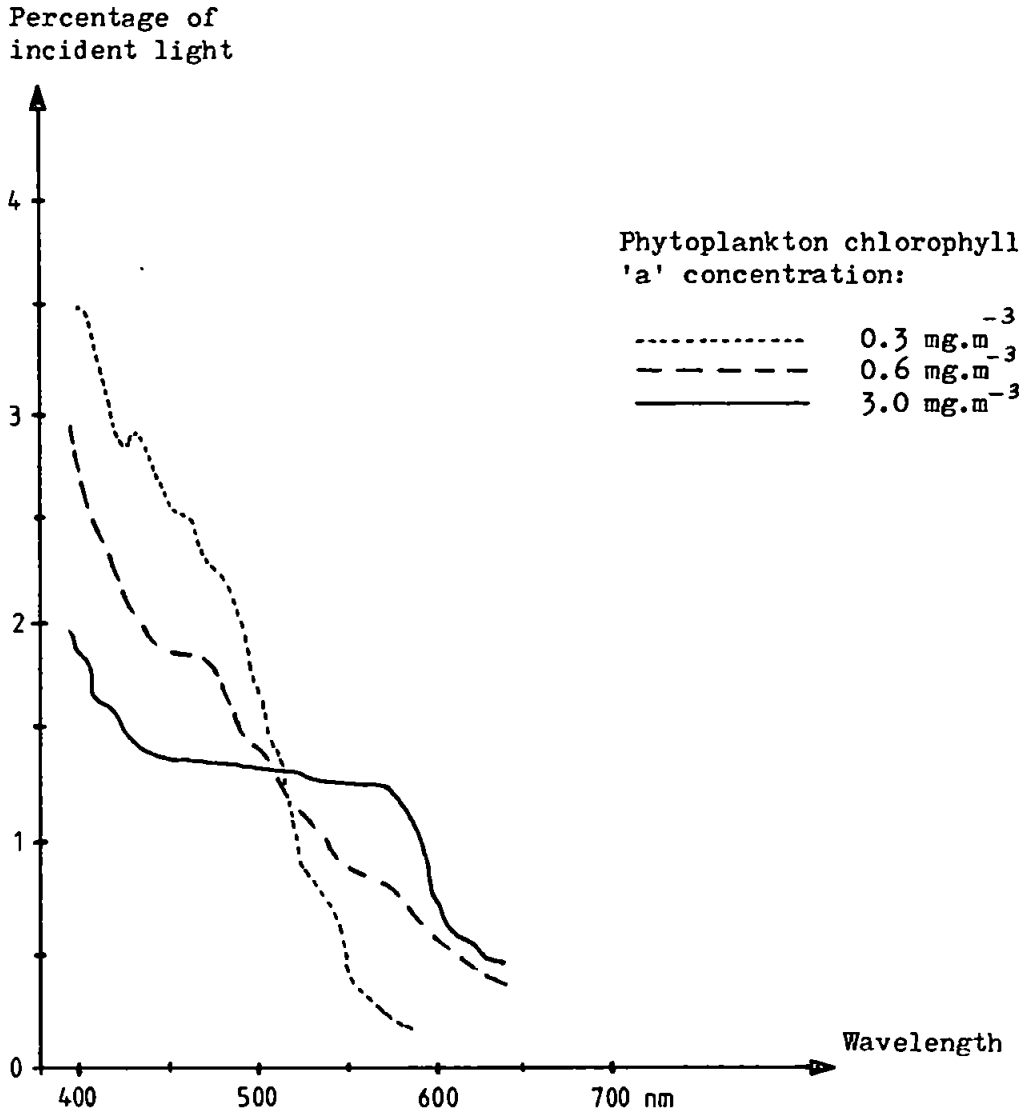

Figure 2.8 Influence of phytoplankton chlorophyll concentration on reflectance (taken from Clarke et al. 1970).

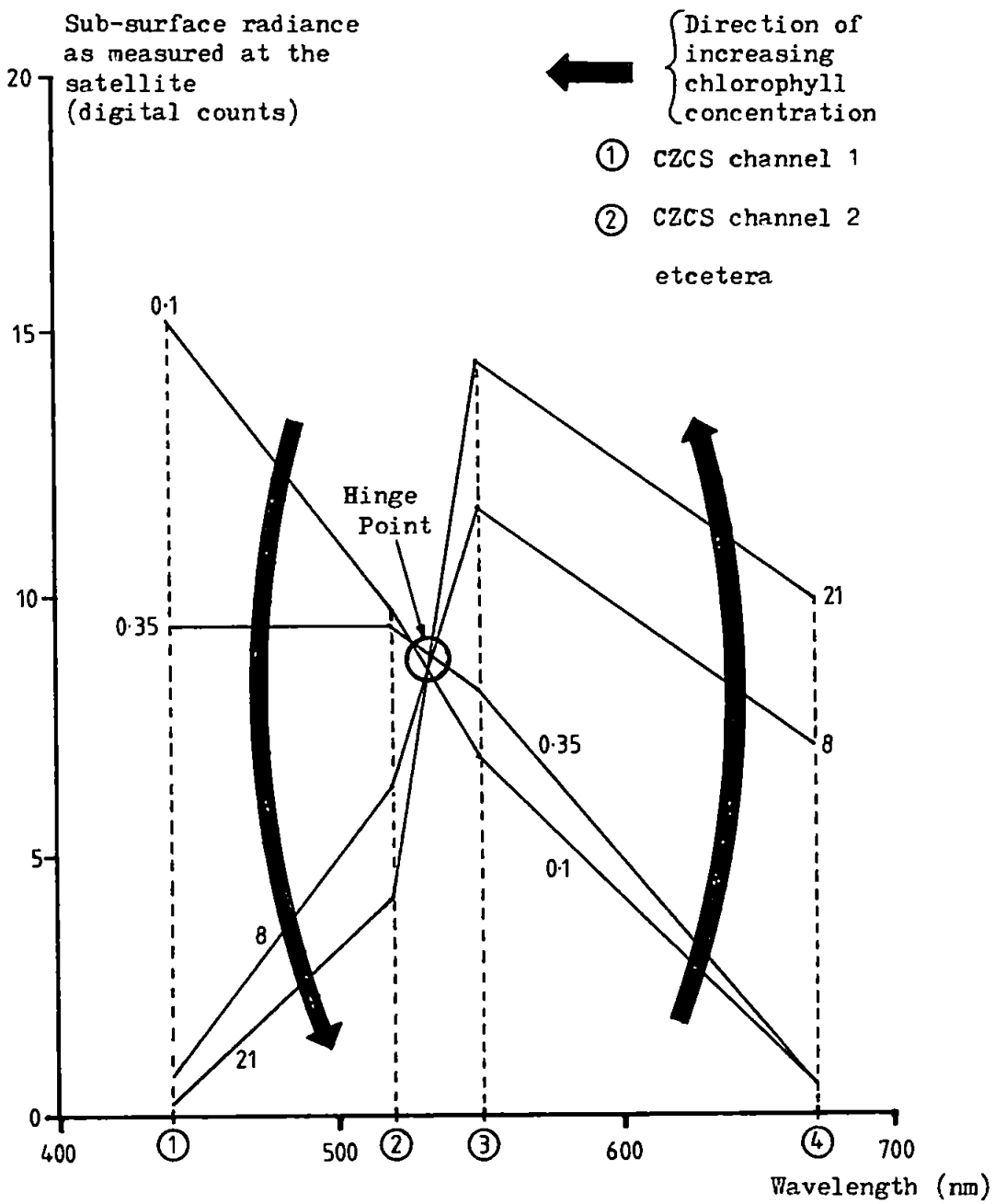

Figure 2.9 Idealised form of radiance spectra for various pigment concentrations in case 1 waters. The chlorophyll concentration is indicated, in $mg.m^{-3}$, for each spectrum. (Taken from Sørensen 1981).

reference, although it will change slightly with the amount of backscattering, and CZCS channel 1 or 2 which are sensitive to chlorophyll concentration.

The total reflectance spectrum for natural waters is governed by the optical characteristics of all the constituents discussed above. The overall absorption and backscattering coefficients are given respectively by (Morel 1980):

$$a = a_W + a_y + a_{Ph} \quad (2.23)$$

$$b_b = b_W/2 + r_p b_p \quad (2.24)$$

assuming that absorption by minerals is negligible, i.e. $a_p = 0$. a_{Ph} is the absorption coefficient for phytoplankton pigments. Changes in absorption modify the spectral shape of R (λ), whereas variations in backscattering cause an overall increase or decrease in R (λ) across the whole visible spectrum (Morel 1980). The perceived colour of natural waters, in terms of dominant wavelength and spectral purity, is highly variable and this variability is also apparent in measured spectra of reflectance (Bartolucci et al. 1977, Morel and Prieur 1977, Morel 1980, Sathyendranath and Morel 1983). This diversity is a direct consequence of the variations in constituents' concentrations and the wavelength-dependent nature of marine optical properties.

Finally there are two additional mechanisms which may contribute to the upwelling radiance and interfere with the remote sensing of ocean composition. The first is reflection from the sea bed which arises in

shallow and/or clear waters, an analysis of which is given by Gordon and Brown (1974). The other mechanism is phytoplankton fluorescence at 685nm caused by chlorophyll 'a', but which amounts to only 1% of the absorbed light (Kirk 1983, Yentsch 1983). Both effects are assumed to be negligible in this work, especially in shelf seas where depths are in excess of 50m.

2.1.4 Other considerations

Downwelling light in the sea is attenuated with depth in an exponential manner (assuming homogeneous optical properties):

$$E_D\ (z) = E_D\ (0)\ \exp\ (-K_D z) \tag{2.25}$$

where $E_D(z)$ and $E_D(0)$ are the downwelling irradiances at depth z and zero depth respectively; the latter being the irradiance just below the surface. K_D is the attenuation coefficient for downwelling irradiance. Eq. 2.25 may be manipulated to define K_D thus:

$$K_D = -\frac{d}{dz}\left[\ln E_D\ (z)\right] \tag{2.26}$$

At great depths the downwelling irradiance becomes vanishingly small and may be considered negligible. In order to establish a measure of significant depth for remote sensing purposes, the concept of 'penetration depth' is introduced, being the depth of the layer (from the surface downwards) from which 90% of the diffusely reflected irradiance originates. Penetration depth is denoted by z_{90} and is approximated (within 10%) by (Gordon and McCluney 1975):

$$z_{90} = 1/K_D \tag{2.27}$$

At this depth the downwelling irradiance falls to 1/e (37%) of its surface value. Since $K_D \geq a$ then:

$$z_{90} \leq 1/a \tag{2.28}$$

Therefore the maximum penetration depth is simply 1/a. When making in-situ measurements of marine parameters for comparison with remotely-sensed estimates, the measurements should be made over the penetration depth at least (Gordon 1978a). The zone in which there is sufficient light to support photosynthesis is known as the euphotic zone and the depth of this zone (as a rule of thumb) corresponds approximately to the depth at which the downwelling irradiance falls to 1% of the surface value. Denoting this depth by z_{eu}, the relation between it and z_{90} is (Gordon et al 1983b).

$$\begin{aligned} z_{eu} &= (\ln 100).z_{90} \\ &\approx 4.6\ z_{90} \end{aligned} \tag{2.29}$$

Both z_{90} and z_{eu} vary with wavelength as K_D is a function of wavelength. For Case 1 waters the maximum value of z_{90} is typically 50m (at 475nm), whereas the maximum for turbid Case 2 waters may only be one or two metres (at 600nm). In the worst case z_{90} may be less than 0.5m at certain wavelengths. The penetration depth cannot be determined from remote measurements (Gordon 1978a).

The influence of an ocean constituent at depth z, compared to the influence it would have just below the surface, is reduced by the

following weighting factor (Smith 1981):

$$g(z) = \exp\left[-2\int_0^z K_D(z')\,dz'\right] \tag{2.30}$$

g(z) accounts for the reduction in the surface irradiance on its downward path to depth z and again for the return path to the surface. At each pixel the remotely sensed parameter is single-valued and so it is impossible to recover the depth profile of pigment concentration C(z) for a stratified ocean. The remotely estimated pigment concentration $\bar{C}$ is related to C(z) by (Gordon and Clark 1980b):

$$\bar{C} = \int_0^{z_{90}} C(z)g(z)dz \Big/ \int_0^{z_{90}} g(z)\,dz \tag{2.31}$$

$\bar{C}$ may be interpreted as that constant pigment concentration (i.e. an homogeneous ocean) which would produce the same water-leaving radiance as the stratified ocean.

Empirical algorithms for the retrieval of pigment concentration commonly use the ratio of water-leaving radiance at two wavelengths λ_1 and λ_2. This ratio is approximately related to the inherent optical properties by:

$$L_w(\lambda_1)/L_w(\lambda_2) = \left[b_b(\lambda_1)/a(\lambda_1)\right]\Big/\left[b_b(\lambda_2)/a(\lambda_2)\right] \tag{2.32}$$

For an ocean containing phytoplankton only, the two backscattering coefficients are nearly equal as backscattering is only slightly dependent upon phytoplankton pigments (Gordon et al. 1983b) and wavelength. Eq. 2.32 therefore simplifies to:

$$L_W(\lambda_1)/L_W(\lambda_2) \approx a(\lambda_2)/a(\lambda_1) \qquad (2.33)$$

Expanding the absorption coefficients in terms of a_W and a^*_{Ph} (the specific absorption coefficient for phytoplankton pigments) gives:

$$L_w(\lambda_1)/L_w(\lambda_2) \approx \left[a_w(\lambda_2) + a^*_{Ph}(\lambda_2).C\right] \Big/ \left[a_w(\lambda_1) + a^*_{Ph}(\lambda_1).C\right] \qquad (2.34)$$

This demonstrates that the relationship between the water-leaving radiance ratio and pigment concentration is inherently non-linear (Gordon et al. 1983b). C is the pigment concentration expressed as the sum of chlorophyll 'a' and phaeopigment concentrations.

2.2 NIMBUS-7 PLATFORM

In 1972 NASA began aircraft investigations to determine whether ocean colour could be measured through the atmosphere (Hovis et al. 1980). Subsequently a prototype ocean colour scanner (OCS) was made and flown in a NASA U-2 plane at an altitude of 20km (Hovis 1981). The results of this experiment (Hovis and Leung 1977) were promising despite the interference of the atmosphere and in 1973 NASA decided to fly the CZCS (based on the OCS) on the Nimbus-G platform due to be launched in 1978. The CZCS was built by Ball Brothers Research Corporation to NASA's specification and hardware development started in January 1975. The Nimbus-G was launched successfully on 24 October 1978, after which it was renamed Nimbus-7.

The Nimbus-7 is the last in the Nimbus series (Baylis 1981) of NASA meteorological satellites intended for research purposes only - it is not an operational system. Besides the CZCS, Nimbus-7 also carries seven other sensors (Slater 1980, Stewart 1985):

i) Earth Radiation Budget (ERB)
ii) Limb Infra-red Monitoring of the Stratosphere (LIMS)
iii) Stratospheric Aerosol Measurement II (SAM II)
iv) Solar Backscattered Ultra-violet and Total Ozone Mapping System (SBUV/TOMS)
v) Stratospheric and Mesospheric Sounder (SMS)
vi) Scanning Multichannel Microwave Radiometer (SMMR)
vii) Temperature - Humidity Infra-red Radiometer (THIR)

The Nimbus-7 must provide a stable platform for the CZCS and the seven other instruments it carries. Due to the effects of roll, pitch and yaw the satellite's attitude will vary slightly but this is usually significantly less than one degree (Wilson et al. 1981).

2.2.1 Orbit and orbital period

A satellite will only maintain a stable orbit of a particular size if its velocity is the correct value; a lower velocity results in the satellite's descent to the ground and a higher one produces a change in orbit or even escape from the Earth's gravitational field altogether. The velocity for a stable orbit is such that the opposing centripetal and gravitational accelerations (and thus forces) are equal. Equating the simple expressions for these two accelerations leads to:

$$v^2 = GM/r \qquad (2.35)$$

where G is the universal gravitational constant and M is the mass of the Earth; the value of GM is 3.98601×10^{14} $m^3.s^{-2}$ (Duck and King 1983). r is the orbit radius from Earth centre to the satellite and v is the satellite's velocity. Since the angular velocity ω (in radians.s^{-1}) is related to v through $v = r\omega$ and the orbital period T is $2\pi/\omega$, then Eq. 2.35 becomes:

$$T = 2\pi\sqrt{\frac{r^3}{GM}} \qquad (2.36)$$

T is in seconds and r is in metres. The CZCS has a nominal altitude of 955km (Hovis 1981) and the equatorial Earth radius is 6378km (King-Hele et al. 1983). Thus r is 7333km, and the orbital period as determined by Eq. 2.36 is 104.15 minutes. This corresponds to 13.83 orbits per day and an orbital speed of 7.4 km.s^{-1}.

The above derivation assumes a perfectly spherical Earth. However the Earth's shape is more accurately described as an oblate spheroid; the equatorial diameter being 43km greater than the polar diameter (Miles 1974). In fact the Earth is slightly elliptical in the equatorial plane. The presence of this oblateness or 'equatorial bulge' prevents the establishment of perfectly circular orbits and results in elliptical ones instead. The CZCS orbit is only very slightly eccentric, having an eccentricity e of 0.0007 (King-Hele et al. 1983). This causes the Earth to be displaced from the centre of the ellipse by approximately 5km and results in a difference of approximately 10km between the perigee height (closest approach to Earth) and apogee height (greatest separation from the Earth) (Fig. 2.10). Despite the Earth's oblateness Eq. 2.36 is still valid for determining orbital periods, being an explicit form of Kepler's third law for elliptical

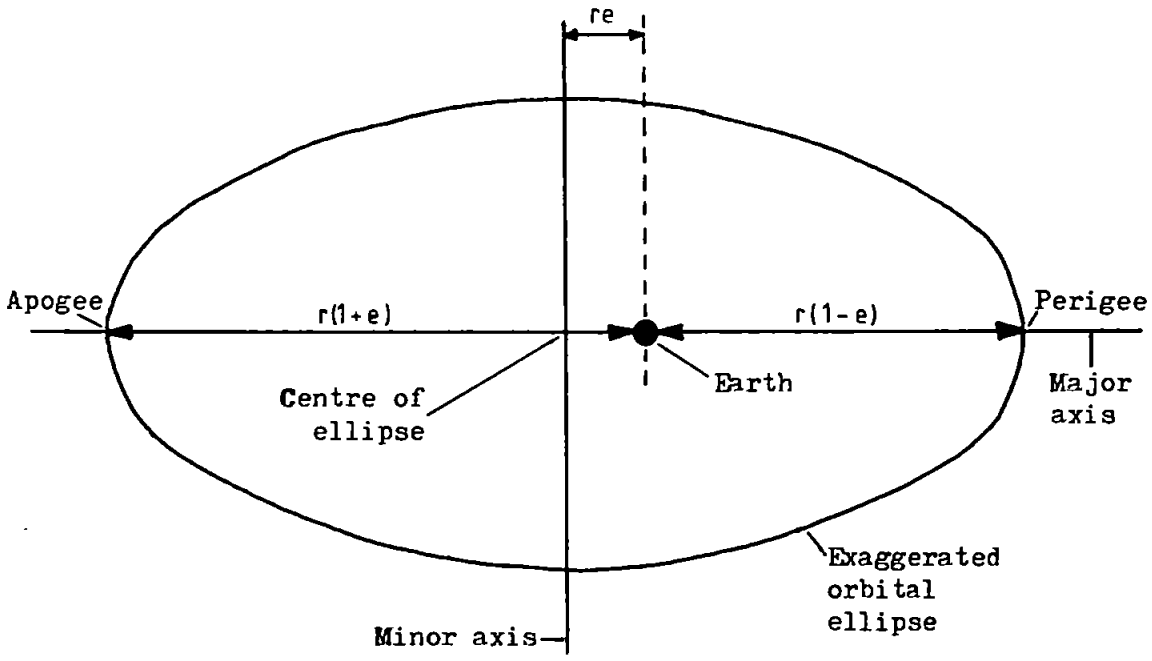

Figure 2.10 Elliptical orbit, apogee and perigee.

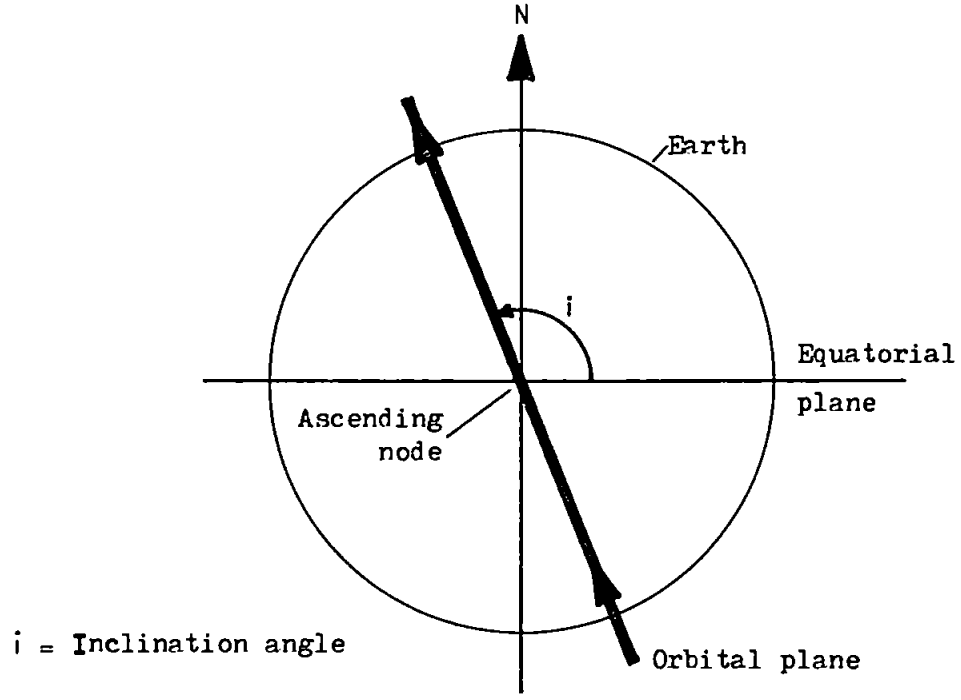

Figure 2.11 Definition of inclination angle.

orbits, provided that r represents the semi-major axis.

2.2.2 Repeat cycle

Since the CZCS orbital period is approximately 104 minutes the Earth rotates through 26° between successive orbits. Therefore the orbital crossing of the equator (from South to North) shifts to the West by this amount with each orbit. In order to establish a repeating trace pattern, an integral number of orbits must occur in an integral number of days. The CZCS repeat period is six days because during this period the CZCS makes exactly 83 orbits of the Earth. Thus the whole trace pattern is repeated every six days (Vanselous et al. 1978, Sathyendranath and Morel 1983). For comparison, Landsat's repeat cycle is 18 days corresponding to 251 orbits. The repeat cycle is easily destroyed by very small perturbations, necessitating orbital adjustments for the maintenance of stable cycles.

2.2.3 Sun-synchronous orbit

The Earth's oblateness not only results in elliptical orbits, but also causes rotation of the satellite's orbital plane about the Earth's polar axis (i.e. precession) and rotation of the orbital ellipse in its own plane. The latter phenomenon is insignificant for the CZCS since the Nimbus-7 orbit has a very small eccentricity. However precession represents a serious perturbation which is a function of the orbital radius r (strictly the semi-major axis) and the orbital inclination i which is defined in Fig. 2.11. Notice that the angle is measured when the satellite is at the ascending node, i.e. crossing the equator from South to North. The precession rate $\dot{\Omega}$ (in radians.s^{-1}) relative to the spatially fixed background of stars is (Stewart 1985):

$$\dot{\Omega} = \frac{-3}{2} J_2 \sqrt{\frac{GM}{r}} \cdot \frac{R^2}{r^3} \cdot \frac{\cos i}{(1-e^2)^2} \qquad (2.37)$$

J_2 equals 1.08263 x 10^{-3} and is the coefficient of the second zonal harmonic of the geopotential (Duck and King 1983) and represents the influence of the Earth's oblateness, and R is the Earth's equatorial radius (6378km). Only polar orbits (i = 90°) have zero precession. The Nimbus-7 orbital plane has an inclination angle i of 99.28° and is therefore a retrograde orbit (Fig. 2.12). Equation 2.37 yields the value of + 1.9918 x 10^{-7} radians.s^{-1} for the Nimbus-7 precession rate, which is equivalent to +0.986° per day or +360.13° per year. This positive precession is such that the orbital plane turns anticlockwise (viewed from the North) at the same rate at which the Earth rotates around the Sun (Fig. 2.13). This precession causes the orbital plane to maintain a fixed orientation to the Sun and the local time at which the Nimbus-7 crosses the equator is constant. Orbits of this type are Sun-synchronous and have the useful property of removing variations in illumination which would otherwise occur with varying solar zenith angles. The Nimbus-7 is in a high noon Sun-synchronous orbit (Hovis 1981, Baylis 1981) and crosses the equator, from South to North, at local noon. However, as the orbit is retrograde the satellite travels slightly westwards of its equatorial crossing position and hence the region around the United Kingdom is viewed typically an hour or so before local noon depending upon the position of the satellite track. The daytime pass is from South to North and the converse applies to the night-time one (Fig. 2.12).

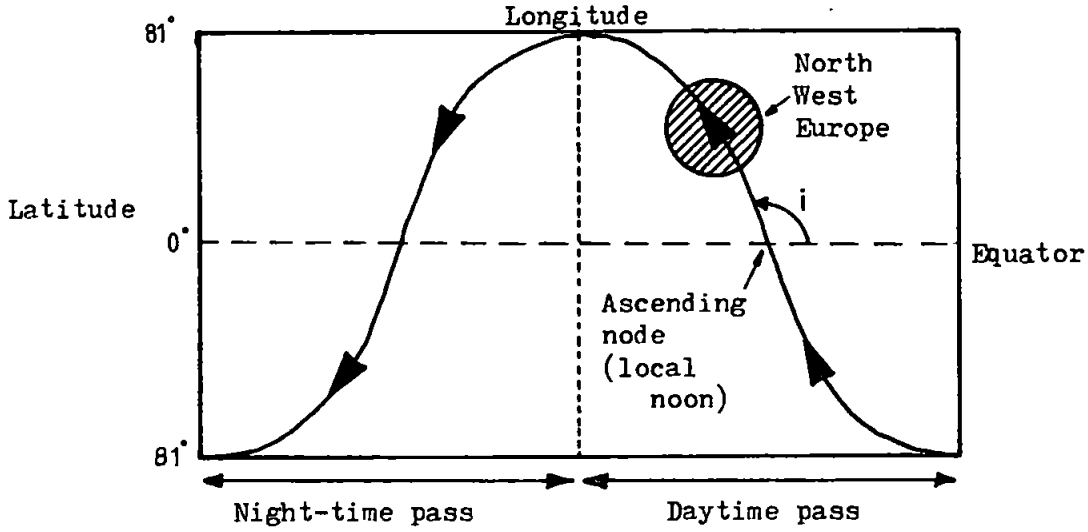

Figure 2.12 Retrograde orbit ($i > 90^\circ$).

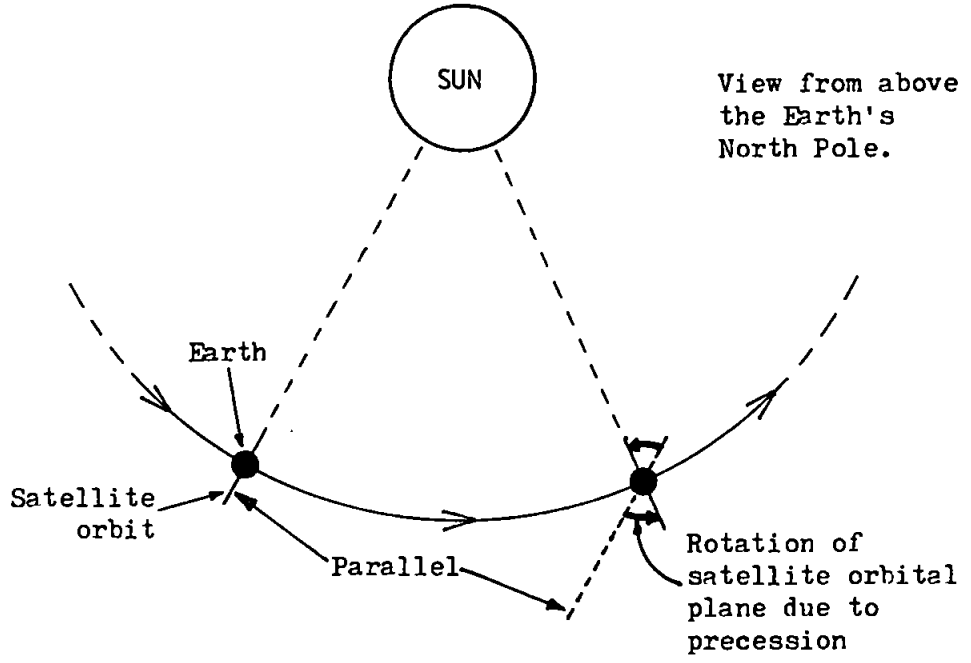

Figure 2.13 Sun-synchronous orbit.

2.2.4 Latitudinal coverage

The Nimbus-7 inclination is 99.28° at the equator or alternatively 9.28° from the direction of North. This skew α from North increases with latitude in accordance with (Wilson et al. 1981):

$$\sin \alpha = \sin 9.28°/[\cos (\text{latitude})] \qquad (2.38)$$

The maximum latitude which may be reached corresponds to $\alpha = 90°$, i.e. when the satellite starts heading South. Thus:

$$1 = \sin 9.28°/[\cos (\text{latitude})]$$

$$\sin 9.28° = \cos (\text{latitude}) = \sin (90° \pm \text{latitude})$$

$$\text{latitude} = \pm (9.28° - 90°) = \mp 80.72°$$

The same reasoning applies to the Southern hemisphere and the Nimbus-7 coverage is limited to 80.72° North and South.

2.2.5 Summary of orbital parameters

Orbit type:	Near-polar and Sun-synchronous
Orbital altitude:	955km
Orbital shape:	Almost circular, eccentricity = 0.0007
Orbital period:	104 minutes, 13.8 orbits per day.
Repeat cycle:	Every 6 days, corresponding to 83 orbits
Inclination:	99.28° (hence retrograde)
Equatorial crossing time:	Local noon for ascending node, i.e. South to North pass.
Ground coverage:	Between 81°N and 81°S.
Daytime coverage:	South to North pass
Night-time coverage:	North to South pass.

2.3 CZCS CHARACTERISTICS

The CZCS is a scanning multispectral radiometer with six spectral channels, four of which are devoted to the measurement of ocean colour. Scanning of the Earth's surface is achieved by a continuously rotating mirror for the direction perpendicular to the satellite track; the satellite's orbital motion provides the other scan direction. The orbital velocity, scan-rate and scan-width are arranged to generate an image of contiguous scanlines. This type of scanner is known colloquially as a 'whiskbroom' scanner (Slater 1980; Fig. 2.14) in order to contrast it with the 'pushbroom' type which uses a linear array of stationary detectors, each one of which measures the radiance for a single pixel in the scanline. This approach does away with mechanical scanning and is used in the French Système Probatoire d'Observation de la Terre (SPOT) satellite which employs 6000 detectors.

Apart from the digital and analogue electronics, the CZCS consists of three main sections: scanner, telescope and spectrometer (Fig. 2.15). These are all mounted on to an optical bench which attaches to the underside of the Nimbus-7. The complete CZCS instrument weighs 42kg and measures 81 x 38 x 56cm, whereas the Nimbus-7 satellite is 3m high and weighs 907kg (Stewart 1985). The most comprehensive sources of information on CZCS characteristics are Ball Aerospace Systems Division (1979a, b), which should be consulted for further details.

2.3.1 The scanner

The scan mirror is attached to an electrically driven horizontal shaft with a balance counterweight at the other end. The angular speed is 8.081 revolutions per second corresponding to 0.12375 seconds per

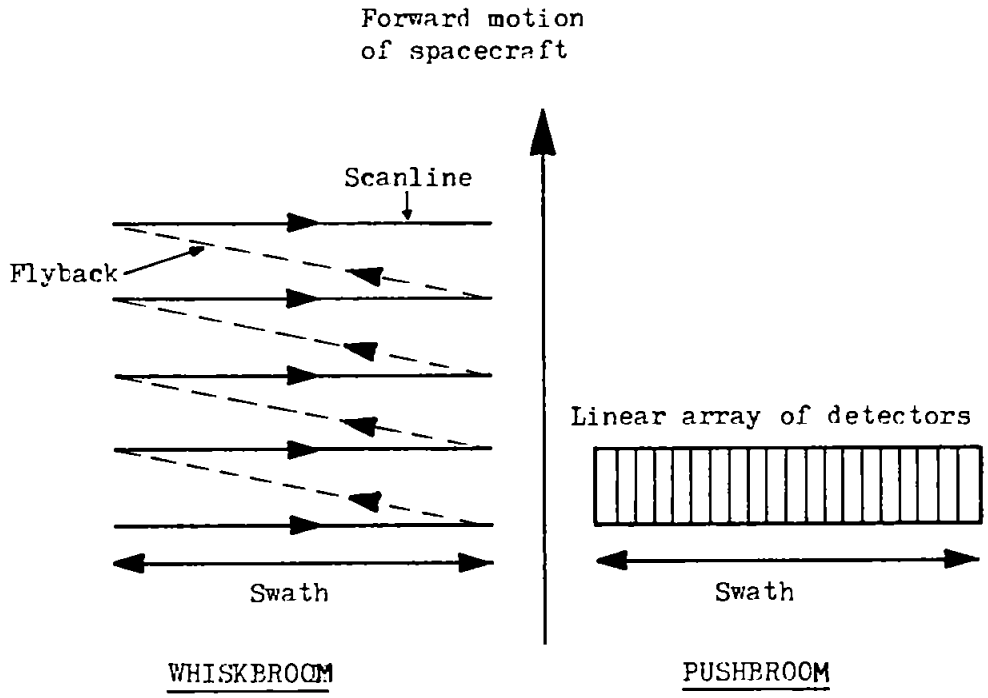

Figure 2.14 Distinction between whiskbroom and pushbroom scanners.

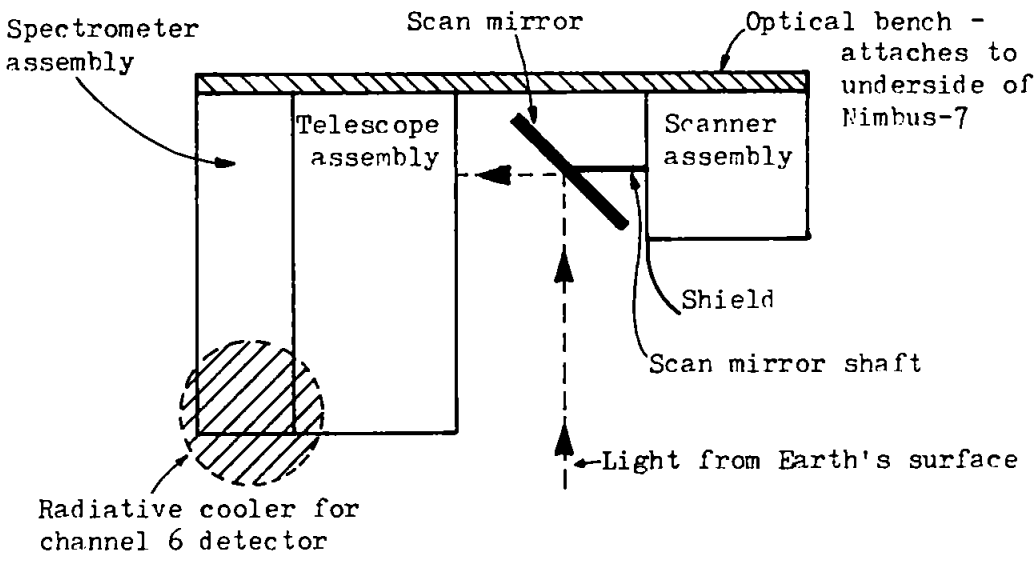

Figure 2.15 Basic structure of the **CZCS.**

revolution. The scanner is fitted with a momentum compensator which produces an angular momentum equal (within 0.05%) and opposite to that produced by the scan mirror and shaft etc. Without this compensation the attitude of the Nimbus-7 would be disturbed. When viewing the nadir direction the scan mirror is inclined at 45° to the horizontal. Although the scan mirror rotates continuously, data is only collected during an active scan of ± 39.36° (Fig. 2.16) and this produces a swath of just over 1600km or 1000 miles which is sufficient to give total global coverage every 72 hours (McClain 1980). The scan direction is from West to East for daytime passes. A further feature provided is a tilt mechanism which permits the scan mirror's inclination to be varied by ± 10° in 1° increments from its nominal position, i.e. from 35° to 55°. This has the effect of shifting the scan plane forwards (in the direction of orbital motion) or backwards of nadir by up to 20° in 2° increments (Fig. 2.16). The purpose of this tilt mechanism is to steer the scan away from the specular image of the Sun (reflected from the water surface); otherwise the detectors would become saturated. A side effect of this is a narrowing of the swath to 1300km with a backward tilt of 20° and a widening to 2300km with a forward tilt of 20° (Gordon and Morel 1983, Sathyendranath and Morel 1983). Full angular momentum compensation is maintained at all tilt angles. The tilt mechanism takes nearly ten seconds per increment, so to change from full forward tilt to full backward tilt takes over three minutes. At any particular time the tilt angle is available as part of the housekeeping information.

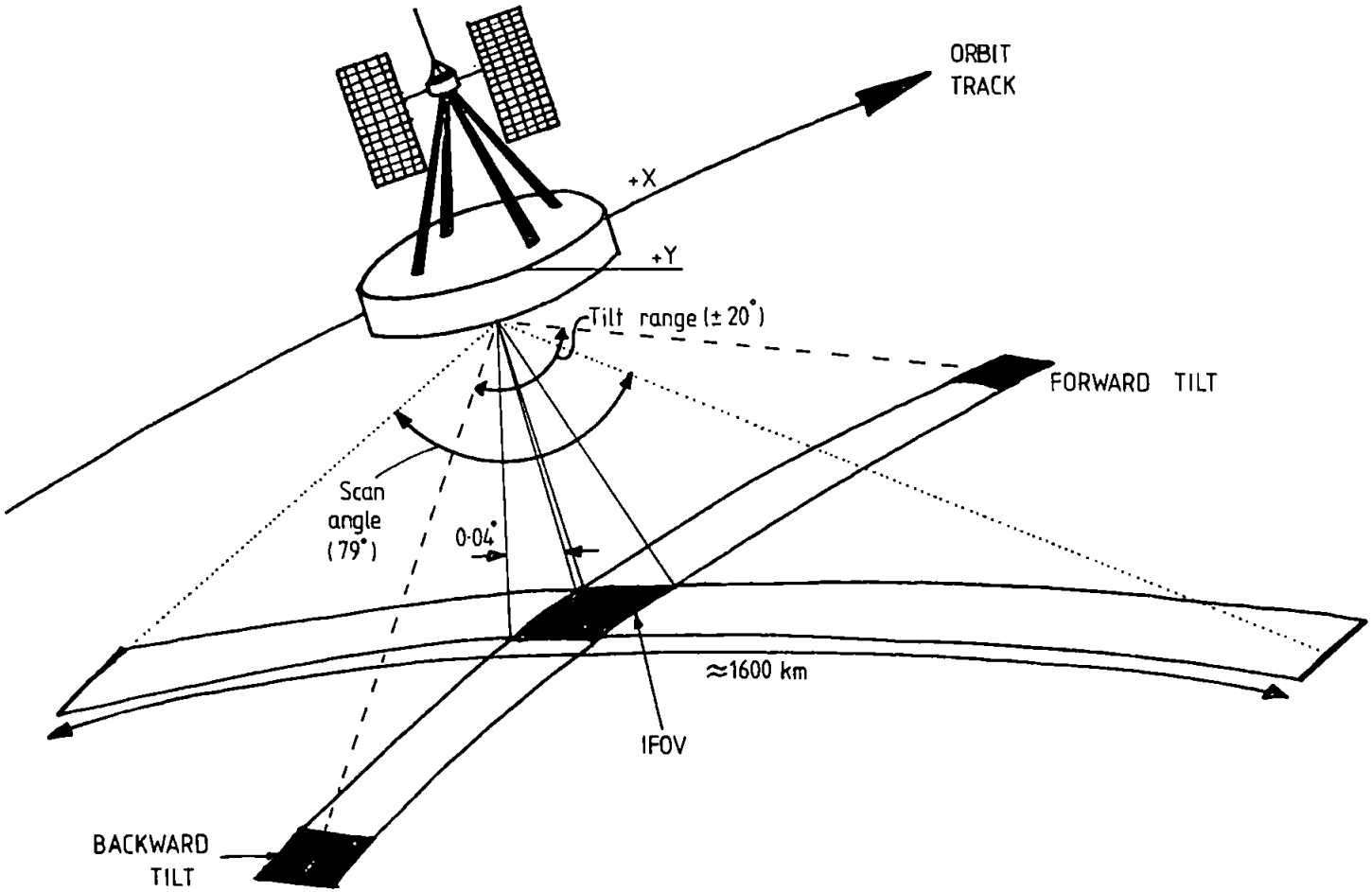

Figure 2.16 Scan geometry and tilt.

2.3.2 The telescope and spectrometer

These two components represent the optical system of the CZCS (Fig. 2.17). The telescope collects and focuses light prior to its spectral measurement by the spectrometer. The telescope, comprising the primary and secondary mirrors, is a Cassegrain configuration (Swain and Davis 1978). This is followed by a dichroic beamsplitter which separates the thermal infra-red energy from the visible and near infra-red energy. The thermal infra-red energy, for channel 6, is reflected back to a small mirror in the centre of the secondary mirror and thence to the detector. The remaining energy, for channels 1 to 5, passes through the beamsplitter and on to the spectrometer. The reason for this separation of the thermal infra-red energy is that the channel 6 detector (HgCdTe photoconductor) alone must be cooled, using a passive radiative cooler, to produce an adequate noise equivalent temperature difference (NETD). Before reaching the spectrometer, the radiance for channels 1 to 5 also passes through a small aperture (<1mm) known as a field stop which, in conjunction with the effective focal length of the instrument, defines the instantaneous field of view (IFOV). The use of a single field stop, common to channels 1 to 5, ensures that they are all exactly co-registered. The radiance is then directed, via a couple of mirrors, onto a concave diffraction grating which disperses the radiance into its spectral components.

The spectral response of the five visible channels is determined by the position, relative to the grating, of each channel's silicon photodiode detector and the size of each channel's exit slit (not shown). Also included in the spectrometer's optical path is a pair of depolarising wedges which scramble the polarisations of the radiance so that the instrument is insensitive to the state of polarisation and thus

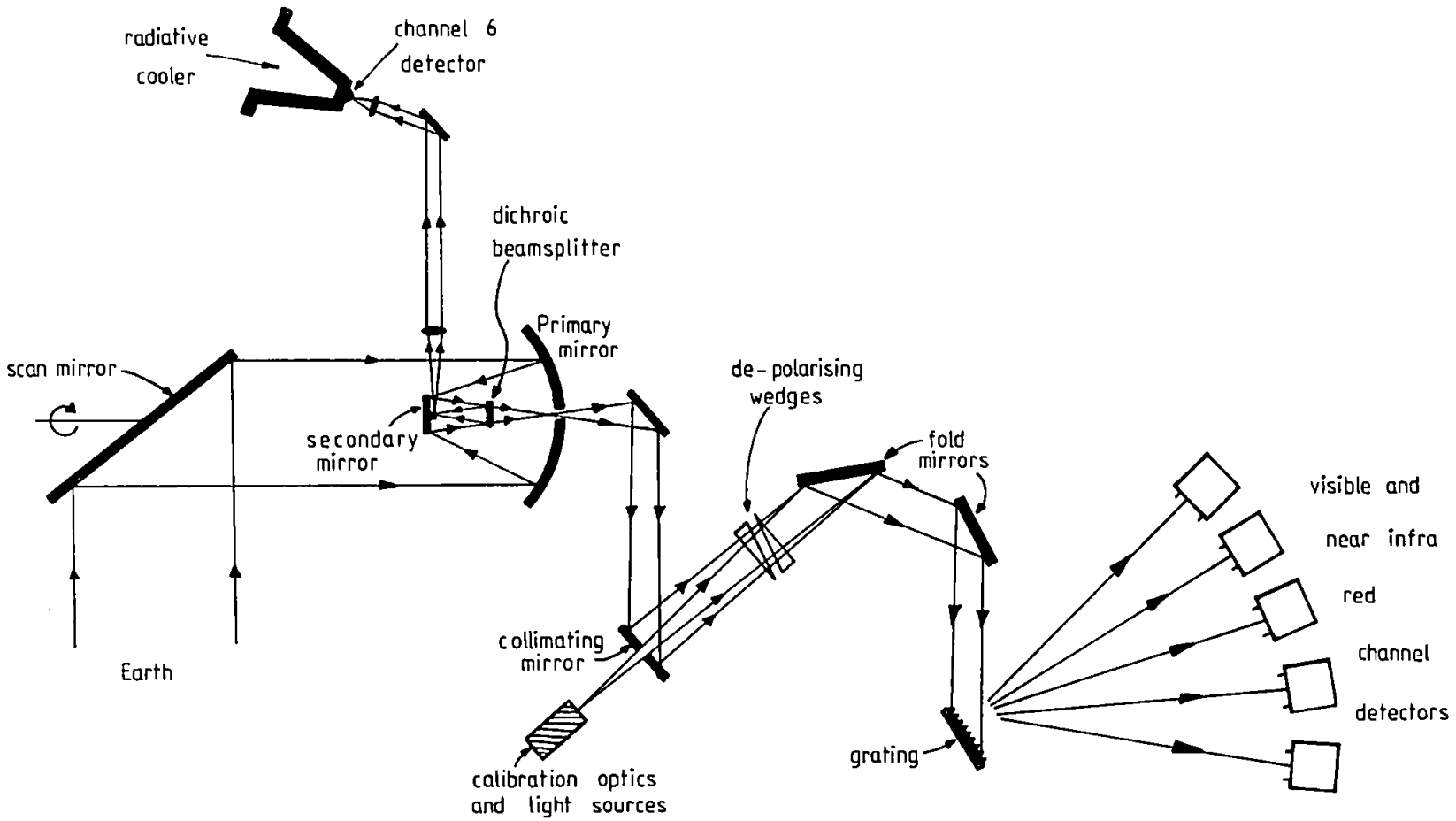

Figure 2.17 CZCS optical system.

measures only the intensity of the radiance. This measure is necessary because a large proportion of the radiance may be highly polarised due to scattering. Every 16 scanlines, when the instrument is not viewing the Earth i.e. outside the active scan, a radiometric calibration signal is injected into the optical path through a hole in the collimating mirror. Two incandescent lamps are available for this purpose which have known radiances in each of the five visible channels. During calibration one of the two lamps is selected by ground command. Channel 6 is calibrated by viewing a honeycomb black body radiator whose temperature may be extracted from the housekeeping information.

Spatial resolution

The design guideline for the IFOV was 865 x 10^{-6} radians or 0.0496°, corresponding to a nadir or sub-satellite resolution of h.tan (IFOV) = 826m, where h is the orbital altitude (955km). However, the final design was based on 9000 sampling intervals per revolution of the scan mirror, which implies an IFOV of 360°/9000 = 0.04° or 698 x 10^{-6} radians. This produces a nadir resolution of 667m or 0.41 miles. The resolution in all other directions along the scanline is inferior to this.

Consider a sensor viewing the ground with a small IFOV, refer to Fig. 2.18. The scan-angle for the centre of the corresponding ground cell is θ; the scan-angles for the extremes of the ground cell are θ-IFOV/2 and θ+IFOV/2. From the latter two scan-angles, the angles subtended at the Earth's centres (Ω_1 and Ω_2 respectively) may be derived, enabling the angle $\Delta\Omega$ to be found. Angles Ω_1 and Ω_2 are given by (Appendix 3):

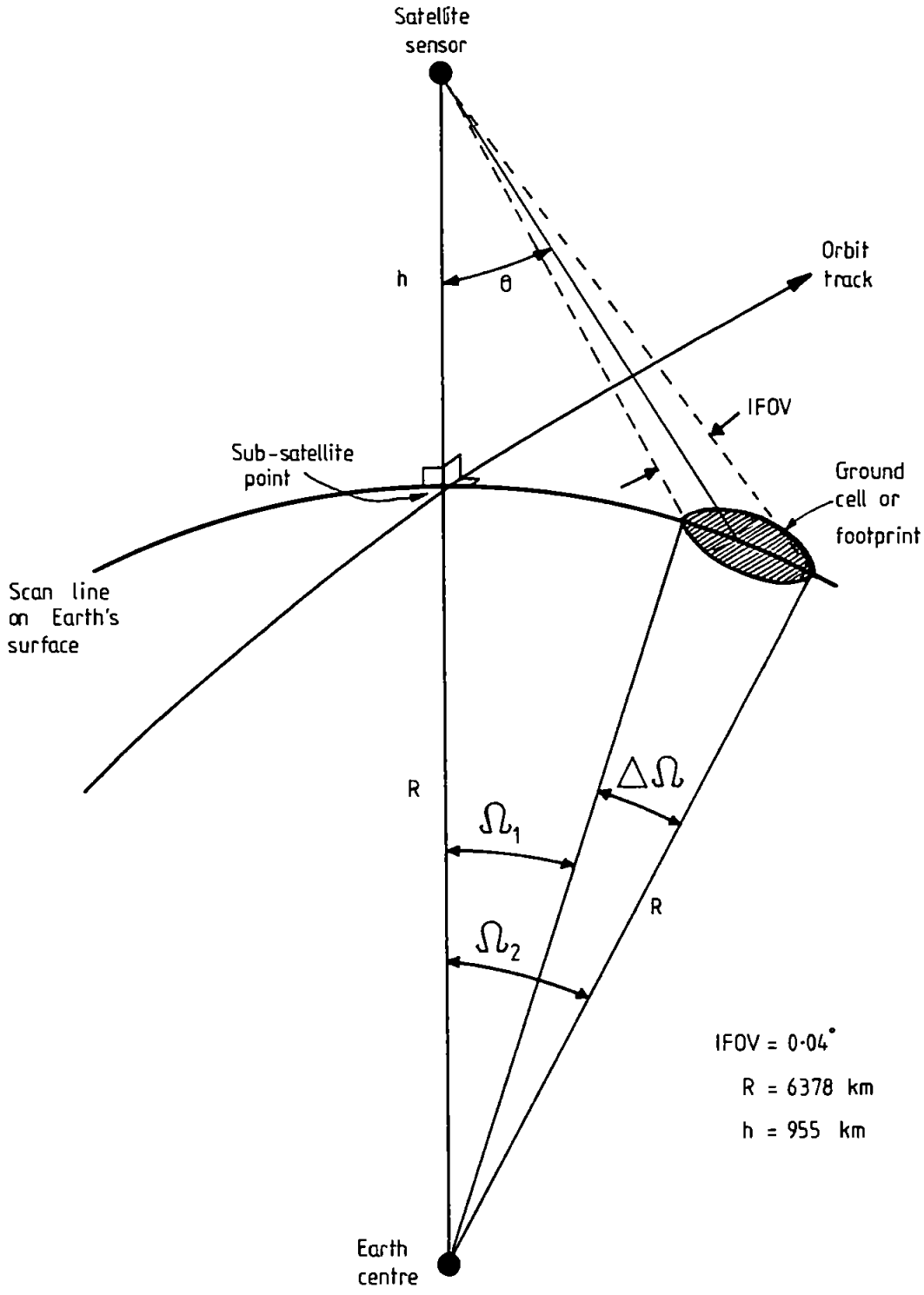

Figure 2.18 Variation of spatial resolution with scan-angle θ.

$$\Omega_1 = \sin^{-1}\left[\left(\frac{R+h}{R}\right)\sin(\theta - IFOV/2)\right] - (\theta - IFOV/2) \qquad (2.39)$$

$$\Omega_2 = \sin^{-1}\left[\left(\frac{R+h}{R}\right)\sin(\theta + IFOV/2)\right] - (\theta + IFOV/2) \qquad (2.40)$$

Therefore the angle $\Delta\Omega$ subtended by the ground cell at the Earth's centre, in the direction of the scanline is:

$$\Delta\Omega = \Omega_2 - \Omega_1$$

$$= \sin^{-1}\left[\left(\frac{R+h}{R}\right)\sin(\theta+IFOV/2)\right] - \sin^{-1}\left[\left(\frac{R+h}{R}\right)\sin(\theta-IFOV/2)\right] - IFOV \qquad (2.41)$$

The size of the ground cell, in the direction of the scanline, is simply $R.\Delta\Omega$, provided that $\Delta\Omega$ is expressed in radians. R is the radius of the Earth (6378 km). The maximum scan-angle for the CZCS is $\pm$ 39.36° and $\Delta\Omega$, as determined from Eq. 2.41, is 0.011958° or 2.0871×10^{-4} radians. Accordingly, the ground cell size or spatial resolution at the ends of the scanline is 1331m in the scanline direction. This is very nearly double the nadir value of 667m. The spatial resolution in the direction of the orbit track also deteriorates with increasing scan-angle and backward/forward tilt of the scan mirror improves/further degrades the resolution. The scan of $\pm$39.36° and IFOV of 0.04° results in 1968 samples per channel per active scan. The CZCS represents a first generation instrument; second generation ones feature much improved resolutions. For example the Japanese Marine Observation Satellite (MOS-1) will carry a Multispectral Electronic Self-Scanning Radiometer (MESSR) which uses charge coupled device (CCD) arrays and has a 50m resolution (Slater 1986, Swinbanks 1986). The French SPOT-1 satellite with two High

Resolution Visible (HRV) sensors does even better with 10m and 20m resolutions in panchromatic and multispectral modes respectively (Slater 1986). Like MOS-1, SPOT-1 employs CCD arrays, but is not intended for ocean colour measurement.

Spectral characteristics

The spectral response of the first four channels is specially tailored for remote sensing of ocean colour, having the following characteristics:

Channel	Colour	Type	Spectral Range (nm)	Saturation Radiance mW/(cm^2. μm.sr)
1	Blue	Visible	443 ± 10	5.41
2	Blue/green	Visible	520 ± 10	3.50
3	Green	Visible	550 ± 10	2.86
4	Red	Visible	670 ± 10	1.34
5	-	Near IR	750 ± 50	23.9
6	-	Thermal IR	11.5 ± 1 μm	-

The wavelength of channel 1 coincides with the maximum chlorophyll 'a' absorption and this channel is a very sensitive chlorophyll indicator. Although channel 2 is near the hinge-point, its response is weakly influenced by chlorophyll 'a' and so it is used for the estimation of chlorophyll 'a' in regions of high concentration. Channel 3 corresponds to the minimum in chlorophyll 'a' absorption (Gordon and Morel 1983) and is sensitive to backscattering by suspended sediments. This channel represents the hinge-point and together with channel 1 or

2, in the form of a ratio, permits the pigment concentration to be retrieved. The high absorption in channel 4 by water is exploited by the atmospheric correction algorithm for the estimation of aerosol radiance. Channel 5 senses reflected solar radiation and has a dynamic range more suitable for land. It corresponds to band 7 of the Landsat Multi-Spectral Scanner (MSS) and is useful for detecting surface vegetation. Channel 6 is a conventional thermal band for measuring surface temperature. The very narrow bandwidth of channels 1 to 4 (only 20nm) results in a low signal strength and noise minimisation techniques were required in the design of the optical system to ensure adequate signal-to-noise ratios. Also shown in the table above are the saturation radiances at maximum gain. These are the radiances at which the detectors saturate and provide an indication of the sensitivity of the instrument. These figures represent almost an order of magnitude improvement over the Landsat MSS (Gordon and Morel 1983). Channels 2 to 4 are normally saturated over land and clouds (Hovis 1982). Channel 6 has proved to be unreliable, being out of operation for very long periods; it is not used in this work. The only other sensor designed for the express purpose of measuring ocean colour is the MESSR on Japan's MOS-1 satellite, which is due for launch in late 1986 or early 1987 (Moore 1986). The MESSR has four channels: 510-590, 610-690, 720-800 and 800-1100 nm (Slater 1986). The two HRVs on SPOT-1 have three channels: 500-590, 610-680 and 790-890 nm (Slater 1986), the first two being very similar to those of MESSR. An Ocean Colour Monitor (OCM) with ten or more channels was proposed for the first European Space Agency (ESA) Remote Sensing Satellite (ERS-1) and this instrument would have represented a considerable improvement over the CZCS (Paci 1980). Unfortunately, the OCM was not approved and the ERS-1 will only be equipped with a payload of microwave instruments (Allan 1983) and one

infra-red instrument (Cracknell 1983).

2.3.3 Analogue and digital electronics

This section is concerned only with the electronic circuits which handle the data generated during the active scan of the Earth; the various electronics for controlling the scan mechanism, the tilt device etc. are not considered. Figure 2.19 outlines the circuitry for each channel, although channels 5 and 6 do not have the threshold and selectable gain facilities. The output of the detector is initially fed to a low-noise preamplifier which then drives an amplifier stage whose gain is selectable, under command from the ground, from four values: 1.0, 1.23, 1.5 and 2.15. This facility permits different levels of solar illumination, caused by varying solar zenith angles, to be accommodated. Next there is a low-pass filter to remove any high frequency signals which would otherwise interfere with the sampling process. There then follows an offset amplifier which inserts a D.C. offset in such a way that any fixed background level in the signal is removed and the full dynamic range then becomes available for the top 30% of the signal. This 'threshold' facility may be switched-in from ground control. The sample and hold circuit samples the signal 9000 times every scan-mirror rotation, i.e. every 0.12375/9000 seconds = 13.75 μs, corresponding to a sampling rate of 72.7 kHz. The output of this stage is taken to the analogue-to-digital converter (ADC) which produces an 8 bit digital output for each sample. At this point the measured radiance is represented by an integer in the range 0 to 255. The departure from linearity for the circuitry in Figure 2.19 is within 2% for all channels and within 1% for most of them. All the detectors exhibit a linear relationship between incident radiance and output voltage. The signal-to-noise ratios, for nadir viewing and minimum

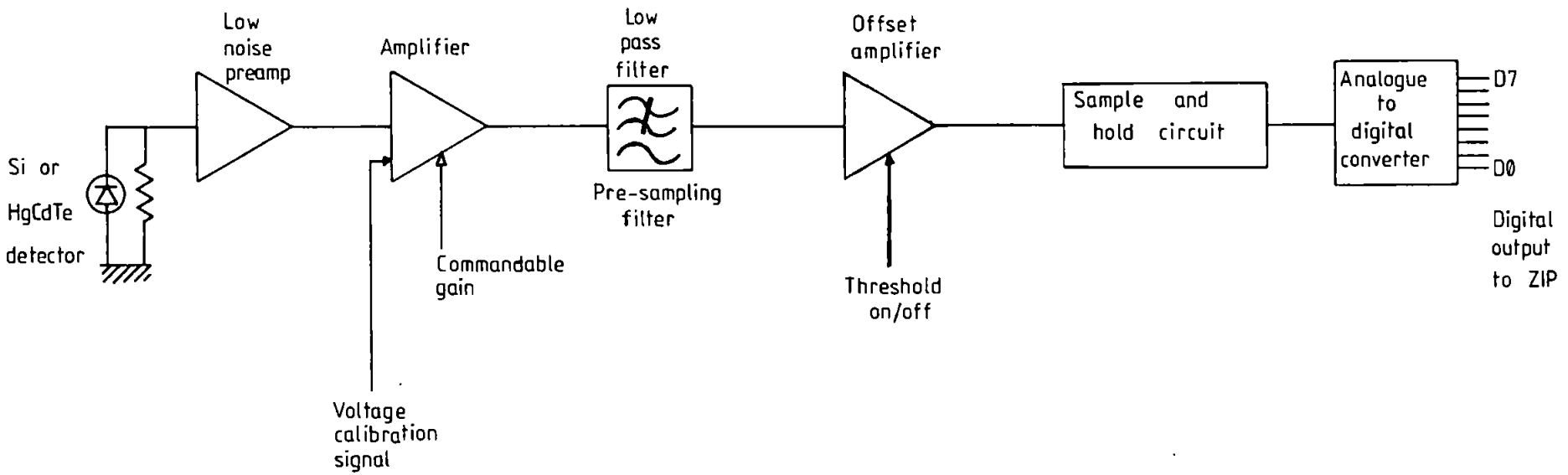

Figure 2.19 Electronics for channels 1-4. Channels 5 and 6 are similar but do not have the commandable gain and threshold facilities.

gain, measured at typical radiance levels are (Hovis et al. 1980, Ball Aerospace Systems Division 1979b):

Channel	Signal-to-noise ratio	Radiance level $mW/(cm^2.\mu m.sr)$
1	158	3.0
2	200	2.5
3	176	1.5
4	118	1.0
5	350	15.0

Channel 6 has an NETD of 0.22°K at 270°K (Hovis et al. 1980).

The digital output from each channel plus housekeeping information (in digital form) is fed to the CZCS Zonal Information Processor (ZIP). The ZIP performs buffering and formatting of the data prior to transmission to the ground or storage on one of the three on-board tape machines if there is no receiving station in range (Hovis et al. 1980). The purpose of buffering is to reduce the peak data rate of 436 $kbytes.s^{-1}$ to a steady rate of 100 $kbytes.s^{-1}$. At this rate the CZCS generates six spectral images, each covering the same area of approximately 1000 miles square, in just over four minutes, corresponding to 24 Mbytes of data in all. Figure 2.20a illustrates the formatting function of the ZIP which is to take digital samples from the six channels of data in strict rotation, i.e. multiplexed format. It also inserts synchronisation and time codes. One complete scan, containing data for all six channels, is formatted into 15 minor frames of 825 bytes each, thus totalling 12375 bytes.

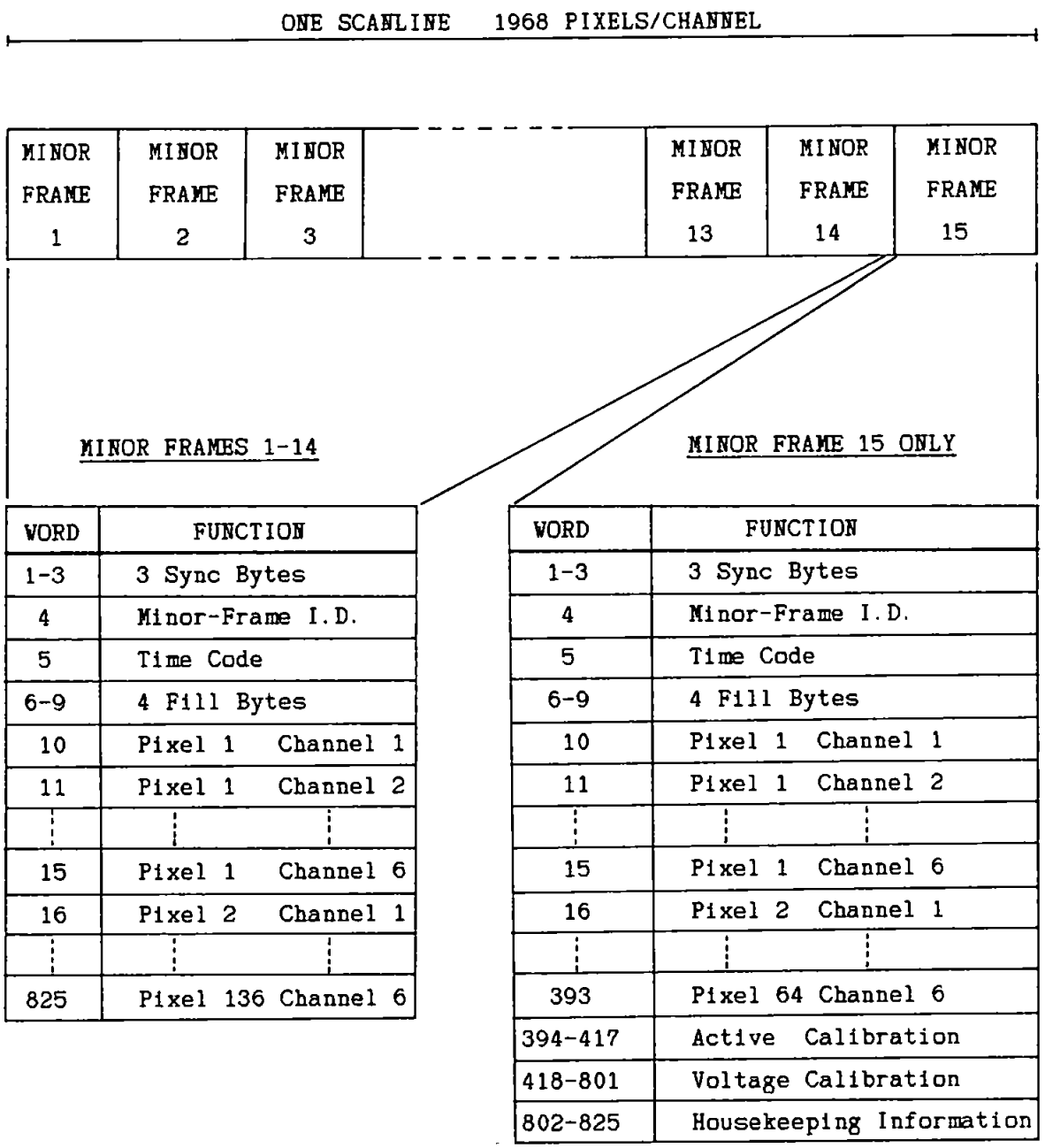

WORD	FUNCTION
1-3	3 Sync Bytes
4	Minor-Frame I.D.
5	Time Code
6-9	4 Fill Bytes
10	Pixel 1 Channel 1
11	Pixel 1 Channel 2
⋮	⋮ ⋮
15	Pixel 1 Channel 6
16	Pixel 2 Channel 1
⋮	⋮ ⋮
825	Pixel 136 Channel 6

WORD	FUNCTION
1-3	3 Sync Bytes
4	Minor-Frame I.D.
5	Time Code
6-9	4 Fill Bytes
10	Pixel 1 Channel 1
11	Pixel 1 Channel 2
⋮	⋮ ⋮
15	Pixel 1 Channel 6
16	Pixel 2 Channel 1
⋮	⋮ ⋮
393	Pixel 64 Channel 6
394-417	Active Calibration
418-801	Voltage Calibration
802-825	Housekeeping Information

Figure 2.20a ZIP formatting and buffering of CZCS data.
Each minor frame consists of 825 words.

The last minor frame also contains active calibration data, 16 levels of voltage calibration data and housekeeping information, which are all sampled four times (Figure 2.20b). There are 32 housekeeping functions which provide information about the status of the CZCS and are transmitted in sequence, one per scanline. Each housekeeping function is identified by an ID number in the range 0 to 31, of which the following four only are important (Singh personal communication):

i) ID = 2 Scan mirror tilt angle, given by 29.37-0.367 x DN degrees. Round off to the nearest even integer.

ii) ID = 3 Gain setting. Most significant bit (MSB) = 0 if DN $\leqslant$ 150 and MSB = 1 for DN > 150.

iii) ID = 4 Gain setting. Least significant bit (LSB) = 0 if DN $\leqslant$ 150 and LSB = 1 for DN > 150.

iv) ID = 5 Threshold is OFF for DN > 150 and ON for DN $\leqslant$ 150.

DN is the digital number. The gain setting is found from the values of LSB and MSB by referring to the following table:

LSB	0	1	0	1
MSB	0	0	1	1
Gain	1.0	1.23	1.5	2.15

Housekeeping ID's of 15 and 31 are used to indicate that the active calibration data for channels 1 to 5 are valid; for all other ID's the active calibration data is disregarded. Channel 6 active calibration data is valid for all ID's/scanlines.

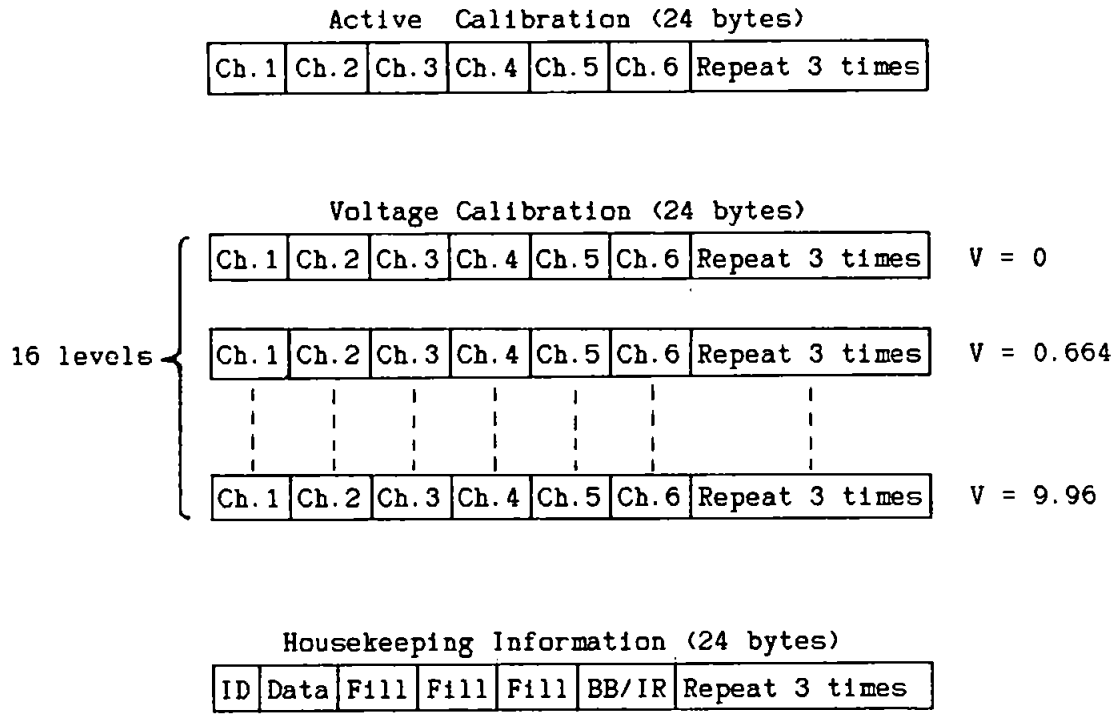

Notes

(1) Total Earth scan = 1968 pixels per channel.

(2) 16 levels of voltage calibration.

(3) Active calibration only valid when housekeeping ID = 15 or 31, for channels 1-5. Channel 6 calibration valid in every scan line.

(4) 32 multiplexed housekeeping functions with ID = 0 to 31.

Figure 2.20b CZCS calibration and housekeeping information.

Data is transmitted from the CZCS, or more accurately from the Nimbus-7, at 2.2 GHz and received by a 3.6m tracking parabolic antenna at Dundee University (Baylis 1981).[(a)] The signal is downconverted to 112.5 MHz and then 10.7 MHz prior to FM discrimination. The demodulated output is squared and fed to a high-bit density tape machine, on which it is stored in digital form.

The Nimbus-7 solar panels generate about 550 Watts of power, although this has reduced with age, and this is insufficient to power simultaneously and continuously all eight instruments carried by the spacecraft. Consequently, the CZCS was allocated a maximum operation of two hours per day. This restriction on power, together with considerations of total spacecraft weight and data rate (for all instruments) are what limits the CZCS data rate. In turn, this dictates the spatial resolution for the six channels of the CZCS (Hovis 1981). The CZCS average power consumption is 50 Watts.

The superior sensitivity of the CZCS detectors, combined with its 8 bit precision (Landsat-1 was only 6 bits), results in an approximate 60-fold improvement in overall sensitivity over the Landsat-1 MSS (Hovis et al. 1980). The only longstanding problem with the CZCS has been sensitivity loss, for which a partial remedy was devised by Gordon et al. (1983a) in the form of an empirical correction scheme; it was also shown that channel 1 (443nm) suffers most from this affliction. The radiometric uncertainty in this channel has become so serious that it is almost unusable for quantitative work. Since retrieval algorithms use two CZCS channels, the errors may be additive (Viollier 1982).

(a) There are also receiving stations in Kiruna (Sweden) and Lannion (France).

2.3.4 Summary of CZCS characteristics

Scan:	± 39.36°
Scan rate:	8.0808 rps, equivalent to 0.12375 s per scan
Tilt:	± 20° in 2° steps
Swath width:	2300 km at +20° tilt
	1600 km at 0° tilt
	1300 km at -20° tilt
IFOV:	0.04°, 698 x 10^{-6} radians
Spatial resolution:	667m (0.41 miles) at nadir and with zero tilt
Samples:	1968 per channel per scan
Visible channels:	1) 433 - 453 nm
	2) 510 - 530 nm
	3) 540 - 560 nm
	4) 660 - 680 nm
Signal-to-noise ratios:	Greater than 150, except channel 4 which is 118

Commandable gain and threshold facilities are provided.

Calibration:	i) Internal voltage calibration generator
	ii) Two lamps and one black-body radiator for active calibration
Data precision:	8 bits
Data rate:	100 kbytes.s^{-1} (buffered)
Operation:	2 hours or less per day.

2.4 SEA TRUTH: THE MEASUREMENT OF CHLOROPHYLL AT SEA

The chlorophyll concentration of discrete sea water samples is usually estimated by the fluorometric method (Lorenzen 1966, 1967) whereby the fluorescence at 670nm is measured by a fluorometer, using blue light (430nm) as the excitation source. The intensity of fluorescence is related to the concentration of chlorophyll 'a' and phaeophytin 'a'. Treatment of the sample with acid enables the concentration of both pigments to be obtained. The fluorometric technique is also applicable to continuous sampling systems in which sea water is pumped on board from a fixed depth. The Undulating Oceanographic Recorder (UOR) (Aiken 1980, 1981a, 1981b) is a towed instrument which permits several marine parameters, including chlorophyll concentration in mg/m^3, to be measured over depths of 50m or more by virtue of its automatic undulating action. Continuous Plankton Recorders (CPR) (Boney 1975) trap plankton on a slowly winding strip of bolting cloth which is analysed later, providing a count of phytoplankton cells. Sea truth measurements are discussed in greater detail by Charlton (1980).

CHAPTER 3

IMAGE PROCESSING FOR REMOTE SENSING

3.1 INTRODUCTION

The manipulation and analysis of images requires a facility for processing two-dimensional data. Analogue image processors (Curran 1985) and optical processors (Wilson 1981) are suitable for images in photographic form. The former is usually based upon a television camera and monitor and only provides density slicing and contrast adjustment. The latter employs a laser to illuminate a transparency and a lens to produce a diffraction pattern, which may be filtered to modify the spatial-frequency properties of the image. However, both of these instruments have been largely superseded by the digital image processor, which handles images in digital form. The advantages of digital image processing are:

i) Ability to process digital or analogue images.

ii) A large number of grey-levels may be accommodated.

iii) Capacity for handling high volumes of data.

iv) A wide range of techniques and software is available, making digital image processing a versatile tool.

v) An increasing amount of remotely-sensed data is available in digital form on computer compatible tape (CCT).

The simplest digital image processor may be constructed from a micro computer with graphics facilities and a floppy-disc drive for data input. At the other extreme, there exist expensive, specialist machines such as the MPP (Massively Parallel Processor), which was built for NASA by Goodyear Aerospace (Potter 1983). This comprises 16,384 processors configured as an array of 128 by 128, and is capable of 6000 million operations per second. Popular medium-cost machines

are the IDP3000 (Plessey) and the I^2S (International Imaging Systems), the latter is used by NERC in Swindon, in conjunction with a large minicomputer. An unusual approach is the CLIP (cellular logic image processor) which processes images in binary form, but may be extended to images with more than two grey-levels. Further information on computer architectures for image processing is given by Duff and Levialdi (1981) and in the special issues of Computer (1981 and 1983). Mainframe computers may also be used for digital image processing, but there is often difficulty in obtaining sufficient disc space and central-processing-unit (CPU) time. The latter implies that the processing must be submitted as a 'batch job', so that the work may be done at some off-peak time; perhaps the middle of the night. This is a serious drawback as it prevents the computer from being used interactively, which is almost essential with remotely-sensed data. Another drawback results from the practice of communicating with mainframe computers via visual display units (VDU), which are perfectly adequate for displaying alphanumeric characters, but offer no provision for viewing images.

Initially, digital image processing relied almost exclusively upon mainframe computers but with the rapid advances in computer technology this dominant position has been steadily eroded by minicomputers. It is also worth mentioning that the distinction between microcomputers and minicomputers is becoming blurred. However, at present microcomputer systems may be ruled out for serious work.

The most popular approach therefore is to use a dedicated mini-computer for image processing; in this way there is no sharing of resources with a large number of users, as occurs with a main-frame machine. The

addition of a tapedrive and high resolution monitor to a minicomputer provides for the input and output of data/images. In fact the tapedrive may also be used for archiving processed images and for storing programs and data; this provides a means of recovery after a system failure. As the cathode ray tube (CRT) of a monitor has a very short persistence time, it is necessary to repeatedly send the image to the CRT to maintain a stable picture. This cannot be done by the computer itself as it is unable to transfer data at a sufficiently high rate. Even if it could, it would have no time for any other tasks. The solution is to arrange for the computer to store the image in a special-purpose semiconductor memory, which is used to refresh the CRT at a rate of 25 times a second. This memory is termed 'refresh memory' and together with the accompanying control electronics, it is known as an imagestore or framestore. The computer transfers the image in its own memory to the image-store just once; it is then free to take on any other task required of it.

When dealing with remotely-sensed data, it is advantageous to speed the computer up in some way because such a large number of pixels may be involved. To this end, various additional devices may be attached to the computer such as floating-point accelerators, which dramatically (e.g. by one order) reduce the execution times for floating-point arithmetic and array processors. The term 'array processor' is a little ambiguous for it could apply to a unit containing an array of processors or a single processor for handling arrays of data (Brumfitt 1983, personal communication). The former category represents true array processors having vectorised instruction sets. Most low-cost array processors however fall into the latter category and act as 'back-end' processors placed on the computer bus for dedicated high-

speed processing, such as fast Fourier transforms. The most recent development has been the incorporation of electronic hardware in the imagestore itself, for arithmetic and logical operations. This 'display processor' concept (Ince 1983) places processing power in the imagestore, thus partially relegating the computer to the rôle of management and housekeeping.

3.2 IMAGE PROCESSING HARDWARE

3.2.1 Initial system

At the outset it was realised that a substantial reduction in the cost of the whole system could be made by constructing the imagestore and writing the image processing software in-house. The cost of software alone may be prohibitive; for example, Logica's image processing software package INSIGHT is in the region of twenty thousand pounds. The imagestore could be constructed at approximately one half of the price of a commercial one, and would permit the incorporation of special features which might not be available commercially.

A Digital Equipment Corporation (DEC) PDP11/23 minicomputer was already available at the start of the project, and this formed the heart of the image processing system. Introduced in 1979, the PDP11/23 is a 16-bit machine with 8 general purpose registers and an address space of 256k bytes (DEC 1979). The remainder of the computer system (Fig. 3.1) comprised:

i) 160k bytes of random access memory, which was increased later to 224k bytes.

ii) One DEC RX02 dual floppy-disc drive; total capacity 1M byte.

iii) One DEC VT52 console/VDU.

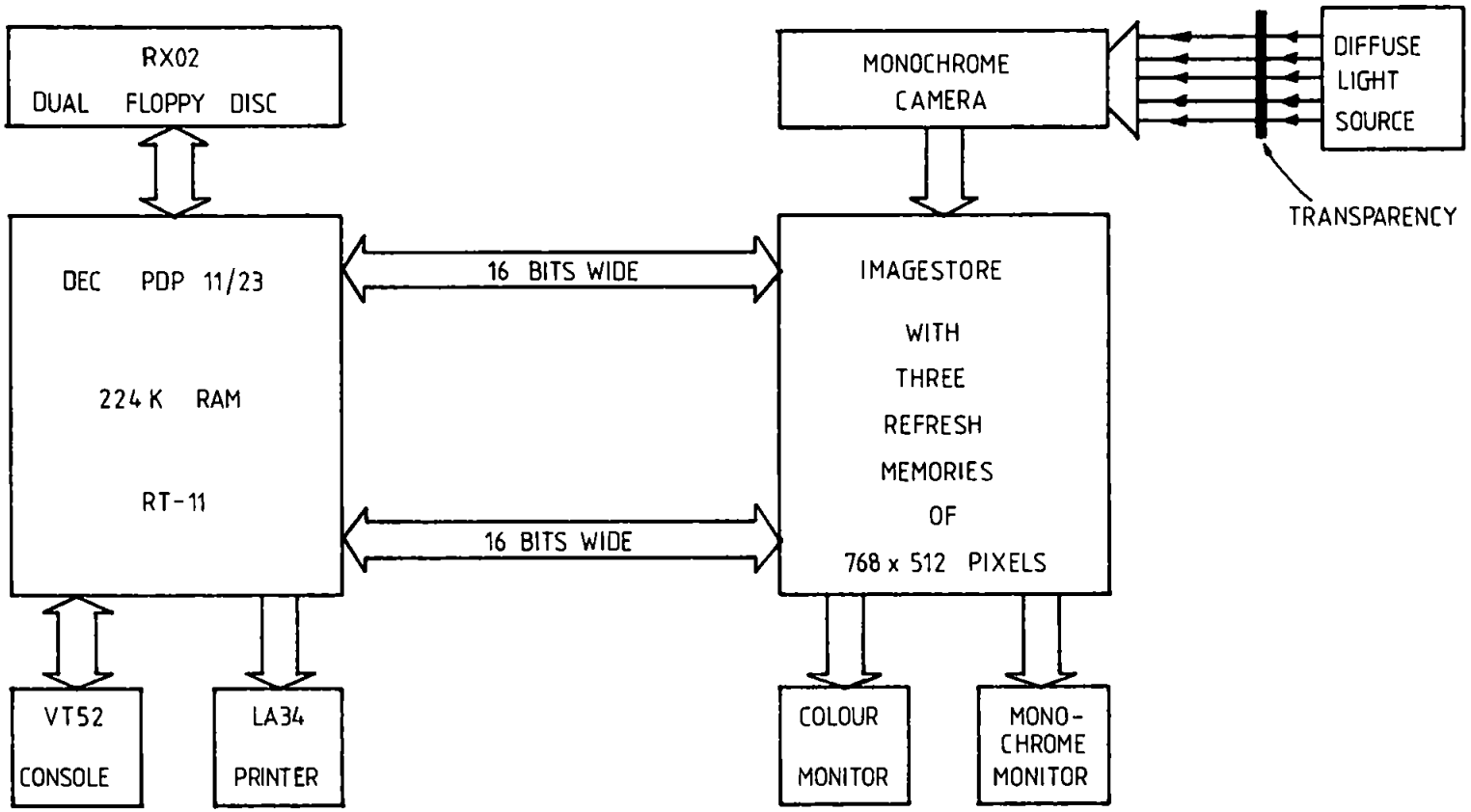

Figure 3.1 Image processing system including imagestore.

iv) One DEC LA34 (DECwriter IV) dot-matrix printer.

v) One DEC DLV11J unit, providing 4 RS-232 serial interfaces for printers and VDUs.

vi) Two DEC DRV11 16-bit parallel interface units, for connecting external devices.

The operating system was DEC's RT-11; a real time system which supports only one user but permits simultaneous foreground/ background program execution. Fortran IV and MACRO-11 assembly language were supplied with RT-11. This afforded easy mixing of Fortran and assembly language which was essential for writing handlers, which interface to the hardware.

The imagestore, described in the next section, was interfaced to the computer via the DRV11 parallel interfaces thus transforming a general purpose minicomputer into an image processing system.

3.2.2 The imagestore

Of all the different types of imagery analysed with image processors, remotely-sensed data is unusual in being multi-spectral. The implication of this is that remotely-sensed data requires as many imagestores as there are spectral channels. Considering the form of typical chlorophyll retrieval algorithms it was decided that 3 image-stores, or rather one imagestore with 3 refresh memories, should be sufficient. This is also convenient for providing a false-colour facility, as each refresh memory can drive one of the three guns (red, green and blue) of a colour monitor.

It was also decided to represent the displayed images as an array of 768 (horizontal) by 512 (vertical) picture elements (pixels) and to

place 393216 (768 x 512) bits of memory on each memory board or bit plane. The number of bits, and thus the number of grey-levels, per pixel is simply determined by the number of bit planes present. However the maximum is eight, thus providing up to 256 (2^8) grey-levels for each pixel.

The choice of the type of memory device was between static and dynamic random access memory (RAM). Bipolar static RAMs were the obvious candidate on account of their very high speed, but the penalties are high cost, large power consumption and small memory size; the last of which exacerbates the first two. Dynamic RAMs are cheap, low power devices, but they are much slower than bipolar RAMs. However, on cost grounds alone, dynamic RAMs of capacity 16,384 (16k) bits were chosen. Superior devices are available now, such as 64k and 256k dynamic RAMs, pseudo-static RAMs and static CMOS RAMs. The read-write cycle time for 16k dynamic RAMs is typically 400 to 500 ns, but with a video sampling frequency of 16.0 MHz (1024 times the line frequency of 15.625 kHz), the pixel period is just 62.5 ns. In order to reduce the effective cycle time of the RAMs, two banks of 24-bit shift registers are used to widen the access path so that 24 consecutive pixels are transferred in one memory cycle. The effective cycle time per bit is then less than 20 ns which is well within the pixel period. Since 24 RAMs are required per bit plane to provide storage for the 384k pixels, the use of 24-bit shift registers means that the RAMs on each bit plane are all loaded or unloaded at the same time. Dynamic RAMs rely upon charge storage for their operation and require refreshing every 2 ms or less to maintain the charge. In this system they are refreshed every four scan lines (0.256 ms) which is well within the specification. One complete 8-bit imagestore requires 192 (8 x 24) RAMs for each refresh

channel.

Since readily available monitors employ interlaced scan rather than progressive scan, it is essential that the refresh memory should take account of the two fields (even and odd) which combine to make one frame of 512 lines. Unfortunately, interlaced scan monitors can cause flicker on fine detail static images. The 16k dynamic RAMs have multiplexed column and row addresses, both 7 bits wide. The relationship between RAM addresses and blocks of 24 pixels, as they appear on the screen, is shown in Fig. 3.2.

The overall structure of the imagestore is illustrated in Fig. 3.3. The input data for the refresh memories may be selected from the analogue-to-digital-converter (ADC) (for the camera) or from the first DRV11 (for the computer) by using the input multiplexers. The outputs are accessed by the computer through the same DRV11 and a multiplexer. The output multiplexers select false- or pseudo-colour operation. The display look-up-tables (LUT) permit an arbitrary transfer function to be introduced into the output section of the refresh channels. The LUTs are implemented with fast (30 ns) bipolar RAMs organised as 256 by 8 bits. Each LUT has eight address and eight data lines. Pixel values are placed on the address lines and the result appears on the data lines. The input-output relationship depends upon the contents of the LUT, which are loaded in from the computer via the second DRV11. Usually the relationship is a linear one, so that the LUTs are 'transparent' to the data. However, by loading different ones into the RAMs, other effects may be obtained, such as contrast stretch and pseudo-colour (density slicing). Pseudo-colour is produced by feeding the output of refresh memory 1 to all three LUTs. When the output of

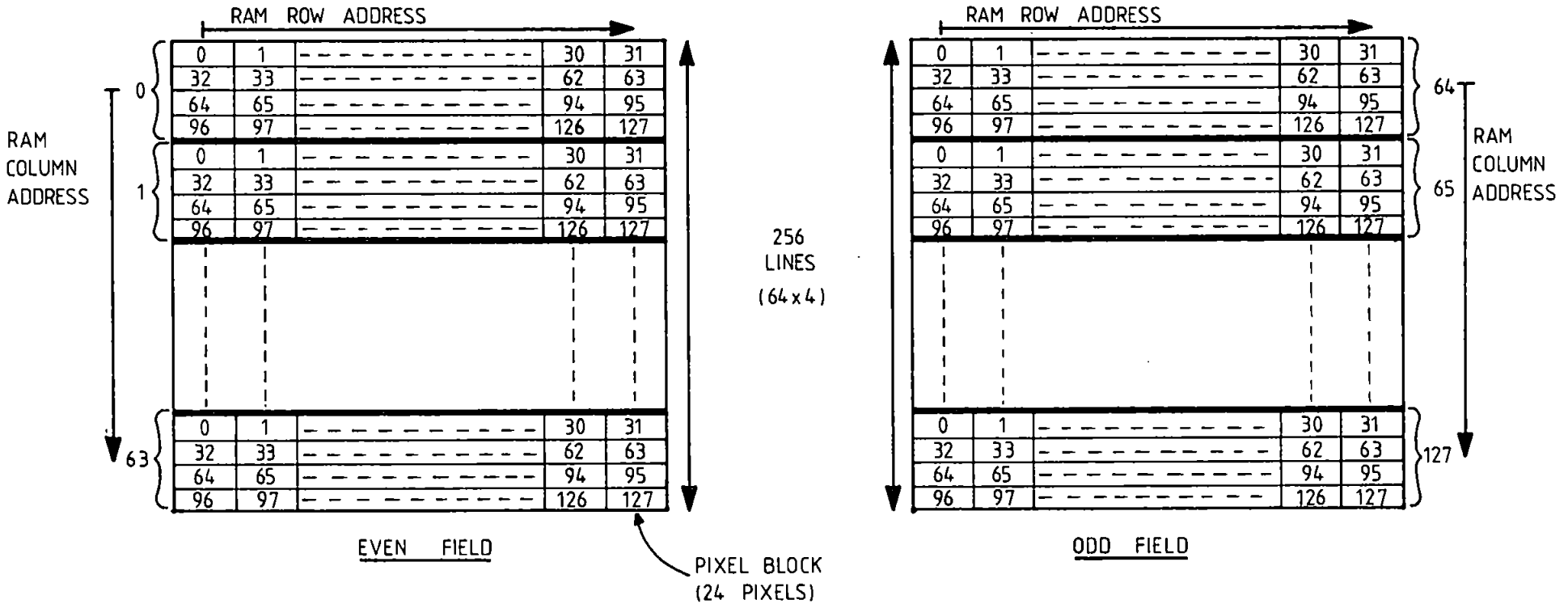

Figure 3.2 Relationship between RAM addresses and pixel blocks.

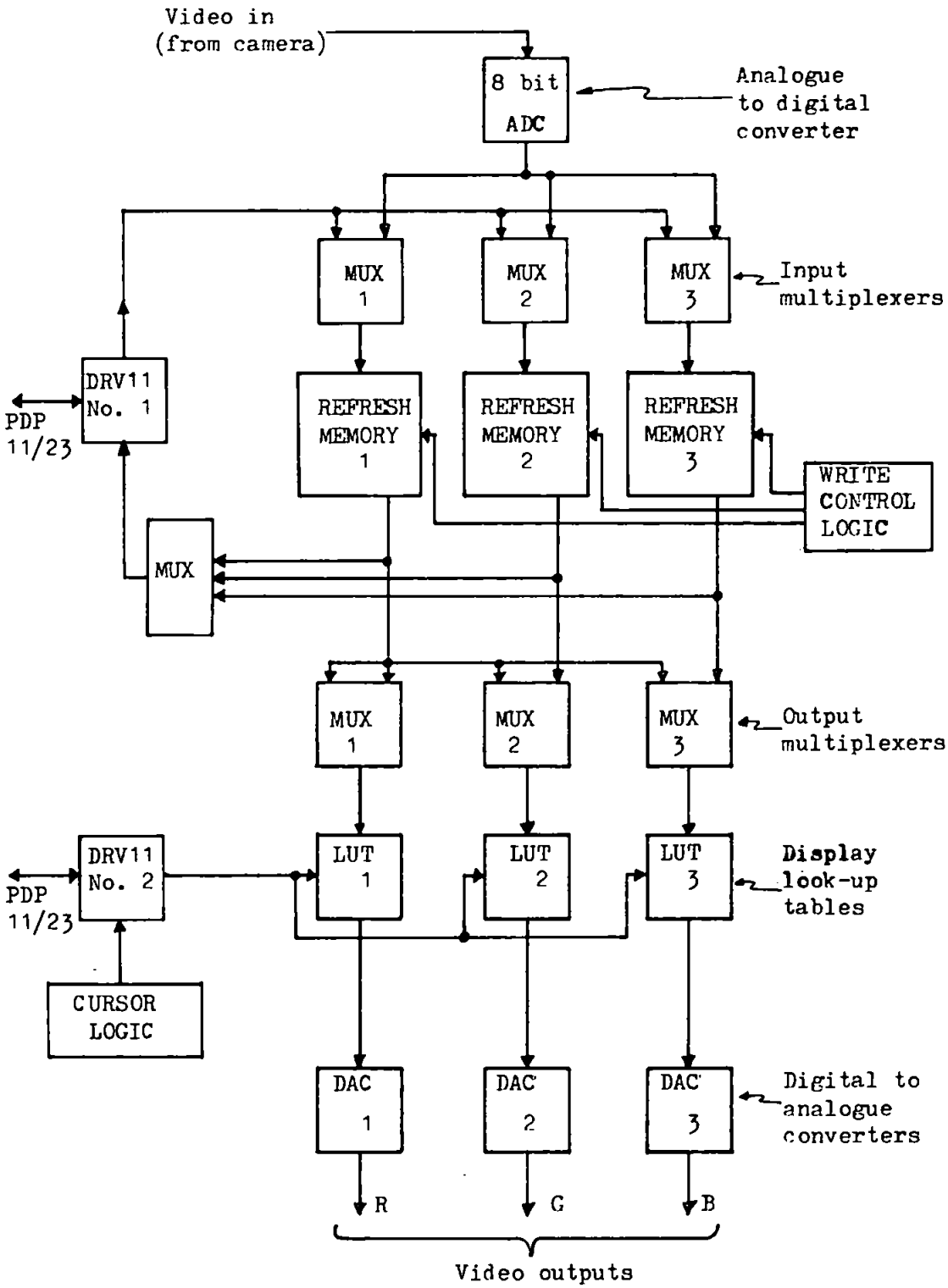

Figure 3.3 Imagestore block diagram.

each refresh channel is fed to its respective LUT, then false-colour images can be generated. Two DRV11 bidirectional interfaces are used; one for data transfer (both directions) and the other for the cursor and loading of the display LUTs. The data transfer rate is limited by the DRV11 to 40,000 words per second, but is usually much slower than this due to software delays. Much faster transfer rates could be achieved by using direct memory access (DMA) techniques. The output of the imagestore is displayed on a colour, double-resolution, shadow-mask monitor which is necessary to achieve the full hardware resolution of 768 by 512 pixels (Watson et al. 1983). All the logic and control circuits associated with Fig. 3.3 are implemented in low-power Schottky TTL.

The first attempts at analysis of remotely-sensed data used aerial photography obtained from a set of four 35mm cameras attached to a Cessna 150 light aircraft. The exposures were taken vertically with Cosina CS-2 cameras fitted with wide-angle lenses and autowinders. Multispectral images were obtained by using different filters and films. The resulting black and white transparencies were illuminated by a diffuse light source and scanned by a broadcast quality Bosch television camera (7 MHz bandwidth), whose output was digitised by a TRW 8-bit analogue-to-digital converter.

The camera employs a Chalnicon tube to ensure a linear relationship between image intensity and output voltage. Each of two or three spectral images may be registered and digitised and then placed in the imagestore ready for analysis. The alignment of spectral images (registration) was performed with a vernier stage and a rotatable mount. However, the quantitative analysis of aerial photographs was

found to be seriously hampered by the following difficulties:

i) Despite the facilities for accurately positioning the transparencies, it proved impossible to register the images properly. This was thought to be caused by the camera axes being slightly skew; thus the viewing angles were not identical.

ii) Coverage is limited to those areas in which there is some land, or other feature, in view because registration may only be achieved by lining up distinct objects or features.

iii) A conflict arises over the bandwidth of the filters. On the one hand the determination of chlorophyll requires narrow filters, while exposure requirements dictate a much broader bandwidth for the levels of illumination usually encountered (Curran 1981).

iv) The relationship between image-tone or density of the transparency and the exposure is subject to large uncertainties introduced in both the manufacture of the film and its development (Swain and Davis 1978). This makes it difficult to establish absolute values of radiance needed for quantitative work.

3.2.3 Addition of pipeline processor to imagestore

The combination of minicomputer and imagestore constitutes a conventional image processor. The addition of processing power to the imagestore converts it into a display processor (Ince 1983) in the sense that some processing may take place independently of the minicomputer. Since many chlorophyll retrieval algorithms use the difference or ratio of two spectral channels, it was felt that special

hardware for the subtraction or division of two images would be a valuable and novel feature. By feeding the outputs of two refresh memories into an arithmetic and logic unit (ALU), various functions of the two inputs could be obtained at video rate, i.e. in real time. The range of functions available may be extended by adding look-up tables both before and after the ALU. The combination of ALU and LUTs represents a programmable pipeline processor. The principle of a pipeline processor is closely analagous to a factory production line with a conveyor belt carrying items to be subjected to various processes or operations (Fig. 3.4). All items are treated the same; i.e. they are all subjected to the same set of operations. The advantage is that all operations occur concurrently, but on different items at different stages of assembly or completion. This speeds the whole procedure up; the improvement depending upon the number of stages. By regarding LUTs as units capable of performing elementary functions, the combination of ALU and LUTs may be regarded as a simple pipeline processor. Furthermore, as the LUTs may be programmed to perform logarithms, exponentiation and multiplication and division by constants, then the pipeline processor becomes a programmable one, i.e. its particular function is amenable to software control. Figure 3.5 shows the structure of the programmable pipeline processor which has three stages. The first pipeline stage has two LUTs only because there are two inputs to the pipeline. The pipeline processor was incorporated in the original imagestore by connecting it between the outputs of refresh memories one and two, and the output multiplexers. The arrangement of the combined imagestore and programmable pipeline processor is illustrated in Fig. 3.6. Again, each LUT was implemented with two bipolar 256 by 4 bit RAMs (type 93422) and two 74S181 Schottky TTL devices were used for the ALU. The latter provides 16 logical and

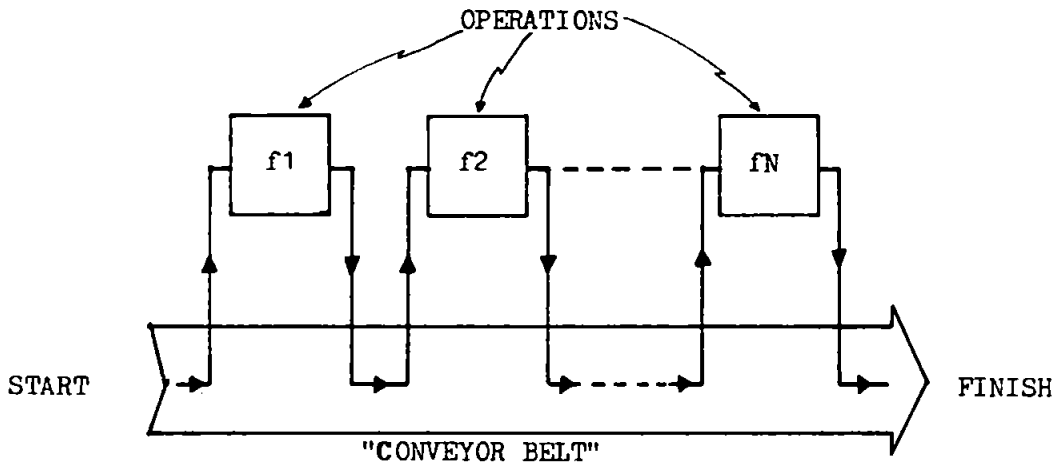

Figure 3.4 Principle of pipelining.

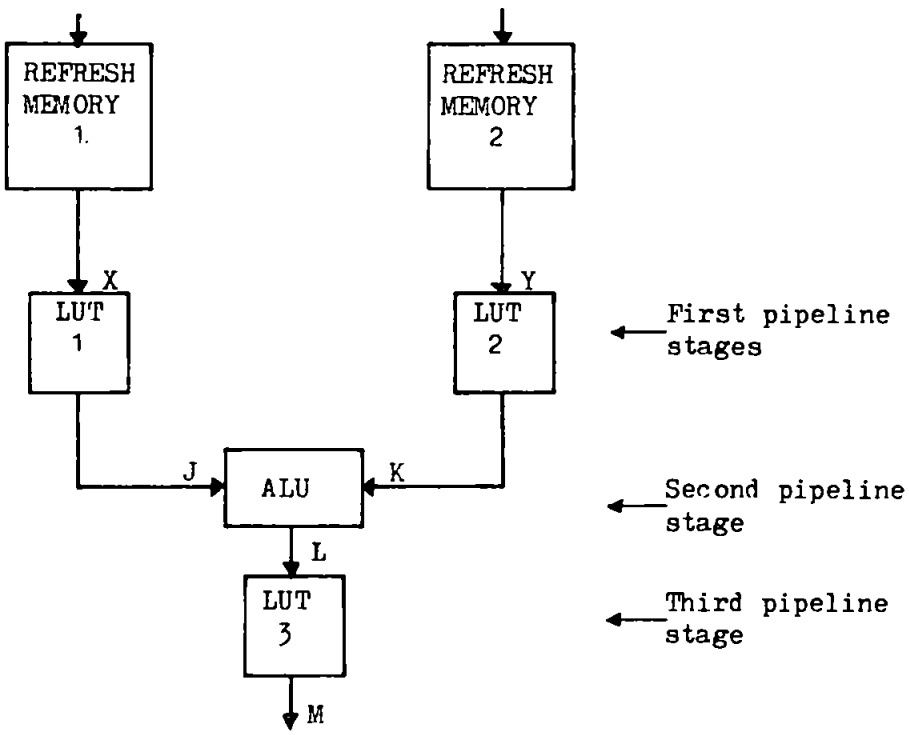

Figure 3.5 Programmable pipeline processor.

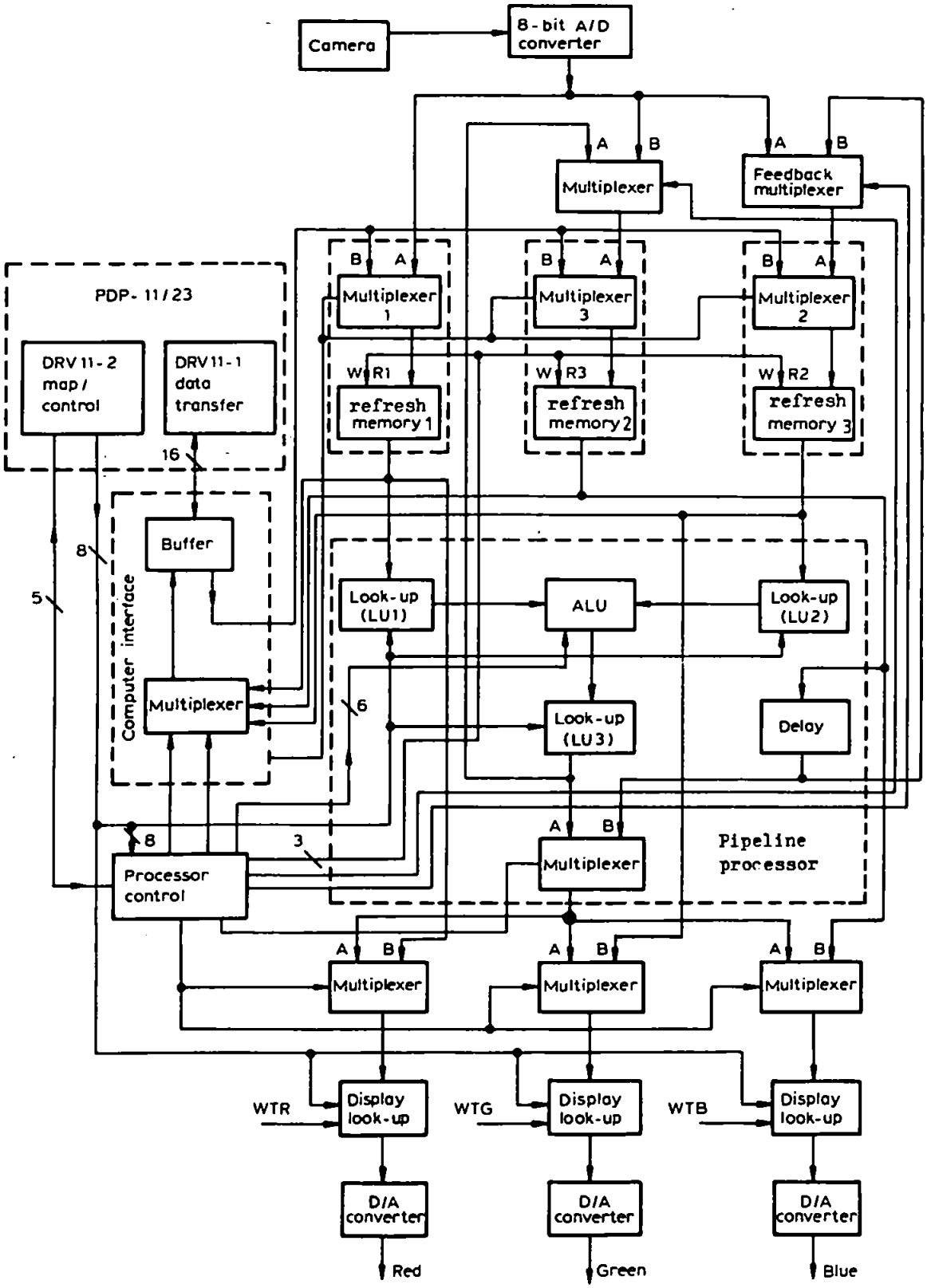

Figure 3.6 Block diagram of combined imagestore and pipeline processor.

arithmetic functions, of which only four are used: logical 'AND', logical 'OR', arithmetic addition and subtraction. The ALU is unable to perform multiplication and division directly, but these may be obtained by the addition and subtraction of logarithms. In this case LUT1 and LUT2 perform the log function and LUT3 performs antilogarithms. The familiar bases of e (2.7182...) and 10 for logs and antilogs cannot be used here because the data are integers in the range 0 to 255 (2^8-1). This limitation is imposed by the 8-bit representation of pixel values.

The optimum base b is such that the input range (0 to 255) is mapped to the range 0 to 255 exactly. For the log function the condition is:

$$\log_b (\text{Maximum input value}) = \text{Maximum output value}$$

$$\log_b 255 = 255$$

$$255 = b^{255}$$

$$b = 255^{1/255} \qquad (3.1)$$

Similarly, for the antilog function:

$$b^{255} = 255$$

$$b = 255^{1/255} \qquad (3.2)$$

The optimum base is therefore the same for both functions and is given by Eqs. 3.1 and 3.2:

$$b = 255^{1/255} = 1.0219682709$$

Logarithms of base b may be calculated from:

$$\log_b x = (\log_{10} x)/\log_{10} b = 105.96 \log_{10} x$$

$$\log_b x = (\ln x)/\ln b = 46.02 \ln x$$

For use in the LUTs, all the values must be rounded off to the nearest integer. A control program for the pipeline processor was written in Fortran and MACRO-11 assembly language to set up the ALU and LUTs for a variety of functions. The program operates by presenting a menu and a number of sub-menus (Fig. 3.7). The user enters a string of characters to select a complex sequence of instructions from the main menu. There are sub-menus for choosing the ALU function and for setting the LUTs up for log, antilog and linear operation. Scaling factors may also be included.

To illustrate how the pipeline processor may be used, the implementation of a retrieval algorithm is considered. For chlorophyll a typical algorithm is:

$$C = a_o \left(\frac{x}{y}\right)^{a_1} \tag{3.3}$$

where C is the chlorophyll concentration, x and y are water-leaving radiances in different spectral channels and a_o and a_1 are constants. As x and y are usually less than 1 mW/(cm^2. sr. μm), they must both be scaled up by a factor α for representation in the imagestore. A typical value for α is 100.

Processor control program

Function	Code
Write to FS1 (from camera or CCT)	A
Write to FS2 (from camera or CCT)	B
Write to FS3 (from camera or CCT)	C
Set up LUT1-4	D
Write to FS2 from FS3	E
Write to FS3 from FS1,FS2 via ALU	F
Set up ALU	G
Display FS1,2 o/p via ALU	H

Function	Code
Display FS3 i/p,o/p alternatively	I
Display FS1,2,3 for colour comp	J
Display FS3 output	K
Software process FS3	L
Software process FS2	M
Software process FS1	N
Write from camera	O
Write from CCT	P

Look-up tables	Code
LUT1 (associated with FS1)	1
LUT2 (associated with FS2)	2
LUT3 (associated with ALU o/p)	3
Enable LUTs on video o/p board	4

Mapping law		Code
Log	optimised base	A
Antilog		B
Linear		C

ALU function	Code
Modulus of (A-B)	1
A plus B	2
A (i.e. FS2 o/p)	3
A.B (logical AND)	4
A+B (logical OR)	5
A-B (-ve forced ϕ)	6
A-B (true ratio)	7

Figure 3.7 Menus for setting-up and controlling the programmable pipeline processor.

Hence Eq. 3.3 becomes:

$$C = a_o\left(\frac{X}{Y}\right)^{a_1} \tag{3.4}$$

where X and Y are the scaled values αx and αy respectively. Note that the scaling factor α cancels out in this algorithm, and so does not affect the result. A second scaling factor β is also introduced to reduce the effects of quantisation, which produce large errors when dealing with small values. This scaling factor also ensures that the chlorophyll map will be bright enough for display on a monitor. Absolute values of chlorophyll concentration will not be obtained, but only relative values are required for display purposes. The modified form of Eq. 3.4 is:

$$C' = \beta a_o\left(\frac{X}{Y}\right)^{a_1} \tag{3.5}$$

C' merely denotes the scaled up chlorophyll concentration. The pipeline processor is programmed for this algorithm by setting up the following functions in the pipeline stages (refer to Fig. 3.5):

LUT1 and LUT2 : $f(x) = \log x$ (3.6)

ALU : $f(x,y) = x-y$ (3.7)

LUT3 : $f(x) = b^{a_1 \cdot x + \log(\beta a_o)}$ (3.8)

The terms x and y in Eqs. 3.6 to 3.8 are only used to specify the functions; they do not refer to radiance. Logarithms are to the base b, where b is the optimum base discussed above.

Referring to Fig. 3.5, the algorithm is evaluated in the following way:

$$J = \log X$$

$$K = \log Y$$

$$L = J-K = \log X - \log Y$$

$$M = b^{a_1 \cdot L} + \log(\beta a_0)$$

$$= b^{a_1 \cdot (\log X - \log Y)} + \log(\beta a_0)$$

$$= b^{\log(\beta a_0)} \cdot b^{\log(X/Y)^{a_1}}$$

$$= \beta a_0 \left(\frac{X}{Y}\right)^{a_1}$$

$$= C'$$

If the second scaling factor β is not used, that is $\beta = 1$, errors of the order of 100% may occur. The error is reduced to less than 10% with $\beta = 10$, after descaling. Although C' does not represent the absolute chlorophyll concentration, the pseudo-colour technique may be used to transform different grey-levels, and hence concentrations, to various colours and so provide a quantitative map of chlorophyll concentration.

3.2.4 Computer upgrade

The memory available with the PDP11/23 was 224 kbytes and could only be expanded to a maximum of 256 kbytes because of the 18-bit address bus. When executing a program, the amount of free memory would be considerably less than this. Certain forms of processing must be undertaken by the PDP11/23 rather than by the pipeline processor, but as each refresh channel has a capacity of 384 kbytes, processing was restricted to approximately one half of the total number of pixels in one image; a complete image could only be processed piecemeal.

Moreover, data may only be input via the camera, so that data supplied on computer compatible tapes (CCT) could not be used. Therefore it was decided to upgrade the computer by purchasing a new central processing unit (CPU) capable of supporting more memory, and also by providing additional peripheral units, such as a tape drive.

However before this upgrade took place, some time was spent analysing CZCS data on the Polytechnic's PRIME 750 mainframe computer. At the time, this machine was the only one at the Polytechnic with a standard 9-track tape drive capable of reading CZCS tapes produced at Dundee University. The possibility of connecting the PRIME 750 to our own PDP 11/23 via a serial line was also considered as a means of transferring CZCS data into the PDP 11/23. However, the very slow data rate and the difficulties in reconciling the incompatible computer protocols ('hand-shaking') militated against this option. A set of Fortran programs was written on the PRIME 750 for CZCS analysis including: data demultiplexing, calibration, radiometric conversion and simple atmospheric correction, which used a method outlined by Ball Aerospace Systems Division (1979b). This technique is now regarded as an over-simplified approach to the problem. The PRIME 750 had no image display facilities, but it was possible to produce very crude images on the lineprinter using a slightly modified version of the overprint technique (Gonzalez and Wintz 1977). With this technique, each pixel is represented by one or more superimposed characters. For example, the lowest/darkest grey-level is printed using M, W, # and 0, while a blank space is used for the highest grey-level. These characters and others are used to generate 16 different grey-levels. An example of the overprint method is shown in Fig. 3.8 using uncorrected, CZCS, channel 3 data for 22/6/1981. Results obtained on the PRIME 750 and

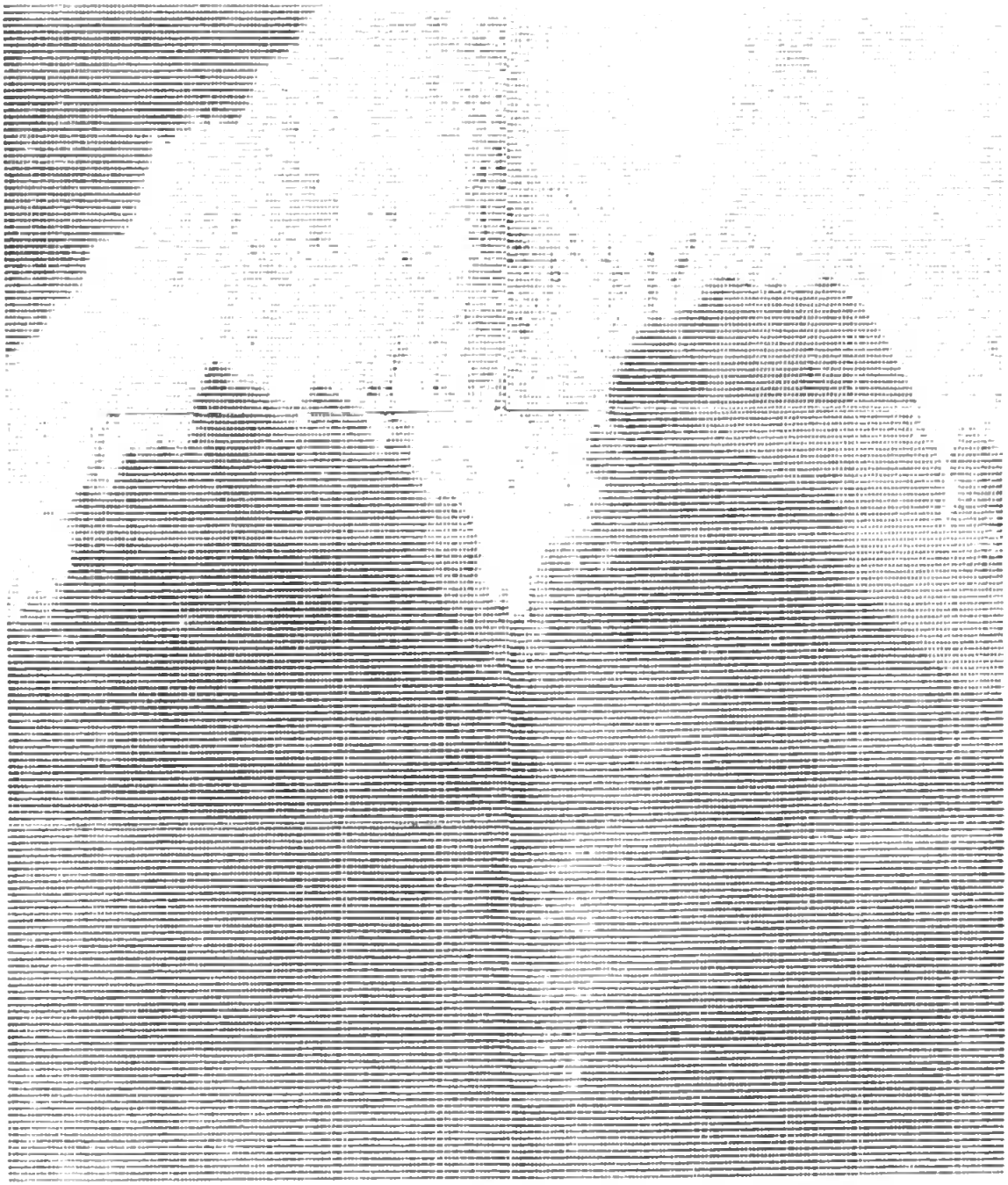

Figure 3.8 Overprint image of uncorrected CZCS scene (channel 3, 22/6/1981).

the simple atmospheric correction method are described by Wade et al. (1984). This work provided a strong basis for producing a complete and proper CZCS analysis system on our own upgraded computer.

The computer was upgraded in October 1983 with a new Motorola 68000 based processor and one megabyte of memory, housed in a Q-BUS backplane with a second one for expansion. The equipment was supplied by Arrow Computer Systems Ltd., of Epsom (UK). The 68000 is Motorola's first 16-bit processor, although in many respects it is a 32-bit device; for example it has seventeen 32-bit registers (Kane 1981). The 68000 has an address space of 16 Mbytes, uses an 8 MHz clock and is considerably more powerful than the PDP11/23. The increased memory can easily accommodate one whole image. Two 20 Mbyte Winchester disc drives and a Thorn-EMI SE8900 1600 bpi tape transport were installed, the latter being used for reading CZCS tapes, archiving images and 'backing-up' or storing programs and system software. A 48 Mbyte Winchester disc drive was added at a later date. Winchester drives provide fast access to large amounts of data and can read or write a whole image in a few seconds. Fig. 3.9 is a block diagram of the new system. The 68000 runs under the UNIX* operating system which is both multi-user and multi-tasking. Not only does it support more than one user, it also enables each user to run several processes concurrently. A DEC VT101 terminal is provided for a second user and more users may be accommodated by adding extra terminals. UNIX also offers the ideal environment for developing and executing programs written in 'C'; in fact 90% of UNIX is written in this language. C is a block-structured language with the necessary constructs for structured programming, and

* UNIX is a Registered Trade Mark of Bell Laboratories.

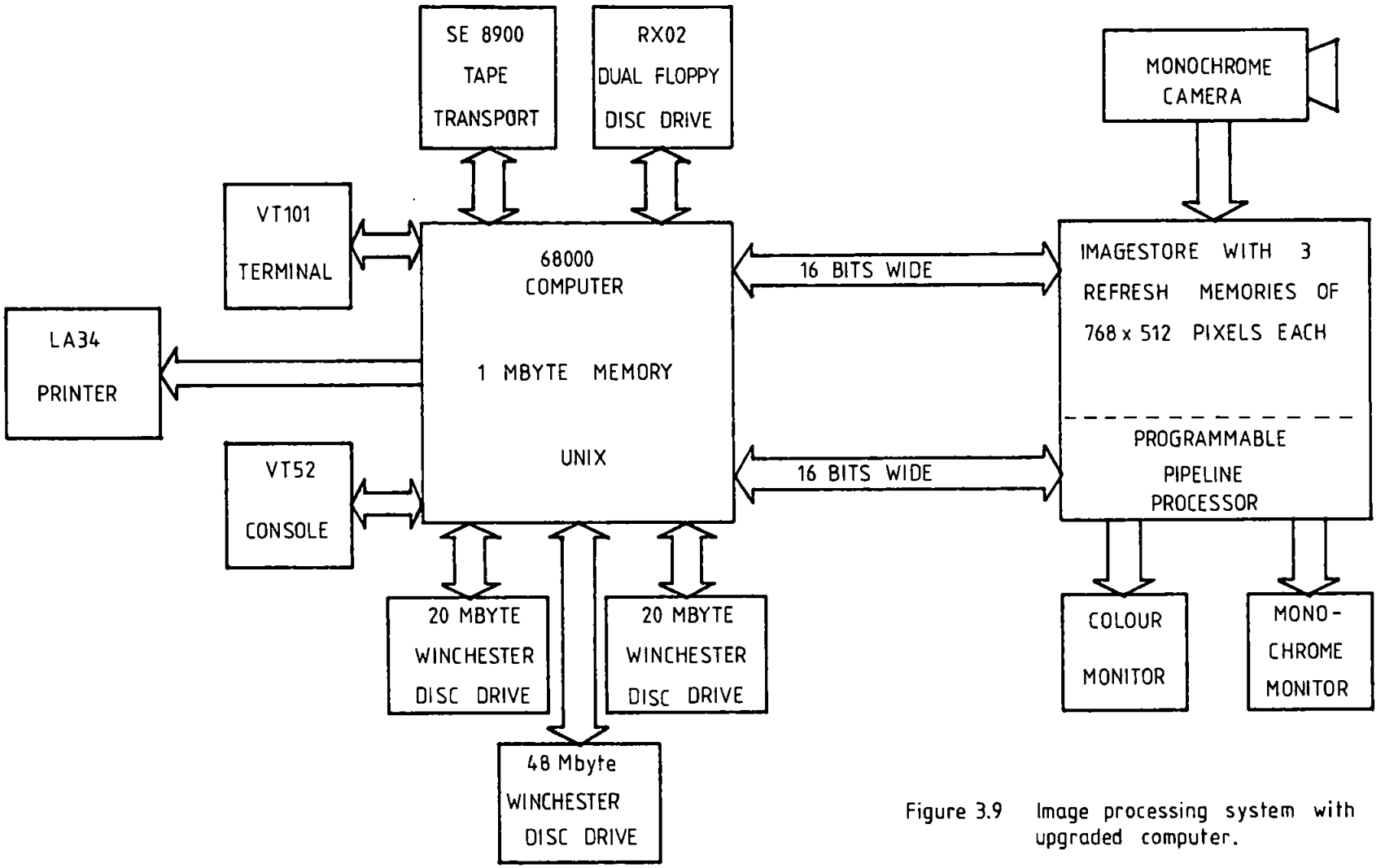

Figure 3.9 Image processing system with upgraded computer.

can perform bit-manipulation directly. UNIX and C are increasingly being used for image processing systems (Landy et al. 1984, Waltuch et al. 1985, Guberek 1985). For further details on UNIX consult Banahan and Rutter (1982) and Kernighan and Mashey (1979); for C refer to Kernighan and Ritchie (1978).

3.3 IMAGE PROCESSING SOFTWARE

Swain and Davis (1978) identified ten broad aspects of image processing and data analysis which occur in the following order:

i) Radiometric transformations
ii) Geometric transformations
iii) Data presentation
iv) Data compression
v) Image enhancement
vi) Statistical analysis
vii) Clustering
viii) Feature extraction
ix) Supervised classification
x) Results presentation

In any one application some of these steps may be omitted. The above list does not include atmospheric correction as it is not usually required for terrestrial remote sensing; it is however essential for CZCS analysis and is described in Chapter 4. The first 5 items above are concerned with the production of images corrected for various defects and enhanced for cosmetic purposes to aid human interpretation. These preprocessing functions are described in Section 3.3.1. The remaining processing stages deal with the extraction of quantitative or statistical information from images and are covered in Section 3.3.2 under the heading of analysis techniques.

Although the computer was upgraded at the end of October 1983, it was not until January 1984 that the image processing system was fully operational again. This long delay was introduced by a problem with the UNIX operating system, which treats everything as a file, including physical devices. Communication with physical devices is thus elegantly achieved using simple read and write commands. However, it is only through the use of a special 'driver' program that a physical device may masquerade as an ordinary file. A set of drivers was supplied for common peripheral devices such as terminals, printers and disc drives. However, for the custom-built imagestore two drivers had to be written: one for data transfer between the computer and image-store, the other for reading the cursor position and controlling the pipeline processor. New drivers are incorporated into the system by recompiling the operating system, i.e. UNIX itself. This work requires a detailed knowledge of the innermost workings of UNIX which is only briefly described in the documentation.

3.3.1 Preprocessing techniques

3.3.1.1 Generation and calibration of CZCS images

The CZCS digital data is supplied on a computer compatible tape without any processing, i.e. as received from the satellite. It therefore comprises the data for all six channels and for the full scan width. The CZCS data format is illustrated in Fig. 2.20a of Chapter Two, but is further structured by the arrangement of blocks and inter-block gaps on the tape (Fig. 3.10). One block of data is the smallest quantity of data that may be read from the tape. As the tape contains data for an area far greater than the 768 by 512 pixel capacity of the image-store, the first step is to extract data for a particular region of interest. The number of scanlines which need to be skipped-over before

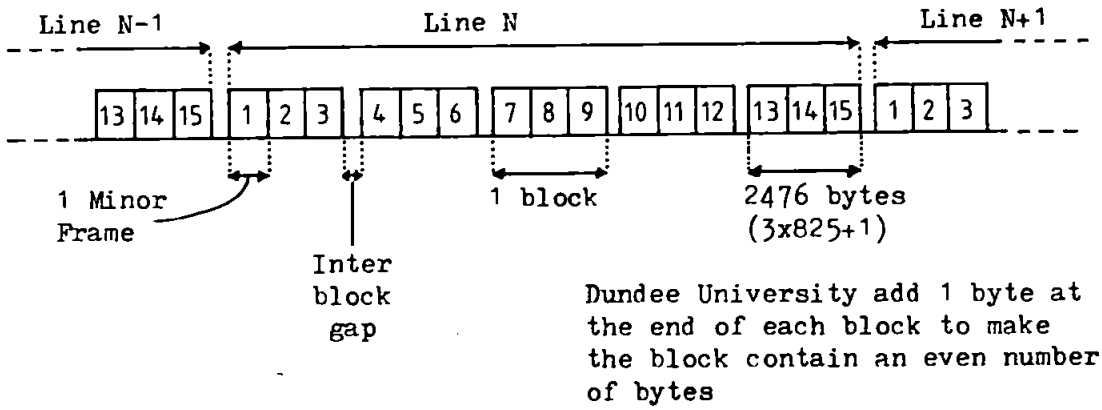

Figure 3.10 Arrangement of blocks on the CCT.

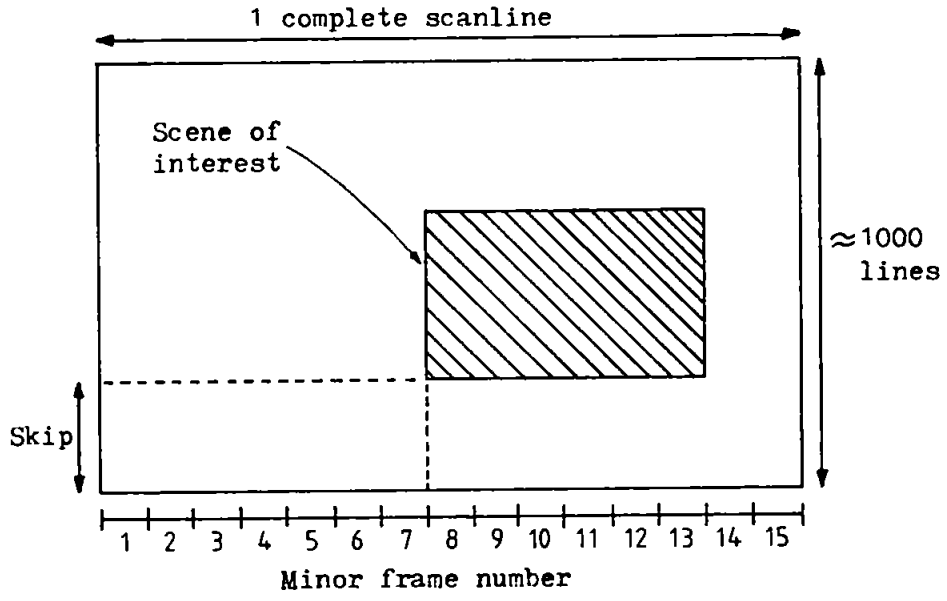

Only part of minor frame 15 contains image data

Figure 3.11 Use of quick-look prints for estimating position of scene of interest on the CCT.

reading data may be estimated from careful examination of a quick-look print (Fig. 3.11). It must be remembered that the start of the CCT does not necessarily correspond to the start of a scanline, and that the minor frames are not evenly distributed across the quick-look print because of the variation in viewing angle and Earth curvature. It is not surprising then that the location of the desired region from the CCT is rather haphazard. Having located the desired starting position, 512 full scanlines are read from the CCT onto a Winchester disc drive. The next stage involves the extraction of calibration data, housekeeping data and the data representing the radiance measured at the satellite. The last of these requires demultiplexing or unscrambling of the data (Ball Aerospace Systems Division 1979a, Singh et al. 1983) so that files of raw digital values (0-255) may be produced for each channel. At this stage the position of the left-hand edge of the region is selected by specifying a minor frame number from one to nine. An image may now be displayed, using a program to send the data to the imagestore, to check that the correct region has been extracted from the CCT.

The calibration data may now be analysed to produce conversion factors for calculating radiances from raw digital values. In order to optimise the signal-to-noise ratios, the radiometric sensitivities, and consequently the radiometric conversion factors, are all different for the six channels. The calibration procedure consists of voltage and active calibration (Singh et al. 1983). Fig. 3.12a shows the CZCS system diagram for deriving the calibration expressions. Normally the sensor views the Earth's surface, but for active calibration purposes it views a standard lamp. For voltage calibration the sensor is switched out of circuit and replaced by a reference voltage source.

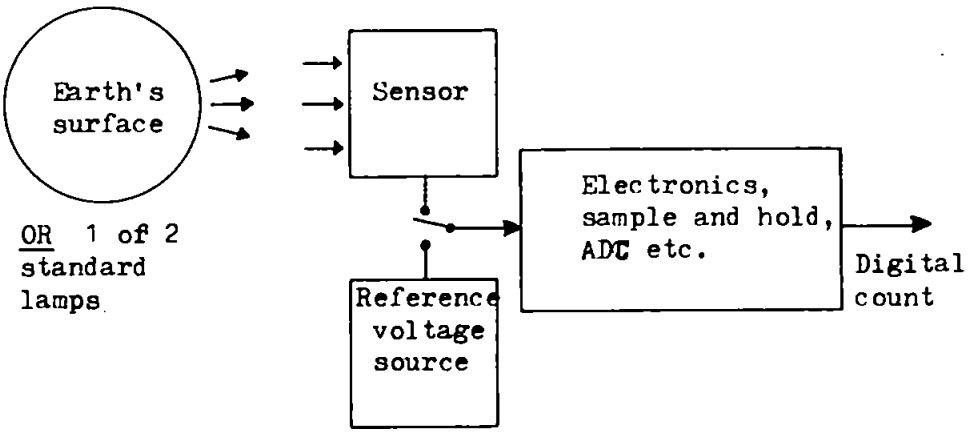

(a) Scanner block diagram. Facilities for programmable voltage gain and thresholding are not shown.

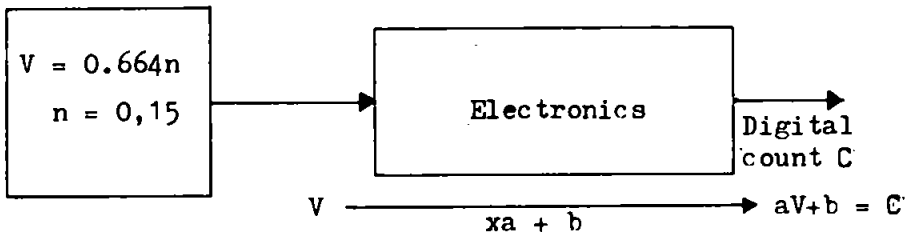

(b) Voltage calibration.

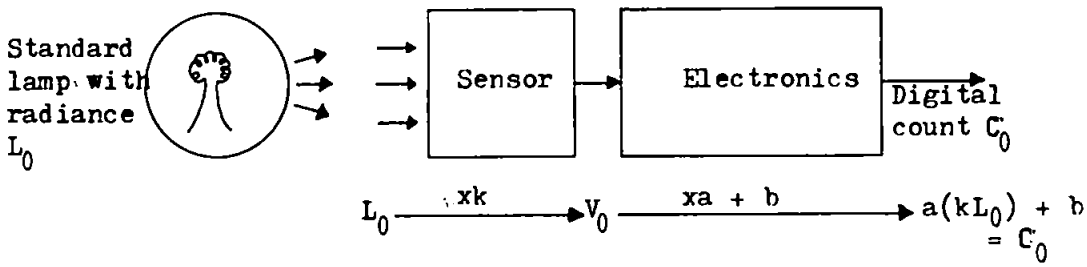

(c) Active calibration.

Figure 3.12 CZCS calibration.

Voltage calibration is concerned with the characterisation of the electronics which follow the sensor, such as sample and hold circuits, analogue to digital converters etc. Sixteen different stepped reference voltages are applied to the inputs of the electronics and the corresponding digital outputs are recorded (Fig. 3.12b).

A relationship of the following form is assumed:

$$C = aV + b \tag{3.9}$$

where V is the input voltage (0.664N, N = 0, 15), C is the digital count (0-255) and a and b are constants determined from simple least squares analysis between C and V. The justification for this simple linear relationship is the very high correlation coefficient, of the order of 0.9999 or higher.

Active calibration is concerned with the characterisation of the sensor itself, i.e. the silicon photodiode detectors and optics. The sensor is exposed to a standard lamp of known radiance L_o and the corresponding digital counts are averaged over the whole scene, giving a mean digital count of C_o (Fig. 3.12c). The following relationship is assumed:

$$V = kL \tag{3.10}$$

Where L is the incident radiance, V is the detector output voltage and k is a constant. Hence:

$$C_o = a\ V_o + b\ = a\ kL_o + b \tag{3.11}$$

However, when the sensor is viewing a radiance L originating from Earth (normal operation) the expression for C is:

$$C = aV + b = akL + b \tag{3.12}$$

Rearranging Eqs. 3.11 and 3.12 gives respectively:

$$akL_o = C_o - b \tag{3.13}$$

$$akL = C - b \tag{3.14}$$

Dividing Eq. 3.14 by Eq. 3.13 gives:

$$\frac{L}{L_o} = \frac{C - b}{C_o - b}$$

$$L = \frac{L_o C}{C_o - b} - \frac{bL_o}{C_o - b}$$

$$L = \text{Slope}.\ C + \text{Intercept} \tag{3.15}$$

where the slope = $L_o/(C_o-b)$ and intercept = $-bL_o/(C_o-b)$. Note that neither a nor k appear in these expressions, which depend only upon L_o, C_o and b. b is usually very much smaller than C_o.

This analysis assumes that the threshold is off and the voltage gain is one, which was the case for all the CZCS scenes analysed in this work. Standard lamp number one is used and values for L_o are (Singh 1982, personal communication):

Channel	Radiance L_o
1	2.04 mW/(cm^2sr. μm)
2	1.55
3	1.37
4	1.11
5	5.25

Channel 6 is calibrated in an altogether different manner, which is not discussed here since this work only makes use of measurements in the visible range.

This straightforward method of calibration has been undermined by the observation of Gordon et al. (1983a) that the sensitivity of the CZCS has been decreasing with time. This conclusion was reached by comparing CZCS derived values of water-leaving radiance with independent estimates or direct measurements. It was found that the loss of sensitivity in channel 1 is quite dramatic, with only modest decreases in the sensitivity of channels 2 and 3. Sensitivity loss in channel 4 may be ignored. This loss of sensitivity is not revealed through the previously described calibration procedure because an optical surface, which is not used during active calibration, is believed to have deteriorated (Austin 1982). Gordon et al. (1983a) suggest a method for the calculation of radiance which obviates the analysis of CZCS generated calibration data. In the first instance L'_T is evaluated:

$$L'_T = (A.\ DN + B).\ C \qquad (3.16)$$

where DN is the digital number (0-255), and A and B are the pre-flight slope and intercept values respectively. C is another constant which improves the consistency between solar irradiance and sensor calibration (Gordon 1981b); it does not account for sensitivity loss. Thus L'_T is the radiance without correction for sensitivity loss. The corrected or true radiance L_T is calculated from:

$$L_T = L'_T/f(N) \tag{3.17}$$

where f(N) accounts for sensitivity loss and is given by:

$$f(N) = a + bN + cN^2 \tag{3.18}$$

where a, b and c are constants (not to be confused with a and b above) and N is the orbit number which is effectively a measure of time elapsed since launch. Eq. 3.18 is an empirical relationship derived from measurements collected over a period of several years. This technique was used for CZCS calibration, except for some earlier work on the PRIME 750 which relied upon the first method.

3.3.1.2. Image enhancement

Image enhancement seeks to improve an image, by whatever means, for visual interpretation and the techniques used depend very much upon the particular application. Image enhancement must be distinguished from image restoration which attempts to recover the original image by using a mathematical model of the image deformation process. Image enhancement is therefore regarded as a cosmetic or heuristic process.

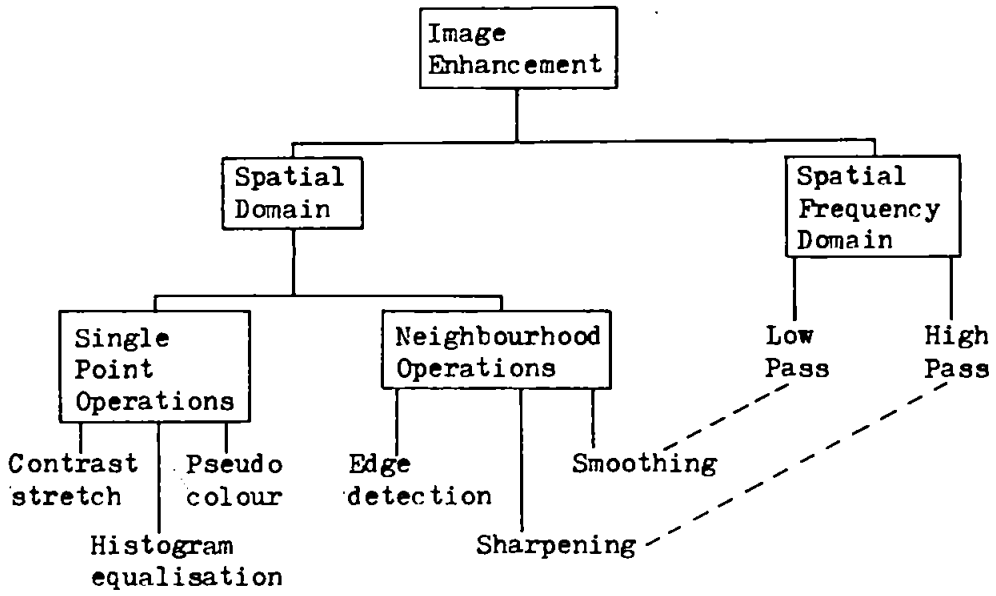

Figure 3.13 Classification of image enhancement operations.

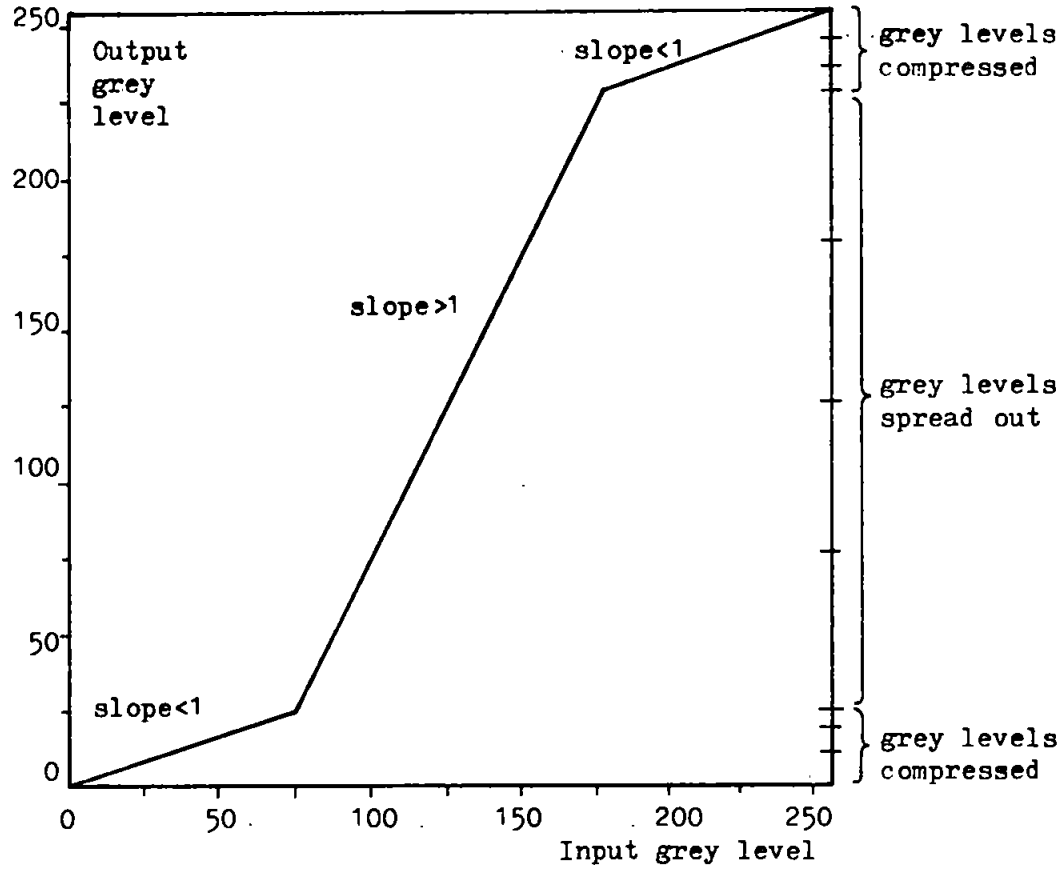

Figure 3.14 Contrast stretch: transfer function.

There are plenty of standard texts on digital image processing with sections on image enhancement, e.g. Castleman (1979), Gonzalez and Wintz (1977), Hall (1979) and Rosenfeld and Kak (1982). Hord (1982) and Schowengerdt (1983) discuss image processing within the context of remote sensing.

The classification of image enhancement operations is shown in Fig. 3.13 and reveals that there are two distinct domains in which operations may be performed: the spatial domain and the spatial frequency domain. The spatial domain is simply the domain represented by a two-dimensional array of pixels, while the spatial frequency domain is reached by taking the Fourier transform of the image. Most of the techniques used in the spatial frequency domain rely upon the modification of the intensity of spatial frequencies, i.e. filtering. The spatial domain operations are further divided into those performed upon single pixels (pointwise operations) and those upon neighbourhoods of pixels. Pointwise operations may be regarded as grey-level mappings, whereas most neighbourhood operations are convolution processes. The terms convolution and correlation are sometimes used interchangeably when dealing with discrete variables; however correlation is best reserved for template matching in which an image is searched for a feature with a particular shape. The convolution of two functions $f(x,y)$ and $h(x,y)$, where x and y are discrete variables, is given by:

$$g(x,y) = \sum_{i=1}^{m}\sum_{j=1}^{n} f(i,j)\ h(x-i,\ y-j) \qquad (3.19)$$

where g(x,y) is the resulting function and m and n represent the extent of the functions. For convenience, Eq. 3.19 is usually denoted by:

$$g(x,y) = f(x,y) \;**\; h(x,y) \tag{3.20}$$

where the convolution operation is represented by two asterisks. For the purpose of image enhancement, f(x,y) and g(x,y) may be interpreted as the original and convolved images respectively, while h(x,y) is a two-dimensional mask or weighting matrix which determines the nature of the operation. Convolution in the spatial domain is equivalent to multiplication in the spatial frequency domain. Thus by switching to the spatial frequency domain, g(x,y) may alternatively be found from:

$$g(x,y) = \mathcal{F}^{-1}[F(u,v).\, H(u,v)] \tag{3.21}$$

where F(u,v) and H(u,v) are the Fourier transforms of f(x,y) and h(x,y) respectively, u and v are spatial frequency variables and $\mathcal{F}^{-1}$ represents the inverse Fourier transform. Therefore the inverse Fourier transform of the product of two Fourier transforms is the convolution of the original functions. H(u,v) is known as the transfer function. Consequently, many enhancement techniques may be realised in either domain; this correspondence is indicated in Fig. 3.13 by dashed lines.

The remainder of this section is devoted to a brief discussion of a few pointwise and convolution-type enhancement techniques implemented on the image processing system. The simplest point-wise technique is contrast stretching which modifies the grey-level or intensity of each pixel so as to increase the contrast by spreading a range of grey-

levels out. In this way, small differences in pixel intensity are accentuated. The transformed grey-level for each pixel is specified by a position-invariant transfer function, i.e. one which depends upon the pixel's grey-level alone and not upon its position in the image. Figure 3.14 depicts such a function and indicates how grey-levels are spread out where the slope is greater than one, and compressed where the slope is less than one. The overall effect is to enhance the contrast of pixels in the middle range at the expense of pixels at the extremes of darkness and brightness. Contrast stretching is accomplished by loading the desired transfer function into the display look-up-tables and is therefore a simple and fast technique. For most purposes the transfer function is represented by a combination of linear sections (piecewise-linear) for simplicity; hence the transfer function in Fig. 3.14 is a three step piecewise-linear one.

Any arbitrary transfer function may be used for contrast stretching; however for a particular image there exists one transfer function which causes the transformed image to have an equal distribution of pixels amongst the grey-levels, i.e. a flat histogram. This technique is termed histogram equalisation and enables the image to be easily interpreted by visual means and removes the experimentation which is necessary for optimum results with contrast stretching. For a continuous grey-scale (infinite number of grey-levels) the transfer function T is evaluated from (Gonzalez and Wintz 1977):

$$s = T(r) = \int_0^r p(w)dw \qquad (3.22)$$

where r and s are the input and output grey-levels (range: 0 to 1), p

is the probability density function of the input grey-levels and w is a dummy variable of integration. The counterpart of Eq. 3.22 for discrete grey-levels is (Gonzalez and Wintz 1977):

$$s_k = T(r_k) = \sum_{j=1}^{k} p(r_j)$$

or:

$$s_k = \frac{1}{N} \sum_{j=1}^{k} n_j \qquad (3.23)$$

where r_k and s_k are the k^{th} input and output grey-levels, $p(r_j)$ is the probability of the j^{th} grey-level, n_j is the number of pixels in the image with grey-level j and N is the total number of pixels in the image. Since s_k lies in the range 0 to 1, and the look-up-tables can only represent the integers 0 to 255, s_k is scaled up by 256 and rounded off to the nearest integer. Denoting this by s'_k gives finally:

$$s'_k = 256\ s_k = \frac{256}{N} \sum_{j=1}^{k} n_j \qquad (3.24)$$

This is easily calculated from the image's histogram. Eq. 3.22 always enables a perfectly flat histogram to be produced, whereas Eqs. 3.23 and 3.24 only permit an approximately flat histogram to be obtained due to their discrete nature, though the approximation improves with increasing number of grey-levels. Fig. 3.15 illustrates the operation of discrete histogram equalisation, in which grey-levels whose pixel population is below par are combined, and over-populated grey-levels have vacant ones placed adjacently so that the local average is near par. Although the equalised histogram may still be uneven, histogram equalisation is nevertheless a powerful technique (Plate 3.1).

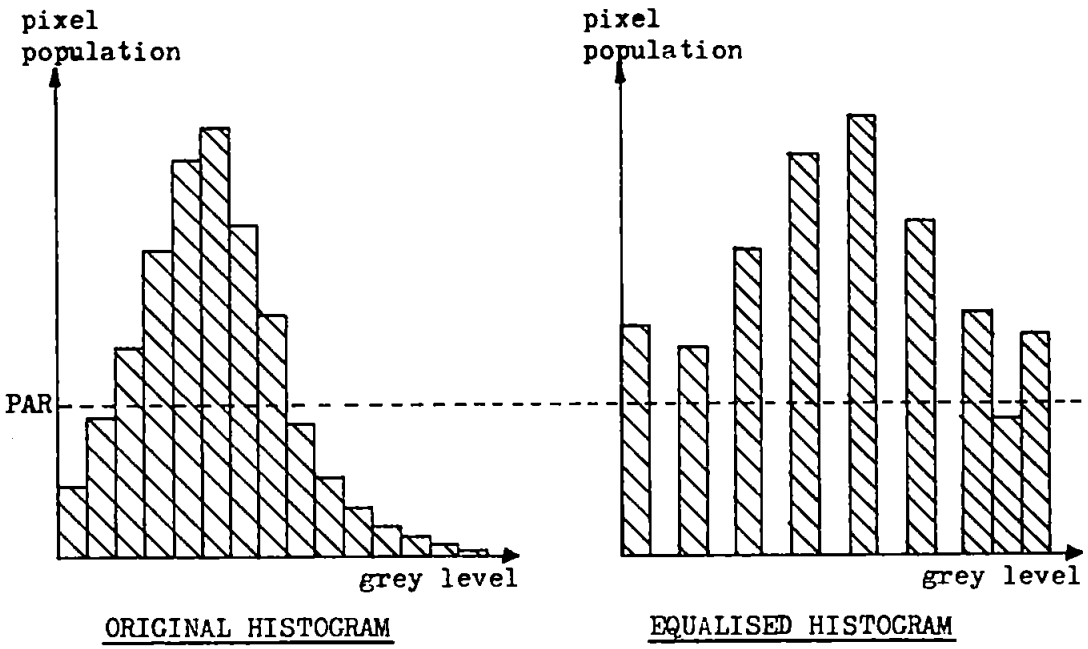

Figure 3.15 Histogram equalisation.

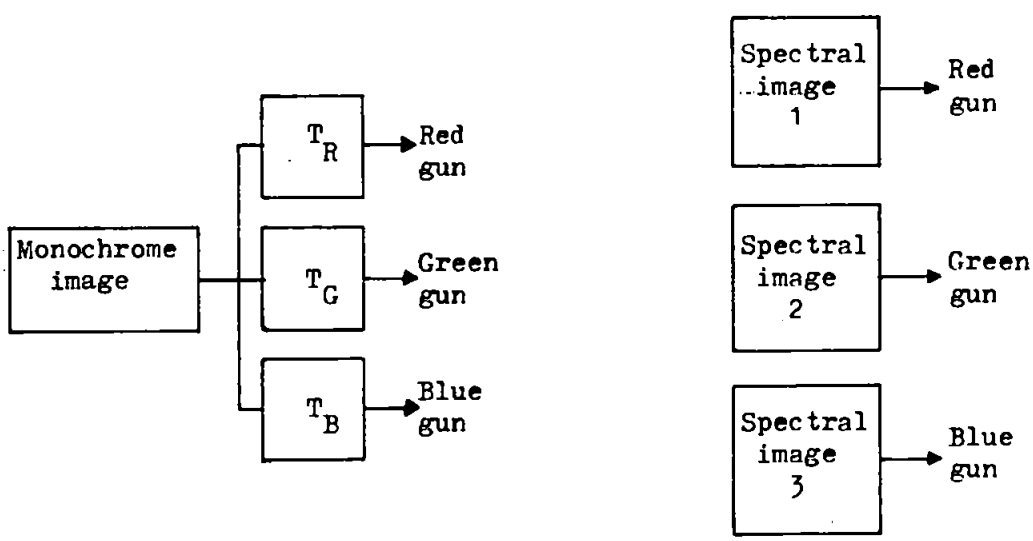

(b) Pseudo-colour

(a) False-colour

Figure 3.16 Pseudo-colour and false-colour.

Plate 3.1a CZCS channel 3 image for 22/6/1981

Plate 3.1b As above but with histogram equalisation

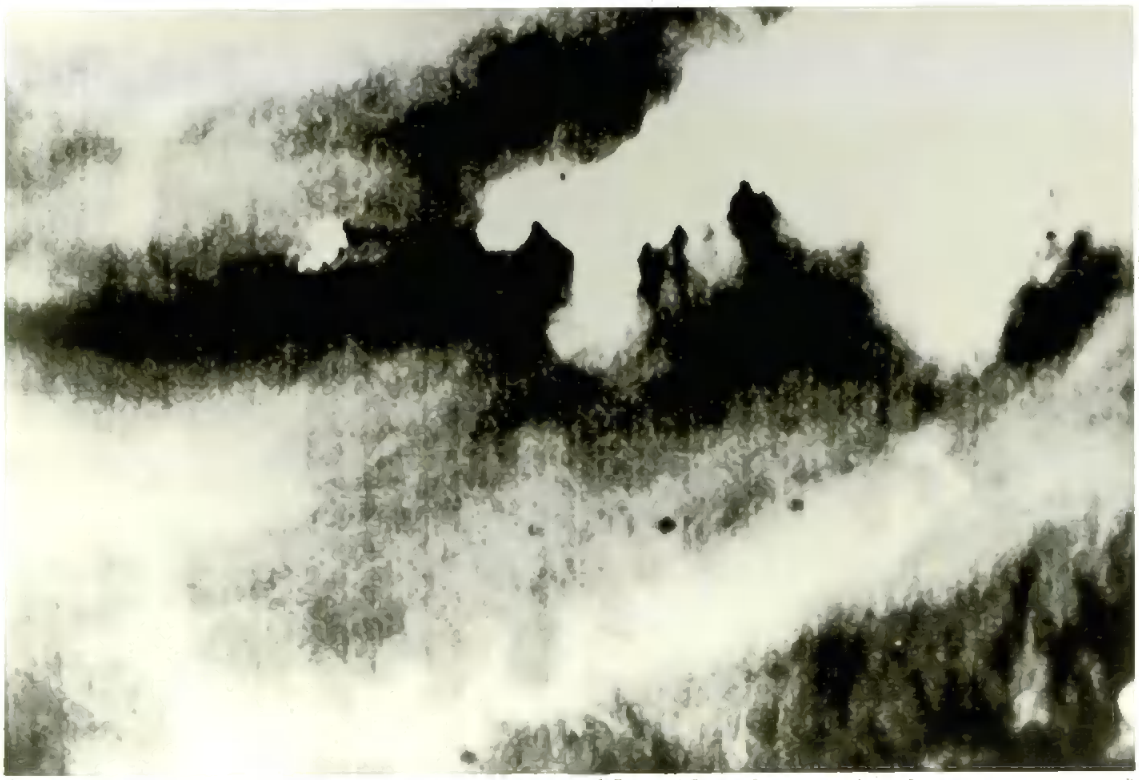

The human eye can only distinguish 20 or so monochrome grey-levels but can differentiate between several thousand colours. This feature is exploited by pseudo-colour processing which transforms each grey-level in an image to a different colour. This technique is only applied to a single monochrome image and should not be confused with false-colour which requires three spectral images (Fig. 3.16a). Pseudo-colour needs a separate look-up-table for each of the three guns (red, green and blue) of the colour monitor (Fig. 3.16b). By the judicious choice of three different transfer functions (T_R, T_G and T_B) any colour from a palette of over 16 million (256^3) may, in principle, be created. In many applications the full grey-scale is separated into several grey-level ranges, each of which is mapped to a different colour. This technique is a special case of pseudo-colour processing termed density slicing and was implemented by using the three display look-up-tables (Figs. 3.3 and 3.6). The three transfer functions are derived from the user's choice of grey-level range (defined by a lower and upper bound), and associated colour by consulting Table 3.1. As this scheme provides 14 colours, the whole grey scale may be split into 14 ranges which is sufficient for most purposes. Saturated colours are produced from combinations of full intensity primary colours, while unsaturated ones correspond to colours which have been rendered impure by the addition of white light. It has been found that density slicing preceded by histogram equalisation is particularly effective in revealing detail hidden in low-contrast areas.

This section concludes with a description of image enhancement techniques performed in the spatial domain, in which each output pixel depends upon a small neighbourhood of input pixels and a weighting matrix. The latter is also referred to as mask, window or template and

COLOUR	SATURATED			UNSATURATED		
	R	G	B	R	G	B
Black	0	0	0	-	-	-
Blue	0	0	255	127	127	255
Green	0	255	0	127	255	127
Cyan	0	255	255	127	255	255
Red	255	0	0	255	127	127
Magenta	255	0	255	255	127	255
Yellow	255	255	0	255	255	127
White	-	-	-	255	255	255

The LUTs associated with the red, green and blue guns are denoted by R, G and B respectively.

Table 3.1 Relationship between colours and display LUT contents.

0	$-\alpha$	0
$-\alpha$	$1+4\alpha$	$-\alpha$
0	$-\alpha$	0

$\alpha > 0$

Figure 3.17 Image-sharpening mask.

is very much smaller than the image; typically three by three pixels. The weighting matrix is convolved with the input image by moving it across and down the image so that the whole image is traversed. At each position the new pixel value g is found from:

$$g = f_1w_1 + f_2w_2 + \ldots + f_8w_8 + f_9w_9 \qquad (3.25)$$

where f_1 ..... f_9 and w_1 ..... w_9 are corresponding elements of the pixel neighbourhood and the weighting matrix respectively, assuming a three by three region. The current pixel position is at the centre of the neighbourhood. Eq. 3.25 is simply an expansion of Eq. 3.19 with h replaced by w, showing the convolution-like nature of this technique. Pixels lying at the edge of the image cannot be convolved because a full neighbour-hood of pixels does not exist around them. This technique enables images to be smoothed or sharpened and permits edges to be extracted. All of these may also be performed in the spatial frequency domain, but the associated Fourier and inverse Fourier transforms are lengthy to compute. Many of the weighting matrices are empirical, having been developed intuitively. Each of the three applications mentioned will be discussed in turn. The simplest of these is smoothing or blurring of an image to reduce noise and is achieved by replacing the pixel value by the average of its immediate neighbours. The elements of the three by three mask are all one except for the central element which is zero, and the resulting sum is divided by eight. This has the effect of eliminating those pixels whose grey-level is very different from the neighbouring ones.

Conversely, an image may be sharpened or deblurred by using the mask shown in Fig. 3.17 to emphasize edges. An edge is the boundary between two regions of different intensity. The mask is a discrete implementation of the following relation (Rosenfeld and Kak 1982) which recreates the original image f from the blurred one g:

$$f = g - \alpha\nabla^2 g \tag{3.26}$$

where α is positive and $\nabla^2 g$ is the Laplacian of g given by:

$$\nabla^2 g = \frac{\partial^2 g}{\partial x^2} + \frac{\partial^2 g}{\partial y^2} \tag{3.27}$$

The degree of sharpening is dictated by α whose value should not exceed two, otherwise image noise will become apparent.

Image sharpening highlights edges whilst retaining the remainder of the image. However, the two pairs of masks in Fig. 3.18 detect edges alone; regions of constant intensity or with little high-frequency detail are reduced to black (Plate 3.2). Areas of the image in which there are large gradients (high rate of change of grey-level) are assumed to contain edges. As the gradient G is a vector quantity, its magnitude is:

$$|G| = (G_x^2 + G_y^2)^{1/2} \tag{3.28}$$

where G_x and G_y are the gradients in the x (vertical) and y (horizontal) directions. Eq. 3.28 is usually approximated by:

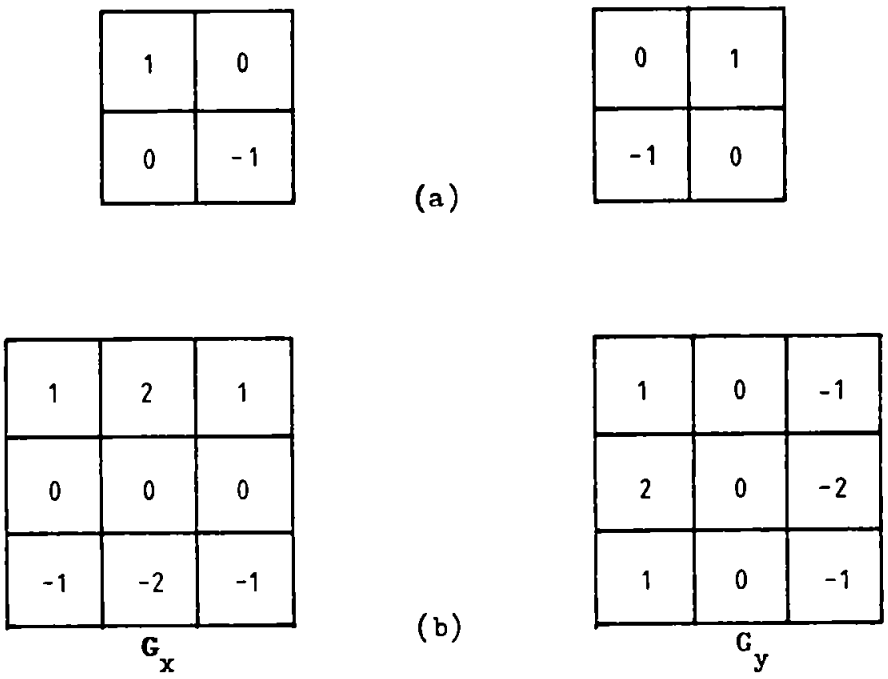

Figure 3.18 Mask pairs for detection of edges : (a) Roberts and (b) Sobel.

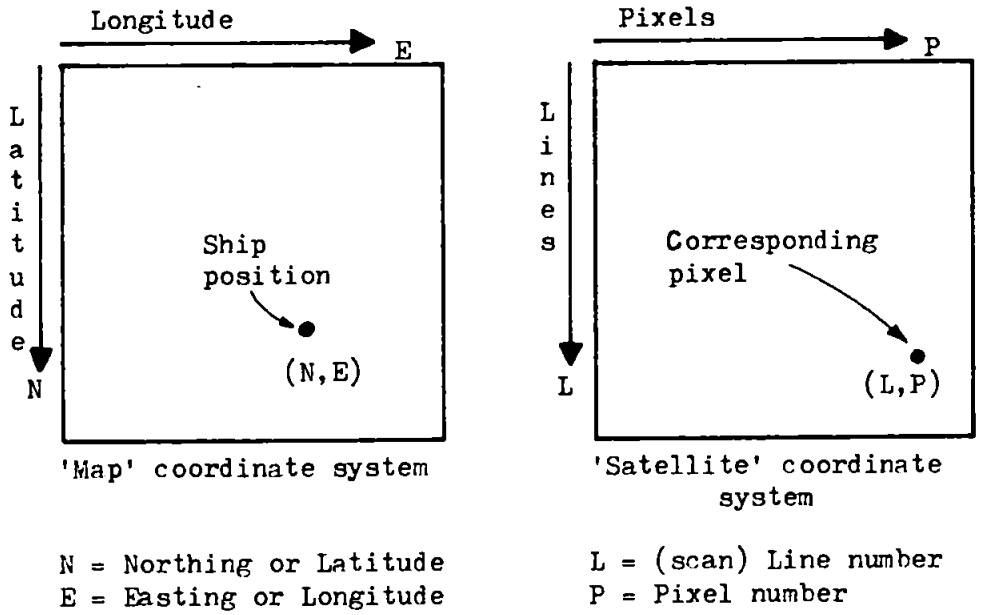

Figure 3.19 The two coordinate systems.

Plate 3.2 Edge detection using the Sobel operator

Plate 3.3 Rectification showing the sampling positions between Plymouth and Roscoff

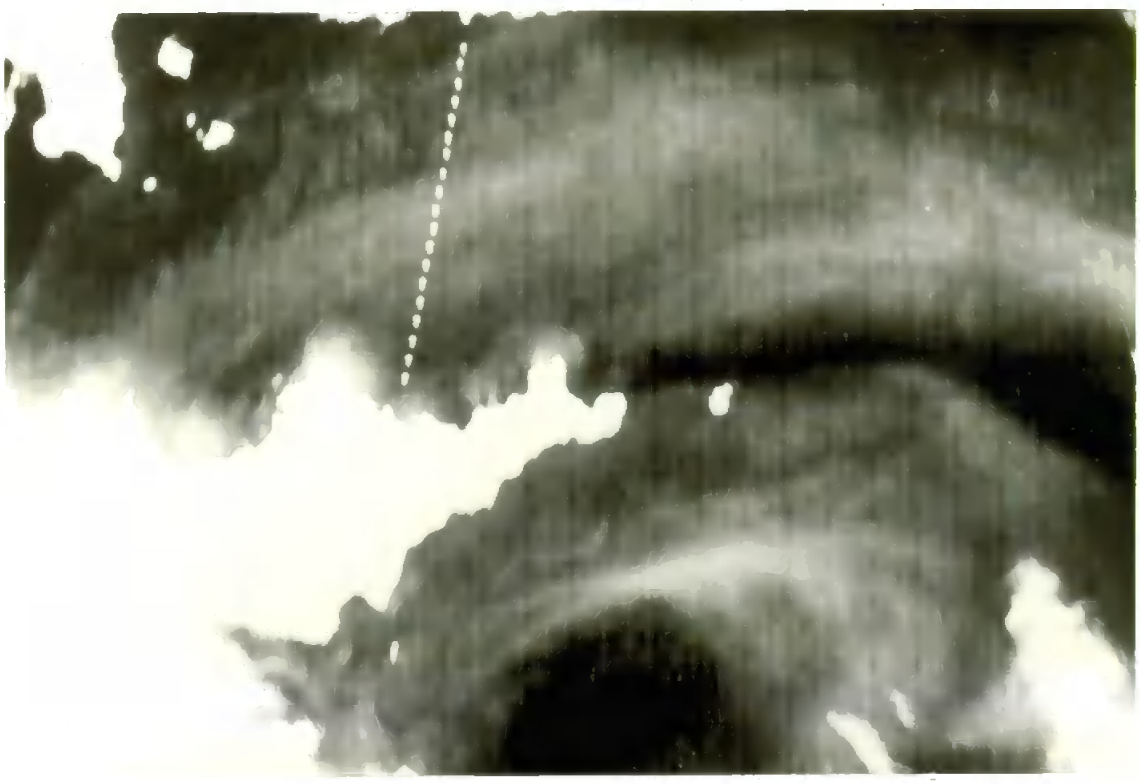

$$|G| \approx |G_x| + |G_y| \qquad (3.29)$$

Eq. 3.29 explains why two masks are needed: one each for G_x and G_y. The Sobel masks are anisotropic, i.e. certain edge orientations give a stronger response. This may be remedied by replacing the values of 2 by $\sqrt{2}$ (Frei and Chen 1977), but the use of non-integer values slows down the computation. Edge detection may be made less vulnerable to noise and spurious edges by thresholding, i.e. an edge is said to exist only if the gradient exceeds some arbitrary value.

A more powerful and discriminating method, due to Frei and Chen (1977) uses a set of nine weighting matrices. Four each are sensitive to edges and lines and the ninth detects isolated points. By convolving a pixel and its neighbourhood with all nine masks and using special decision rules, the pixel may be classified as an isolated point, an edge pixel or a line pixel. The latter is a narrow strip whose intensity is different from the surrounding region. This method was not implemented due to its complexity.

3.3.1.3 Rectification

The comparison of CZCS-derived estimates of chlorophyll concentration with direct in-situ measurements requires the location of those pixels in the satellite image which correspond to positions at which ship samples were taken. Ship positions are usually specified in terms of latitude and longitude or are easily converted into this form. However, the position of a pixel in an image is specified by line and pixel numbers. Latitude and longitude values specify position on the surface of a sphere which is merely an approximation of the Earth's

shape, whereas line and pixel numbers specify position on a plane, upon which the Earth's three dimensional curved surface has been projected. Thus the difficulty of establishing a relationship between these two independent coordinate systems arises (Fig. 3.19). The process of finding and then using this relationship is called rectification and is not to be confused with the term registration which applies to the alignment of images (with similar geometry) to bring them into correspondence. The term rectification is also used to describe the process of making an image's geometry planimetric.

In addition there are other spatial distortions which introduce further complications (Van Wie and Stein 1977):

i) Pixel overlap due to sensor oversampling. The CZCS instantaneous field of view is nominally equivalent to 825m on the ground, but the sampling rate is such that the distance between pixel centres is less than this.

ii) Anomalies in satellite orbit and attitude caused by fluctuations in altitude, velocity, roll, pitch and yaw.

iii) Image skew caused by Earth rotation as the image is scanned, the magnitude of which varies with latitude.

The desired relationship or transformations between coordinate systems can be found by two methods. The first relies upon an accurate model to simulate all the factors involved, from which the transformations may be derived. The second is an empirical one which requires no explicit knowledge of the distortion effects, but uses ground control points (GCP) to derive the transformations. GCPs are features visible in the satellite image for which the latitude and longitude values are

known. The additional spatial distortion effects listed above may also be incorporated and corrected by the rectification procedure. As some of these are random and cannot be predicted, the second method of rectification is used. Besides, a model for the sensor-view geometry and Earth projection would be needed. The empirical method assumes that the relationship between coordinate systems may be approximated by a polynomial; the higher the degree of this polynomial, the greater the accuracy of the transformation. The polynomial coefficients are calculated from a set of GCPs, for which the coordinates are known in both coordinate systems. Small islands or distinctive features on the coastline, such as headlands, are used for GCPs. The following second degree non-linear polynomials are used:

$$L_E = a_0 + a_1E + a_2N + a_3E^2 + a_4EN + a_5N^2 \qquad (3.30)$$

$$P_E = b_0 + b_1E + b_2N + b_3E^2 + b_4EN + b_5N^2 \qquad (3.31)$$

where N and E are the Northing (latitude) and Easting (longitude) of the position respectively and L_E and P_E are estimates of the line and pixel number respectively for the corresponding pixel. Eqs. 3.30 and 3.31 are of the same form and may be generalised:

$$Z_E = c_0 + c_1E + c_2N + c_3E^2 + c_4EN + c_5N^2 \qquad (3.32)$$

Z_E represents either L_E or P_E. The two transformations will each have its own set of six coefficients $c_0,\ldots,c_5$, the determination of which requires just six GCPs. However by using more and employing least-squares analysis a measure of the quality of fit may be found by calculating the correlation coefficient. The justification for using second degree polynomials is provided by the very high correlation coefficients produced.

Eq. 3.32 is a non-linear polynomial with two independent variables: N and E. However, the following substitutions:

$$x_0 = 1$$
$$x_1 = E$$
$$x_2 = N$$
$$x_3 = E^2$$
$$x_4 = EN$$
$$x_5 = N^2$$

transform Eq. 3.32 into a linear polynomial with six variables:

$$Z_E = c_0x_0 + c_1x_1 + c_2x_2 + c_3x_3 + c_4x_4 + c_5x_5 \qquad (3.33)$$

Note that x_0 (equal to one) is only included for mathematical consistency. Each GCP furnishes a pair of N and E values and a pair of L and P values. Two sets of coefficients must be determined: one for calculating L_E from N and E, the other for calculating P_E from N and E. In both cases, the coefficients are chosen so as to minimise the total error (between L and L_E or P and P_E) for all GCPs. This is achieved by applying the least-squares criterion; the objective

being to minimise the following error function:

$$\sum_{i=1}^{n} \left(Z_i - Z_{Ei}\right)^2 \qquad (3.34)$$

where n is the number of GCPs. Again Z_E is either L_E or P_E, depending upon which set of coefficients is sought. Eq. 3.34 may be expanded by substituting for Z_{Ei} from Eq. 3.33 and by introducing $x_{0i},\ldots,x_{5i}$ for the i^{th} GCP:

$$\sum_{i=1}^{n} \left(Z_i - c_0x_{0i} - c_1x_{1i} - c_2x_{2i} - c_3x_{3i} - c_4x_{4i} - c_5x_{5i}\right)^2 \qquad (3.35)$$

The solution of this criterion involves partial differentiation and arrangement of the resulting equations in matrix form, which is then solved by Gaussian Elimination (Dorn and Greenberg 1967). The mathematical details are described in Appendix 4. The correlation coefficients (r) exceed 0.999 for the CZCS images analysed. The position defined by L_E and P_E (as found from Eq. 3.33) may not coincide with an exact pixel position as Z_E is not an integer value. The pixel value, corresponding to the ship sample, may then be derived through one of three possible resampling techniques: nearest neighbour, bilinear interpolation or cubic convolution (Lillesand and Kiefer 1979). The nearest neighbour method was used, being the simplest of the three; the latter two take into account the nearest 4 and 16 pixels respectively. The rectification program operates by first displaying the CZCS scene and accepting GCPs selected by the cursor, from which the line and pixel numbers are ascertained; each GCP's latitude and longitude must also be supplied. After calculating the coefficients for both polynomials, the latitude and longitude of each ship position is entered, each of which is converted into a pixel

position and displayed as a small cross on the image (Plate 3.3).

3.3.2 Analysis techniques

3.3.2.1 Determination of ship's latitude and longitude

The rectification process requires that the latitude and longitude are specified at each sample position. This is not always the case however, and these must then be found indirectly from the time elapsed since the ship's departure. In order to do this, the ship's course and average speed are also needed. The geometry of curved surfaces is non-Euclidean and the calculation of angles and distances on the Earth's surface relies upon oblique spherical trigonometry (Ayres 1954), which approximates the Earth's shape by a sphere. If the latitudes and longitudes of both the initial and final positions are known, then the ship's course and the total distance travelled may be calculated assuming that the ship's path is along a great circle. The course is the ship's direction as measured clockwise from North. The situation is represented by the spherical triangle in Fig. 3.20; note that a, b and c are arclengths expressed as angles subtended at the Earth's centre. The latitude and longitude of A and B are used to find a, b and γ as follows:

$$a = 90° - (\text{Latitude of B})$$

$$b = 90° - (\text{Latitude of A})$$

$$\gamma = \left|(\text{Longitude of A}) - (\text{Longitude of B})\right|$$

The following two Napier equations (Universal Encyclopedia of Mathematics 1964) are used to find $(\alpha + \beta)/2$ and $(\alpha - \beta)/2$:

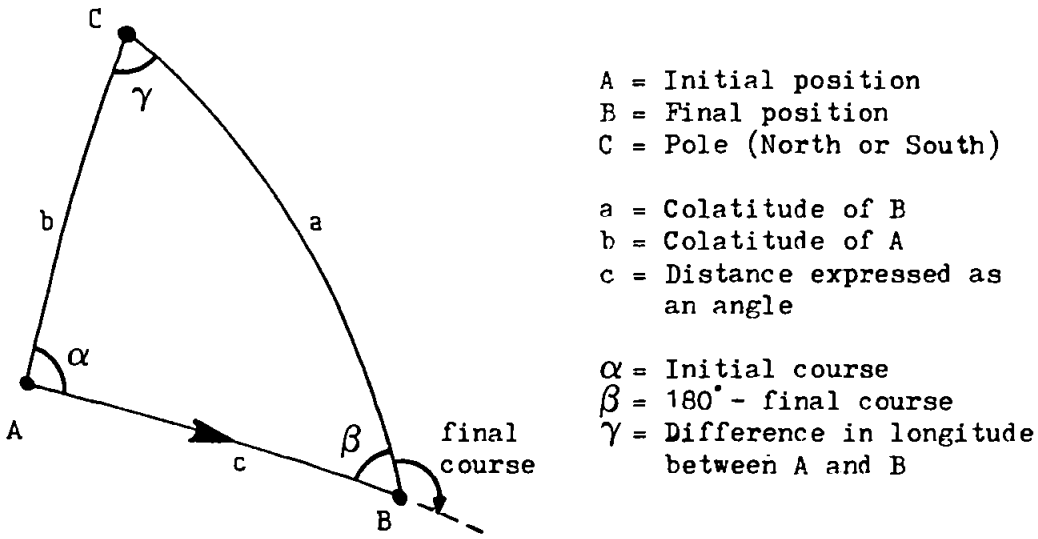

Figure 3.20 Spherical triangle for calculating the latitude and longitude of B.

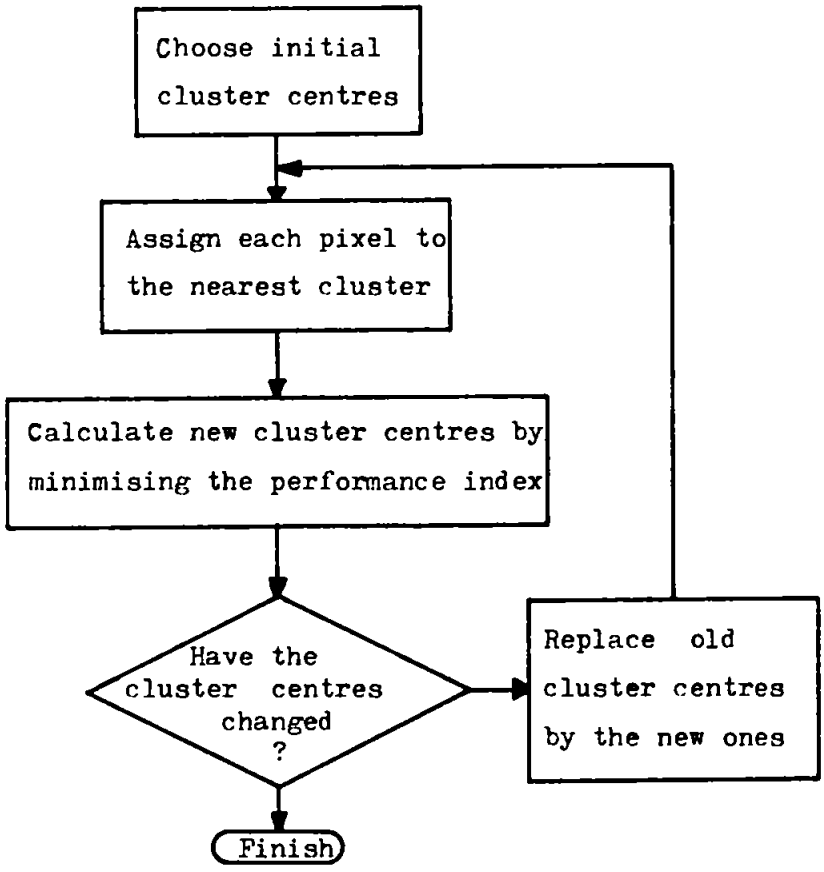

Figure 3.21 Block diagram of the K-means clustering algorithm.

$$\tan\left(\frac{\alpha+\beta}{2}\right) = \cos\left(\frac{a-b}{2}\right) \Big/ \left[\cos\left(\frac{a+b}{2}\right).\tan\left(\frac{\gamma}{2}\right)\right] \qquad (3.36)$$

$$\tan\left(\frac{\alpha-\beta}{2}\right) = \sin\left(\frac{a-b}{2}\right) \Big/ \left[\sin\left(\frac{a+b}{2}\right).\tan\left(\frac{\gamma}{2}\right)\right] \qquad (3.37)$$

Hence:

$$\alpha = \left(\frac{\alpha+\beta}{2}\right) + \left(\frac{\alpha-\beta}{2}\right)$$

$$\beta = \left(\frac{\alpha+\beta}{2}\right) - \left(\frac{\alpha-\beta}{2}\right)$$

If the final position is East of the initial one, the initial course is α and the final course is $180° - \beta$. Otherwise, the initial course is $360° - \alpha$ and the final course is $360° - (180° - \beta) = 180° + \beta$.

The length of arc c (as an angle) is determined from:

$$\tan\left(\frac{c}{2}\right) = \tan\left(\frac{a-b}{2}\right).\sin\left(\frac{\alpha+\beta}{2}\right) \Big/ \sin\left(\frac{\alpha-\beta}{2}\right) \qquad (3.38)$$

The length of arc c is 60c nautical miles, since one nautical mile subtends one minute of arc (1/60°) at the Earth's centre. One nautical mile is equivalent to 1.15078 statute miles or 1.852km. The ship's average speed may be found from the distance, provided that the total time is known. Spherical trigonometry provides a general solution; however there are two special cases which may be solved more easily. The first arises when the ship's path is along a meridian, i.e. the longitudes of A and B are equal. In this case the distance in nautical miles is simply:

$$60 \left|(\text{latitude of A}) - (\text{latitude of B})\right|$$

with the condition that the latitudes are expressed in degrees. The course is either due North or due South, depending upon the final position. The second special case is parallel sailing, i.e. A and B have the same latitude. The distance in nautical miles is:

$$60 \left| (\text{longitude of A}) - (\text{longitude of B}) \right| .\cos (\text{latitude})$$

The course is either due West or due East, depending upon the final position.

Knowing the ship's initial position, course and average speed, the position of a sample point may now be found from the corresponding elapsed time. The distance from the departure position in nautical miles is:

$$\frac{\text{Average speed (knots) x Elapsed time (minutes)}}{60}$$

Thus the value of c in degrees is:

$$c = \frac{\text{Average speed (knots) x Elapsed time (minutes)}}{60^2}$$

As before, b is 90° - (latitude of A), and α is the initial course. With these values for b, c and α, the following equations are solved for $(\beta + \gamma)/2$ and $(\beta - \gamma)/2$:

$$\tan\left(\frac{\beta+\gamma}{2}\right) = \frac{\cos\left(\frac{b-c}{2}\right)}{\cos\left(\frac{b+c}{2}\right) \cdot \tan\left(\frac{\alpha}{2}\right)}$$

$$\tan\left(\frac{\beta-\gamma}{2}\right) = \frac{\sin\left(\frac{b-c}{2}\right)}{\sin\left(\frac{b+c}{2}\right) \cdot \tan\left(\frac{\alpha}{2}\right)}$$

These two equations are identical in form to Eqs. 3.36 and 3.37 and differ only in the variables. Further forms may be produced by cyclic permutation of the variables. γ is simply:

$$\gamma = \left(\frac{\beta+\gamma}{2}\right) - \left(\frac{\beta-\gamma}{2}\right)$$

The longitude of the sample position is:

$$(\text{longitude of A}) + \gamma$$

The latitude of the sample position is found by solving the following equation for a/2:

$$\tan\left(\frac{a}{2}\right) = \frac{\tan\left(\frac{b-c}{2}\right) \cdot \sin\left(\frac{\beta+\gamma}{2}\right)}{\sin\left(\frac{\beta-\gamma}{2}\right)}$$

This equation has the same form as Eq. 3.38. The latitude of the sample position is just 90° - a. The latitude and longitude of the sample position may now be submitted to the rectification program to find the corresponding pixel in the CZCS image.

The method described in this section was verified by comparing its results with those produced by a special-purpose navigational calculator, namely the Tamaya Digital Navigation Computer NC77.

3.3.2.2. Spectral clustering techniques

Spectral clustering is an alternative method to spectral ratios for mapping chlorophyll concentration in which each data sample or pixel is represented by a vector in multi-dimensional measurement space. It operates by locating distinct clusters of pixels in multispectral space; a cluster being a collection of pixels sharing approximately the same spectral characteristics. Clustering thus detects the inherent or natural structure of data and is well suited to the analysis of land cover, in which the different soils, vegetation etc. are assumed to have unique spectral signatures or positions in multispectral space. However, data collected by the CZCS over the sea does not fall into distinct classes as chlorophyll concentration varies continuously throughout an image. Fortunately, clustering may be pressed into service here by forcing it to split the one chlorophyll class into an arbitrary number of sub-classes, each corresponding to a different range of chlorophyll concentrations. Therefore the clustering described here is not clustering in the usual sense of the term. Clustering is a useful technique because it can function without any a priori knowledge of the sea. The resulting sub-classes may be ordered to represent an increasing chlorophyll scale, and so may be used to produce a map of relative concentration. There still remains the problem of assigning absolute concentrations to each sub-class, which cannot be achieved without recourse to seatruth.

Clustering is an example of statistical pattern recognition; more specifically it is unsupervised classification since the clusters or sub-classes generated are solely a function of the spectral images. In contrast, supervised classification requires 'training data' to characterise the expected classes before analysis commences. In fact, unsupervised classification does not operate in a totally independent manner as the user must specify certain parameters. An introduction to pattern recognition is provided by Swain and Davis (1978) while a more detailed text is available by Tou and Gonzalez (1974).

One of the simplest clustering algorithms is the 'K-means' one (Tou and Gonzalez 1974), a block diagram of which is presented in Fig. 3.21. The algorithm operates iteratively by minimising a performance index, which indicates the total error in the representation of the data as clusters. The performance index is defined as the sum of the squared distances between each vector in a cluster and the centre of the cluster. The vector represents the pixel's response in several spectral channels. The specific steps involved are:

i) Choose K initial cluster centres, each of which is defined by a vector. The selection is arbitrary and may simply be the first K samples or pixels from the image. The value of K is specified by the user.

ii) Using a distance metric to measure the distance between a pixel and a cluster centre, each pixel is assigned to the cluster whose centre is nearest the pixel. Several distance metrics are discussed later.

iii) New cluster centres are found by calculating the mean vector from those pixels currently belonging to each cluster. This has the effect of minimising the performance index mentioned above.

iv) The algorithm terminates when the updated cluster centres are the same as those in the previous iteration. This condition may be relaxed by introducing a convergence threshold, so that convergence is achieved when the difference between successive cluster centres is below the threshold.

Three distance or point-to-point metrics were used: Hamming (Devijver and Kittler 1982), Euclidean (Tou and Gonzalez 1974) and weighted distance (Michael and Lin 1973). These are defined respectively by:

$$d_H(X,M) = \sum_{l=1}^{n} |x_l - m_l|$$

$$d_E^2(X,M) = \sum_{l=1}^{n} (x_l - m_l)^2 = (X-M)^T(X-M)$$

$$d_W^2(X,M) = \sum_{l=1}^{n} \frac{(x_l - m_l)^2}{sd_l^2} \qquad (3.39)$$

where d is the distance between X and M, X is the vector representing the pixel's radiance in n spectral channels, and M is the mean vector representing the centre of the cluster. Elements of vectors X and M are represented by x_l and m_l and superscript T denotes the vector transpose. sd_l is the standard deviation of the samples belonging to the cluster in channel l.

The algorithm terminates or converges when successive mean vectors (representing the cluster centres) differ by less than a user-specified convergence threshold. This threshold affects both the accuracy of classification and the computer time (Fig. 3.22), and its value must be chosen carefully. As clustering of a large region may take several hours, a trial-and-error approach is inconvenient for selecting the optimum value. This difficulty is addressed here. Assume that the difference between iterations (r) and (r+1) is just one sample X_s for the j^{th} class:

$$\sum_{X \epsilon \omega_j(r+1)} X \quad - \quad \sum_{X \epsilon \omega_j(r)} X \quad = \quad X_s \tag{3.40}$$

where X is a vector representing each sample and $X \epsilon \omega_j(r)$ signifies that the samples belong to class j for the r^{th} iteration. Eq. 3.40 is simply a comparison of the membership of the j^{th} class before and after the $(r+1)^{th}$ iteration. Dividing Eq. 3.40 by the number of samples C_j in the j^{th} class gives:

$$\frac{1}{C_j} \sum_{X \epsilon \omega_j(r+1)} X \quad - \quad \frac{1}{C_j} \sum_{X \epsilon \omega_j(r)} X \quad = \quad \frac{X_s}{C_j} \tag{3.41}$$

Assuming that $C_j \gg 1$, Eq. 3.41 becomes:

$$M_j(r+1) \quad - \quad M_j(r) \quad = \quad \frac{X_s}{C_j} \tag{3.42}$$

where M_j represents the mean vector of class j. Thus the mean vector has changed by an amount equal to the 'new member' X_s divided by the total number of samples in the class. Hence, if the difference between successive mean vectors exceeds X_s/C_j, then one may conclude that one or more samples have been reallocated to

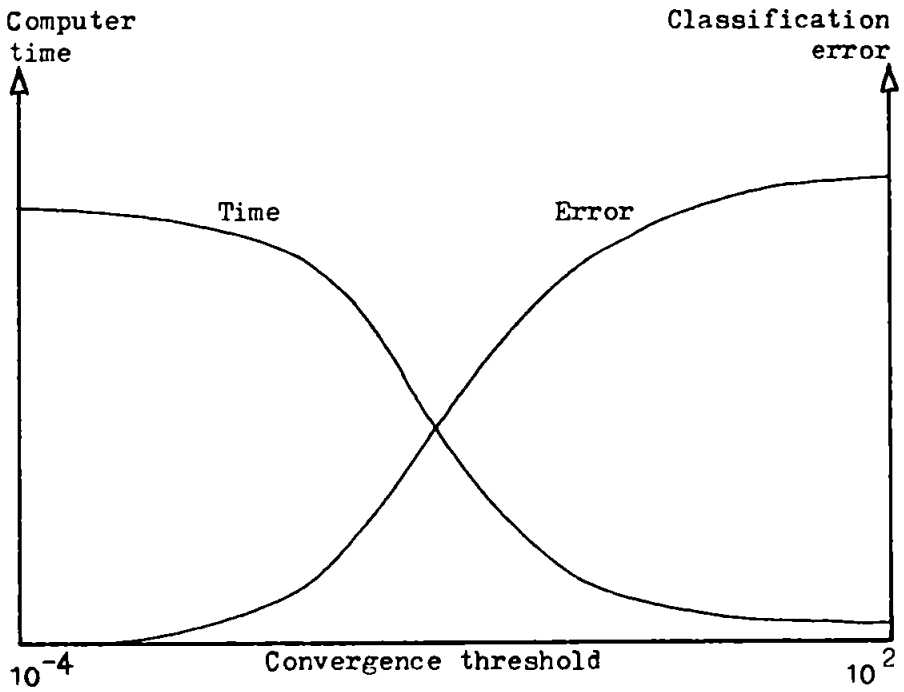

Figure 3.22 Graph showing typical variation of classification error and computer time against the convergence threshold.

class j during the $(r+1)^{th}$ iteration. Eq. 3.42 may be extended to all classes by replacing X_s by the mean value of the j^{th} class M_j; it may also be generalised by replacing C_j by C, the mean number of samples per class:

$$M_j(r+1) - M_j(r) \approx M_j(r)/C \tag{3.43}$$

The convergence threshold is then estimated by the right-hand side of Eq. 3.43, but this quantity is a vector and only applies to the j^{th} class. This is remedied by substituting the following scalar quantity for $M_j(r)$ which is valid for any class and any channel because it is an average over all classes and channels:

$$\frac{1}{n}\sum_{l=1}^{n}\left(\frac{1}{K}\sum_{j=1}^{K} m_{jl}\right)$$

$$= \frac{1}{nK}\sum_{l=1}^{n}\sum_{j=1}^{K} m_{jl}$$

where n is the number of spectral channels, K is the number of classes and m_{jl} is the radiance in channel l of a pixel belonging to class j. The convergence threshold CONV is therefore:

$$CONV = \frac{1}{C}\cdot\frac{1}{nK}\sum_{l=1}^{n}\sum_{j=1}^{K} m_{jl}$$

or:

$$CONV = \frac{1}{nN}\sum_{l=1}^{n}\sum_{j=1}^{K} m_{jl} \tag{3.44}$$

where N = KC is the total number of pixels or samples. Despite the fact that several gross assumptions were made in the derivation of Eq. 3.44, it provides a very useful method for estimating the convergence

threshold. This was incorporated into the clustering program so that an appropriate threshold was calculated automatically for each iteration.

Unfortunately, the results produced by the K-means algorithm are affected by the following factors (Tou and Gonzalez 1974):

i) The number of initial clusters specified.

ii) The choice of initial cluster centres.

iii) The order in which the samples are taken.

iv) The geometrical properties of the data.

If the data comprises compact, distinct classes which are well separated from each other, then these factors have negligible effect. However, this is not the case for CZCS data and it is difficult to produce consistent results with this method. For this reason, the K-means method was abandoned, and instead the ISOCLS technique was investigated.

The ISOCLS clustering algorithm (E.S.L. 1976, Townshend and Justice 1980) is an iterative algorithm incorporating intuitive mechanisms which permit clusters to be split or combined and which prevent clusters containing very few pixels from being formed. Initially, all pixels are placed in one large cluster or class which is then partitioned into two clusters, whose centres are plus/minus one standard deviation from the original cluster centre. Each of these classes is then split in a similar way, and the process is continued until all classes have a mean standard deviation less than a threshold value or until the number of pixels per class becomes too small. At

this stage lumping commences, such that any pair of classes whose intercluster distance is less than a lumping threshold are merged. This process is repeated until all intercluster distances exceed the lumping threshold. The ISOCLS algorithm is outlined in Fig. 3.23 and in full detail by the following sequence of steps:

1) Store image or region in an array, such that each pixel is a multispectral vector X. Specify the following parameters:

   i) MAXSD - Maximum value of the mean standard deviation for any class. If a cluster's standard deviation exceeds this threshold then it will be split into two.
   ii) MINP - Minimum number of pixels per class. Used to prevent clusters becoming smaller than this size.
   iii) LC - Lumping coefficient.
   iv) Distance metric - Hamming, Euclidean or weighted distance.

2) Distribute the samples between the current K clusters using the following criterion:

$$X \in \omega_j \quad \text{if} \quad \sum_{l=1}^{n} \left| x_l - m_{jl} \right| \; < \; \sum_{l=1}^{n} \left| x_l - m_{il} \right|$$

$$i = 1,2,\ldots,k; \; j \neq i$$

This criterion uses the Hamming metric but equivalent criteria apply for the Euclidean and weighted minimum distance metrics. $X \in \omega_j$ denotes that the sample or pixel X is assigned to class

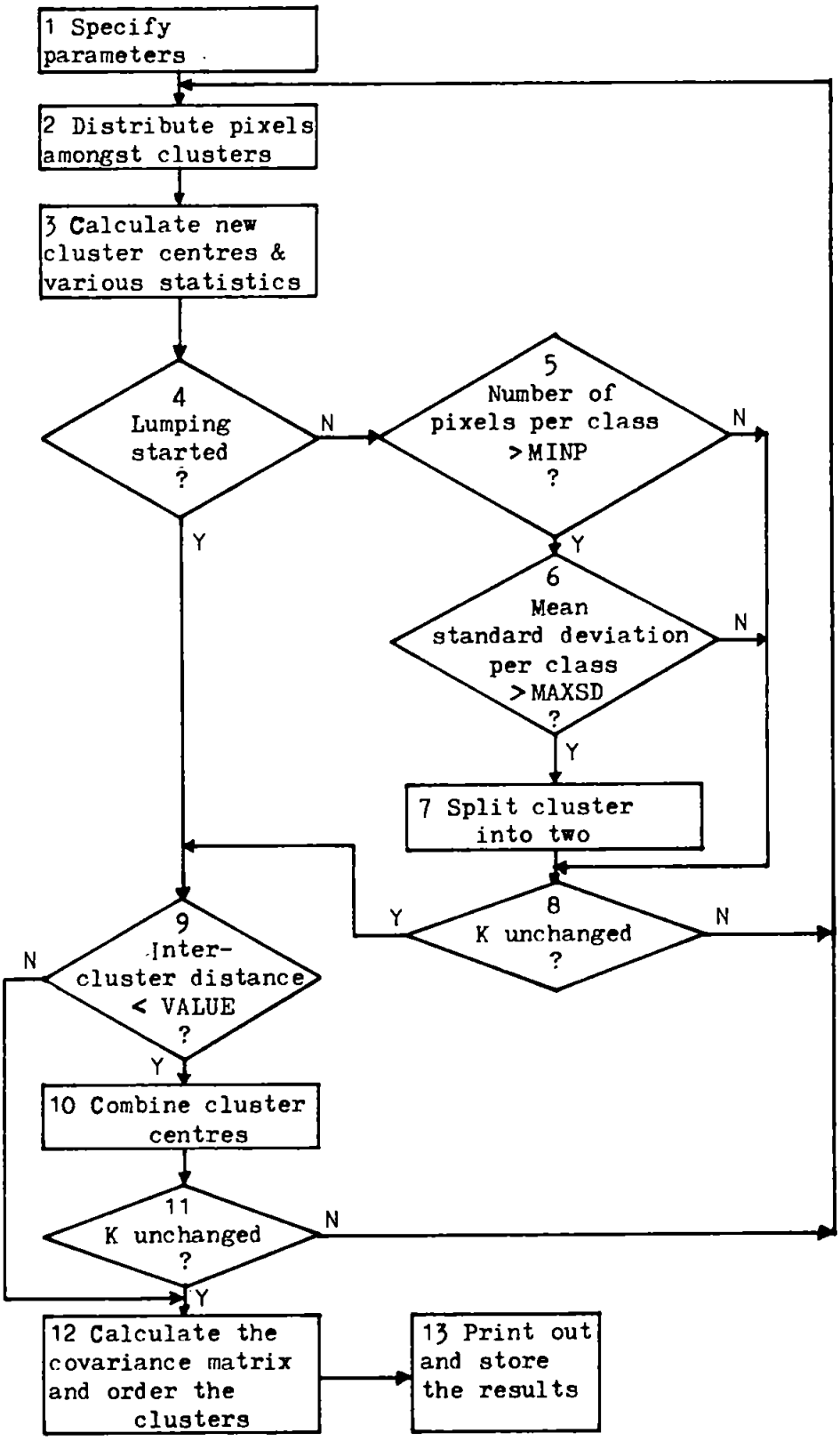

Figure 3.23 Flowchart for the ISOCLS clustering algorithm.

j if the criterion is satisfied. n is the number of spectral channels, x_l is the l^{th} element or channel of the sample vector X and m_{il}, m_{jl} are the l^{th} elements of the mean vector M for classes i, j. The criterion simply asserts that the pixel is assigned to the cluster whose centre is nearest.

3) i) Calculate the mean value m_{il} of each class/cluster i for each channel or element. The new class centres M_i are then:

$$M_i = \begin{pmatrix} m_{i1} \\ \vdots \\ m_{in} \end{pmatrix}$$

ii) Calculate the standard deviation vector for class i:

$$sd_i = \begin{pmatrix} sd_{i1} \\ \vdots \\ sd_{in} \end{pmatrix}$$

where sd_{i1}, sd_{i2} etc. are the standard deviations of the x_1 values, x_2 values, etc. with:

$$X = \begin{pmatrix} x_1 \\ \vdots \\ x_n \end{pmatrix}$$

Of course, only those samples (X) in class i are considered.

iii) Calculate the mean standard deviation per class, sdm_i. This is a scalar quantity calculated as:

$$sdm_i = \frac{1}{n}\sum_{l=1}^{n} sd_{il}$$

This is simply the mean of the elements of the standard deviation vector sd_i.

iv) Calculate the distance between clusters i and j, d_{ij} (Townshend and Justice 1980):

$$d_{ij} = \sum_{l=1}^{n} \frac{(m_{il} - m_{jl})^2}{sd_{il} \cdot sd_{jl}}$$

d_{ij} is known as the intercluster distance.

4) If the lumping process has started, go to (9), i.e. skip over the splitting stage. Otherwise, proceed to (5).

5) If the number of pixels per class is less than MINP, go to (8), i.e. avoid the splitting stage. Otherwise, proceed to (6).

6) If the mean standard deviation per class is less than MAXSD, go to (8), i.e. avoid splitting. Otherwise, proceed to (7).

7) Split cluster centre M_i into two new clusters with centres M_i^+ and M_i^-, displaced from M_i by ± 1 standard deviation, i.e. (Townshend and Justice 1980):

$$M_i^- = M_i - sd_i$$

$$M_i^+ = M_i + sd_i$$

These are both vector equations. Also increase the number of clusters K by one. Proceed to (8).

8) If K has increased by one, or is greater than one, go to (2), i.e. commence next iteration. Otherwise, proceed to (9).

9) If the intercluster distance d_{ij} of any pair of clusters (i and j) is less than the following quantity:

$$\left(\frac{C_i.sdm_i + C_j.sdm_j}{C_i + C_j}\right).LC$$

then go to (10), i.e. the merging or lumping stage; C_i and C_j are the numbers of pixels in clusters i and j. Otherwise, go to (12).

10) Combine clusters i and j by calculating the new combined cluster centre M_i^* from:

$$M_i^* = \frac{C_i M_i + C_j M_j}{C_i + C_j}$$

where M_i and M_j are the old cluster centres. Again, this is a vector equation, and hence must be performed for each channel in turn, in order to produce all the elements of the

vector quantities. The class number K is reduced by one. Proceed to (11).

11) If the class number K has decreased by one or exceeds 1, go to (2), i.e. commence next iteration. Otherwise, proceed to (12).

12) Calculate the covariance matrix. Order the class/cluster numbers such that they represent a scale of increasing chlorophyll concentration, i.e. class 1 - lowest concentration up to class K - highest concentration. This is achieved by referring to the difference in radiance between CZCS channels 1 and 2, which are both dependent upon chlorophyll concentration, but with different sensitivities. Proceed to (13).

13) Print out statistics and store the covariance matrix and class mean values (cluster centres) M_i in a file for later use. The class number for each pixel is stored in another file.

The algorithm essentially consists of two loops: one for splitting clusters (stages 2, 3, ..., 8) and the other for combining clusters (stages 2, 3, 4, 9, 10, 11); refer to Fig. 3.23. The number of classes cannot be directly specified and depends upon MAXSD, LC and the structure of the data in an unpredictable manner. Therefore, if a particular number of classes is required, the only approach is a trial-and-error one. The results with the ISOCLS algorithm do not depend upon the choice of initial cluster centres or the order in which

samples are taken because the algorithm starts with just one cluster containing all samples.

The ISOCLS algorithm may be applied directly to an image or region, but like most clustering algorithms it has a colossal appetite for computer time. For example, unsupervised ISOCLS clustering of a 73 by 185 pixel region took six hours yet this region represents only 3.4% of a full image (768 by 512 pixels). At this juncture, the technique of 'mono-cluster blocks' (Fleming and Hoffer 1977) was introduced to dramatically reduce the computer time. This is a two stage hybrid technique which overcomes the difficulty of clustering all the image's pixels by only clustering a small number which are representative of the image as a whole. The resulting classes are characterised statistically in order to classify the whole image by extrapolation. The first stage is the selection of small heterogeneous blocks (1000 - 2000 pixels) which between them must include pixels from all classes present in the image. The ISOCLS clustering algorithm is then applied to these blocks en masse to produce a mean vector for each class and the covariance matrix which collectively characterise the classes or clusters. The second stage is the use of these statistics by one of two extrapolation methods (described below) to classify the whole image. This does not involve any clustering and is a much faster process, e.g. the classification of one full image (768 by 512 pixels) took just 90 minutes using the quicker of the two extra-polation methods. The mono-cluster blocks technique is outlined in Fig. 3.24a.

The two extrapolation methods used were: maximum likelihood and weighted minimum distance. The former assumes that each class or cluster is a multivariate normal (or Gaussian) distribution which may be

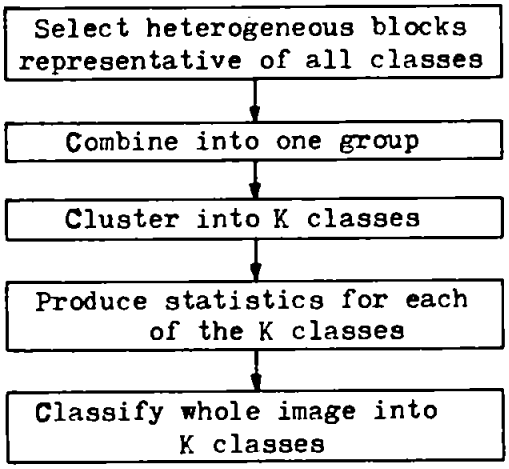

(a)

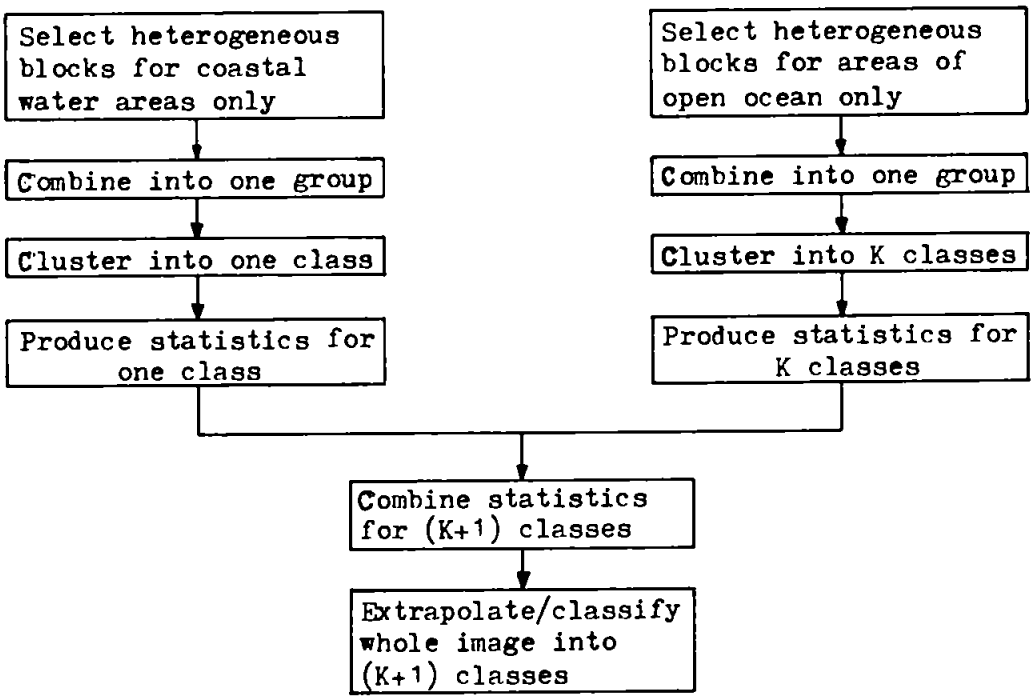

(b)

Figure 3.24 Flowcharts for: (a) mono-cluster blocks approach and (b) modified mono-cluster blocks method which accounts for coastal waters.

characterised by its mean and standard deviation. However, since the distribution is multivariate, each standard deviation is replaced by the covariance matrix whose elements denote variances and covariances (Tou and Gonzalez 1974). These statistics permit the calculation of the probability of a given pixel or sample belonging to each of the classes. Naturally, the class for which the probability is a maximum is the one to which the pixel is assigned. The probability density function for the normal multivariate distribution is (Swain and Davis 1978):

$$p(X|\omega_i) = \frac{e^{-\Gamma_i/2}}{(2\pi)^{n/2} \cdot |\Sigma_i|^{1/2}} \qquad (3.45a)$$

with:
$$\Gamma_i = (X-M_i)^T \Sigma_i^{-1} (X-M_i) \qquad (3.45b)$$

where $p(X|\omega_i)$ is the conditional probability density function, i.e. the probability density of X assuming that X is from class i. n is the number of channels, X is the sample vector and M_i is the mean vector for class i. Σ_i does not represent a summation but is the covariance matrix for class i and $|\Sigma_i|$ is the determinant of Σ_i. The 'T' and '-1' superscripts denote the transpose and inverse respectively. However, the maximum likelihood decision rule is that X belongs to class ω_i if and only if (Swain and Davis 1978):

$$p(X|\omega_i).p(\omega_i) > p(X|\omega_j).p(\omega_j) \qquad (3.46)$$
$$j=1,2,\ldots,K;\ j\neq i$$

where $p(\omega_i)$ is the probability of occurrence of class ω_i. This decision rule is an example of the Bayes classification strategy with a zero-one loss function. The essence of Bayes classifiers is the minimisation of the average loss or misclassification, which is equivalent to the maximisation of the likelihood or correct classification. In most circumstances though, the values of $p(\omega_i)$ are not known and the usual practice is to assume that they are all equal, in which case the decision rule is:

$$p(X|\omega_i) > p(X|\omega_j) \qquad (3.47)$$

$$j=1,2,\ldots,K;\ j\neq i$$

This strategy discriminates in favour of those classes which occur rarely. For classification purposes, the specific probability densities are not required; only an indicator of the most likely class is needed. Eq. 3.45 may therefore be converted into a simpler form by taking natural logs (Tou and Gonzalez 1974):

$$\ln\left[p(X|\omega_i)\right] = -\frac{n}{2}\ln(2\pi) - \frac{1}{2}\ln\left|\Sigma_i\right| - \Gamma_i/2 \qquad (3.48)$$

Since the term including 2π is the same for all classes, the maximum likelihood classifier operates by maximising the following decision function:

$$g_i(X) = -\frac{1}{2}\ln\left|\Sigma_i\right| - \frac{1}{2}(X-M_i)^T \Sigma_i^{-1} (X-M_i) \qquad (3.49)$$

The class to which X is assigned is therefore the one which maximises Eq. 3.49, since this is the class which maximises the likelihood of correct classification. Alternatively, by taking the negative of Eq. 3.49, the classification may be performed by minimising $g_i'(X)$:

$$g_i'(X) = -g_i(X)$$

$$= \frac{1}{2}\ln\left|\Sigma_i\right| + \frac{1}{2}(X-M_i)^T \Sigma_i^{-1} (X-M_i) \qquad (3.50)$$

The second extrapolation method is much simpler and uses the weighted minimum distance function, as given by Eq. 3.39. This may be regarded as an Euclidean distance measure inversely weighted by the standard deviation. In this case the pixel is assigned to the nearest cluster, i.e. the one with the smallest weighted distance:

$$X \in \omega_i \quad \text{if} \quad d_w(X,M_i) < d_w(X,M_j) \qquad j=1,2,\ldots,K;\ j\neq i$$

This method tends to assign any pixels, which do not lie in close proximity to a cluster centre, to a class with a large standard deviation. In this way, 'stray' pixels are placed in clusters which are highly dispersed. From limited tests the weighted minimum distance classifier was found to be about three times as fast as the maximum likelihood one and the discrepancy in classification between these two methods amounted to no more than 5% of all pixels.

The straightforward mono-cluster blocks technique (Fig. 3.24a) was extended to take account of coastal waters, whose spectral characteristics are distinct from those of open oceans. The modified method (Fig. 3.24b) therefore treats Case I and II waters separately in the production of statistics for extrapolation.

Finally, the various clustering parameters were adjusted on each occasion to generate seven or eight chlorophyll sub-classes, each of which was displayed as a different colour using the pseudo-colour facility.

CHAPTER 4

ATMOSPHERIC CORRECTION - THE REMOVAL OF UNWANTED ATMOSPHERIC SIGNALS

The literature on atmospheric correction is very dispersed and no single source provides a full description and detailed solution of the problem. For this reason, the first seven sections of this chapter represent a unique collation of material from a wide variety of sources. The remaining sections (4.8 to 4.11) consider more detailed aspects which do not appear in the literature.

4.1 INTRODUCTION

Passive remote sensing of the sea is achieved by measuring the solar energy which has interacted with the constituents within the water body. In the visible part of the electromagnetic spectrum, in which the CZCS operates, there are also interactions both between sunlight and the water surface, and the atmosphere. This renders the extraction of the water-leaving radiance from the total radiance measured by the satellite a less straightforward task. This may only be accomplished by making an accurate estimate of the radiance generated by these unwanted interactions. At short visible wavelengths the water-leaving radiance may comprise only 20% or less of the total satellite radiance (Hovis and Leung 1977); the remaining 80% or more conveys information about the atmosphere and the sea-surface state. The problem is less acute with terrestrial remote sensing due to the larger radiance reflected from the land's surface. Although the term 'atmospheric correction' is used to describe the process of removing unwanted signals, it takes into account the reflection of radiance at the sea surface in addition to the atmospherically generated radiance.

The principal interactions which need to be considered when dealing with atmospheric correction in the visible region are scattering or scattering with a small amount of absorption. Atmospheric turbulence and refraction are negligible (Fleagle and Businger 1980). Of secondary importance is the reflection of sunlight at the water surface due to the change in refractive index.

In order to produce a practical solution, a model is required to account for the unwanted radiances. This model is developed after considering the appropriate background physics and characteristics of the Sun and atmosphere.

4.2 THE PHYSICS OF ENERGY-MATTER INTERACTIONS

Electromagnetic energy interacts with matter in several complex ways; largely through the electric vector. In visible remote sensing it is the interaction between light and atmospheric or hydrospheric material, either in the form of individual particles or in bulk, with which we are concerned.

4.2.1 Scattering

Pure scattering is the absorption and re-radiation of incident energy with no loss of energy (Sears 1949). Electromagnetic energy incident upon an atom causes its electrons to behave as dipoles which oscillate in sympathy with the electric field, and in so doing emit radiation (Rossi 1967, Stone 1963). This mechanism is the basis of the scattering process and the theory was first developed by Lord Rayleigh (1871a,b,c) who at the time was investigating the colour of the sky. He also showed that atmospheric gases (nitrogen and oxygen) are responsible and not dust as previously believed. Rayleigh's theory,

however, only applies to particles whose size is much smaller than the radiation's wavelength, such as molecules. The amount of scattered energy is inversely proportional to the fourth power of wavelength and the variation with scattering angle ψ is given by the Rayleigh phase function $P_R(\psi)$:-

$$P_R(\psi) = {}^3/_4(1 + \cos^2\psi) \qquad (4.1)$$

See Figs. 4.1 and 4.2. This expression is only valid for unpolarised light. Hence the amount of scattered energy in the forward and backward directions ($\psi = 0, \pi$) is double that in the direction perpendicular to the incident beam ($\psi = \pi/2$).

An almost completely general theory of scattering was developed by Mie (1908), which applies to spherical particles and is valid for any particle size and radiation wavelength. Mie's theory differs from Rayleigh's in considering the particle as a collection of multipoles, not simply a single dipole. The solution takes into account phase differences due to contributions from different sections of the particle and involves integration of Maxwell's equations. This mathematically complex theory shows how the phenomena of scattering, reflection, absorption, diffraction and refraction all stem from the solution of the same set of equations (Fleagle and Businger 1980). The scattering behaviour of a single spherical particle is fully determined by just two parameters in Mie's theory: the difference in refractive index between the particle and the surrounding medium and a size factor which is defined by $2\pi r/\lambda$, where r is the particle's radius and λ is the wavelength of the incident energy (Meyer-Arendt 1972). The dependence of Mie scattering upon wavelength varies from λ^0, i.e.

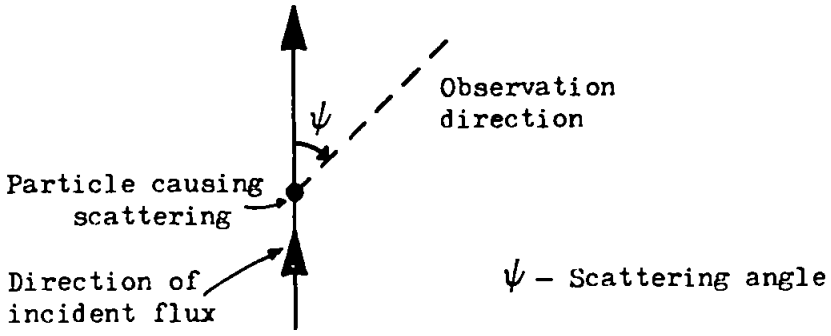

Figure 4.1 Definition of scattering angle.

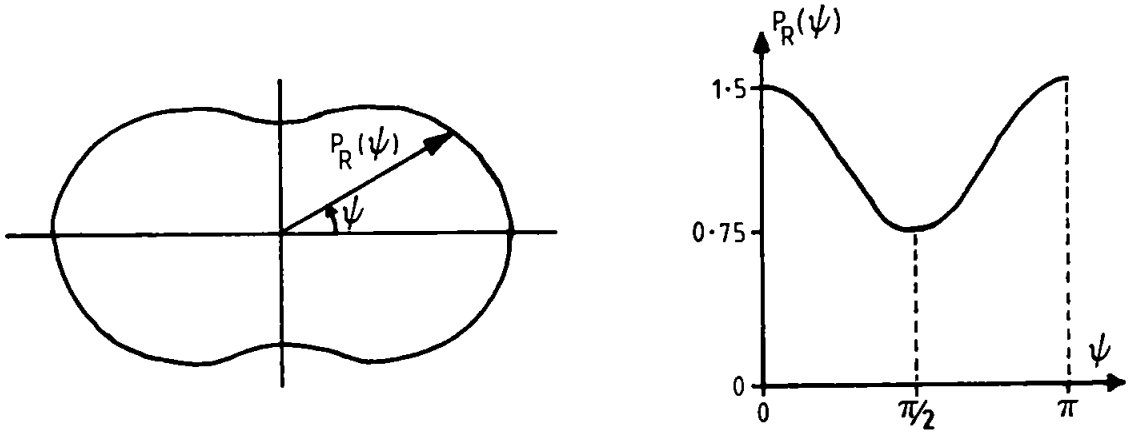

(a) Polar (b) Rectangular

Figure 4.2 Rayleigh phase function.

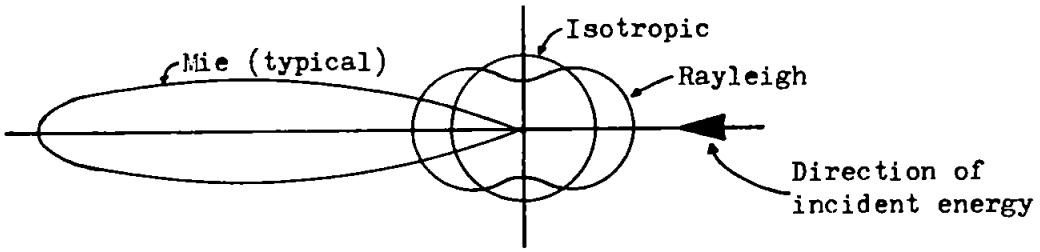

Figure 4.3 Comparison of phase functions. The isotropic and Rayleigh ones have been scaled up for comparison purposes.

independent, to λ^{-4} (Slater 1983). The phase function for particles whose size is comparable with λ is highly asymmetric with most of the scattering occurring within small forward angles (Fig. 4.3).

The full rigour of Mie theory is only necessary when the particle radius is of the same order as the incident wavelength. Thus the whole range of scattering may be divided into three categories:-

i) Rayleigh, $r \ll \lambda$.

ii) Mie, $\lambda/10 < r < 10\lambda$.

iii) Non-selective, $r \gg \lambda$.

Non-selective scattering only arises when the particle size is much larger than the incident wavelength. Of course Mie's theory may be employed, but this type of scattering can be more easily handled with the techniques of diffraction and geometrical optics. Non-selective scattering is independent of wavelength, and causes the flux to be scattered mostly in the forward direction. Scattering at small forward angles is largely due to diffraction; at larger forward angles the combined effects of reflection, refraction and transmission are responsible. The latter three mechanisms are described by geometrical optics.

The angular distribution of scattered flux, as given by the phase function, is determined from the volume scattering function which depends only upon the polar angle and not the azimuth angle. The terms polar and azimuth angle are defined by their use in the spherical polar coordinate system (Arfken 1970). Therefore, the scattering is radially

symmetric about the axis of the incident beam. The scattering coefficient (for all directions), the forward scattering coefficient and the backscattering coefficient may all be derived from the volume scattering function (see Appendix 2).

4.2.2 Absorption

Absorption describes the transfer of energy from an incident beam to material lying in its path. The material heats up, and since this is a thermodynamically irreversible process, it represents a loss of energy.

A molecule may possess energy by virtue of rotational, vibrational or electronic activity (Kirk 1983). The energy associated with a change in level in each of these cases is shown below:-

Absorption Mode	Energy	Corresponding wavelength
Rotational	Small	> 20μm (Far IR & microwave)
Vibrational	Medium	< 20μm (Infra-red)
Electronic	Large	Visible range

4.2.3 Reflection

Reflection at a smooth plane boundary between two transparent media of different refractive index is known as specular reflection. The incident ray, reflected ray and the normal to the boundary all lie in the same plane, with the angles of incidence and reflection being equal. The amount of energy reflected, as a fraction of the incident unpolarised energy, is given by Fresnel's reflection formula (Singh et al. 1983):-

$$\rho(i) = \frac{1}{2}\left[\frac{\sin^2(i-r)}{\sin^2(i+r)} + \frac{\tan^2(i-r)}{\tan^2(i+r)}\right] \qquad (4.2)$$

where i and r are the angles of incidence and refraction measured from the normal to the boundary. These two angles are related by Snell's law:-

$$n_i \sin i = n_r \sin r$$

where n_i and n_r are the refractive indices in the incident and refracting media respectively. For very small angles of i and r, the expression for $\rho(i)$ simplifies to:

$$\rho = \left(\frac{n_r - n_i}{n_r + n_i}\right)^2$$

The refractive index may be a function of temperature and wavelength. Figure 4.4 shows the typical variation of $\rho(i)$ with i. The reflectance remains small and almost constant for a considerable range and then increases dramatically.

4.2.4 Overall attenuation

Although Mie's theory is ostensibly a theory of scattering, it also takes into account absorption unlike Rayleigh's theory. This is achieved by extending the refractive index to a complex number, whose

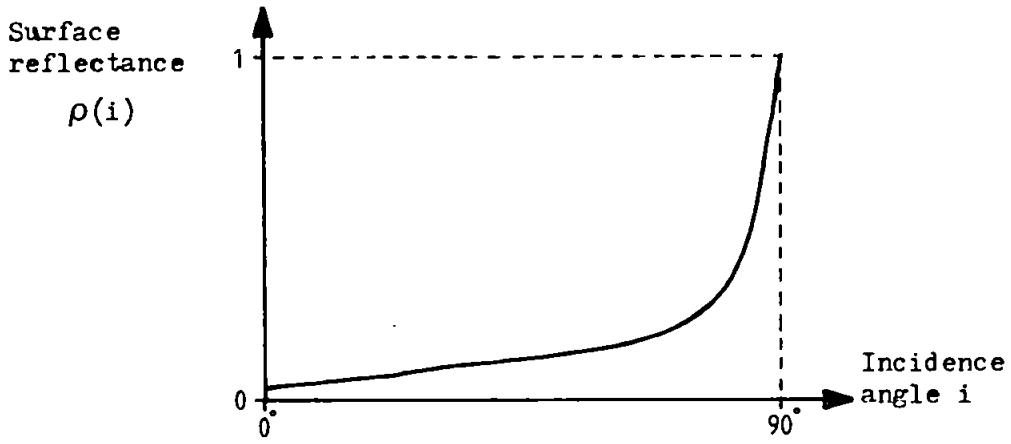

Figure 4.4 Variation of reflectance with incident angle.

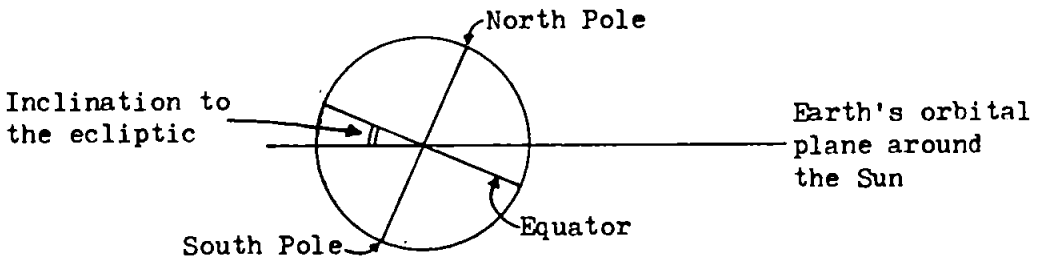

Figure 4.5 Inclination to the ecliptic.

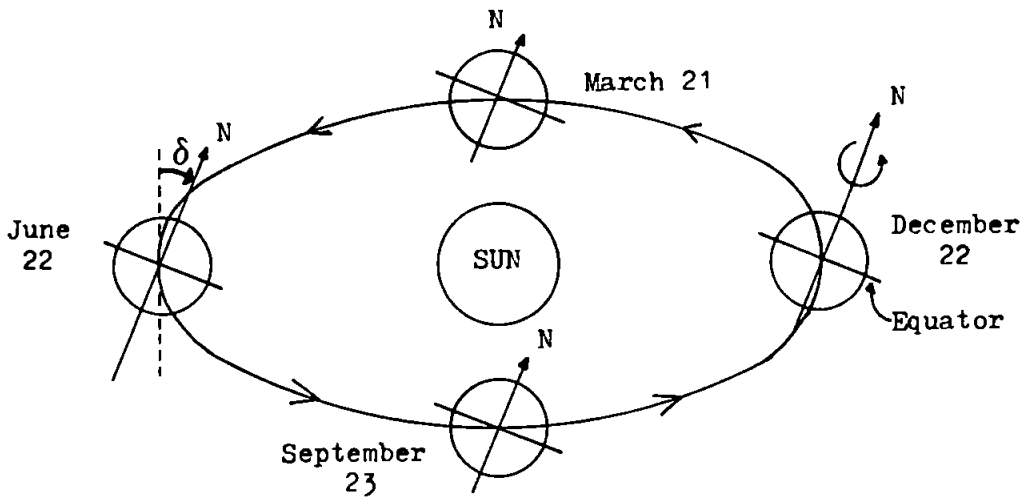

Figure 4.6 Variation of solar declination angle.

imaginary part represents the absorption index.

Rotational mechanisms or translational vibrations cause molecules to absorb energy strongly at certain characteristic resonant frequencies. If the incident frequency is close to one of these, then absorption will predominate over scattering, otherwise scattering is dominant (Swain and Davis 1978).

Overall reduction in the intensity of an incident beam of energy is due to the combined effect of scattering and absorption, and is referred to as attenuation. The overall attenuation is expressed in terms of the transmittance which may be derived from the scattering and absorption coefficients or alternatively from the optical thicknesses for scattering and absorption processes (see Appendix 5). It should also be noted that there are in fact two types of transmittance: direct and diffuse. This distinction is explained in Section 4.6.4.

The area of an incident beam which is scattered by a particle may be larger than the particle's geometric cross-section and is known as the scattering cross-section. This leads to the idea of an efficiency factor for scattering which is defined as the ratio of the scattering cross-section to the particle's geometric cross-section. In a similar manner an efficiency factor for absorption may be defined. Both efficiency factors may be found from Mie theory.

4.3 PROPERTIES AND CHARACTERISTICS OF THE SUN AND ATMOSPHERE

4.3.1 The Sun and the effects of the Earth's orbit

The Sun subtends an angle of approximately 0.5° at the Earth and its surface temperature is in the region of 6000°K. A black body at this

temperature will radiate energy over a wide range with a peak, in terms of energy per unit wavelength, at about 480nm.

The Earth's equator does not lie in the same plane as its orbit around the Sun (Fig. 4.5). This tilt is referred to as the 'inclination to the ecliptic' and is equal to 23.44° (Singh 1982 private communication, Kraus 1966). Consequently, there is an annual variation in the solar declination angle δ, which is the angle through which the Northern hemisphere is tilted towards the Sun (Fig. 4.6). δ ranges between $\pm$23.44° and some values are given below:

Date	δ
March 21	0
June 21	+23.44°
September 23	0
December 22	-23.44°

The precise variation of δ with daynumber D is given by:

$$\sin\delta = \sin 23.44^{\circ} . \sin [2\pi (D-80.25)/365] \qquad (4.3)$$

the daynumber D ranges from 1, for January 1, to 365 for December 31. The value 80.25 corresponds to the vernal equinox (March 21) when the Sun crosses the celestial equator from South to North.

The intensity of the solar irradiance also changes with daynumber since the Earth's orbit is slightly eccentric, and this causes a small fluctuation in the Earth-Sun distance. The solar irradiance variation is given by:

$$E_o = \bar{E}_o (1 + e.\cos [2\pi (D-3)/365])^2 \qquad (4.4)$$

e is the eccentricity of the Earth's orbit (0.0167). The D-3 term accounts for the occurrence of the Earth's perihelion (minimum Earth-Sun distance) on January 3. $\bar{E}_o$ is the mean solar irradiance.

In the case of a vertically overhead Sun, the reduction of solar irradiance is 14% with a clean, dry atmosphere, increasing to 40% when the atmosphere is dusty and moist. Some of the direct solar beam is scattered and this flux constitutes skylight which typically accounts for 15 to 25% of the total irradiance, assuming cloudless conditions. As the solar zenith angle increases, the proportion of solar flux removed by the atmosphere increases due to the greater atmospheric pathlength. This pathlength is proportional to the reciprocal of the cosine of the zenith angle (See Appendix 5).

4.3.2 The atmosphere

The composition, and therefore the properties of the atmosphere vary distinctly with altitude. The air density also changes markedly, being about 1 $kg.m^{-3}$ at sea level but dropping to 10^{-12} $kg.m^{-3}$ or less at 955 km, which is the altitude of the CZCS. Approximately a half of the atmosphere is contained in the first 6 km, and 99% within 30 km.

The atmosphere may be divided into four layers for descriptive purposes (Fig. 4.7). They are defined here by altitude, but the figures given are very approximate. The bottom layer, the troposphere, exists up to 10 km or so and is the layer in which the weather occurs. It also

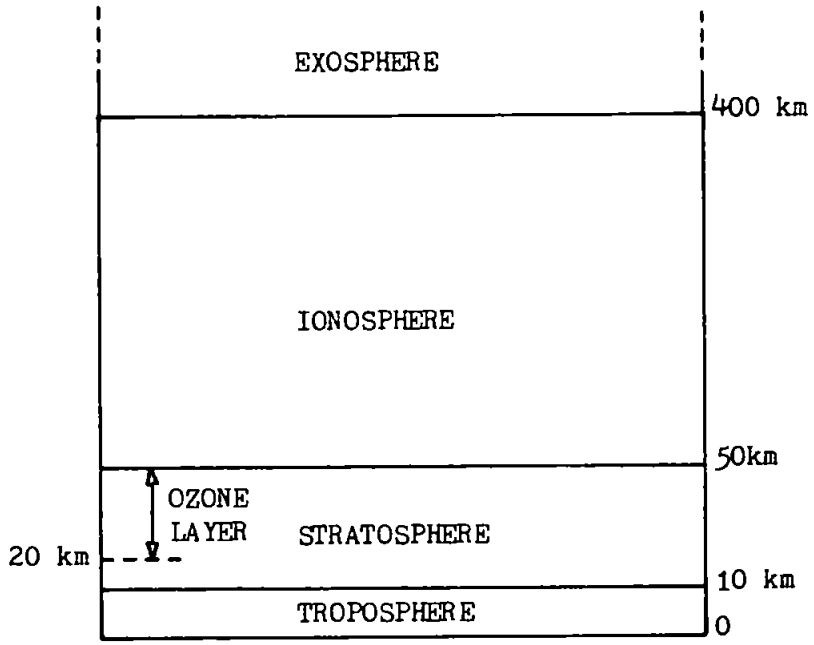

Figure 4.7 Atmospheric structure.

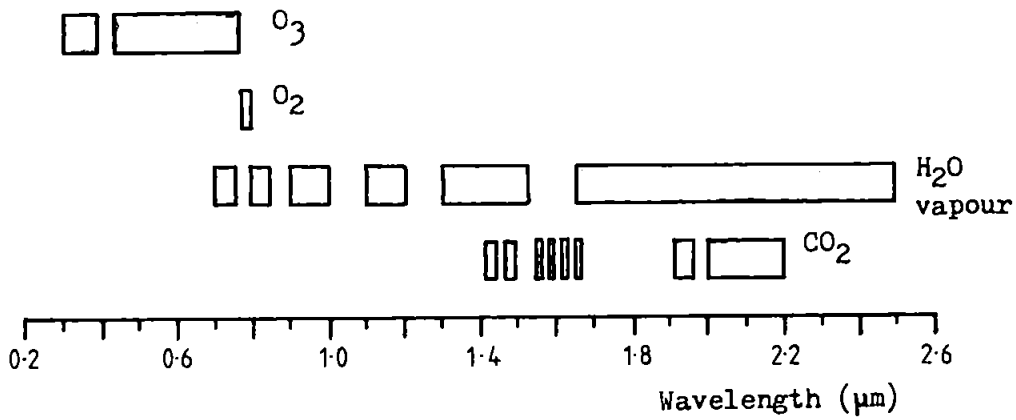

Figure 4.8 Absorption bands of atmospheric gases (after Dave 1978).

contains 80% by mass of the atmosphere and 90% of water vapour and aerosols. The stratosphere, from 10 to 50 km, is a stable layer which also contains the ozone layer lying between 20 and 50 km. Between 50 and 400 km lies the ionosphere in which atoms and molecules exist as electrically charged ions. The final layer, beyond 400 km is the exosphere.

The atmosphere is composed of three different groups of materials. The first consists of nitrogen, oxygen and argon which, in the absence of water vapour, are present in the following proportions:

N_2	78%	
O_2	21%	(By volume)
Ar	1%	

These proportions are maintained up to an altitude of approximately 90 km and so these gases are regarded as permanent. Above 90 km the proportion of lighter gases increases. Secondly, there is a group of variable gases whose proportions lie in the following ranges:

Water vapour	0 - 7	% by volume
Carbon dioxide	0.01 - 0.1	of the air
Ozone	0 - 0.01	

The final group of atmospheric constituents is aerosols which are dispersions of solid and/or liquid particles suspended in air (Slater 1980) and whose concentration varies considerably with time and space with a very pronounced decrease with increasing altitude (Sturm 1981). Typical atmospheric aerosols are particulate matter (dust and smoke)

and water droplets (fog and haze). Junge (1972) distinguishes five different aerosol components of the atmosphere in the marine environment. Combustion gases and volcanic emission are also sources of aerosols. The effective radius for atmospheric aerosols ranges from 0.005 to 20 μm (Junge 1955). Several investigators have established simple approximations for the aerosol size distribution. Junge (1955) and Ångström (1964) propose respectively:

$$\frac{dN}{d(\log r)} = \frac{\text{Constant}}{r^3} \tag{4.5}$$

and

$$dN = \text{Constant} \cdot \frac{dr}{r^4} \tag{4.6}$$

where dN is the number of particles with radius between r and r+dr. Junge (1955) adds that Eq. 4.5 is only valid for $r > 0.1$ μm. These two relationships can be shown to be equivalent by employing the mathematical identity:

$$\frac{d}{dr}(\log r) = \frac{1}{r}$$

Eq. 4.5 may be interpreted physically to imply that the mass of aerosol particles contained in equal intervals of log r is a constant (Sturm 1981). Aerosol size distributions are generally very similar with the exception of industrial areas. This similarity is due to the mechanisms of coagulation, for small aerosol particles, and precipitation for the very large ones.

Figure 4.8 shows the position and extent of the absorption bands for atmospheric gases. In the visible region, 400 to 700nm, the atmosphere is almost transparent; only a small amount of attenuation is caused by ozone absorption.

Even a very clear atmosphere is not a Rayleigh one, in the sense that scattering is not governed by a λ^{-4} relationship. The exponent is usually 2 or less and is determined by atmospheric composition.

4.4 DEVELOPMENT OF ATMOSPHERIC CORRECTION MODEL

For the purpose of developing a model for atmospheric correction, the atmosphere may conveniently be regarded as several distinct layers (Singh 1982), each of which is composed of one or more gases or materials (Fig. 4.9). The only atmospheric constituents included in this model are those that cause significant scattering or absorption in the visible region; this only occurs below 50 km. Ozone is the sole cause of significant absorption in the visible region and may be treated separately from scattering because ozone is only present at high altitudes (Viollier et al. 1980). Below 20 km the atmosphere is considered to comprise of permanent gases and aerosols only; the latter are assumed to be present only in the bottom few kilometres of the atmosphere. Morel (1980) suggests that the effects of aerosols may be ignored above 3.6 km within the marine environment. The presence of water vapour is disregarded.

A feasible algorithm for atmospheric correction may only be realised by simplifying certain aspects of the problem and the first comprehensive approach for the CZCS was devised by Gordon (1978b). He employed five simplifying assumptions (Gordon & Clark 1980a):-

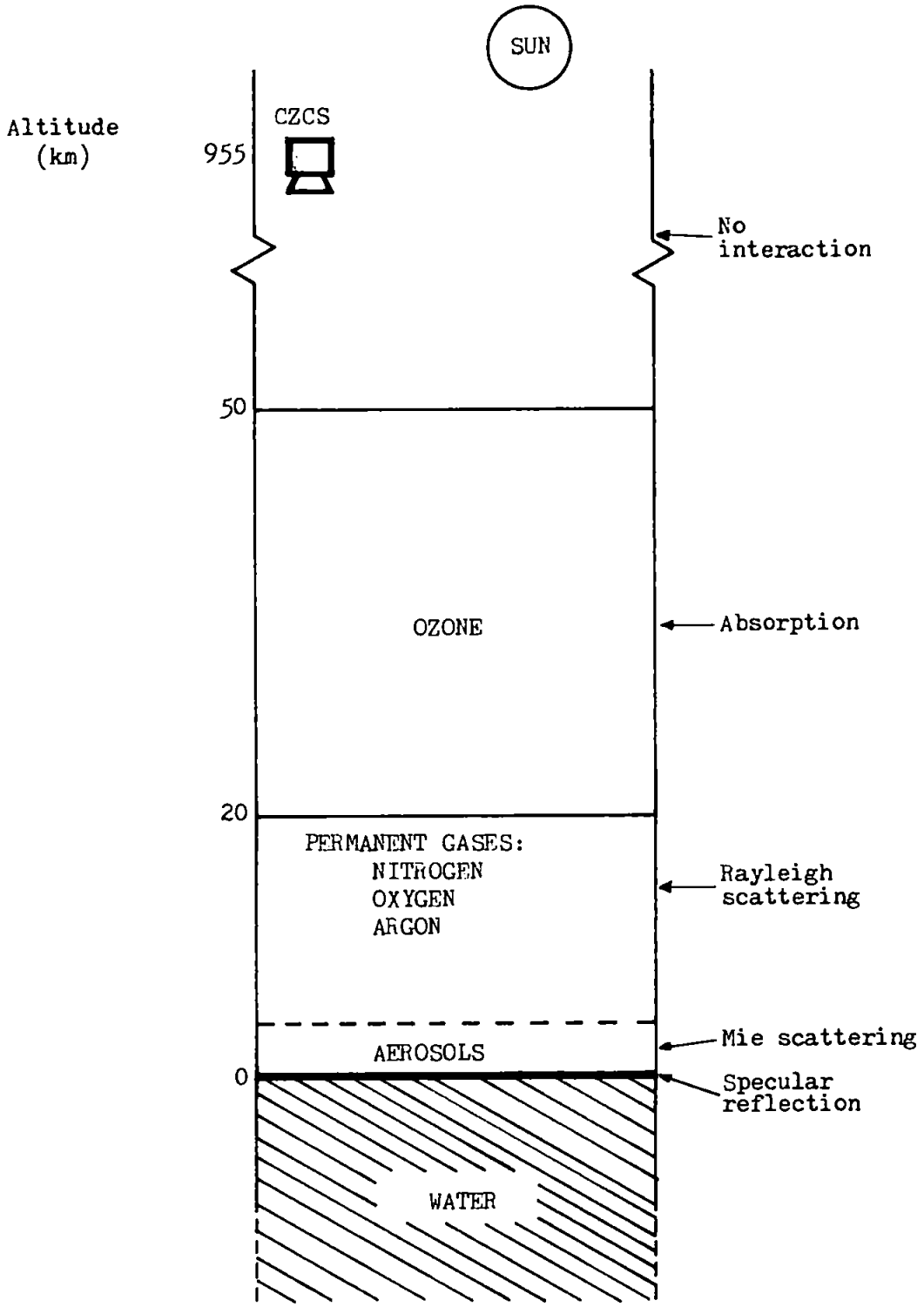

Figure 4.9 Atmospheric composition and interactions.

1) The radiance contributions caused by Rayleigh and aerosol scattering (path radiance) can be treated separately.
2) The phase function for aerosol scattering is almost independent of wavelength.
3) The Rayleigh component can be accurately computed without knowledge of the sea surface roughness (caused by waves).
4) The aerosol component is virtually a linear function of the optical thickness for aerosol scattering.
5) The upwelling radiance just beneath the sea surface is zero at 670nm (CZCS channel 4).

Assumption (1) implies that no multiple scattering occurs in the atmosphere, i.e. the presence of aerosols does not interfere with Rayleigh scattering and vice versa. This is known as the single scattering assumption and is valid provided that the scattering optical thicknesses are not too large, which is normally the case.

In addition to Rayleigh scattering of sunlight into the sensor (Fig. 4.10a) the Rayleigh component of the path radiance also includes two terms which correspond to cases where specular reflection at the sea surface is involved (Figs. 4.10c and 4.10d). Hence, it would appear that the Rayleigh component is a function of sea surface roughness. However, the Fresnel reflectance at the sea surface is typically only 2% and so the effect of a perturbed sea surface upon the Rayleigh component is minimal and may be ignored with the proviso that the specular image of the Sun is well away from the pixel under view. In this way assumption (3) is justified.

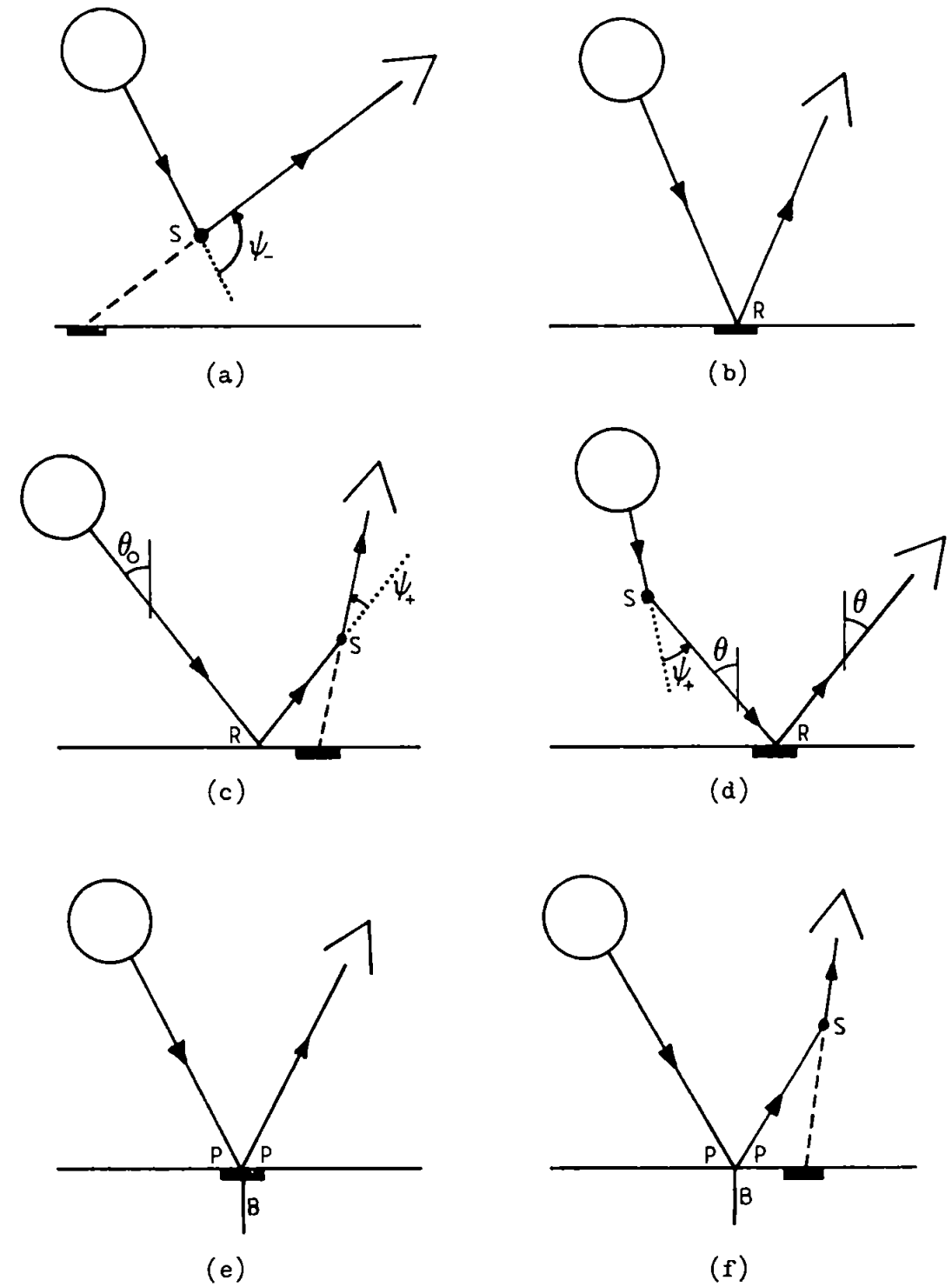

Figure 4.10 Contributions to the total radiance.

An alternative and less rigorous form of assumption (5) is that the water-leaving radiance (just above the sea surface) is equivalent to no more than one or two digital counts at the sensor after diffuse transmission through the atmosphere (Gordon et al. 1982, Gordon and Clark 1981). This assumption is valid except in regions of extremely high pigment and/or sediment concentration, i.e. high turbidity waters (Gordon and Clark 1980a).

4.5 INTERACTIONS BETWEEN LIGHT AND ATMOSPHERE/HYDROSPHERE

Figure 4.10 illustrates the different sequences of interactions occurring in the atmosphere and hydrosphere which contribute to the total radiance measured by the satellite sensor. Sequences involving more than one scattering process are not considered.

Scattering by various particles in the atmosphere (Fig. 4.10a) causes some of the incident light to be redirected into the sensor's field of view (FOV). Specular reflection at the water surface (Fig. 4.10b), which is assumed to be smooth, would normally introduce some extra radiance; in this case however it may be ignored as the CZCS has a tilt mechanism which prevents the sensor from viewing the specular image of the Sun. However, this feature does not prevent the sensor from receiving the radiance caused by reflection at the water surface with subsequent scattering, even though the sensor is not viewing the specular image of the Sun (Fig. 4.10c). Direct sunlight which is atmospherically scattered constitutes sky radiance or skylight and this may be specularly reflected at the water surface into the sensor's field of view (Fig. 4.10d). The water-leaving radiance just above the water surface, which is directly related to the sub-surface upwelling radiance, propagates through the atmosphere to the sensor and

represents the component which has interacted with the water's constituents (Fig. 4.10e). Water-leaving radiance may also be detected by the sensor, even though it originates from outside the sensor's FOV, through scattering (Fig. 4.10f).

Of all the processes, only that in Fig. 4.10e carries the desired information, that in Fig. 4.10b may be ignored and the other four must be accurately estimated in order to retrieve the water-leaving radiance.

4.6 PRACTICAL SOLUTION FOR ATMOSPHERIC CORRECTION

The approach taken here to CZCS atmospheric correction is based upon the pioneering work of Gordon. Refer to Gordon (1978b, 1981a), Gordon and Clark (1980a), Gordon et al. (1982), Gordon et al. (1980b) and Gordon et al. (1980a). The most recent and comprehensive account is given in Gordon et al. (1983b).

4.6.1 Total radiance at the satellite

The total radiance L_T^λ measured by the satellite sensor at wavelength λ is related to the water-leaving radiance L_w^λ and the radiance scattered by the atmosphere (path radiance) L_p^λ through (Sorensen 1981):

$$L_T^\lambda = t_D^\lambda L_w^\lambda + L_p^\lambda \qquad (4.7)$$

The λ superscript is only used to indicate wavelength dependent terms; it is not a power index. t_D^λ is the diffuse transmittance, which accounts for the attenuation of L_w^λ resulting from transmission through the atmosphere. The path radiance also suffers attenuation due to

ozone absorption; this is considered later. The path radiance may be expressed simply as the sum of Rayleigh and aerosol radiance (assumption 1), provided that the Rayleigh optical thickness is less than 0.25 and the aerosol optical thickness is less than 0.6 (Gordon and Morel 1983). This is justified by the assertion of Viollier et al. (1980) that the interaction between Rayleigh and aerosol scattering contributes less than 3% to the path radiance. Under this assumption Eq. 4.7 becomes:

$$L_T^\lambda = t_D^\lambda . L_w^\lambda + L_R^\lambda + L_A^\lambda \qquad (4.8)$$

However Eq. 4.8 does not account for the contributions represented by Figs. 4.10c and 4.10d, i.e. reflected sunlight scattered into the direction of the sensor and reflected skylight respectively. Since these two contributions are relatively small, they may be 'lumped in' with the atmospheric contribution (Fig. 4.10a).

This section has so far considered all the processes outlined in Fig. 4.10 except direct reflection of sunlight into the sensor (Fig. 4.10b), which is eliminated by the CZCS tilt mechanism, and the process represented by Fig. 4.10f. The latter corresponds to water-leaving radiance, originating from pixels outside the sensor's field of view, being scattered into the sensor direction. This additional component is included by using the diffuse transmittance rather than the direct transmittance, which would otherwise be appropriate.

Eq. 4.8 is the basis of the atmospheric correction algorithm, since it may be used to extract L_w^λ from L_T^λ once L_R^λ, L_A^λ and t_D^λ have been found.

4.6.2 Rayleigh radiance

Assumption 3 (see Section 4.4) permits the radiance due to Rayleigh scattering L_R^λ to be calculated accurately from the following equation, which is a reformulated version of that given by Gordon et al. (1983b):

$$L_R^\lambda = \frac{\omega_R^\lambda \tau_R^\lambda}{4\pi\mu} \cdot P_R(\psi_-) E_o^\lambda T_{O_3}^\lambda(\mu) T_{O_3}^\lambda(\mu_o) \qquad (4.9)$$

Again, λ is only used to denote wavelength dependence; it is not a power index. The terms in this equation represent the following quantities:

ω_R^λ — Single scattering albedo. Defined by the ratio of scattering cross-section to attenuation cross-section and may be regarded as the probability that an interaction will result in scattering. $\omega_R^\lambda = 1$.

τ_R^λ — Optical thickness due to Rayleigh materials, i.e. the permanent atmospheric gases.

μ — cos θ, where θ is the zenith angle of the direction between the pixel-under-view and the sensor.

μ_o — cos θ_o, where θ_o is the solar zenith angle.

$P_R(\psi_-)$ — Phase function for Rayleigh scattering in the backwards direction. See Eq. 4.1.

ψ_- — Backscattering angle. Defined in Section 4.7.

E_o^λ — Seasonally adjusted solar irradiance. See Eq. 4.4.

$T_{O_3}^\lambda(\mu)$ — Direct transmittance for an atmospheric path with zenith angle θ; $\theta = \cos^{-1}\mu$. Represents the attenuation of L_R^λ, due to ozone, on its upward path to the sensor.

$T_{O_3}^{\lambda}(\mu)$ = exp [$-\tau_{O_3}^{\lambda}/\mu$], where $\tau_{O_3}^{\lambda}$ is the optical thickness due to ozone absorption.

$T_{O_3}^{\lambda}(\mu_o)$ exp [$-\tau_{O_3}^{\lambda}/\mu_o$]; represents the attenuation of the solar flux on its passage through the ozone layer.

The two additional contributions, mentioned earlier, may be 'lumped-in' with the dominant atmospheric one by extending Eq. 4.9 thus:

$$L_R^{\lambda} = \frac{\omega_R^{\lambda}\tau_R^{\lambda}}{4\pi\mu}\left\{P_R(\psi_-) + \left[\rho(\theta) + \rho(\theta_o)\right] P_R(\psi_+)\right\} E_o^{\lambda} T_{O_3}^{\lambda}(\mu) T_{O_3}^{\lambda}(\mu_o) \quad (4.10)$$

where $P_R(\psi_+)$ is the phase function for Rayleigh forward scattering and ψ_+ is the forward scattering angle defined in Section 4.7. $\rho(\theta)$ and $\rho(\theta_o)$ are the Fresnel reflectances for incident angles of θ and θ_o, and are calculated from Eq. 4.2, with typical values of 2% or so. The $\rho(\theta_o)$ term represents reflected solar flux which is subsequently scattered into the sensor (Fig. 4.10c), while the $\rho(\theta)$ term corresponds to the case where skylight is reflected into the sensor (Fig. 4.10d). In principle (Sturm 1982, private communication) there is a transmittance factor associated with these two components, but as $P_R(\psi_-)$ and $P_R(\psi_+)$ are of the same order and $\rho(\theta)$ and $\rho(\theta_o)$ are only a few percent and the transmittance factor is close to unity, it is not included and hence introduces negligible error.

The Rayleigh radiance may be accurately calculated from Eq. 4.10 quite independently of any CZCS measurements. Values for τ_R^{λ} are available in tabular form (Trees 1982).

4.6.3 Aerosol radiance

The evaluation of L_A^λ may be approached by using an equation analogous to the one for Rayleigh radiance L_R^λ:

$$L_A^\lambda = \frac{\omega_A^\lambda \tau_A^\lambda}{4\pi\mu}\left\{P_A(\psi_-) + \left[\rho(\theta) + \rho(\theta_o)\right]P_A(\psi_+)\right\}E_o^\lambda T_{O_3}^\lambda(\mu)T_{O_3}^\lambda(\mu_o) \qquad (4.11)$$

This relation relies on assumption 4, which Gordon et al. (1980b) have shown is only valid for single scattering ($\tau_A^\lambda < 0.1$); significantly larger values of τ_A^λ destroy the linear dependence of L_A^λ upon τ_A^λ by making multiple scattering significant. However, it may still be employed usefully for CZCS atmospheric correction, introducing errors of 5% or less (Gordon et al. 1980b) provided that the sensor views ocean areas that are well away from the centre of the sun glitter pattern (Gordon et al. 1983b). The relation also incorporates two extra terms to account for aerosol scattering in Figs. 4.10c and 4.10d.

Unfortunately Eq. 4.11 may not be used directly because there is no simple analytic expression for the aerosol phase function and τ_A^λ is indeterminate because atmospheric aerosols are highly variable, i.e. the aerosol concentration and composition both vary with position and time. To circumvent this difficulty, the ratio of L_A at two different wavelengths, λ and λ_o, is taken using Eq. 4.11. By invoking assumption 2, which states that the aerosol phase function is only a weak function of wavelength in the visible region despite the fact that the optical thickness may depend strongly on wavelength (Gordon 1978b),

the resulting expression is considerably simplified:

$$\frac{L_A^{\lambda}}{L_A^{\lambda_o}} = \frac{\omega_A^{\lambda}\,\tau_A^{\lambda}}{\omega_A^{\lambda_o}\,\tau_A^{\lambda_o}} \cdot \frac{E_o^{\lambda} T_{O_3}^{\lambda}(\mu) T_{O_3}^{\lambda}(\mu_o)}{E_o^{\lambda_o} T_{O_3}^{\lambda_o}(\mu) T_{O_3}^{\lambda_o}(\mu_o)} \tag{4.12}$$

Since ω_A is usually a weak function of wavelength (Gordon et al. 1983b) Eq. 4.12 becomes:

$$\frac{L_A^{\lambda}}{L_A^{\lambda_o}} = \epsilon^{\lambda} \cdot \frac{E_o^{\lambda} T_{O_3}^{\lambda}(\mu) T_{O_3}^{\lambda}(\mu_o)}{E_o^{\lambda_o} T_{O_3}^{\lambda_o}(\mu) T_{O_3}^{\lambda_o}(\mu_o)} \tag{4.13}$$

with $\epsilon^{\lambda} \equiv \tau_A^{\lambda} \Big/ \tau_A^{\lambda_o}$

The wavelength dependence of the aerosol scattering coefficient, and hence τ_A, is $\lambda^{3-\gamma}$ (Ångström 1964) where γ is the index which characterises the aerosol size distribution. Hence ϵ^{λ} can be recast as:

$$\epsilon^{\lambda} = \frac{\lambda^{3-\gamma}}{\lambda_o^{3-\gamma}} = \left(\frac{\lambda}{\lambda_o}\right)^{3-\gamma}$$

$$\text{or} \quad \epsilon^{\lambda} = \left(\frac{\lambda_o}{\lambda}\right)^{m} \tag{4.14}$$

where $m = \gamma - 3$ and is known as the Ångström exponent. γ is typically around 4 (Eq. 4.6), which implies that m is approximately one. Viollier et al. (1980) measured m over ocean areas as 0.93 with a variance of 0.3. Provided that the Ångström exponent can be estimated, Eqs. 4.13 and 4.14 enable the aerosol radiance at one wavelength λ to be derived from the aerosol radiance at a different wavelength λ_o. Assumption 5 permits CZCS channel 4 to be used for estimating the aerosol radiance at λ_o (670nm), because Eq. 4.8 may be rearranged as:

$$L_A^{\lambda_o} = L_T^{\lambda_o} - L_R^{\lambda_o} \qquad (4.15)$$

since L_W at 670nm is zero. The final expression for the aerosol radiance is produced by substituting Eqs. 4.14 and 4.15 into Eq. 4.13:

$$L_A^{\lambda} = \left(L_T^{\lambda_o} - L_R^{\lambda_o}\right)\left(\frac{\lambda_o}{\lambda}\right)^m \frac{E_o^{\lambda} T_{O_3}^{\lambda}(\mu) T_{O_3}^{\lambda}(\mu_o)}{E_o^{\lambda_o} T_{O_3}^{\lambda_o}(\mu) T_{O_3}^{\lambda_o}(\mu_o)} \qquad (4.16)$$

Even with a horizontally inhomogeneous atmosphere, L_A^{λ} may be determined throughout a whole CZCS scene using the same value for the Ångström exponent m. The only condition, which is reasonably well satisfied (Gordon and Morel 1983), is that the aerosol type (such as continental or marine) should be constant over the image. This is tantamount to the aerosol refractive index and size distribution (normalised to the total concentration) being independent of position.

4.6.4 Transmittance factors

Transmittance factors (see Appendix 5) account for the loss in radiance which occurs when light travels downwards or upwards through the atmosphere. Two cases need to be considered:

i) The loss associated with the Rayleigh and aerosol radiance due to the ozone layer.

ii) The attenuation of water-leaving radiance caused by the ozone layer and the combined layer of aerosols and permanent gases.

As the former only involves absorption by ozone, the direct or beam transmittance T_{O3}^{λ} is required. In fact it is required twice: for the attenuation of E_o^{λ} on its downward path before scattering occurs and also for the attenuation of L_R^{λ} and L_A^{λ} on their paths to the sensor

after scattering has taken place. Expressions for T_{03}^{λ} are given in Section 4.6.2.

The second case is more complex as both absorption and scattering are involved. The direct transmittance term is given by:

$$T = e^{-(\tau_A + \tau_R + \tau_{O_3})/\mu} \qquad (4.17)$$

This is only valid if the radiance is in the form of an infinitesimally narrow beam, however scattering is present in this case and the CZCS has a finite field of view, so radiance from adjacent pixels (Fig.4.10f) will also be detected and the direct transmittance will overestimate the loss. Eq. 4.17 may be modified to yield the diffuse transmittance t_D by replacing the scattering optical thicknesses with the backscattering optical thicknesses. This formulation implicitly assumes that the water-leaving radiance only suffers attenuation when backscattered downwards and away from the sensor; any forward scattering is taken to correspond to radiance from adjacent pixels. The Rayleigh scattering phase function is symmetric in the forwards and backwards direction and so the Rayleigh backscattering optical thickness is simply $\tau_R/2$.

The aerosol backscattering optical thickness is $(1- \omega_A F).\tau_A$ where ω_A is the aerosol single scattering albedo and F is the probability that a photon is scattered through an angle of less than $\pi/2$, i.e. forwards. The diffuse transmittance t_D is then given by (Gordon and Morel 1983):

$$t_D = e^{-[\tau_R/2 + \tau_{O_3} + (1-\omega_A F)\tau_A]/\mu} \quad (4.18)$$

Absorption due to aerosols is assumed to be negligible as ω_A is close to unity. The term $(1-\omega_A F)$ is usually smaller than 1/6 (Gordon and Clark 1981) so that the aerosol term may be neglected, giving:

$$t_D \approx e^{-[\tau_R/2 + \tau_{O_3}]/\mu} \quad (4.19)$$

This expression is simplified even further by Sørensen (1981) and is the form used in this work:

$$t_D \approx e^{-\tau_R/(2\mu)} \quad (4.20)$$

Note that $0 \ll T < t_D \ll 1$. Values for τ_R and τ_{O_3} may be found in (Trees 1982).

4.6.5 Final algorithm

Rearranging Eq. 4.8 and substituting Eq. 4.16 for L_A^λ gives the final correction algorithm for retrieving L_W^λ:

$$t_D^\lambda L_w^\lambda = L_T^\lambda - L_R^\lambda - \left(L_T^{\lambda_o} - L_R^{\lambda_o}\right)\left(\frac{\lambda_o}{\lambda}\right)^m \cdot \frac{E_o^\lambda T_{O_3}^\lambda(\mu) T_{O_3}^\lambda(\mu_o)}{E_o^{\lambda_o} T_{O_3}^{\lambda_o}(\mu) T_{O_3}^{\lambda_o}(\mu_o)} \quad (4.21)$$

L_R^λ is given by Eq. 4.10. λ_o is 670nm and λ is 443, 520 or 550nm for CZCS channels 1, 2 or 3 respectively. L_T^λ and $L_T^{\lambda_o}$ are measured by the sensor and all the other terms are known or may be calculated with the exception of the Ångström exponent m. In situ measurements of the sub-surface upwelling radiance, simultaneous with the satellite pass, at one or more points in the image permit values of L_W^λ to be

derived and hence an estimate for m may be obtained. Failing this, m must be estimated in some other way, such as the examination of the total number of negative radiance pixels in the image which increases dramatically when the image has been overcorrected, i.e. m is too large. A further clue for a suitable m value may be gleaned from a study of the effect of m upon correlation coefficients when comparing CZCS derived pigment concentrations with ship measurements. Alternatively, the concept of clear water radiance (Gordon and Clark 1981) may be used to overcome this difficulty with the Ångström exponent; this technique provides inherent radiance values, which depend upon the solar zenith angle only, for regions of clear water, i.e. phytoplankton pigment concentrations less than 0.25 $mg.m^{-3}$. This procedure requires the location of clear water areas within the image and has not been implemented in this work.

Eq. 4.21 relies strongly upon the $L_W^{\lambda_o} = 0$ assumption, which is not a particularly stringent condition as Gordon and Clark (1981) have shown that $L_W^{\lambda_o}$ corresponds to less than three digital counts even when the pigment concentration is as high as 1 $mg.m^{-3}$. In general though this condition is not satisfied in coastal regions. Smith and Wilson (1980) have developed an iterative technique which obviates the $L_W^{\lambda_o} = 0$ requirement altogether; replacing $(L_T^{\lambda_o} - L_R^{\lambda_o})$ in Eq. 4.21 by $(L_T^{\lambda_o} - L_R^{\lambda_o} - L_W^{\lambda_o})$. For the first iteration, $L_W^{\lambda_o}$ is taken as zero when calculating L_W^{λ} for channels 1 to 3, which are then used in an empirical relationship to generate a new non-zero $L_W^{\lambda_o}$ value. This is used in the second iteration to produce a new set of L_W^{λ} values, from which yet another $L_W^{\lambda_o}$ value is obtained. The whole process is repeated until both $L_W^{\lambda_o}$ and L_W^{λ} converge.

Before attempting atmospheric correction, however, it is necessary to evaluate the forward and backward scattering angles ψ_+ and ψ_- and also θ and θ_0, the polar angle (equivalent to sensor zenith angle) and solar zenith angle respectively. These are all treated in the next section on Sun-satellite geometry.

4.7 SUN-SATELLITE GEOMETRY

The directions defined by the Sun to pixel-in-view vector and pixel-in-view to sensor vector determine the forward and backward scattering angles ψ_+ and ψ_- respectively. These directions are specified in terms of zenith and azimuth angles, although the former is alternatively known as the polar angle (Singh 1982). The Sun direction (θ_0, ϕ_0) depends upon the solar declination, the local time and the latitude for the pixel-in-view, while the sensor direction (θ, ϕ) is governed by the pixelnumber i.e. position along the scanline, the scan-mirror tilt angle and the latitude for the pixel-in-view.

The procedure for determining the scattering angles requires the evaluation of θ, θ_0, ϕ and ϕ_0 and is presented here in a step by step manner:

i) The daynumber D is calculated by referring to a table of the number of days in each month. Leap years must also be taken into account and occur when the year is exactly divisible by four, with the exception of century years unless they are exactly divisible by 400.

ii) The solar declination angle δ is found from Eq. 4.3 using the daynumber calculated above.

iii) The solar zenith angle θ_o is computed from (Singh 1982, private communication):

$$\cos \theta_o = \sin \theta_1 \sin \delta + \cos \theta_1 \cos \delta \cos \omega t \qquad (4.22)$$

where θ_1 is the latitude of the pixel-in-view, t is the local time for the pixel, and ω is $2\pi/24$. For the sake of clarity here, both θ_1 and t are assumed to be known, although the calculation of their values represents a further problem which is covered in Section 4.8.

iv) The solar azimuth angle ϕ_o, from the North direction Eastwards, is determined from (Singh 1982, private communication):

$$\cos \phi_o = \frac{\sin \delta - \sin \theta_1 \cos \theta_o}{\sin \theta_o \cos \theta_1} \qquad (4.23)$$

if the local time t is positive, i.e. after local noon, then the correct value of ϕ_o is given by $2\pi - \phi_o$.

v) The view-angle θ_v is the angle between the sensor to pixel-in-view direction and the sensor to nadir pixel direction that would be measured when there is zero tilt, and is given by:

$$\theta_v = \text{IFOV (Pixel-number} - \text{nadir pixel number)} \qquad (4.24)$$

where IFOV is the instantaneous field of view (0.698×10^{-3} radians), the pixel number ranges from 114 (West end of scan-line) to 2081 (East end of scan-line) and the nadir pixel

number is 1090 (Ball Aerospace Systems Division 1979a). The mean value of the extreme pixel numbers is not the same as the nadir pixel number as there is a slight skew in the CZCS scan.

vi) The pixel-in-view to sensor polar (or zenith) angle θ is calculated from:

$$\cos \theta = \cos \theta_v \cdot \cos \theta_t \qquad (4.25)$$

where θ_t is the scan-mirror tilt angle found from the housekeeping data. Eq. 4.25 is derived in Appendix (6).

vii) The azimuth angle ϕ of the pixel-in-view to sensor direction is equal to the sum of angles Δ and ϕ'' as shown in Fig. 4.11. Δ may be found from the orbital inclination α, which is a function of latitude θ_1, and is computed from (Wilson et al. 1981):

$$\sin\alpha = \frac{\sin 9.28^\circ}{\cos\theta_1} \qquad (4.26)$$

where the angle 9.28° is the inclination (West of North) of the CZCS orbital trackline at the equator. Since Δ equals $\pi/2 - \alpha$ then:

$$\Delta = \pi/2 - \sin^{-1}\left[\frac{\sin 9{\cdot}28^\circ}{\cos\theta_1}\right]$$

$$\text{or} \quad \Delta = \cos^{-1}\left[\frac{\sin 9{\cdot}28^\circ}{\cos\theta_1}\right] \qquad (4.27)$$

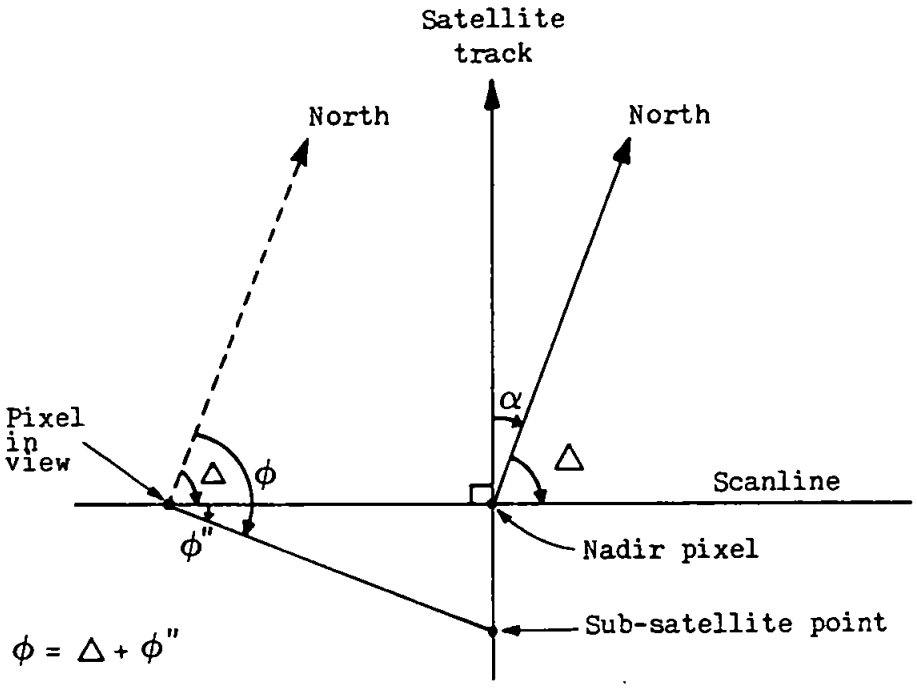

Figure 4.11 Azimuth angle of pixel-in-view to sensor direction.

	$\theta_v > 0$	$\theta_v = 0$	$\theta_v < 0$
$\theta_t > 0$	$\pi - \phi'$	$\pi/2$	ϕ'
$\theta_t = 0$	π	0	0
$\theta_t < 0$	$\pi + \phi'$	$3\pi/2$	$2\pi - \phi'$

Table 4.1 Calculation of ϕ'' from ϕ'.

viii) The determination of ϕ'' requires a value for ϕ' which is given by:

$$\phi' = \left| \tan^{-1}\left(\frac{\sin\theta_t}{\tan\theta_v}\right) \right| \qquad (4.28)$$

This expression is derived in Appendix (7). ϕ'' is then found from Table 4.1 (Singh 1982). Note that the situation depicted in Fig. 4.11 corresponds to just one of the nine possible ones covered by Table 4.1.

Finally:

$$\phi = \Delta + \phi'' \qquad (4.29)$$

ix) Since all four angles θ, θ_o, ϕ and ϕ_o are now known, then the scattering angles $\psi_{\pm}$ may be computed from:

$$\cos\psi_{\pm} = \pm\cos\theta \cdot \cos\theta_o - \sin\theta \cdot \sin\theta_o \cdot \cos(\phi - \phi_o) \qquad (4.30)$$

which is derived in Appendix (8). Both the azimuth angles ϕ and ϕ_o are with respect to the same azimuth reference direction, namely North. In this way $(\phi - \phi_o)$ gives the correct value for the difference in azimuth angle.

4.8 PRACTICAL CONSIDERATIONS OF IMPLEMENTATION

This section addresses the problems of solving the atmospheric correction equations for a very large number of pixels and also the evaluation of the latitude θ_1 and local time t of the pixel-in-view, both of which have been taken as known quantities in previous sections.

4.8.1 Computational overheads associated with Sun-satellite geometry

The Sun-satellite geometry varies with each pixel in the scene, so in principle nearly all the equations in Section 4.7 must be evaluated for each pixel in the image. Only then may the final correction equation (Eq. 4.21) be evaluated, which also requires the evaluation of associated expressions. Considering that one spectral image comprises nearly 400,000 pixels and that two or three atmospherically corrected spectral images are required for ratioing or clustering respectively, the total number of pixels involved is of the order of 10^6. This number of calculations cannot be performed in a reasonable time without floating-point hardware or access to a mainframe computer. Some form of compromise is therefore necessary; the most obvious one being to perform all the geometric calculations just once for the centre of the image and use these values for all pixels. However, an image of 768 x 512 pixels subtends angles of approximately 30° by 20° at the satellite, and this approach would introduce unacceptable errors. The technique adopted here is based upon the partitioning of the image into 24 square cells (Fig. 4.12), within which the Sun-satellite geometry may be regarded as constant. All parameters which are a function of geometry are calculated once for the centre of each cell; the final correction is then performed for each pixel. In this way, only Eq. 4.21 needs to be evaluated for each pixel, while all the geometric ones are evaluated 24 times (once for each cell centre). Each cell comprises 128 by 128 pixels and subtends angles of approximately 5° by 5° at the sensor.

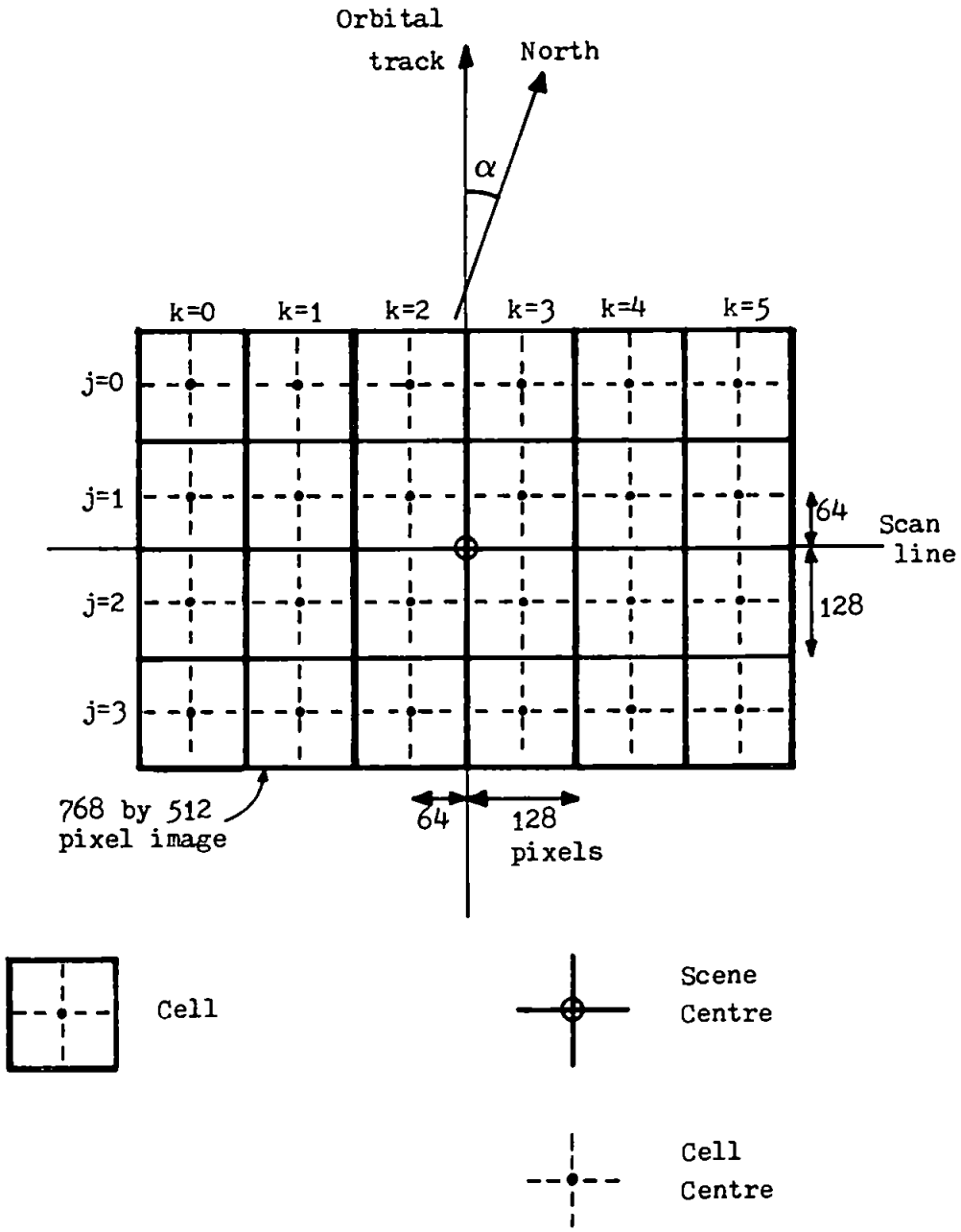

Figure 4.12 Partition of image into 24 square cells.

4.8.2 Determination of latitude and longitude

As a consequence of the image partition, values of latitude θ_1 are needed for each cell centre. In addition, the longitude θ_2 is required for the calculation of the local time t. θ_1 and θ_2, for each cell centre, have to be extrapolated from the latitude Θ_1 and longitude Θ_2 for the centre of the image, assuming that Θ_1 and Θ_2 may be estimated in some way. This may be achieved by inverting the image rectification transformations (generated from ground control points) or by careful inspection of detailed maps, provided that some land is present in the image. From now on, the symbols θ_1 and θ_2 are reserved for cell centres and Θ_1 and Θ_2 are reserved for the image centre. An image of 768 by 512 pixels subtends angles of less than 4° by 6° at the Earth's centre, which permits the effects of Earth curvature to be neglected. Thus the image may be regarded as lying in a plane and simple linear extrapolation may be used to find θ_1 and θ_2. The displacements of cell centres from the image centre in the scanline direction are 64, 192 and 320 pixels, and in the direction of the orbital track they are 64 and 192 pixels (Fig. 4.12). All these are multiples of 64 and so it is natural to base the increments in the extrapolation process upon this number of pixels. Two increments are necessary: one each for latitude and longitude, denoted by a and b respectively. Increment a is 64 x 0.782 km or 64 x 0.782/1.852 nautical miles, where 0.782 km is the mean ground resolution for channels 1 to 5 in the direction of the satellite track (Ball Aerospace Systems Division 1979a). One nautical mile is one-sixtieth of a degree of latitude and the expression for a in degrees of latitude is therefore:

$$a = \frac{64 \times 0.782}{1.852 \times 60} = 0.4504° \quad (4.31)$$

The mean ground resolution for channels 1 to 5 in the scanline direction is 0.765 km (Ball Aerospace Systems Division 1979a) and one degree of longitude is equivalent to 60cosine(latitude) nautical miles (Ayres 1954), hence increment b is given by:

$$b = \frac{64 \times 0.765}{1.852 \times 60 \times \cos\Theta_1} = \frac{0.4406}{\cos\Theta_1} \quad (4.32)$$

These increments are such that 2a and 2b represent degrees of latitude and longitude subtended by each cell. The latitude $\theta_1(j,k)$ and longitude $\theta_2(j,k)$ for cell (j,k) are found from:

$$\theta_1(j,k) = \Theta_1 + a.(3-2j) \quad (4.33)$$

$$\theta_2(j,k) = \Theta_2 + b.(2k-5) \quad (4.34)$$

where j is 0,1,2 or 3 and k is 0,1,2,3,4 or 5. By convention, longitudes West of Greenwich are represented by negative values and those East of Greenwich are positive. The CZCS scene is assumed to be in the Northern hemisphere and all latitudes are represented by positive quantities.

4.8.3 Non-alignment of coordinate systems

Eqs. 4.33 and 4.34 were derived assuming that the satellite coordinate system is aligned with the terrestrial one. However, it is apparent from Eq. 4.26 that the orbital inclination α is 9.28° at the equator and increases with increasing latitude, so the two different coordinate

systems are never in alignment. This may be remedied by incorporating a clockwise rotation of α into the extrapolation equations. Clockwise rotation of a point (x,y) in a two dimensional rectangular coordinate system through an angle α about the origin maps the point to (Arfken 1970):

$$(x \cos\alpha - y \sin\alpha \ , \ y \cos\alpha + x \sin\alpha \ )$$

The modified expressions for extrapolating θ_1 and θ_2 from Θ_1 and Θ_2 are therefore:

$$\theta_1(j,k) = \Theta_1 + a\,[(3-2j).\cos\alpha + (2k-5).\sin\alpha\,] \qquad (4.35)$$

$$\theta_2(j,k) = \Theta_2 + b\,[(2k-5).\cos\alpha - (3-2j).\sin\alpha\,] \qquad (4.36)$$

The orbital inclination α exhibits a small variation over the scene, but is assumed to be constant for simplicity. The lack of alignment also implies that the expressions for increments a and b should include a $\cos\alpha$ term as the ground resolutions are specified in the satellite coordinate system. However, for latitudes of 60° or less, $\cos\alpha$ is between 0.95 and 0.99. Therefore, the $\cos\alpha$ term can be taken as one, bearing in mind that ground resolutions vary from channel to channel and with position along the scanline. The value of α for use in Eqs. 4.35 and 4.36 is given by:

$$\sin\alpha = \frac{\sin 9.28°}{\cos\Theta_1} \qquad (4.37)$$

and corresponds to the orbital inclination for the centre of the scene.

4.8.4 Calculation of local time

The zenith angle of the Sun to pixel-in-view direction, θ_o depends upon the local time t at the pixel-in-view, and the azimuth angle ϕ_o of this direction depends upon θ_o. Thus the Sun to pixel-in-view direction is influenced by the local time, which is the time at which the pixel was viewed by the sensor, relative to local noon. This local time is not directly available and must be derived from the picture time noted at the receiving station. The picture time represents the time of closest approach of the CZCS to the receiving station and indicates the approximate time at which the CZCS has the same latitude as the receiving station. Picture time is given in Greenwich Mean Time (GMT), i.e. local to the Greenwich meridian and is converted to local time for the pixel-in-view by making two corrections. The first C_1, converts the picture time at the receiving station to the time at which the pixel was viewed. The latter is corrected to local time by C_2. Both of these corrections are applied at each cell centre. Fig. 4.13 depicts a typical situation in which the receiving station is North of the pixel and the scan mirror is tilted forwards, i.e. $\theta_t > 0$. The pixel-in-view is shown at the centre of the scanline whose duration is only 0.12375 seconds, during which time the Sun position is essentially static. This implies that all pixels on the same scanline are viewed at the same time as far as the calculation of local time is concerned. The correction to local time however, will vary as there is a significant variation in longitude along the scanline.

C_1 represents the time taken for the CZCS sub-satellite point to cover the distance d_1 plus d_2. d_1 is the distance in km between the pixel-in-view and receiving station as measured along a meridian and is found from the difference in latitudes:

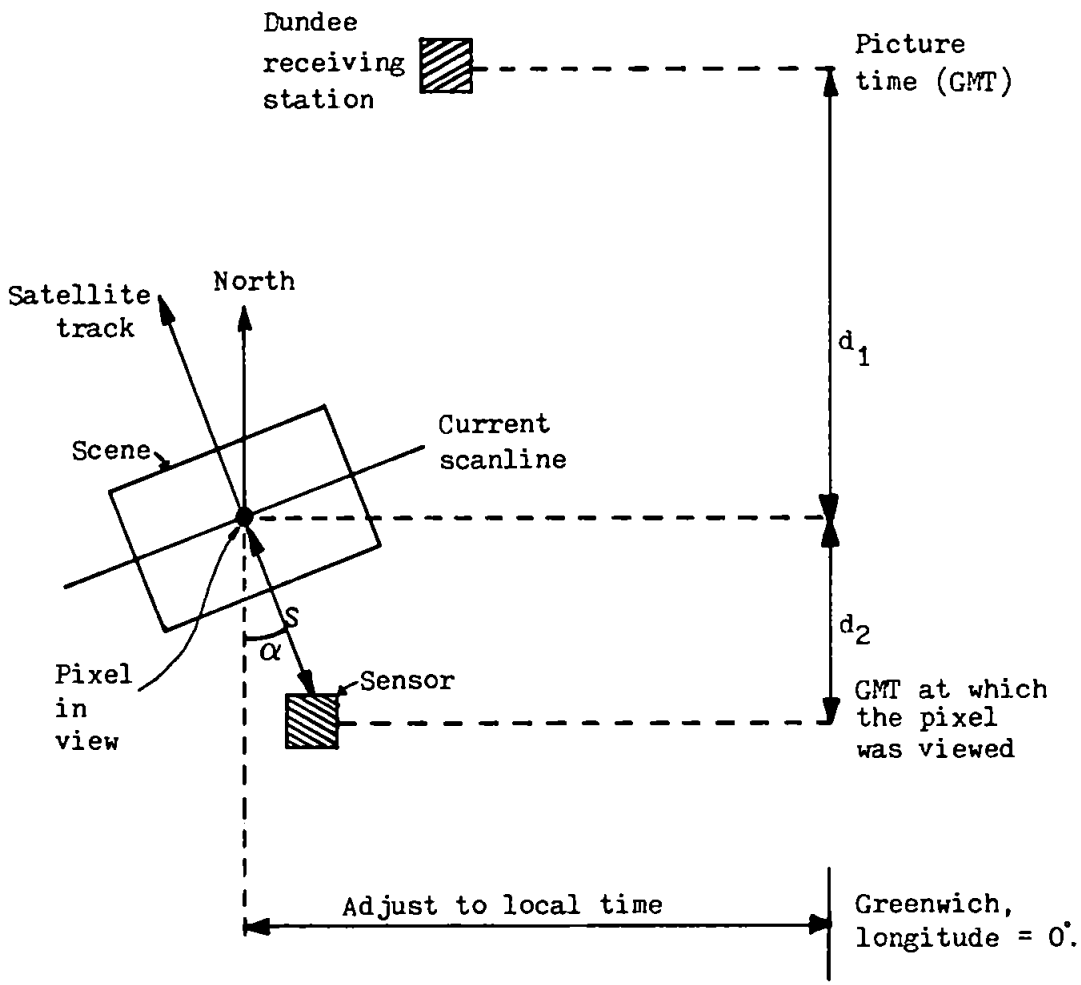

Sensor is shown with forward tilt of the scan mirror ($\theta_t > 0$) and with the pixel-in-view at the centre of the scanline ($\theta_v = 0$).

Figure 4.13 Calculation of local time.

$$d_1(j,k) = [\theta_1(j,k) - 56.4667] \times 60 \times 1.852 \qquad (4.38)$$

$\theta_1(j,k)$ is the latitude in degrees for the appropriate cell centre and 56.4667° is the latitude of Dundee. The distance d_2 is a function of the orbital inclination and the displacement s of the sub-satellite point from the pixel-in-view caused by tilt of the scan mirror as follows:

$$d_2(j,k) = s. \cos [\alpha(j,k)] \qquad (4.39)$$

where $\alpha(j,k)$ is the orbital inclination for cell (j,k) and is calculated from Eq. 4.26. s, in km, is determined from the following equation (Appendix 3):

$$\frac{s}{R} = \sin^{-1}\left[(1+h/R)\sin\theta_t\right] - \theta_t \qquad (4.40)$$

s is positive/negative when θ_t is positive/negative and is zero when θ_t equals zero. R is the mean Earth radius (6371 km) and h is the CZCS altitude (955 km). This equation is only valid if the right-hand side is expressed in radians. C_1 is simply:

$$C_1(j,k) = \frac{d_1(j,k) + d_2(j,k)}{V_g \times 60^2} \quad \text{hours} \qquad (4.41)$$

where V_g is the sub-satellite velocity at the ground and is equal to the mean ground resolution in the direction of the satellite track (0.782 km) divided by the duration of the scanline (0.12375 seconds) which is 6.319 km.s^{-1}. It may also be determined from the CZCS orbital characteristics (Slater 1980).

C_2 converts from the GMT at which the pixel was viewed to local time (Singh 1982, private communication) and is derived from the longitude of the cell centre in degrees $\theta_2(j,k)$, and exploits the fact that 360° of longitude or one Earth rotation takes 24 hours, thus:

$$C_2(j,k) = \theta_2(j,k) \times \frac{24}{360}$$

$$= \frac{\theta_2(j,k)}{15} \text{ hours} \qquad (4.42)$$

Adding the two corrections to the picture time and adjusting to local noon gives the local time t for cell (j,k) as:

$$t(j,k) = \text{Picture-time} + C_1(j,k) + C_2(j,k) - 12 \text{ hours} \qquad (4.43)$$

Both C_1 and C_2 may be positive or negative, depending upon the latitude and longitude of the pixel in relation to those of the receiving station and Greenwich.

4.8.5 Evaluation of pixel-number

Since the view-angle θ_v is a function of pixel-number (Eq. 4.24), the pixel-number for each cell centre across the image is required in order to find the six view-angles. The pixel-number ranges from 114 to 2081 for a full CZCS scanline of 1968 pixels, whereas the image width is restricted to 768 pixels. The left-hand edge of the image corresponds to the start of one of the first nine minor-frames of the CZCS data format. The pixel-number for column k is established from:

$$\text{Pixel-number } (k) = 114 + 136\,[(\text{initial minor-frame number}) - 1] + 63 + 128k \qquad (4.44)$$

where the initial minor-frame number (1-9) is the one associated with the left-hand edge of the image, and 136 is the number of pixels in each minor-frame. The value of 63 accounts for the fact that the pixel-number is required at the centre of each cell and not at the cell's boundary. The column number k (0-5) specifies the cell centre. Atmospheric correction of a whole image requires all six pixel-numbers.

4.8.6 Selection of Rayleigh and ozone optical thicknesses

The Rayleigh and ozone optical thicknesses, τ_R and τ_{03}, for each CZCS wavelength are selected from Table 4.2 (Trees 1982) as a function of zone, which depends upon the latitude of the scene centre Θ_1, and the season. The term season is used here in an unorthodox way to distinguish between the two seasons of Summer and Winter, rather than the usual four. The conventional four seasons are defined in the following way:

Season	Commences on	Date	Daynumber
Spring	Vernal equinox	March 21	80
Summer	Summer solstice	June 21	172
Autumn	Autumnal equinox	September 23	266
Winter	Winter solstice	December 22	356

The two seasons of Summer and Winter used in selecting the zone are taken as starting at mid-Spring and mid-Autumn respectively (Fig. 4.14) and therefore their daynumbers are given by:

Rayleigh optical thickness τ_R

	1	2	3	4	5
443	0.2329	0.2311	0.2316	0.2300	0.2303
520	0.1231	0.1222	0.1224	0.1214	0.1218
550	0.0969	0.0962	0.0964	0.0956	0.0959
670	0.0444	0.0440	0.0442	0.0438	0.0439

Ozone optical thickness τ_{O_3}

	1	2	3	4	5
443	0.0066	0.0067	0.0069	0.0068	0.0071
520	0.0166	0.0200	0.0237	0.0213	0.0275
550	0.0261	0.0323	0.0390	0.0346	0.0461
670	0.0158	0.0191	0.0226	0.0202	0.0264

Zone	Latitude	Region	Season
1	0° - 25°	Tropical	——
2	25° - 55°	Mid-latitude	Summer
3	25° - 55°	Mid-latitude	Winter
4	> 55°	Sub-polar	Summer
5	> 55°	Sub-polar	Winter

Table 4.2 Rayleigh and ozone optical thicknesses.

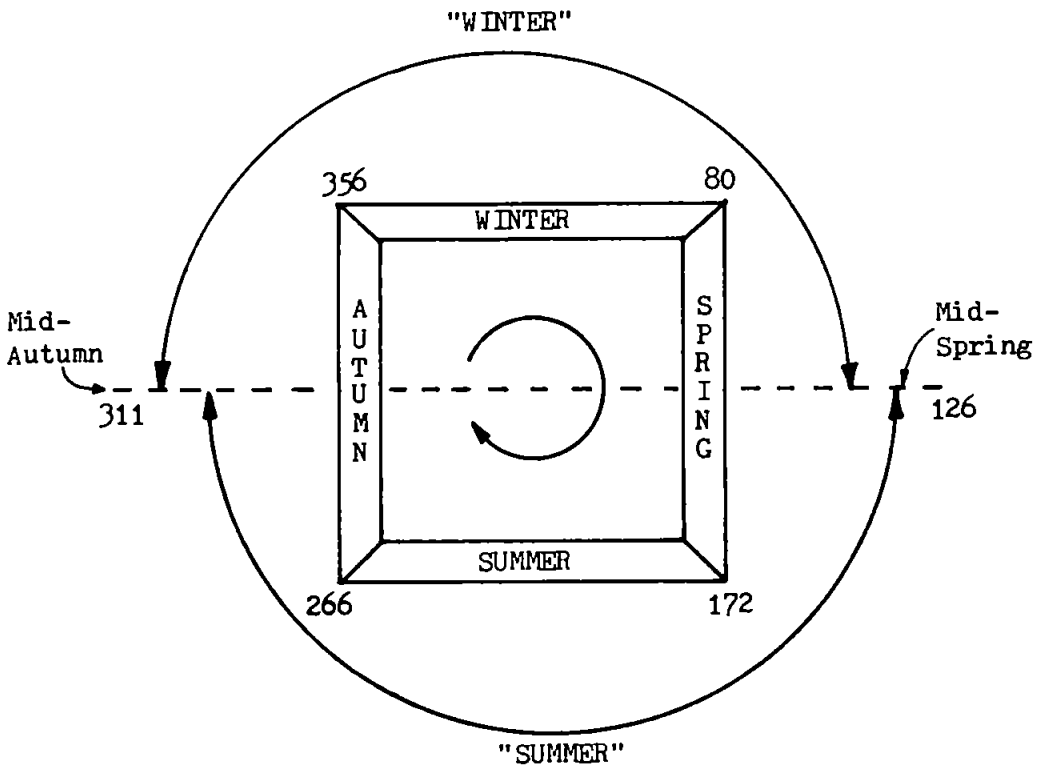

Figure 4.14 Selection of season for determination of optical thicknesses.

mid-Spring daynumber = (80 + 172)/2 = 126

mid-Autumn daynumber = (266+ 356)/2 = 311

4.8.7 Mean solar irradiance values

The mean solar irradiance values $\bar{E}_o^{\lambda}$, used by Eq. 4.4 in the evaluation of the seasonally-adjusted solar irradiances E_o^{λ}, are taken from Austin (1982) with the following values:

CZCS Channel	Wavelength nm	$\bar{E}_o^{\lambda}$ mW/(cm^2.μm)
1	443	186.42
2	520	185.34
3	550	184.76
4	670	151.52

The radiation sources and detectors used as calibration standards for irradiance suffer from poor stability and consequently there is considerable uncertainty in the measurement of irradiance (Slater 1980). For this reason $\bar{E}_o^{\lambda}$ values are subject to revision. Gordon (1981b) discusses the implications of this uncertainty in the estimation of water-leaving radiance.

4.9 SOFTWARE DESCRIPTION

The atmospheric correction program developed for this work may be used in two different ways: to correct a full image of 768 by 512 pixels for display purposes or for the correction of a set of pixels corresponding to those locations in the image for which ship samples have been taken. In the former case, the water-leaving radiance values

are scaled up to appropriate integer values for the imagestore, but in the latter case a stable of absolute radiance values is generated for comparison with ship measurements. Plates 4.1a and b show CZCS channel 2, for the 29/7/1981, before and after atmospheric correction. The latter displays sub-surface features which are not evident in the uncorrected image. Similarly, Plates 4.1c and d show CZCS channel 2 for the 22/6/1981. Execution time for the correction of one full image is approximately 15 minutes when running under multi-user UNIX.

4.9.1 User-supplied parameters

The following parameters are supplied by the user for each image or set of pixels that is to be corrected:

CZCS channel number (1, 2 or 3)
Date of the CZCS pass
Picture time
Latitude for the centre of the image
Longitude for the centre of the image
Scan-mirror tilt angle
Initial minor-frame number
Channel 1/2/3 slope)
Channel 1/2/3 intercept) For radiometric
Channel 4 slope) conversion
Channel 4 intercept)
Angstrom exponent
Scale factor for display purposes (when applicable)

The default value for the refractive index of seawater is 1.341 (Sturm 1982, private communication) in the visible region.

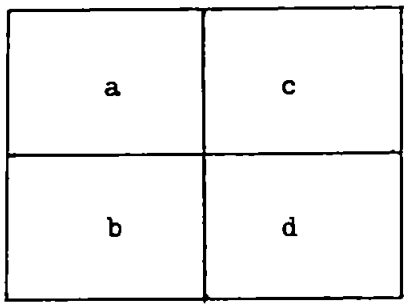

Plate 4.1

(a) CZCS channel 2 image for 29/7/1981 before atmospheric correction.

(b) As (a), but after atmospheric correction.

(c) CZCS channel 2 image for 22/6/1981 before atmospheric correction.

(d) As (c), but after atmospheric correction.

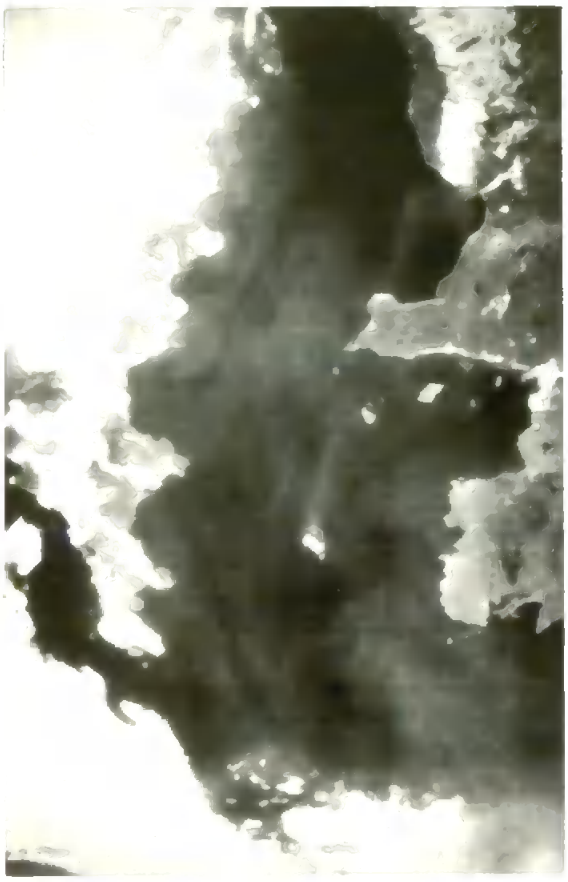

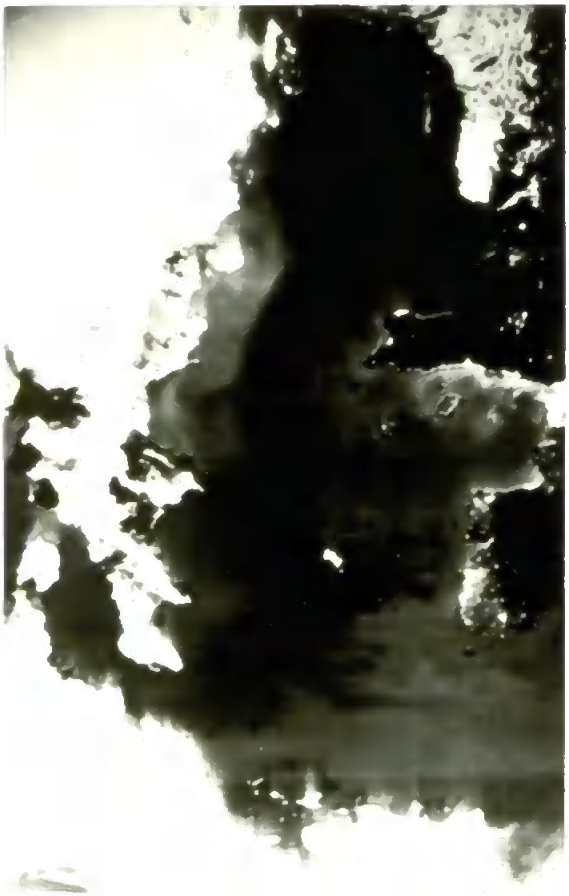

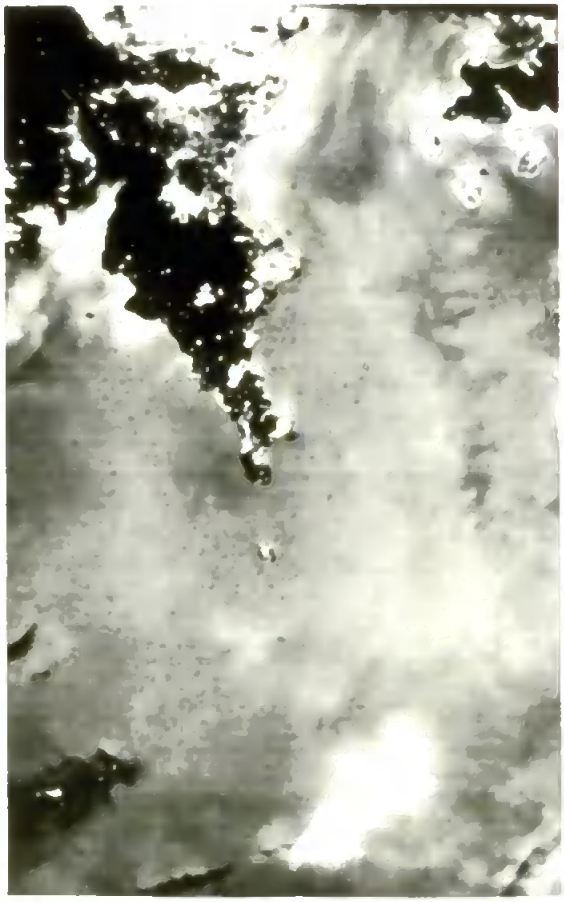

4.9.2 Useful constants

The correction program makes use of the following constants:

Name	Value	Description
ALTITUDE	955km	CZCS altitude
CONVERSION	1.852 km.mile^{-1}	Number of km in one nautical mile
EARTHRADIUS	6371 km	Mean Earth radius
ECCENTRIC	0.0167	Eccentricity of the Earth's orbit.
FIRSTPIXEL	114	Pixel-number for the left-hand end of the scanline
FRAMESIZE	136	Number of pixels in a minor-frame
GRESX	0.782 km	Ground resolution in 'X' direction (along track)
GRESY	0.765 km	Ground resolution in 'Y' direction (along scanline)
IFOV	0.000698	Instantaneous field of view (radians)
INCLINATION	23.44°	Inclination of equator to the ecliptic
LATRXSTAT	56.4667°	Latitude of receiving station (Dundee)
MIDAUTUMN	311	Daynumber for the middle of Autumn
MIDSPRING	126	Daynumber for the middle of Spring
NADIRPIX	1090	Nadir pixel number

SCANTIME	0.12375s	Duration of one CZCS scanline
SOLIRR1	186.42	Mean solar irradiance for channel 1
SOLIRR2	185.34	Mean solar irradiance for channel 2
SOLIRR3	184.76	Mean solar irradiance for channel 3
SOLIRR4	151.52	Mean solar irradiance for channel 4
TRACKINC	9.28°	Trackline inclination at the equator
VELOCITY	6.319 $km.s^{-1}$	Ground velocity of the sub-satellite point
VERNALDAY	80.25	Daynumber for the vernal equinox (March 21)

The units for the mean solar irradiances are $mW.cm^{-2}.\mu m^{-1}$.

4.9.3 Program structure

The overall structure of the program is illustrated in Fig. 4.15 and in greater detail in Fig. 4.16. The global values are independent of Sun-satellite geometry and therefore apply to the whole image. In contrast, local values are a function of Sun-satellite geometry and are evaluated for each cell. Radiometric conversion is carried out by the program prior to atmospheric correction. The program is written in 'C' (approximately 1100 lines) and comprises one main program and 21 functions; a function being the equivalent of a subroutine in Fortran. A complete program listing is given in Appendix 9. A summary of these functions is given below:

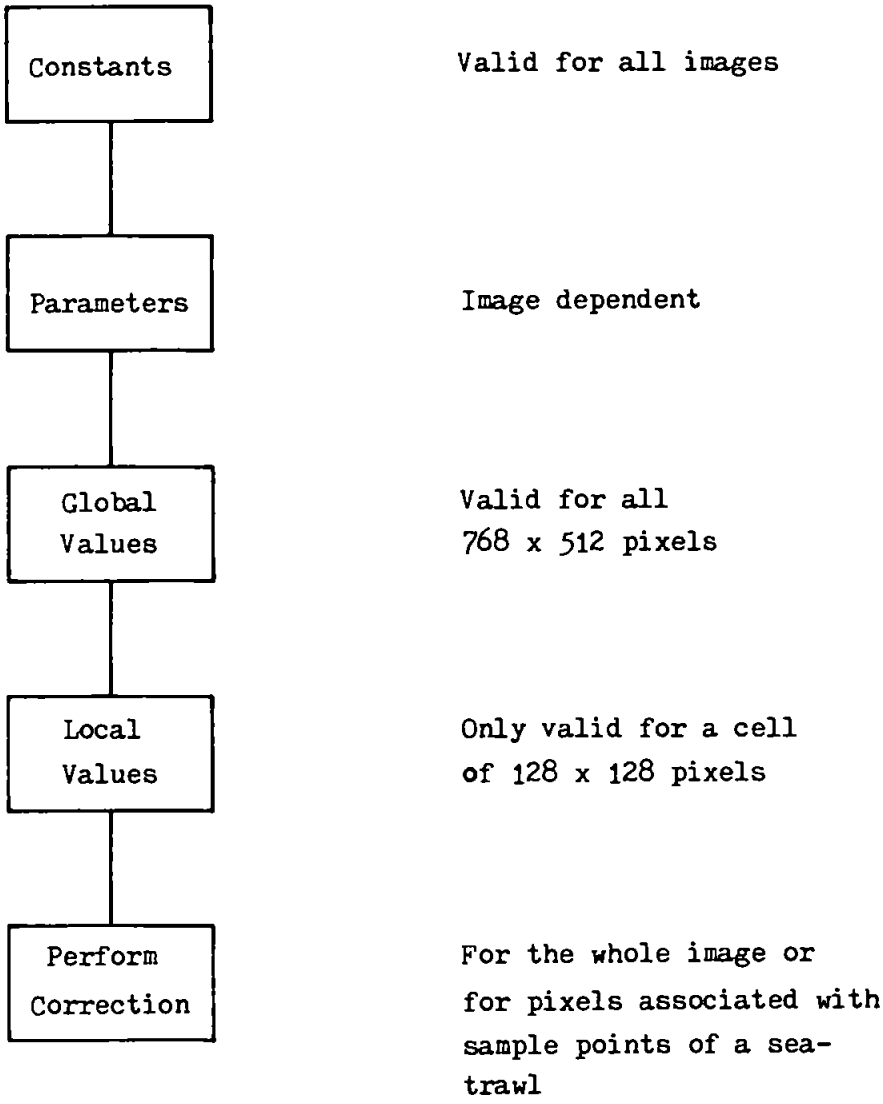

Figure 4.15 Overall structure of the atmospheric correction program.

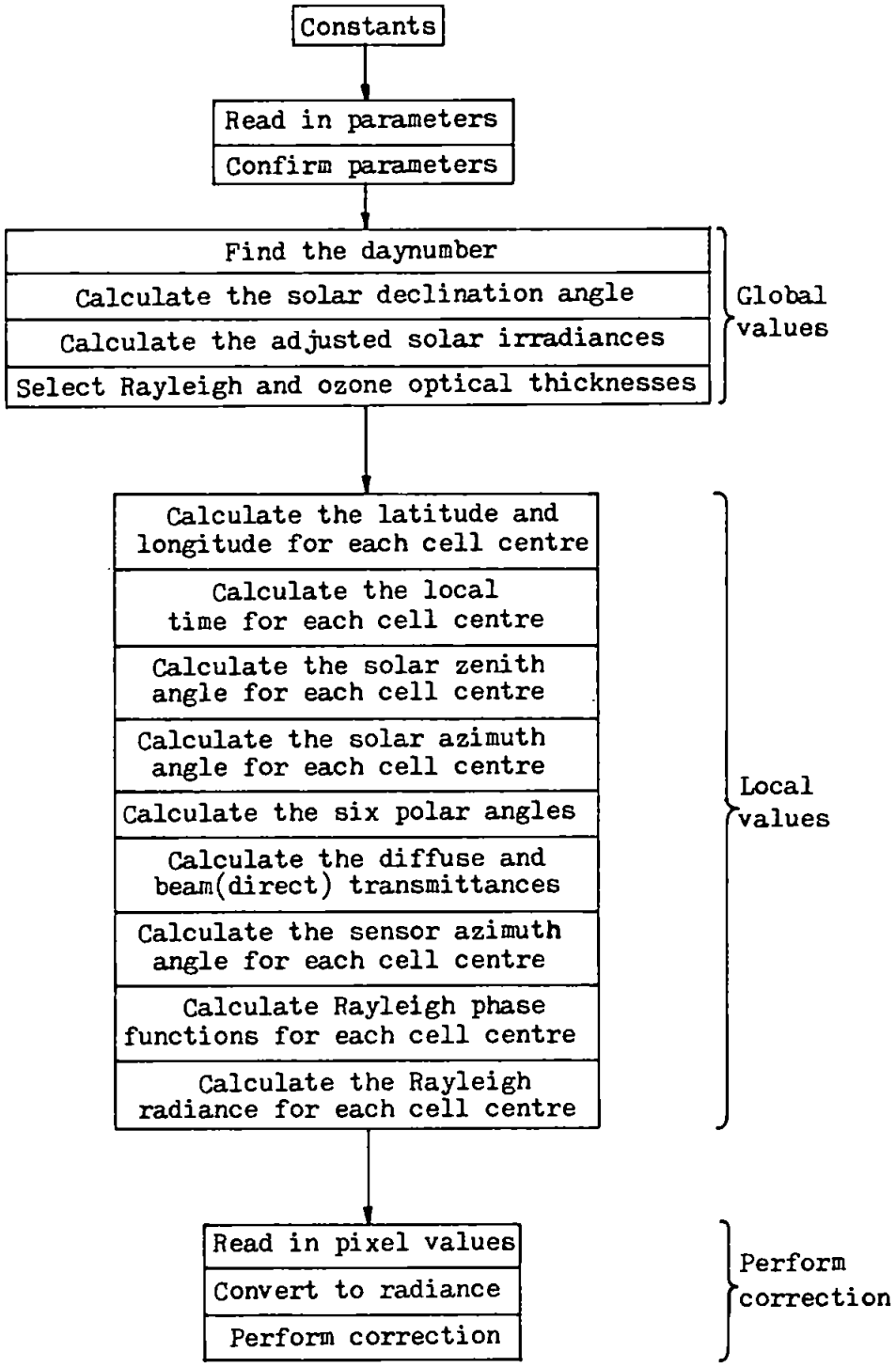

Figure 4.16 Detailed structure of the atmospheric correction program.

Function name	
atmos1	Evaluates final correction algorithm for the whole image
atmos2	Evaluates final correction algorithm for sample points
cellcent	Calculates latitude and longitude for cell centres
confirm	Confirms choice of parameters
day-of-year	Calculates the daynumber from the date
decline	Calculates the solar declination angle
fresnel1	Calculates reflection coefficient for air to water
fresnel2	Calculates reflection coefficient for water to air
globalval	Determines global values
localval	Determines local values
optdepth	Selects Rayleigh and ozone optical thicknesses
params	Reads in user-defined parameters
phasefuncs	Calculates forward & backward Rayleigh phase functions
polarang	Calculates the six polar angles
rayleigh	Calculates the Rayleigh radiance for each cell centre
scannerazim	Calculates the scanner azimuth angle for each cell centre
solarazim	Calculates the solar azimuth angle for each cell centre
solarirrad	Calculates the adjusted solar irradiances

solarzen	Calculates the solar zenith angle for each cell centre
times	Calculates the local time for each cell centre
transmit	Calculates diffuse and direct (beam) transmittances

4.10 CONSIDERATIONS FOR ATMOSPHERIC CORRECTION WITH DIFFERENT SENSORS

The technique presented here for atmospheric correction may be modified for use with other sensors provided that a suitable channel exists for the estimation of aerosol radiance (one in which the water-leaving radiance is zero) and the only significant atmospheric constituents are aerosols, ozone and permanent gases. Naturally, the sensor must possess sufficient radiometric sensitivity and resolution to estimate the water-leaving radiance accurately. Other instruments may not have the CZCS tilt facility, in which case the zenith angle of the pixel-to-sensor direction simply equals the view angle.

Two orbital parameters warrant consideration: the altitude and the trackline inclination at the equator. The former determines the ground velocity of the sub-satellite point.

Certain sensor characteristics also require examination, namely the instantaneous field-of-view, which determines the ground resolution and the spectral characteristics as specified by the bandwidth and central wavelength of each channel. In addition, the values of mean solar irradiance and Rayleigh and ozone optical thickness must be appropriate to the spectral characteristics of each channel. This is achieved by weighting the values by the channel's spectral response.

4.11 LIST OF SYMBOLS

a	Latitude subtended by 64 pixels (half cell)
α	Orbital inclination; function of latitude
b	Longitude subtended by 64 pixels (half cell)
C_1	Difference between picture-time and time at which image is viewed
C_2	Difference between GMT and local time
d_1	Distance between receiving station and pixel (along a meridian)
d_2	Distance between pixel and sub-satellite point (along a meridian)
D	Day-number (1-365)
δ	Solar declination angle
Δ	Azimuth angle between scanline and North
e	Eccentricity of the Earth's orbit; 0.0167
E_o	Seasonally adjusted solar irradiance
$\overline{E}_o$	Mean solar irradiance
ϵ	$\tau_A^\lambda / \tau_A^{\lambda_o}$
F	Probability that a photon is scattered forwards
FOV	Field of view
γ	Index which characterises the aerosol size distribution
h	CZCS altitude; 955km
i	Angle of incidence
IFOV	Instantaneous field of view of the sensor; 6.98×10^{-4} radians
j,k	Row and column respectively; selects one of the 24 cells

L_A	Radiance due to aerosol scattering
L_P	Path radiance
L_R	Radiance due to Rayleigh scattering
L_T	Total radiance at the sensor
L_W	Water-leaving radiance
λ	Wavelength
λ_o	670 nm, CZCS channel 4
m	Ångström exponent
μ	$\cos\theta$
μ_o	$\cos\theta_o$
n	Refractive index of sea-water; 1.341
N	Number (of particles)
ω	$2\pi/24$
ω_A, ω_R	Single scattering albedo for aerosol and Rayleigh scattering respectively. Equals the probability of a photon being scattered. $\omega_R = 1$.
$P_A(\psi_+)$	Phase function for aerosol forward scattering
$P_A(\psi_-)$	Phase function for aerosol backward scattering
$P_R(\psi_+)$	Phase function for Rayleigh forward scattering
$P_R(\psi_-)$	Phase function for Rayleigh backward scattering
ϕ	Azimuth angle of pixel-to-sensor direction
ϕ_o	Azimuth angle of Sun-to-pixel direction
ϕ', ϕ''	Used in the determination of ϕ
ψ_+	Forward scattering angle
ψ_-	Backward scattering angle
r	Angle of refraction. Also used for particle radius
R	Mean Earth radius, 6371 km
ρ	Fresnel reflectance
s	Ground distance between sub-satellite point and

	current scan-line
t	Local time
t_D	Diffuse transmittance
T	Direct or beam transmittance
T_{O_3}	Direct or beam transmittance due to ozone
τ_A	Optical thickness due to aerosols
τ_{O_3}	Optical thickness due to ozone
τ_R	Optical thickness due to Rayleigh materials
θ	Zenith angle of the pixel-to-sensor direction. Also known as polar angle
θ_o	Zenith angle of the Sun-to-pixel direction
θ_1	Latitude of the centre of a 128 by 128 pixel cell
θ_2	Longitude of the centre of a 128 by 128 pixel cell
θ_t	Scan mirror tilt angle
θ_v	View angle; function of pixel number only
Θ_1	Latitude for the centre of a 768 by 512 pixel image
Θ_2	Longitude for the centre of a 768 by 512 pixel image
V_g	Sub-satellite velocity at the ground; 6.319 $km.s^{-1}$

CHAPTER 5

RESULTS AND CONCLUSIONS

5.1 PREAMBLE

The purpose of this chapter is to present data and compare water-leaving radiances derived from CZCS data (suitably processed for radiometric conversion and atmospheric correction) with datasets derived from in-situ ship measurements in order to establish and test chlorophyll retrieval algorithms. The CZCS data is used in the form of water-leaving radiance ratios (channel 3 to channel 1 or channel 3 to channel 2). The surface data are either CPR measurements or fluorometric determinations of chlorophyll (plus phaeophytin) concentration. CPR data only provides a relative measure of phytoplankton levels unlike fluorometric data which gives absolute values of chlorophyll concentration. Morel and Gordon (1980) identified three types of algorithm for relating spectral values of water-leaving radiance to pigment concentration: empirical, semi-analytical and analytical. The empirical method is used here as the other two require knowledge of the specific optical properties (a^* and b^*_b) for each constituent. Not only is this data unavailable, but it is commonly acknowledged that there is great difficulty in establishing optical coefficients which are truly representative of each constituent (Morel 1980). Furthermore, in the case of algal cells, the specific absorption coefficient is a function of cell size and intracellular pigment concentration (Morel and Bricaud 1981); this implies that the coefficient will depend upon which phytoplankton species are present and their relative populations.

Also presented is an alternative and unusual application of ISOCLS clustering (unsupervised classification), refer to section 3.3.2.2. This method does not constitute a statistical comparison between surface and remote data, as with orthodox ratios or differences of water-leaving radiance. Instead, a partitioning of pixels in multispectral space is performed such that each pixel may be assigned to one of ten or so sub-classes. Each sub-class corresponds to an arbitrary range of chlorophyll concentration and these sub-classes are ordered to produce a relative and discrete index of chlorophyll concentration. The effects of variations in Ångström exponent are also examined.

Raw CZCS data, for all six channels, covering North-West Europe, was obtained for four dates: 22/6/1981, 29/7/1981, 17/6/1984 and 3/7/1984. Sea truth was available in the form of CPR data collected from a ship-of-opportunity on one occasion: 23/6/1981 (Plymouth-Roscoff). In addition, fluorometric data were obtained for 30/6/1981, 21/7/1981 and 19/6/1984 (all UOR) and for the period from 22/7/1981 to 2/8/1981 (Holligan et al. 1983).

5.1.1 Overall methodology

The overall methodology for analysis and comparison of CZCS data with sea truth (chlorophyll concentration) is outlined in Fig. 5.1. Names surrounded by quotation marks denote programs that have been developed specially for the purpose. The sampling positions of data collected from ships-of-opportunity (on routes such as Plymouth to Roscoff) are not usually specified by latitude and longitude, but instead by times elapsed from the ship's departure. These times are converted to latitude and longitude by the 'locate' program (see section 3.3.2.1)

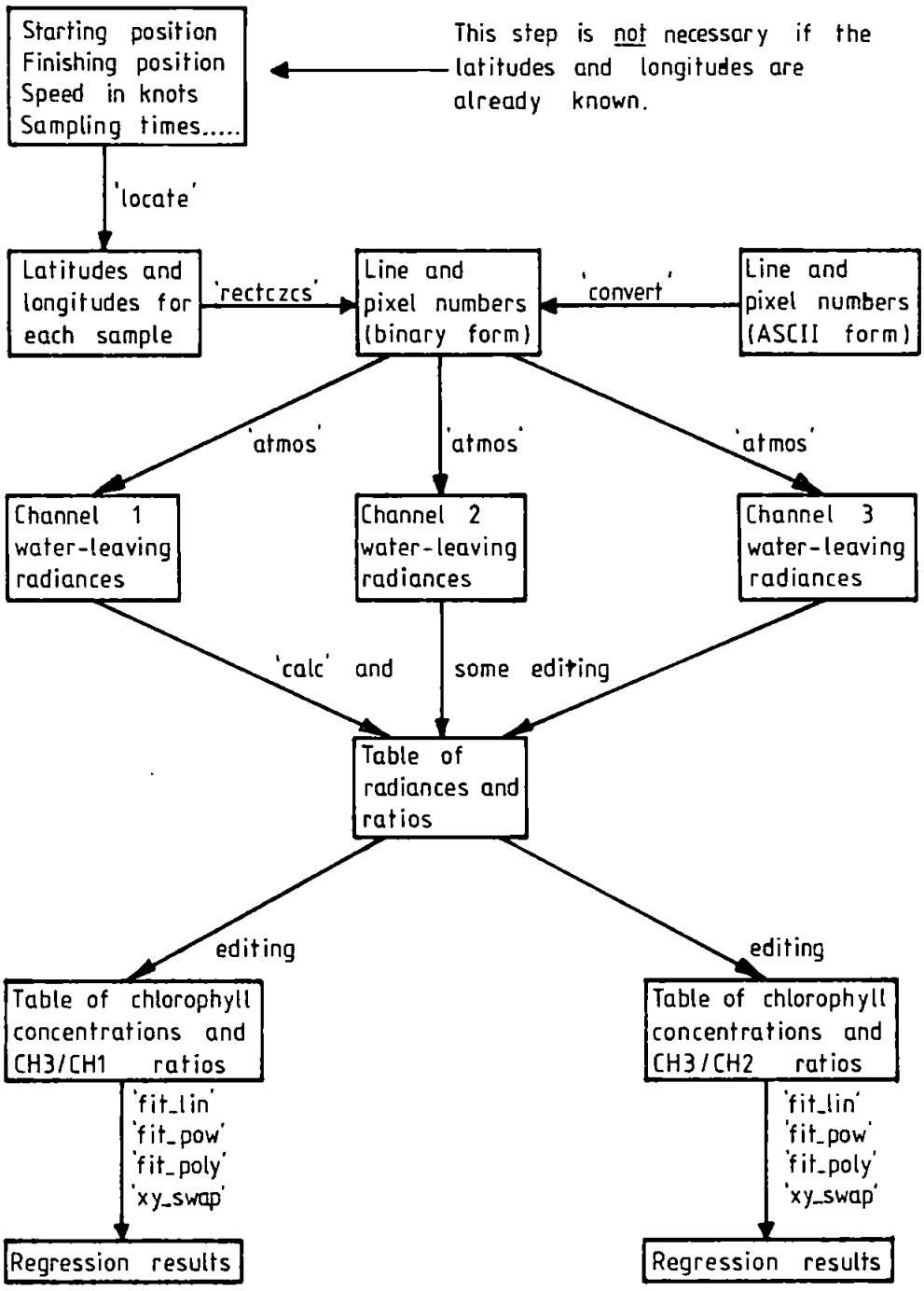

Figure 5.1 Overall methodology.

and then into line-pixel coordinates by 'rectczcs' (see section 3.3.1.3), see Table 5.1. Each file of CZCS data for a single spectral channel contains 768 x 512 bytes (being the size of the imagestore) and the line-pixel coordinates select a single byte in the file corresponding to the sample. Once these coordinates have been found they may be stored in American Standard Code for Information Interchange (ASCII) form for later use, thus eliminating unnecessary repetition of the 'locate' and 'rectczcs' stages. With these coordinates and three appropriate CZCS files of raw data (one per spectral channel) as inputs, 'atmos' performs radiometric conversion and atmospheric correction (see Chapter 4), producing a table of water-leaving radiances. Tables 5.2 - 5.4 show some typical results produced by the atmospheric correction program. The first two columns are the line and pixel numbers and the next two columns show the raw digital numbers for the channel to be corrected (1-3) and channel 4. The final two columns are the total uncorrected radiance (L_t) and the water-leaving radiance (L_w). Negative radiance pixels are forced to zero. It can be seen that the uncorrected radiances lie between about 4 and 8 mW/(cm^2.μm.sr) whereas the water-leaving radiances are all less than 0.5 mW/(cm^2.μm.sr), i.e. the latter are typically 10% or less of the total radiance at the sensor.

In fact atmospheric correction also requires the specification of certain parameters, which are different for each image and channel; these are also stored in files in ASCII form for convenience. The parameters used for atmospheric correction are listed in Table 5.5 and those for radiometric conversion (section 3.3.1.1) are given in Table 5.6. The water-leaving radiances for channels 1 to 3 are combined to produce a table (Table 5.7) of atmospherically corrected water-leaving

TABLE 5.1 LIST OF LATITUDES AND LONGITUDES FOR UOR SAMPLES TAKEN ON 21/7/81 AND CORRESPONDING LINE-PIXEL COORDINATES FOR CZCS IMAGERY OF 29/7/81.

TIME MINUTES	LATITUDE	LONGITUDE	LINE NUMBER	PIXEL NUMBER
0	50.25	-4.13	210	347
11	50.21	-4.13	214	346
20	50.18	-4.13	219	345
30	50.15	-4.12	223	343
39	50.12	-4.12	227	343
48	50.09	-4.12	231	341
57	50.06	-4.11	235	340
66	50.03	-4.11	238	339
75	50.00	-4.11	242	339
84	49.97	-4.10	247	337
93	49.94	-4.10	251	336
102	49.91	-4.10	254	335
111	49.88	-4.09	258	333
120	49.85	-4.09	263	333
129	49.82	-4.09	266	332
138	49.79	-4.08	270	330
147	49.76	-4.08	274	329
156	49.73	-4.08	277	329
165	49.70	-4.07	282	328
174	49.67	-4.07	286	326
183	49.64	-4.07	289	325
192	49.61	-4.06	292	325
202	49.57	-4.06	297	323
211	49.54	-4.06	301	322
220	49.51	-4.05	305	320
229	49.48	-4.05	309	320
238	49.45	-4.05	313	319
247	49.42	-4.04	316	318
256	49.39	-4.04	321	316
264	49.36	-4.04	324	315
273	49.33	-4.04	327	315
283	49.30	-4.03	332	313

The column headed 'TIME' lists the time in minutes since the ship's departure.

All latitudes are North of the Equator and the negative longitude values denote longitudes West of Greenwich.

TABLE 5.2 TOTAL (L_t) AND WATER-LEAVING (L_w) RADIANCES FOR CHANNEL 1. CZCS DATA: 29/7/1981. COMPARABLE UOR SEA TRUTH: 21/7/1981. ANGSTRÖM EXPONENT = 0.5 .

LINE NUMBER	PIXEL NUMBER	DN(443)	DN(670)	L_t(443)	L_w(443)
210	347	137	196	7.802	0.074
214	346	136	189	7.745	0.151
219	345	135	188	7.689	0.106
223	343	134	184	7.632	0.123
227	343	133	180	7.576	0.139
231	341	134	178	7.632	0.244
235	340	133	176	7.576	0.220
238	339	133	176	7.576	0.220
242	339	134	180	7.632	0.204
247	337	134	181	7.632	0.184
251	336	131	179	7.462	0.030
254	335	131	178	7.462	0.050
258	333	131	178	7.462	0.030
263	333	132	180	7.519	0.054
266	332	132	182	7.519	0.014
270	330	132	184	7.519	-0.027
274	329	134	182	7.632	0.143
277	329	135	183	7.689	0.188
282	328	137	191	7.802	0.155
286	326	135	187	7.689	0.107
289	325	134	184	7.632	0.103
292	325	134	186	7.632	0.062
297	323	135	181	7.689	0.228
301	322	138	187	7.858	0.301
305	320	138	190	7.858	0.240
309	320	143	198	8.141	0.402
313	319	152	235	8.651	0.235
316	318	149	227	8.481	0.203
321	316	139	187	7.915	0.366
324	315	137	182	7.802	0.338
327	315	138	186	7.858	0.321
332	313	138	184	7.858	0.362

DN is the raw digital number.
The units of radiance are mW/(cm^2.μm.sr).

TABLE 5.3 TOTAL (L_t) AND WATER-LEAVING (L_w) RADIANCES FOR CHANNEL 2. CZCS DATA: 29/7/1981. COMPARABLE UOR SEA TRUTH: 21/7/1981. ANGSTRÖM EXPONENT = 0.5 .

LINE NUMBER	PIXEL NUMBER	DN(520)	DN(670)	L_t(520)	L_w(520)
210	347	153	196	5.073	0.325
214	346	151	189	5.008	0.373
219	345	149	188	4.942	0.320
223	343	147	184	4.877	0.317
227	343	146	180	4.844	0.350
231	341	146	178	4.844	0.383
235	340	145	176	4.811	0.382
238	339	144	176	4.779	0.347
242	339	146	180	4.844	0.350
247	337	145	181	4.811	0.298
251	336	144	179	4.779	0.296
254	335	143	178	4.729	0.278
258	333	143	178	4.729	0.270
263	333	144	180	4.779	0.271
266	332	144	182	4.779	0.238
270	330	144	184	4.779	0.204
274	329	146	182	4.844	0.308
277	329	146	183	4.844	0.291
282	328	150	191	4.975	0.296
286	326	148	187	4.910	0.294
289	325	145	184	4.811	0.239
292	325	146	186	4.844	0.240
297	323	147	181	4.877	0.360
301	322	150	187	4.975	0.364
305	320	151	190	5.008	0.348
309	320	159	198	5.270	0.494
313	319	173	235	5.728	0.361
316	318	169	227	5.597	0.356
321	316	150	187	4.975	0.364
324	315	149	182	4.942	0.413
327	315	148	186	4.910	0.311
332	313	147	184	4.877	0.309

DN is the raw digital number.
The units of radiance are mW/(cm^2.µm.sr).

TABLE 5.4 TOTAL (L_t) AND WATER-LEAVING (L_w) RADIANCES FOR CHANNEL 3. CZCS DATA: 29/7/1981. COMPARABLE UOR SEA TRUTH: 21/7/1981. ANGSTRÖM EXPONENT = 0.5 .

LINE NUMBER	PIXEL NUMBER	DN(550)	DN(670)	L_t(550)	L_w(550)
210	347	170	196	4.217	0.247
214	346	164	189	4.071	0.202
219	345	161	188	3.998	0.141
223	343	161	184	3.998	0.203
227	343	159	180	3.949	0.215
231	341	158	178	3.925	0.220
235	340	157	176	3.900	0.226
238	339	156	176	3.876	0.200
242	339	158	180	3.925	0.189
247	337	158	181	3.925	0.173
251	336	159	179	3.949	0.230
254	335	158	178	3.925	0.220
258	333	156	178	3.876	0.163
263	333	160	180	3.973	0.235
266	332	160	182	3.973	0.203
270	330	161	184	3.998	0.198
274	329	161	182	3.998	0.229
277	329	163	183	4.046	0.265
282	328	168	191	4.168	0.268
286	326	165	187	4.095	0.254
289	325	162	184	4.022	0.224
292	325	163	186	4.046	0.218
297	323	163	181	4.046	0.296
301	322	166	187	4.119	0.280
305	320	167	190	4.144	0.258
309	320	172	198	4.265	0.262
313	319	193	235	4.776	0.223
316	318	188	227	4.655	0.219
321	316	166	187	4.119	0.280
324	315	164	182	4.071	0.307
327	315	165	186	4.095	0.270
332	313	163	184	4.046	0.249

DN is the raw digital number.
The units of radiance are mW/(cm^2.μm.sr).

TABLE 5.5 ATMOSPHERIC CORRECTION PARAMETERS

Date	22/6/1981	29/7/1981	17/6/1984	3/7/1984
Picture time (GMT)	11.20	10.50	10.41	12.06
Latitude for centre of image	50° 20'	50° 0'	50° 25'	49° 33'
Longitude for centre of image	5° 30' W	3° 20' W	0° 2' W	8° 19' W
Tilt angle	+20°	+18°	+20°	+20°
Initial minor-frame number	5	1	2	9
Ångström exponent	0.5	0.5*	0.5	0.5
Refractive index	1.341	1.341	1.341	1.341

* Values of 0.3, 0.7 and 1.0 also used.

TABLE 5.6 RADIOMETRIC FACTORS AND ORBIT NUMBERS

1) 22/6/1981 Orbit Number = 13437 (N56/07)

Channel	1	2	3
Slope	0.05658	0.03272	0.02434
Intercept	0.05036	0.06707	0.07885

2) 29/7/1981. Orbit Number = 13948 (N60/06)

Same radiometric factors as in (1) above.

3) 17/6/1984 Orbit Number = 28517 (N129/03)

Channel	1	2	3
Slope	0.05985	0.03600	0.02541
Intercept	0.05327	0.07381	0.08232

4) 3/7/1984 Orbit Number = 28739 (N129/04)

Channel	1	2	3
Slope	0.05978	0.03606	0.02542
Intercept	0.05321	0.07392	0.08237

In all cases the slope and intercept values are both 0.01136 for Channel 4.

The slopes decrease with increasing channel number since L_λ is smaller at the red end of the spectrum (i.e. L_λ decreases with increasing λ).

TABLE 5.7 WATER-LEAVING RADIANCES (CHANNELS 1-3) & RATIOS FOR 29/7/1981; UOR CHLOROPHYLL CONCENTRATIONS FOR 21/7/1981.
ANGSTRÖM EXPONENT = 0.5 .

CHANNEL 1	CHANNEL 2	CHANNEL 3	RATIO 3/1	RATIO 3/2	CHLOROPHYLL CONCENTRATION
0.074	0.325	0.247	3.355	0.760	16.4
0.151	0.373	0.202	1.341	0.542	22.6
0.106	0.320	0.141	1.323	0.440	35.3
0.123	0.317	0.203	1.658	0.641	58.5
0.139	0.350	0.215	1.543	0.614	----
0.244	0.383	0.220	0.901	0.574	42.2
0.220	0.382	0.226	1.026	0.591	52.9
0.220	0.347	0.200	0.909	0.577	65.1
0.204	0.350	0.189	0.926	0.540	91.4
0.184	0.298	0.173	0.944	0.582	86.7
0.030	0.296	0.230	7.731	0.777	86.7
0.050	0.278	0.220	4.397	0.792	96.0
0.030	0.270	0.163	5.404	0.604	47.6
0.054	0.271	0.235	4.318	0.865	63.7
0.014	0.238	0.203	14.640	0.856	80.3
-0.027	0.204	0.198	-7.444	0.971	47.8
0.143	0.308	0.229	1.599	0.744	121.9
0.188	0.291	0.265	1.411	0.911	----
0.155	0.296	0.268	1.729	0.906	128.0
0.107	0.294	0.254	2.377	0.864	----
0.103	0.239	0.224	2.174	0.936	64.2
0.062	0.240	0.218	3.501	0.907	96.8
0.228	0.360	0.296	1.297	0.823	81.9
0.301	0.364	0.280	0.929	0.768	----
0.240	0.348	0.258	1.075	0.741	62.4
0.402	0.494	0.262	0.651	0.529	80.8
0.235	0.361	0.223	0.948	0.617	51.2
0.203	0.356	0.219	1.082	0.617	61.9
0.366	0.364	0.280	0.764	0.768	79.8
0.338	0.413	0.307	0.908	0.741	83.3
0.321	0.311	0.270	0.838	0.868	69.8
0.362	0.309	0.249	0.689	0.807	----

---- denotes bad data.

The units of water-leaving radiance are mW/(cm^2.μm.sr).

radiances and ratios (channel 3 to channel 1 and channel 3 to channel 2). Some workers have used radiance differences (e.g. Tassan 1981, Viollier et al. 1978), but there are sound theoretical grounds (see section 2.1.4) for preferring the radiance ratio and this is now the form most often used. The ratios are combined with the corresponding surface measurements of chlorophyll concentration. These combination operations are easily accomplished under the UNIX operating system which provides useful utilities known as 'cat' and 'paste'. The tables of chlorophyll concentrations and radiance ratios are submitted to 'fit-lin', 'fit-pow' and 'fit-poly' for linear, power and polynomial (third degree) regression respectively (Tables 5.8 and 5.9). The independent and dependent variables may be swapped by using 'xy-swap' to reverse the regression.

5.1.2 Statistical analysis

Three empirical regression functions were used to establish the relationship between chlorophyll concentration, including phaeopigments, and the ratio of water-leaving radiances at 550 nm to 443 nm or 550 nm to 520 nm. The three regression functions are linear, power and polynomial (third degree):

$$Y = AX + B$$

$$Y = AX^{B}$$

$$Y = A + BX + CX^{2} + DX^{3}$$

Linear regression is performed through the method of simple least squares (Alder & Roessler 1977, Daniel & Wood 1971) and regression with

TABLE 5.8 REGRESSION RESULTS FOR UOR (21/7/1981) AND CZCS (29/7/1981), USING RATIO OF CHANNEL 3 TO CHANNEL 1. ANGSTRÖM EXPONENT = 0.5 .

CHLOROPHYLL CONCENTRATION	RATIO 3/1	CHLOROPHYLL CONCENTRATION	RATIO 3/1
16.4	3.355	80.3	14.640
22.6	1.341	121.9	1.599
35.3	1.323	128.0	1.729
58.5	1.658	64.2	2.174
42.2	0.901	96.8	3.501
52.9	1.026	81.9	1.297
65.1	0.909	62.4	1.075
91.4	0.926	80.8	0.651
86.7	0.944	51.2	0.948
86.7	7.731	61.9	1.082
96.0	4.397	79.8	0.764
47.6	5.404	83.3	0.908
63.7	4.318	69.8	0.838

UOR integrated chlorophyll concentration (in mg/m^2) is the independent variable; CZCS Channel 3 to Channel 1 is the dependent variable.
26 data pairs.

1) LINEAR: $Y = AX + B$

Slope A = 0.0101
Intercept B = 1.8059
Correlation coefficient (r) = 0.089

2) POWER: $Y = AX^B$

Multiplier A = 1.5163
Power B = 0.0273
Correlation coefficient (r) = 0.016

3) POLYNOMIAL: $Y = A + BX + CX^2 + DX^3$

Coefficient A = 5.9325
Coefficient B = -0.2565
Coefficient C = 0.0045
Coefficient D = -0.000021
Correlation coefficient (r) = 0.243

TABLE 5.9 REGRESSION RESULTS FOR UOR (21/7/1981) AND CZCS (29/7/1981), USING RATIO OF CHANNEL 3 TO CHANNEL 2. ANGSTRÖM EXPONENT = 0.5 .

CHLOROPHYLL CONCENTRATION	RATIO 3/2	CHLOROPHYLL CONCENTRATION	RATIO 3/2
16.4	0.760	80.3	0.856
22.6	0.542	47.8	0.971
35.3	0.440	121.9	0.744
58.5	0.641	128.0	0.906
42.2	0.574	64.2	0.936
52.9	0.591	96.8	0.907
65.1	0.577	81.9	0.823
91.4	0.540	62.4	0.741
86.7	0.582	80.8	0.529
86.7	0.777	51.2	0.617
96.0	0.792	61.9	0.617
47.6	0.604	79.8	0.768
63.7	0.865	83.3	0.741
		69.8	0.868

UOR integrated chlorophyll concentration (in mg/m²) is the independent variable; CZCS Channel 3 to Channel 2 is the dependent variable.
27 data pairs.

1) LINEAR: $Y = AX + B$

Slope A = 0.0020
Intercept B = 0.5768
Correlation coefficient (r) = 0.359

2) POWER: $Y = AX^B$

Multiplier A = 0.3683
Power B = 0.1548
Correlation coefficient (r) = 0.339

3) POLYNOMIAL: $Y = A + BX + CX^2 + DX^3$

Coefficient A = 0.6023
Coefficient B = 0.00066
Coefficient C = 0.000019
Coefficient D = 0.0000
Correlation coefficient (r) = 0.359

the power function operates by first taking logarithms of the independent (X) and dependent (Y) variables and then using the least squares method. Polynomial regression uses an extended form of the least squares method involving Gaussian Elimination (see section 3.3.1.3 and Appendix 4). Regression analysis produces values for A, B, C and D and the correlation coefficient r is also calculated. Finally, the significance level of the correlation coefficient was evaluated using the Student's t distribution (Edwards 1976, Kennedy and Neville 1986).

5.1.3 Calculation of chlorophyll 'a' and phaeophytin concentrations from fluorescence measurements

Since the CZCS cannot distinguish between chlorophyll and phaeopigments, joint chlorophyll plus phaeopigment data must be included in the sea truth measurements. The established fluorometric technique for chlorophyll determination responds to both of these pigments, but quantitative interpretation of the fluorescence data is not valid when both pigments are present because the chlorophyll to phaeopigment ratio is unknown. However, treatment of samples with weak or dilute acid converts chlorophyll 'a' to phaeophytin (Lorenzen 1967) and by recording fluorescence readings both before and after acidification, it becomes possible to make independent determinations of chlorophyll 'a' and phaeophytin, and hence the combined pigment concentration.

The following relations for chlorophyll 'a' and phaeophytin concentrations were provided by Holligan (personal communication), but are based on the work of Lorenzen (1966, 1967):

$$\text{chlorophyll 'a' } (mg.m^{-3}) = (F_b - F_a).\frac{V_e}{V_f}.K \quad (5.1)$$

$$\text{phaeophytin } (mg.m^{-3}) = (2F_a - F_b).\frac{V_e}{V_f}.K \times 0.975 \quad (5.2)$$

where F_b and F_a are the fluorescences before and after acidification respectively, and V_e and V_f are the volumes extracted and filtered respectively. K is the calibration constant, which was 0.112 for Holligan's data collected in July/August 1981. The 0.975 factor accounts for the different molecular weights of chlorophyll 'a' and phaeophytin.

The ratio of F_b to F_a indicates the proportion of phaeophytin in the sample, being 2.0 for pure chlorophyll 'a' and decreasing as the proportion of phaeophytin increases. From now on, the term chlorophyll is taken to include phaeophytin.

5.1.4 Integration of chlorophyll concentration over one optical depth

For comparison with CZCS data, in-situ measurements of chlorophyll need to be integrated over one optical depth or penetration depth z_{90}, which is simply $1/K_d$ where K_d is the attenuation coefficient for downwelling irradiance (section 2.1.4). K_d is found from (Aiken, personal communication):

$$K_d = 0.12 + 0.015\ \bar{C} \quad (5.3)$$

where $\bar{C}$ is the mean concentration of chlorophyll 'a' and phaeophytin in

$mg.m^{-3}$. The 0.12 term accounts for attenuation by pure water while the 0.015 term is the attenuation corresponding to unit concentration of chlorophyll 'a' and phaeophytin. This empirical relation for K_d is very much a compromise as K_d varies significantly with wavelength and retrieval algorithms use radiances at 550 and either 520 or 443 nm. The penetration depth z_{90} is therefore:

$$z_{90} = 1/(0.12 + 0.015\ \bar{C}) \tag{5.4}$$

As expected, z_{90} decreases with increasing $\bar{C}$. The integrated value of chlorophyll concentration (including phaeophytin) from z=0 to $z=z_{90}$ is simply:

$$z_{90}.\bar{C}$$

$$= \bar{C}/(0.12 + 0.015\ \bar{C})$$

$$= 1/(0.015 + 0.12/\bar{C}) \tag{5.5}$$

The value of $\bar{C}$ is obtained by taking the mean of all measurements which apply down to depths of 10 metres. The integrated chorophyll concentration is in $mg.m^{-2}$, i.e. per unit area rather than unit volume. The maximum value of integrated chlorophyll, as given by Eq. 5.5, is 1/0.015 or 67 $mg.m^{-2}$ irrespective of C's value. The integration of chlorophyll concentration over one optical depth represents an unusual approach which ensures that the in-situ measurement of chlorophyll is appropriate for comparison with remotely-assessed values.

5.2 REGRESSION ANALYSIS

5.2.1 CPR - CZCS (June 1981)

CPR data for 23/6/1981 was collected from a ship-of-opportunity crossing the English Channel from Plymouth to Roscoff (101PR), providing counts of diatoms (= phytoplankton) and zooplankton for eight stations (evenly spaced, 11 or 12 nautical miles apart). The diatom count only provides a relative measure of chlorophyll concentration, but it was believed that the region contained low concentrations at this time. The nearest, clear CZCS pass was at 11.20 GMT on 22/6/1981, orbit number 13437 (N56/07). The CZCS imagery was corrected assuming an Ångström exponent of 0.5. Figure 5.2 shows the variation in surface and remote measurements across the channel. Although the CZCS has 8-bit resolution, the ratio of CZCS water-leaving radiances appears noisy because the effective resolution after removal of the dominant atmospheric components is too coarse (Gordon et al. 1980a). The diatom peak appears just beyond mid-channel (nearer the French coast) and this is confirmed by the position of the phytoplankton bloom in the CZCS imagery (Plate 5.1). A distinct peak appears in the ratio of water-leaving radiances at 550 nm (channel 3) and 443 nm (channel 1), although it is displaced from the diatom peak. Correlation results for the three types of regression are presented in Table 5.10, but should be regarded with some caution as there are only five non-zero diatom values. However, in each case the correlation coefficient for channel 3 : channel 1 is higher than for channel 3 : channel 2, which is consistent with the premise of a low chlorophyll concentration region. Only one of the correlation coefficients is significant at the 5% level. The linear relationship between CPR count and CZCS ratio is:

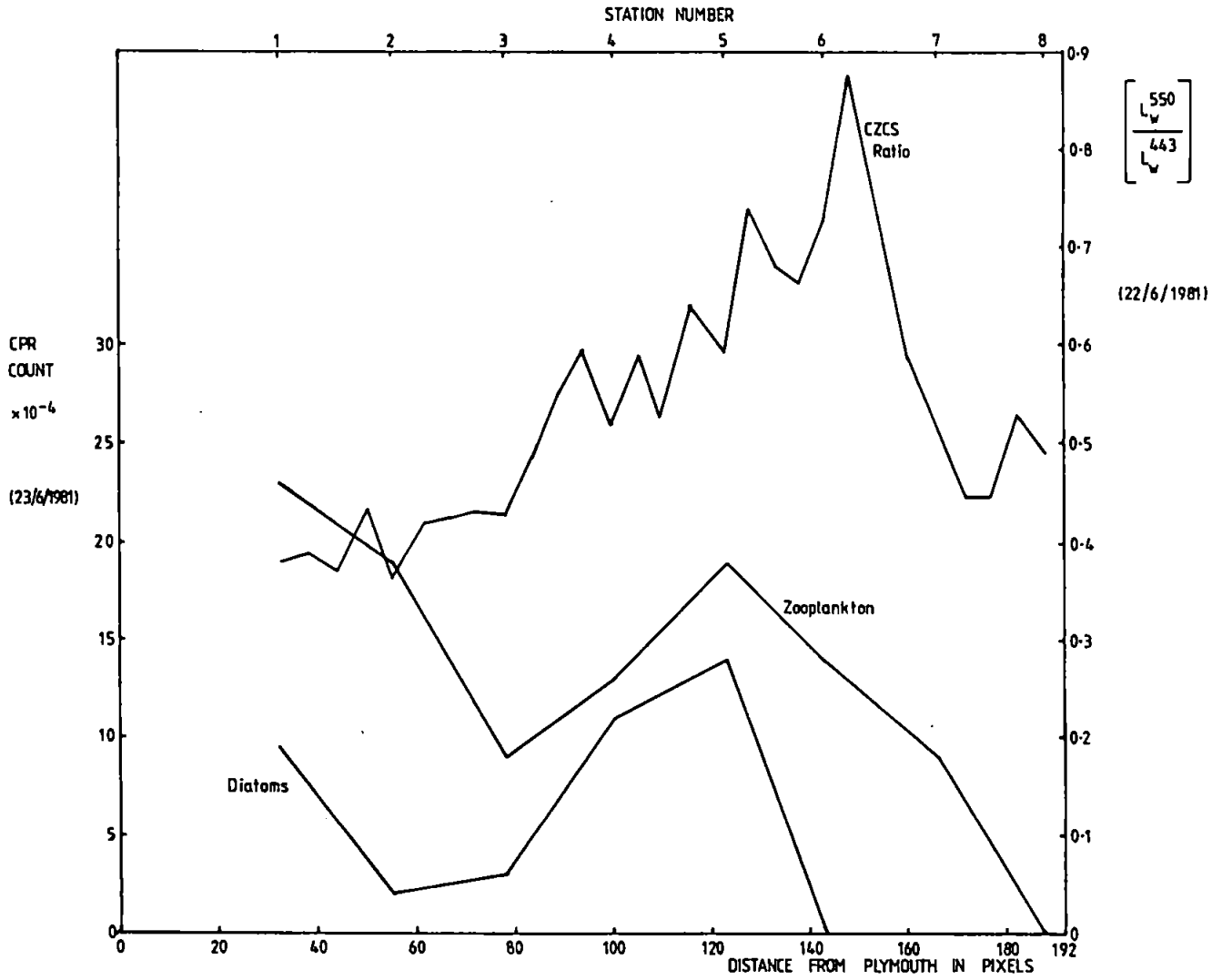

Figure 5.2 Variation of CPR count and CZCS ratio across the English Channel for June 1981.

Plate 5.1 Pseudo-colour image for 22/6/1981 using the channel 3 to channel 1 ratio. High concentrations of chlorophyll are denoted by red and low concentrations by magenta.

Plate 5.2 Pseudo-colour image for 29/7/1981 using the channel 3 to channel 2 ratio. The chlorophyll concentration ranges are as follows:

Black	0-10 $mg.m^{-2}$
Magenta	10-15
Blue	15-20
Cyan	20-25
Green	25-30
Yellow	30-40
Red	40-80

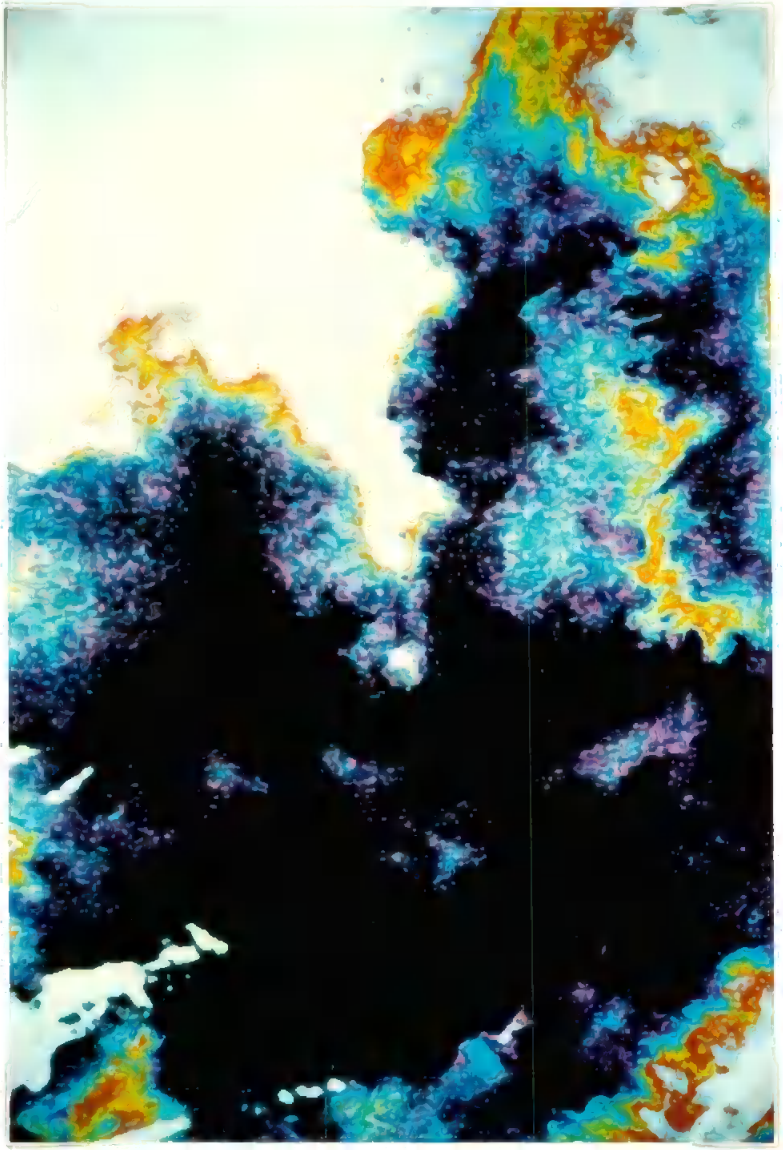

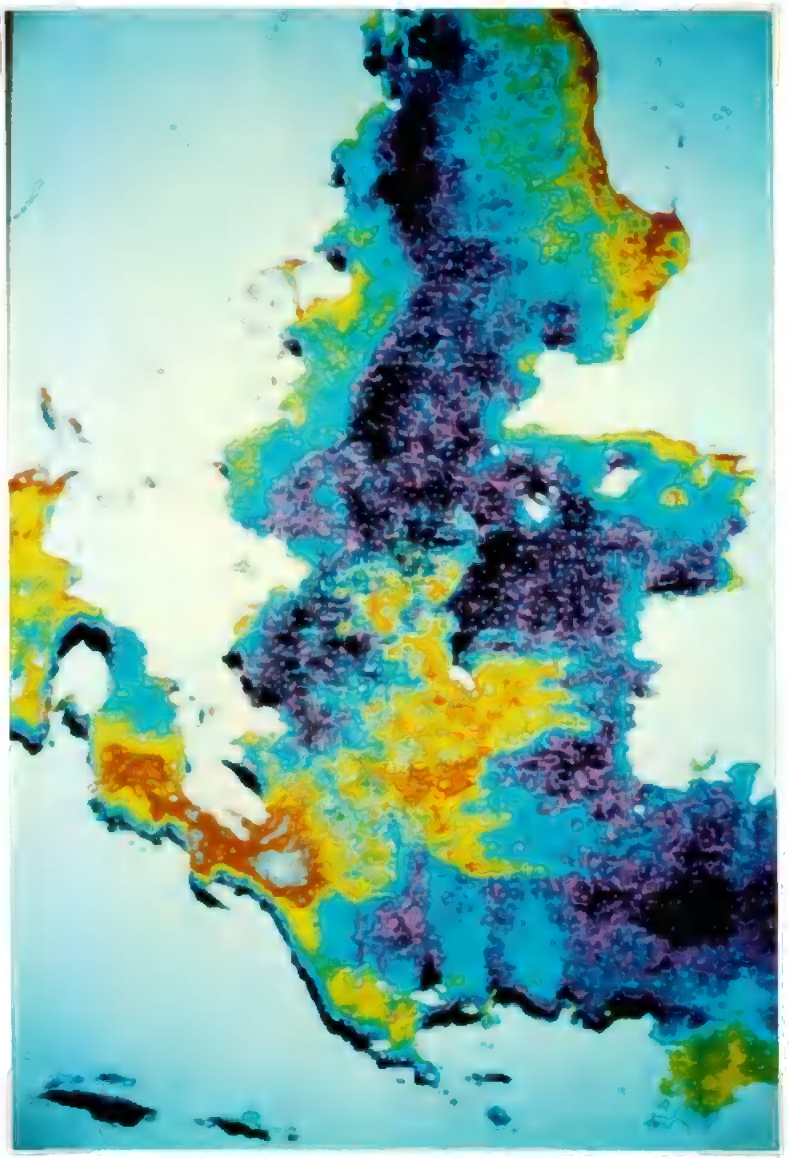

TABLE 5.10 CORRELATION COEFFICIENTS FOR CPR (23/6/81) AND CZCS (22/6/81)

X	Y	LINEAR	POWER	POLYNOMIAL
Diatom count	CZCS Ch3/Ch1	0.78	0.71	0.89*
Diatom count	CZCS Ch3/Ch2	0.43	0.41	0.61

* Significant at the 5% level. Number of samples = 5.
Imagery corrected assuming an Ångström exponent of 0.5 .

TABLE 5.11 CORRELATION COEFFICIENTS FOR UOR (30/6/1981) AND CZCS (22/6/1981)

X	Y	LINEAR	POWER	POLYNOMIAL
Integrated chlorophyll	CZCS Ch3/Ch1	0.33	0.28	0.43
Integrated chlorophyll	CZCS Ch3/Ch2	0.34	0.34	0.37

Number of samples = 37. Chlorophyll (+ phaeophytin) integrated over 10 metres. Imagery corrected assuming an Ångström exponent of 0.5 .

TABLE 5.12 CORRELATION COEFFICIENTS FOR UOR (21/7/1981) AND CZCS (29/7/1981)

X	Y	LINEAR	POWER	POLYNOMIAL	NUMBER OF SAMPLES
Integrated chlorophyll	CZCS Ch3/Ch1	0.09	0.02	0.24	26
Integrated chlorophyll	CZCS Ch3/Ch2	0.36	0.34	0.36	27

Chlorophyll (+ phaeophytin) integrated over 10 metres. Imagery corrected assuming an Ångström exponent of 0.5 .

$$\text{CPR count} = 0.00413 \left[\frac{L_w(550)}{L_w(443)}\right] - 0.00109 \qquad (5.6)$$

It is difficult to establish a meaningful relationship between CZCS and CPR data since the CPR only records the number of phytoplankton cells at one depth and not the chlorophyll concentration. However despite this and the small dataset in this case, these initial results still indicate that the CZCS is capable of assessing plankton patchiness bearing in mind that there is a one day discrepancy between the CZCS pass and the sea truth.

5.2.2 UOR - CZCS (June 1981)

UOR measurements of chlorophyll concentration for the 30/6/1981 were taken across the English Channel between 50° 10.5' N, 4° 16' W and 48° 48.4' N, 3° 59.5' W; this represents a distance of 83 nautical miles. The chlorophyll concentrations were integrated over 10 metres and ranged from 14 to 66 $mg.m^{-2}$, so this is a high chlorophyll region. This sea truth was compared with CZCS data gathered on 22/6/1981 at 11.20 GMT (orbit number 13437, N56/07). The time lapse between these two datasets is eight days and an Ångström exponent of 0.5 was used in the atmospheric correction. The variation in chlorophyll concentration and two CZCS spectral ratios across the Channel is shown in Fig. 5.3. The two spectral ratios display a similar variation which tracks the chlorophyll concentration in places, particularly the latter part of the route, i.e. for 'time since departure' of 200 to 320 minutes, assuming that some displacement has occurred. Table 5.11 shows the statistical results, with only one case failing to meet the 5% level of significance. Even so, this is not a

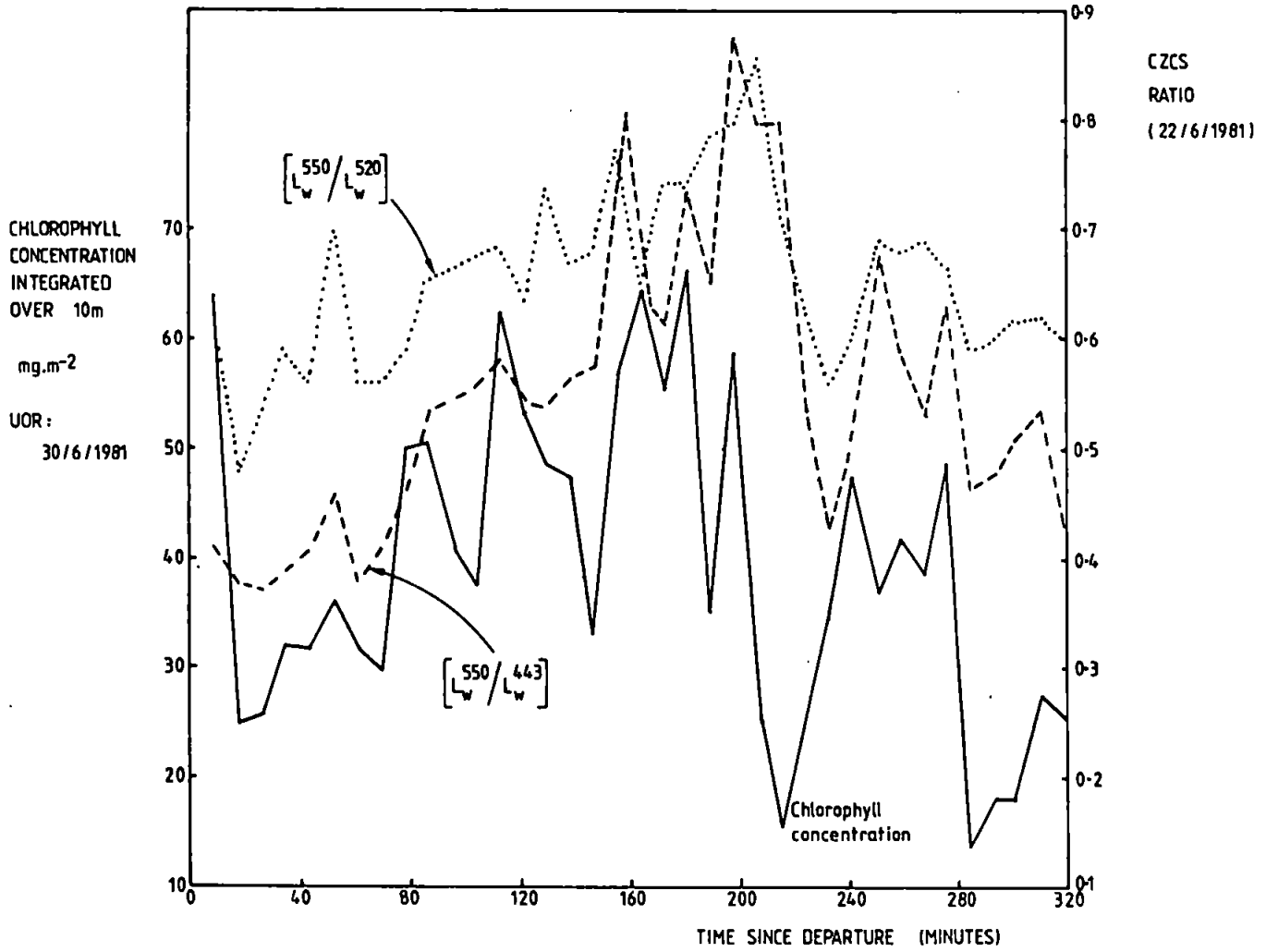

Figure 5.3 Variation of chlorophyll concentration (UOR) and CZCS ratio for June 1981.

reliable basis for developing empirical relationships between CZCS and surface measurements as the time difference is too large.

5.2.3 UOR - CZCS (July 1981)

UOR data, covering the English Channel on 21/7/1981, provided integrated (0 - 10 metres) chlorophyll concentration ($mg.m^{-2}$) along a 56 nautical mile track. Most of the samples had concentrations greater than 40 $mg.m^{-2}$ which signifies a high-chlorophyll concentration region. This sea truth was compared with CZCS data for 29/7/1981, 10.50 GMT (orbit number 13948, N60/06), which was atmospherically corrected taking the Ångström exponent as 0.5. There is an eight day discrepancy between these two datasets and inspection of Fig. 5.4 does not indicate any obvious association between the surface and remote measurements. In the case of the channel 3 to channel 1 ratio, one of the values is negative due to a small negative water-leaving radiance in channel 1. This value has not been included in the statistical analysis and suggests that the atmospheric correction program is slightly over-compensating for atmospheric effects. The regression results are shown in Table 5.12, none of which are significant at the 5% level.

5.2.4 Holligan's data - CZCS (July/August 1981)

The datasets presented so far are inadequate for the development of chlorophyll retrieval algorithms because the CPR does not measure chlorophyll concentration and the two other cases both entail large time discrepancies. However, the data presented in this section does not suffer from these difficulties and provides greater scope for examining the influence of various parameters, such as the Ångström exponent, under different circumstances. Furthermore, sea truth was

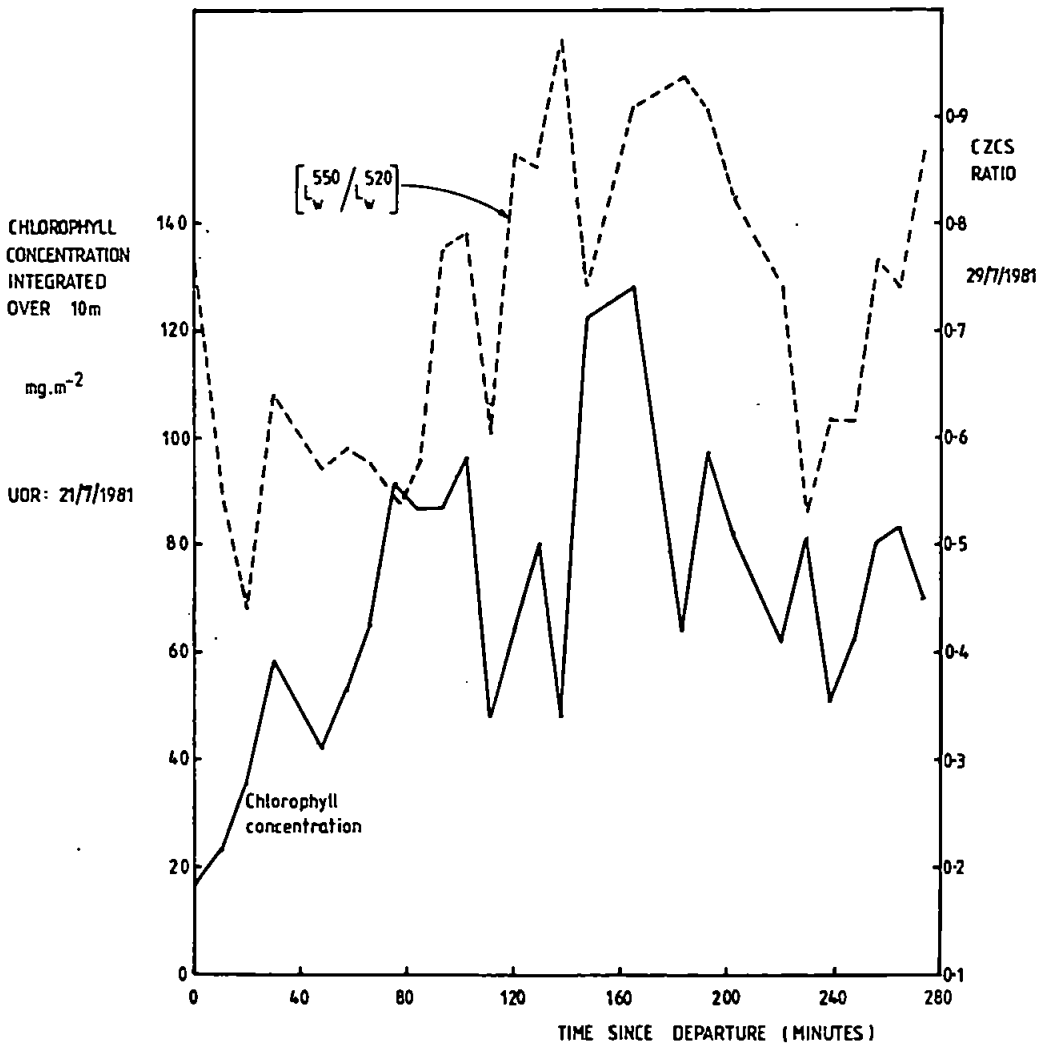

Figure 5.4 Comparison of chlorophyll concentration (UOR) and CZCS ratio for July 1981.

available on the very day of the CZCS pass as well as a number of days before and after. The in-situ data was collected in the English Channel over a 12 day period from 22/7/1981 to 2/8/1981 from Research Vessel 'Frederick Russell' (Holligan et al. 1983). Chlorophyll concentration was measured fluorometrically at various depths, with most of the 51 sampling positions located in three distinct regions - mixed, frontal and stratified waters; refer to Fig. 5.5 and Holligan et al. (1983). The frontal region was dominated by one species of dinoflagellate (Gyrodinium aureolum) with chlorophyll concentrations between 40 and 60 $mg.m^{-2}$. In the mixed area, the concentration was between 10 and 15 $mg.m^{-2}$ with diatoms as the dominant species. The stratified area was variable (1 to 30 $mg.m^{-2}$), but generally less than 10 $mg.m^{-2}$. A mixture of flagellates was present in this area. All these concentrations are integrated over one optical depth. The frontal and mixed areas are essentially extended homogeneous regions displaying little variation in chlorophyll concentration, whereas the stratified area contains sharp horizontal concentration gradients and is highly variable. The CZCS data chosen for comparison (with sea truth) was collected on 29/7/1981 at 10.50 GMT, orbit number 13948 (N60/06). Ångström exponents of 0.3, 0.5, 0.7 and 1.0 were used in the atmospheric correction in order to assess the influence of this parameter on the correlation. Plate 5.2 shows a very large phytoplankton bloom ($3x10^4$ km^2) in the CZCS imagery for 29/7/1981.

Figure 5.6 is a plot of integrated chlorophyll against the (atmospherically corrected) ratio of water-leaving radiances in channels 3 and 2, assuming an Ångström exponent of 0.5. This plot appears scattered but the frontal and mixed samples form two separate

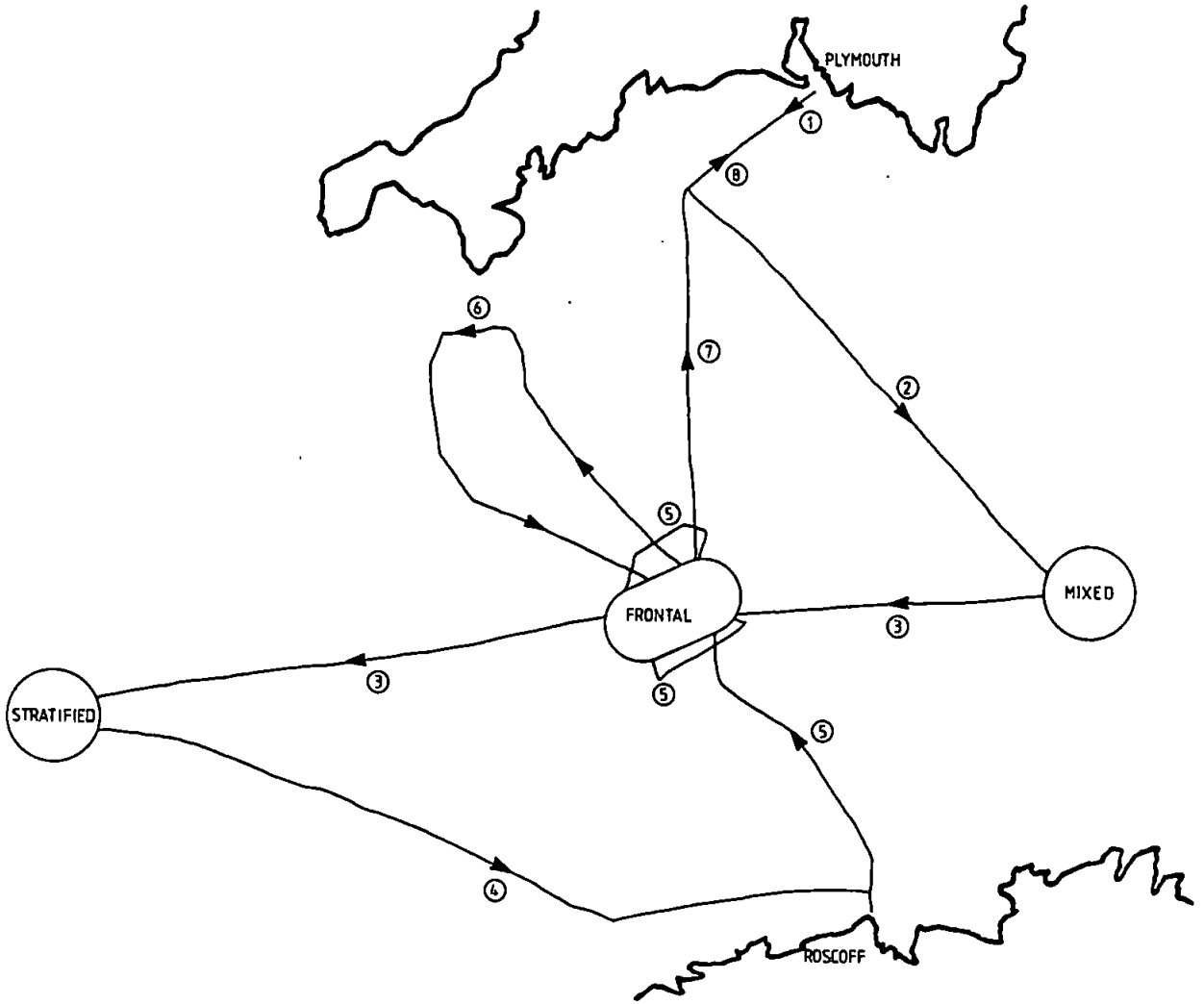

Figure 5.5 Location of mixed, frontal and stratified regions (July/August 1981).

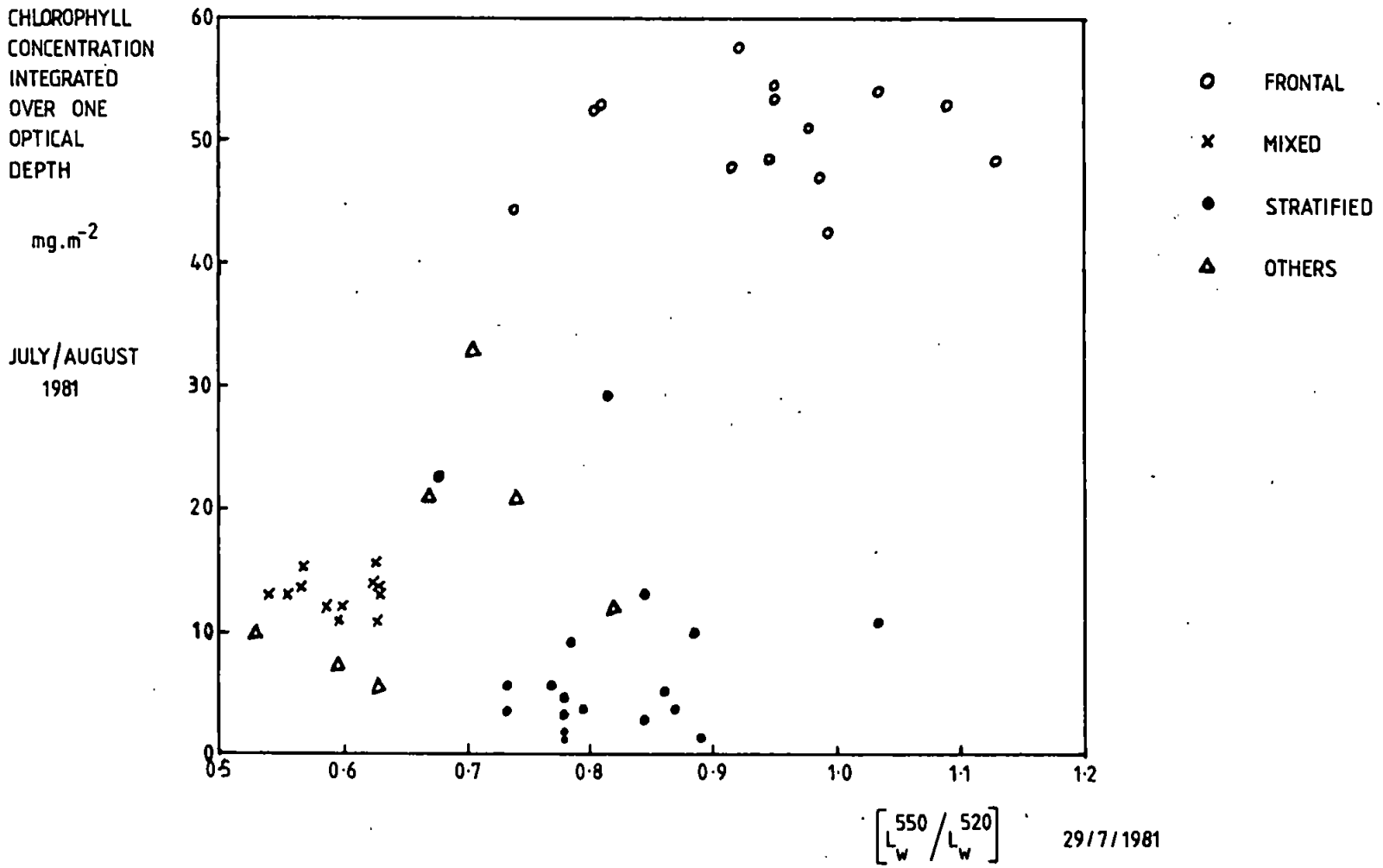

Figure 5.6 Integrated chlorophyll concentration against CZCS ratio (July/August 1981).

clusters - this is also apparent from Fig. 5.7 which illustrates the distribution of samples in channel 3 : channel 2 spectral space. The stratified points lie between the distinct mixed and frontal groups. The frontal samples have a lower response in both channels than the mixed ones because the chlorophyll concentration is higher in the frontal region. The variation in response is greater in channel 2 than in channel 3 as expected.

Of importance is the influence of the Ångström exponent 'm' upon atmospheric correction and indirectly upon the correlation between remote and in-situ estimates of chlorophyll concentration. The proper estimation of 'm' requires optical measurements of the atmosphere taken at the sea surface, concurrent with the CZCS pass. Without these measurements, as in this work, 'm' is chosen as that value which optimises correlation coefficients. Table 5.13 presents the correlation coefficients for four values of m (0.3, 0.5, 0.7 and 1.0) and for the three forms of regression. For m = 1.0, the number of samples has fallen to 41 because 10 of the water-leaving radiances became negative due to over-correction. The variation of r with m is plotted in Fig. 5.8 using the channel 3 to channel 2 ratio as it outperforms the channel 3 to channel 1 ratio in all cases. With linear and power regression r increases slowly and then falls sharply with the onset of over-correction. Polynomial regression is ambiguous as it produces two plots depending upon which variable is used for the independent one in the regression. However, polynomial A (integrated chlorophyll as independent variable) produces the best correlation and exhibits the same behaviour as the linear and power regressions. A suitable value for m is between 0.5 and 0.7 and even 0.7 is slightly high as it produced a couple of negative radiances in channel 1. A

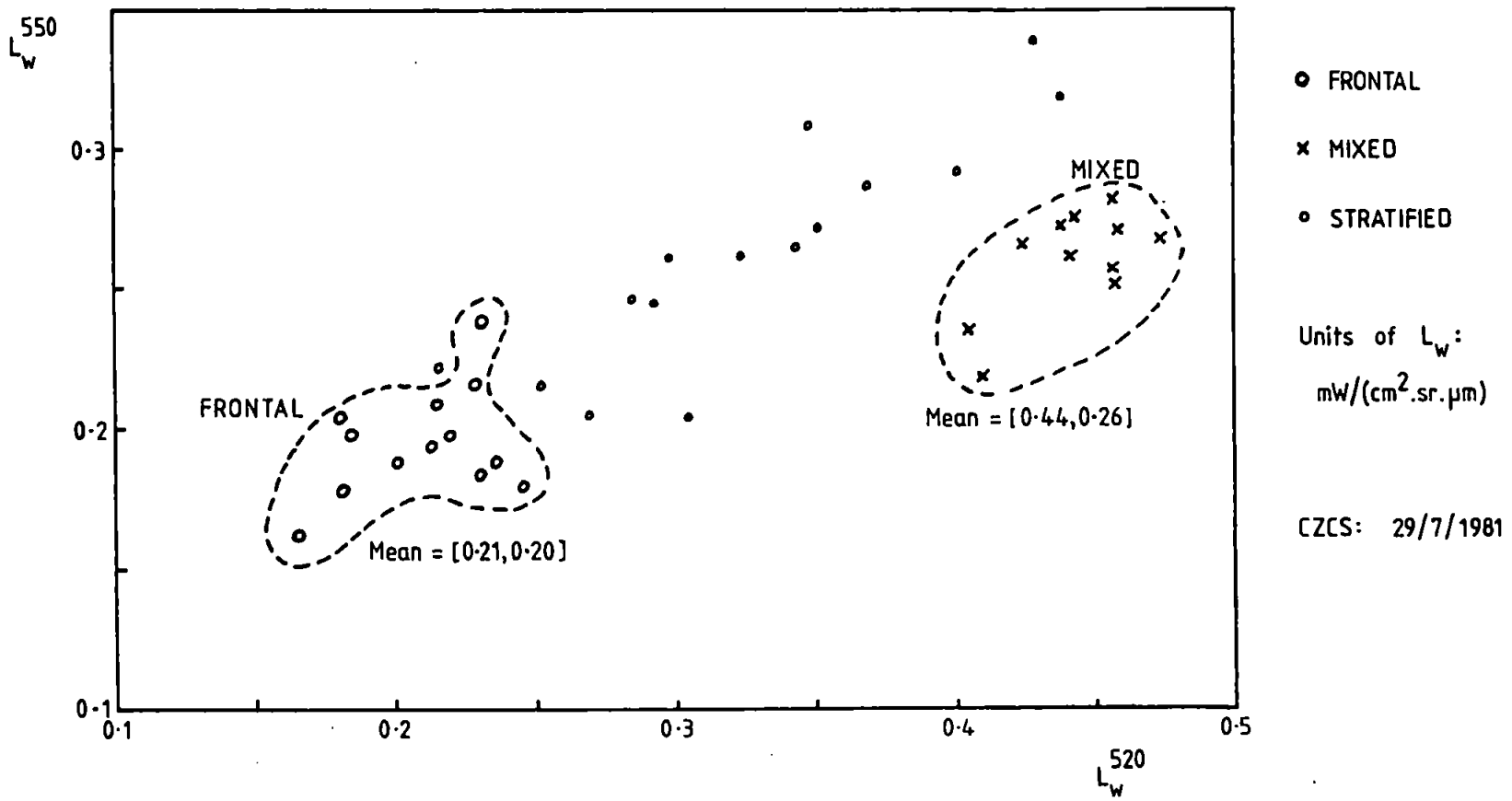

Figure 5.7 Distribution of samples in channel 3 : channel 2 spectral space.

TABLE 5.13 CORRELATION COEFFICIENTS (r) FOR VARIOUS VALUES OF ANGSTRÖM EXPONENT (m).

A) LINEAR

	m = 0.3	m = 0.5	m = 0.7	m = 1.0
Ch3/Ch1	0.07	0.18	----	----
Ch3/Ch2	0.54	0.57	0.60	0.28
Number of samples	51	51	51	41

B) POWER

	m = 0.3	m = 0.5	m = 0.7	m = 1.0
Ch3/Ch1	-0.09	0.01	----	----
Ch3/Ch2	0.28	0.30	0.35	0.14
Number of samples	51	51	51	41

C) POLYNOMIAL

	m = 0.3	m = 0.5	m = 0.7	m = 1.0
Ch3/Ch1	0.35 (0.18)	0.35 (0.28)	----	----
Ch3/Ch2	0.74 (0.60)	0.74 (0.62)	0.74 (0.64)	0.47 (0.71)
Number of samples	51	51	51	41

For linear and power regression the same correlation coefficient is produced with integrated chlorophyll or the CZCS ratio as independent variable. However, with polynomial regression this is not the case and the first value applies when integrated chlorophyll is the independent variable while the second (in parentheses) applies when the CZCS ratio is the independent variable. Based upon CZCS (29/7/1981) and Holligan's data.

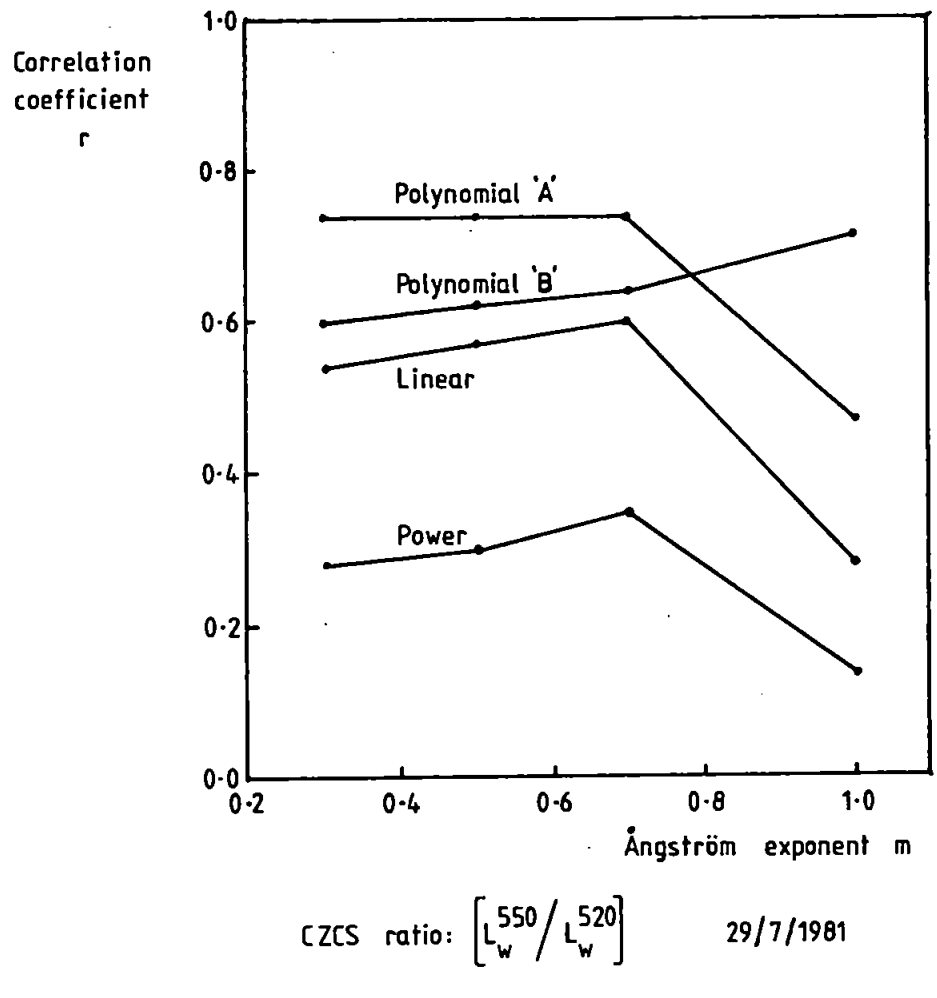

Figure 5.8 Variation of correlation coefficient with Ångström exponent for July 1981.

safe value then is 0.5 or 0.6 for 29/7/1981. Figure 5.8 reveals that polynomial regression is superior to linear regression, while power regression is clearly the poorest form of regression. The significance levels for polynomial, linear and power regression are <0.00002%, 0.002% and 5% respectively for m = 0.5.

5.2.5 Reduced datasets (July/August 1981)

A difference of a few days between in-situ and remote measurements may render the two sets of data incomparable because a phytoplankton patch may show some movement and/or growth (or decay) in this time. It was therefore decided to study the variation of the correlation coefficient with the sample period, which varied from ±1 day of the CZCS pass (29/7/1981) to ±4 days; the full set of 51 samples was spread over an interval of -7 to +4 days centred on the 29/7/1981. These results are presented in Table 5.14. The linear correlation coefficient shows a steady increase with increasing sample period, as does the polynomial one except for a small drop at ±3days. However, power regression peaks at ±3 days and does not produce convincing values of correlation coefficient. Overall, these findings are contrary to what would be expected of a phytoplankton patch in a state of rapid flux and instead they support the notion of a comparatively stable distribution. A possible explanation for this improvement in correlation coefficient with sample period (for linear and polynomial regression) is that regression performed with all 51 samples incorporates a wide range of chlorophyll concentrations and results in a meaningful regression equation. In contrast, when a smaller dataset is considered, there may not be a sufficient range of concentrations.

TABLE 5.14 VARIATION OF CORRELATION COEFFICIENT (r) WITH SAMPLE PERIOD. SEA TRUTH: JULY/AUGUST 1981, CZCS: 29/7/1981.

SAMPLE PERIOD	NUMBER OF SAMPLES	CORRELATION COEFFICIENTS		
		LINEAR	POWER	POLYNOMIAL
±1	14	0.45	0.27	0.55
±2	28	0.52	0.39	0.61
±3	35	0.54	0.42	0.59
±4	43	0.55	0.35	0.68
All	51	0.57	0.30	0.74

The correlation coefficients are between integrated chlorophyll (measured fluorometrically) and the ratio of CZCS channel 3 to channel 2. An Ångström exponent of 0.5 was used.

TABLE 5.15 CORRELATION COEFFICIENTS FOR REDUCED DATASET: ALL STRATIFIED SAMPLES EXCLUDED. SEA TRUTH: FLUOROMETER (HOLLIGAN) JULY TO AUGUST 1981; CZCS: 29/7/1981.

X	Y	LINEAR	POWER	POLYNOMIAL
Integrated chlorophyll	CZCS Ch3/Ch1	0.48	0.45	0.49
CZCS Ch3/Ch1	Integrated chlorophyll	0.48	0.45	0.49
Integrated chlorophyll	CZCS Ch3/Ch2	0.88	0.86	0.89
CZCS Ch3/Ch2	Integrated chlorophyll	0.88	0.86	0.91

Number of samples = 33.
Chlorophyll (+ phaeophytin) integrated over 1 optical depth.
Imagery corrected assuming an Ångström exponent of 0.5 .

An examination of Fig. 5.6 indicates that most of the stratified samples lie well away from the main sequence of mixed and frontal ones. It is believed that these stratified samples are drawn from an area containing large horizontal gradients in chlorophyll concentration; observe the sharp edge on the West side of the phytoplankton bloom in Plate 5.2. These sharp gradients leave no room for spatial error between the two datasets (Gordon et al. 1983b), whereas the mixed and frontal regions can accommodate such errors as they are extended regions with almost homogeneous properties.

Figure 5.9 is the same as Fig. 5.6, but with the stratified samples excluded; the three regressions are superimposed upon the data. The corresponding correlation coefficients (Table 5.15) are much improved and those for the CZCS channel 3 to channel 2 ratio are all significant at a level of less than 0.00002%. The difference in performance between the three forms of regression is now much smaller, but power regression still comes in last. Although the polynomial regression produces the best correlation, it does look as if it is attempting to account for the spread of samples in the frontal region and in this sense it is too 'clever' for its own good.

Pursuing the idea of reduced datasets one step further, an analysis of just the mixed and frontal samples was undertaken. The correlation coefficients (Table 5.16) show some improvement, with the power regression finally overtaking the linear one.

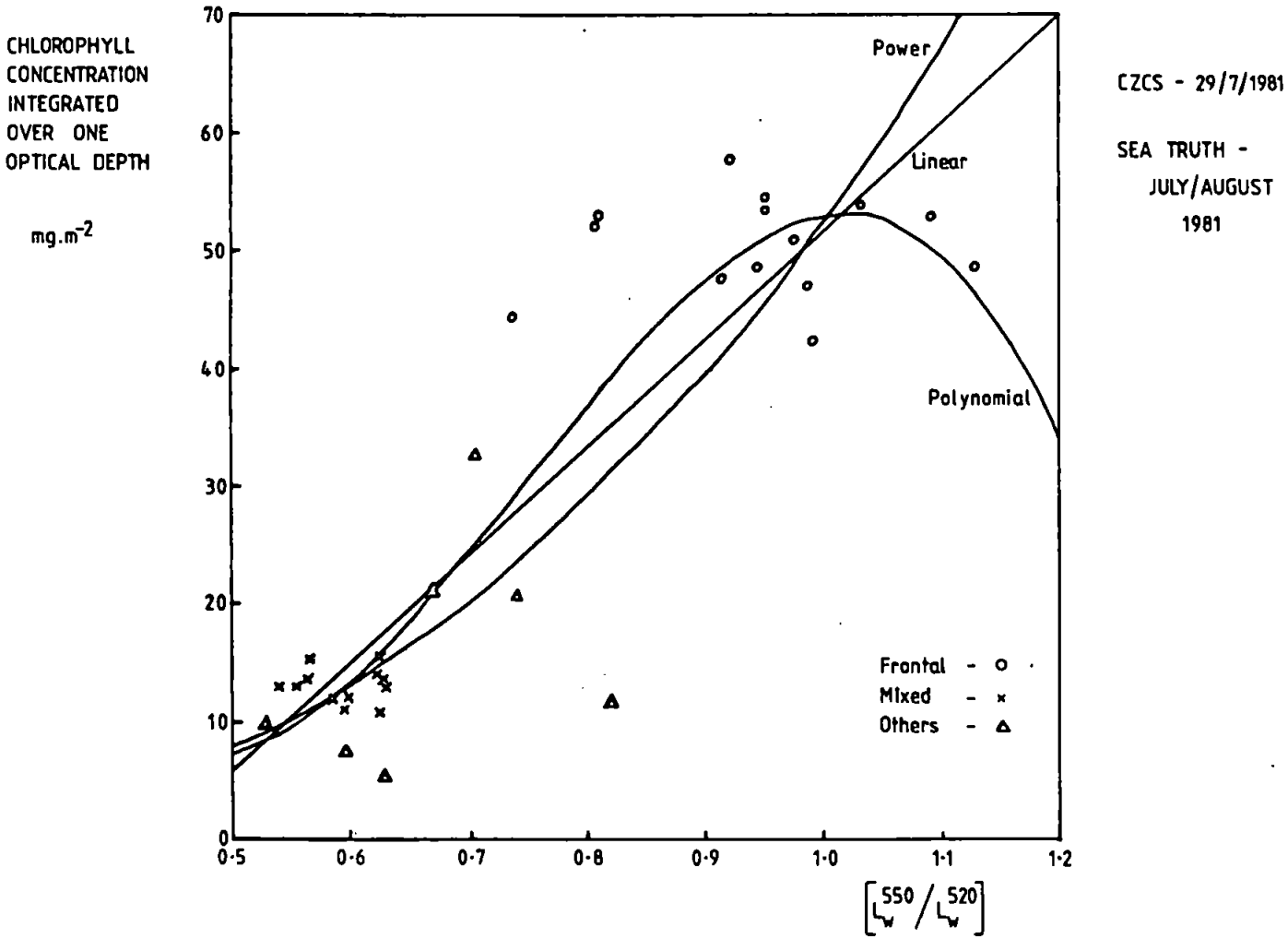

Figure 5.9 Three forms of regression between integrated chlorophyll concentration and CZCS ratio for July/August 1981.

TABLE 5.16 CORRELATION COEFFICIENTS FOR REDUCED DATASET: MIXED AND FRONTAL SAMPLES ONLY. SEA TRUTH: FLUOROMETER (HOLLIGAN) JULY TO AUGUST 1981; CZCS: 29/7/1981.

X	Y	LINEAR	POWER	POLYNOMIAL
Integrated chlorophyll	CZCS Ch3/Ch2	0.90	0.92	0.91
CZCS Ch3/Ch2	Integrated chlorophyll	0.90	0.92	0.95

Number of samples = 26.
Chlorophyll (+ phaeophytin) integrated over 1 optical depth.
Imagery corrected assuming an Ångström exponent of 0.5 .

TABLE 5.17 CORRELATION COEFFICIENTS FOR UOR (19/6/84) AND CZCS (17/6/84)

X	Y	LINEAR	POWER	POLYNOMIAL
Averaged chlorophyll	CZCS Ch3/Ch1	0.54	0.48	0.58
CZCS Ch3/Ch1	Averaged chlorophyll	0.54	0.48	0.54
Averaged chlorophyll	CZCS Ch3/Ch2	0.38	0.37	0.39
CZCS Ch3/Ch2	Averaged chlorophyll	0.38	0.37	0.39

Number of samples = 52.
Chlorophyll (+ phaeophytin) averaged over 10 metres.
Imagery corrected assuming an Ångström exponent of 0.5 .

5.2.6 UOR - CZCS (June 1984)

Chlorophyll concentration was measured by the UOR in the English Channel on 19/6/1984. The tow covered a distance of 44 nautical miles from 49° 35' N, 4° 8' W to 50° 17.2' N, 4° 13.2' W; this is a South to North route. Over this distance the undulator made 52 complete undulations and the chlorophyll concentration was averaged over 10 metres for each undulation, resulting in 52 values of chlorophyll concentration. These concentrations ranged from 0.2 to 4.14 $mg.m^{-3}$ with over a half being less than 1 $mg.m^{-3}$; this is representative of a low chlorophyll region, Figure 5.10 shows the distribution. This sea truth was compared with CZCS data collected on 17/6/1984 at 10.41 GMT (orbit number 28517, N129/03). The time difference between datasets was two days. An Ångström exponent of 0.5 was used in the atmospheric correction. Table 5.17 shows the statistical results with the channel 3 to channel 1 ratio consistently producing a higher correlation than the channel 3 to channel 2 ratio. This is to be expected in this low-chlorophyll case as channel 1 is more sensitive than channel 2. The channel 3 to channel 1 ratio is significant at levels between 0.05% and 0.001%, whereas the channel 3 to channel 2 ratio is only significant at levels of 0.5% and 1%. These results justify the atmospheric correction scheme because this is a low-chlorophyll scene with a high orbit number, conditions under which the algorithm is most likely to breakdown.

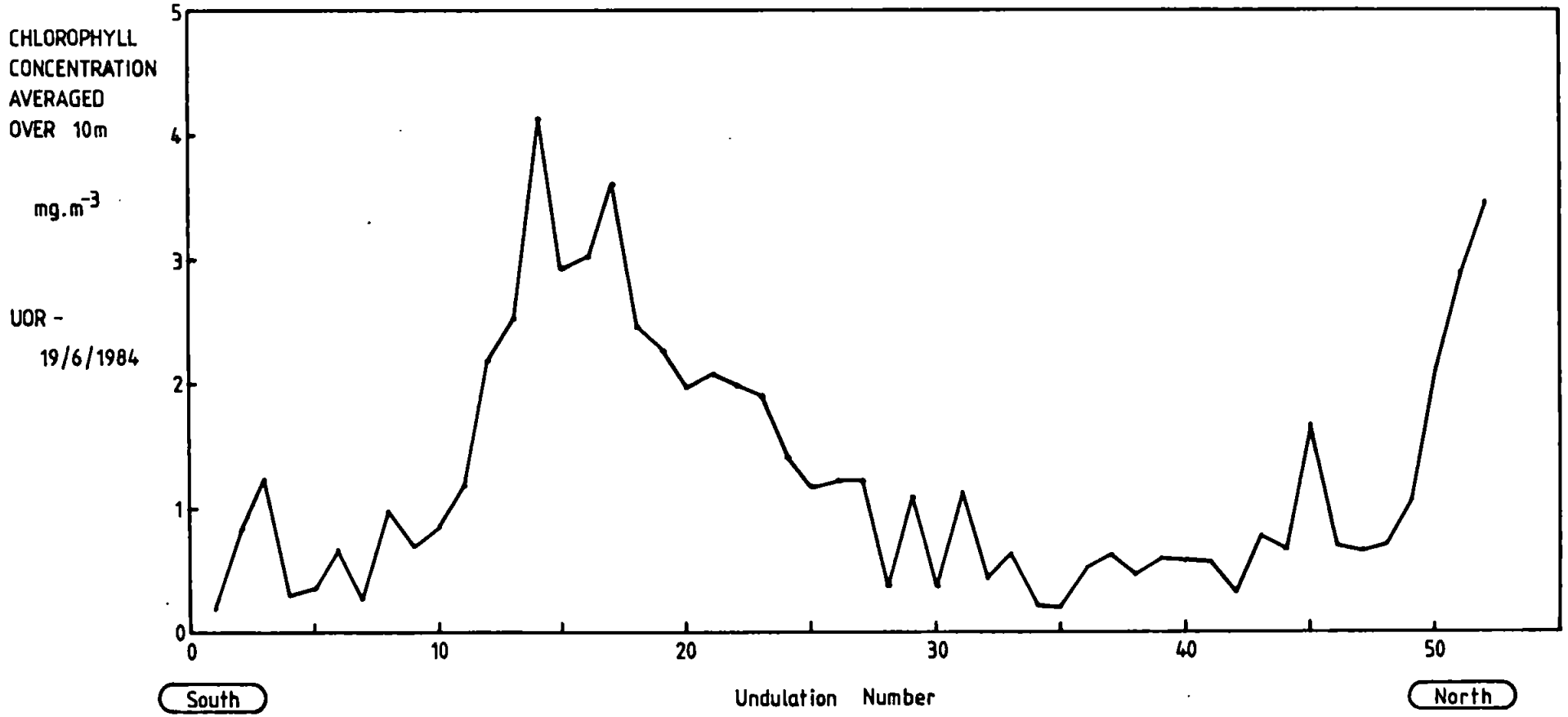

Figure 5.10 Variation of chlorophyll concentration (UOR) across the English Channel for 19/6/1984. This is a low chlorophyll scene.

5.3 CHLOROPHYLL RETRIEVAL ALGORITHMS

Before suggesting some chlorophyll retrieval algorithms, a comparison of my regressions with those of Holligan et al. (1983) is presented for CZCS imagery of 29/7/1981. Although the data and my regression curves appear in Fig. 5.9, Fig. 5.11 is simply a log-log plot of the same data (but excluding stratified samples) with an inversion of the CZCS ratio to enable a comparison of regressions. This inversion arises from a difference in formulation of regression equations. For the power relation I use:

$$C = A\left[\frac{L_w(550)}{L_w(520)}\right]^B \tag{5.7}$$

whereas the formulation of Holligan et al. (1983) is:

$$\log C = a + b \log\left[\frac{R(520)}{R(550)}\right] \tag{5.8}$$

These two relations are in fact directly comparable provided that $B = -b$ and $a = \log A$, i.e. $A = 10^a$. A more fundamental difference is the use of in-situ sub-surface reflectance R rather than remotely-sensed water-leaving radiance, i.e. Eq. 5.8 is independent of CZCS measurements. The former, of course, is not subject to the vagaries of atmospheric interference. Fortunately, L_w and R are directly related (see Eq. 2.13) but the effective conversion factor varies with wavelength; this variation together with the effects of atmospheric correction must be borne in mind therefore when comparing the two forms of regression.

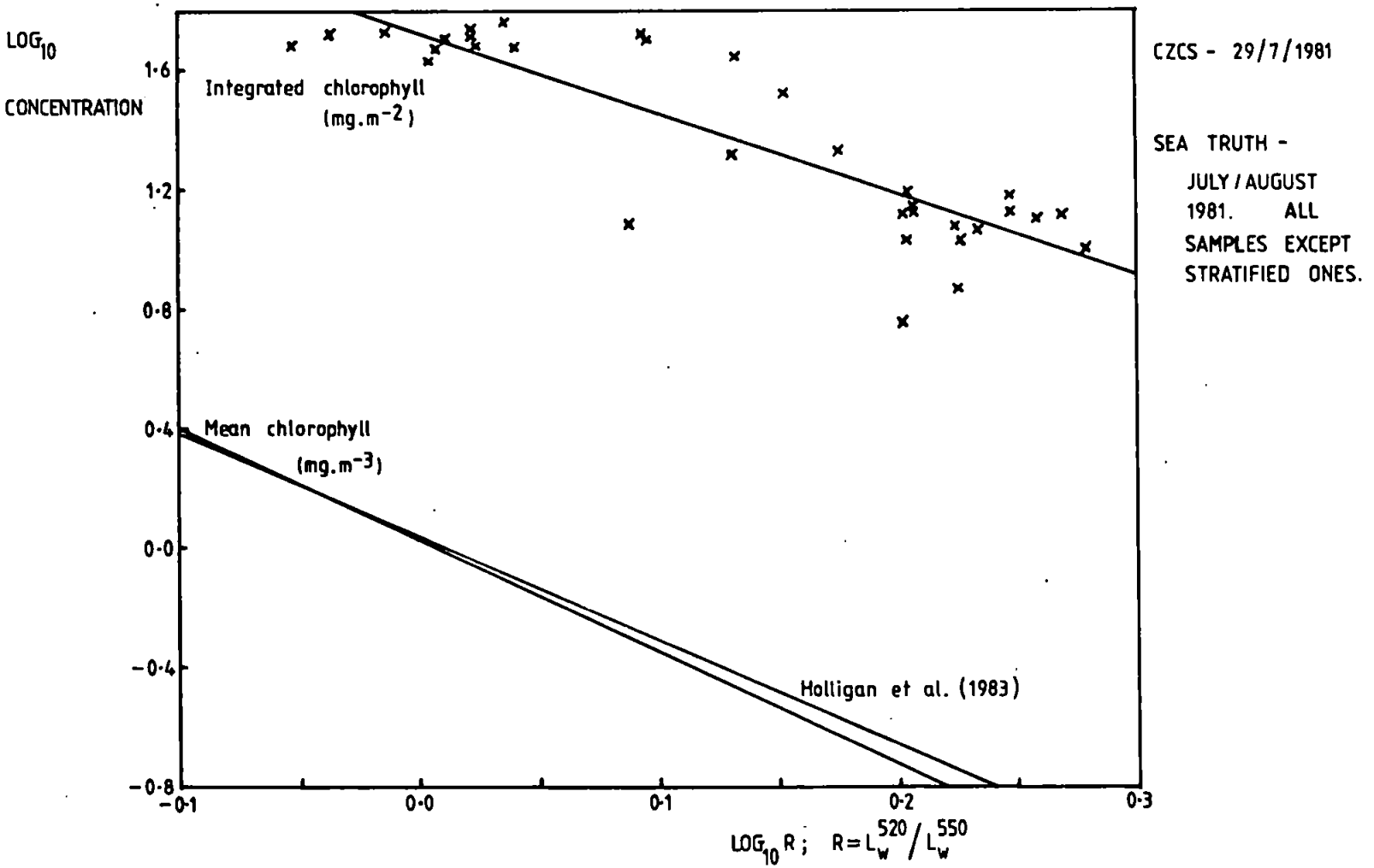

Figure 5.11 Comparison of power regression with that of Holligan et al. (1983).

Superimposed on Fig. 5.11 are two regression lines taken from Holligan et al. (1983); one is based upon optical measurements made on 16/7/1981 and the other upon all relevant data collected between June and September 1981. It must be stressed again that these regressions are derived from in-situ measurements of both chlorophyll concentration and sub-surface reflectance.

Whilst the slopes are comparable, the intercepts are markedly different from those in this work. This is a direct consequence of integrating chlorophyll over one optical depth, which produces higher but more realistic values than mean ones. Although a proper scheme for weighting the contributions to water-leaving radiance from different depths has been devised (section 2.1.4), it may only be used when concurrent values of the diffuse attenuation coefficient K(z) are available. It is not surprising then that many retrieval algorithms (Gordon and Clark 1980a, Smith and Wilson 1981) are based upon surface chlorophyll at one depth or mean values over a depth range.

The slopes of my regression (2.66 and 2.56) are a little less than those (3.48 and 3.73) obtained by Holligan et al. (1983), and again this is due to using integrated values of chlorophyll concentration. The slope is reduced because the integration procedure (see section 5.1.4) has the effect of increasing low values of chlorophyll concentration much more than high values. This may be understood by recalling that the integrated concentration is the product of mean concentration $\bar{C}$ and optical depth z_{90} and that z_{90} depends inversely upon $\bar{C}$ (Eq. 5.4). Physically this means that at low chlorophyll concentrations the water is clearer i.e. the optical depth is greater. Accordingly the concentration is integrated over a greater depth.

Tables 5.18 and 5.19 present the coefficients for linear and power regression respectively assuming a high chlorophyll concentration and using the CZCS ratio (channel 3)/(channel 2). Although there is a large spread in coefficients, when those cases corresponding to surface values, over-correction and low chlorophyll concentration are eliminated the spread is reduced. Ignoring these cases, the slope for linear regression ranges from 62.32 to 90.86; the intercepts however display a larger spread: -39.36 to +23.23. The case of 'mixed and frontal samples only' produces the highest correlation coefficient and so the suggested linear algorithm for chlorophyll retrieval in regions of high concentration (> 5 $mg.m^{-2}$) is:

$$\text{Integrated chlorophyll } (mg.m^{-2}) = 89.18\left[\frac{L_w(550)}{L_w(520)}\right] - 36.53 \qquad (5.9)$$

Again, ignoring those cases stated above, the multiplier for power regression (Table 5.19) lies between 21.17 and 82.88 with the exponents varying between 0.74 and 2.66. A suggested power algorithm for the retrieval of high levels of chlorophyll concentration (> 5 $mg.m^{-2}$), based upon mixed and frontal samples, is:

$$\text{Integrated chlorophyll } (mg.m^{-2}) = 54.55\left[\frac{L_w(550)}{L_w(520)}\right]^{2.56} \qquad (5.10)$$

Algorithms for the retrieval of low levels of chlorophyll concentration (< 5 $mg.m^{-2}$) were derived from a comparison of CZCS ratio (channel 3)/(channel 1) for 17/6/1984 and sea truth collected by the

TABLE 5.18 CHLOROPHYLL RETRIEVAL ALGORITHMS BASED UPON A LINEAR RELATIONSHIP

$$\text{Chlorophyll concentration} = A \frac{L_w(550)}{L_w(520)} + B$$

A	B	n	r	CZCS DATE	COMMENTS
62.32	-1.48	37	0.34	22/6/81	Compared with UOR (30/6/81) [chlorophyll: 0 to 10m]
64.61	23.23	27	0.36	29/7/81	Compared with UOR (21/7/81) [chlorophyll: 0 to 10m]
54.58	-33.07	51	0.61	29/7/81	Surface values only (0 to 2m)
68.79	-31.64	51	0.57	29/7/81	Integrated chlorophyll
1.20	13.68	41	0.28	29/7/81	Over-corrected *
90.86	-39.36	33	0.88	29/7/81	All samples except stratified ones
89.18	-36.53	26	0.90	29/7/81	Mixed and frontal samples only
11.86	-4.39	52	0.38	17/6/84	Low chlorophyll concentration

Range of A (slope) values is from 1.20 to 90.86; mean is 55.43

Range of B (intercept) values is from -39.36 to 23.23; mean is -13.70

n is the number of samples and r is the correlation coefficient

* Angström exponent = 1.0; all other cases use 0.5 .

TABLE 5.19 CHLOROPHYLL RETRIEVAL ALGORITHMS BASED UPON A POWER RELATIONSHIP

$$\text{Chlorophyll concentration} = A \left(\frac{L_w(550)}{L_w(520)} \right)^B$$

A	B	n	r	CZCS DATE	COMMENTS
59.52	1.14	37	0.34	22/6/81	Compared with UOR (30/6/81) [chlorophyll: 0 to 10m]
82.88	0.74	27	0.34	29/7/81	Compared with UOR (21/7/81) [chlorophyll: 0 to 10m]
6.05	3.33	51	0.38	29/7/81	Surface values only (0 to 2m)
21.17	1.57	51	0.30	29/7/81	Integrated chlorophyll
10.56	0.13	41	0.14	29/7/81	Over-corrected *
52.28	2.66	33	0.86	29/7/81	All samples except stratified ones
54.55	2.56	26	0.92	29/7/81	Mixed and frontal samples only
26.71	4.50	52	0.37	17/6/84	Low chlorophyll concentration

Range of A (multiplier) values is from 6.05 to 82.88; mean is 39.22

Range of B (exponent) values is from 0.13 to 4.50; mean is 2.08

n is the number of samples and r is the correlation coefficient

* Angström exponent = 1.0; all other cases use 0.5 .

UOR on 19/6/1984; the latter was in the form of chlorophyll concentration averaged over the top 10 metres. An analysis was also undertaken of CZCS imagery for 3/7/1984 but the concentrations were too low to generate a valid algorithm. Based upon 17/6/1984 imagery, low-concentration expressions for linear and power regression are respectively:

$$\text{Averaged chlorophyll } (mg.m^{-3}) = 1.744\left[\frac{L_w(550)}{L_w(443)}\right] - 0.836 \qquad (5.11)$$

$$\text{Averaged chlorophyll } (mg.m^{-3}) = 0.723\left[\frac{L_w(550)}{L_w(443)}\right]^{1.646} \qquad (5.12)$$

Many algorithms have been developed; see for example the algorithm tables in Gordon and Morel (1983) and Sathyendranath and Morel (1983), nearly all of which employ the power relation based upon the ratio of two CZCS channels. The two most often used ratios are (channel 1 or channel 2) with channel 3, abbreviated by R_{13} and R_{23} respectively. In addition the ratios R_{12} (Gordon & Clark 1980a, Smith & Wilson 1981) and R_{24} (Clark 1981) have been used. The coefficients of these published algorithms vary considerably, even for a ratio based upon the same two CZCS channels. The algorithm represented by Eq. 5.10 has a realistic exponent (2.56), but its multiplier (54.55) exceeds published ones due to the integration procedure discussed above.

The algorithm for low chlorophyll concentration (Eq. 5.12) is directly comparable with published ones as its derivation is based upon average concentrations (0 to 10m). The multiplier (0.723) and power (1.646) compare very favourably with published coefficients, such as respectively: 0.50, 1.27 (Gordon & Clark 1980a), 0.78, 1.33 (Clark 1981) and 0.78, 2.12 (Smith and Wilson 1981).

5.4 CLUSTER ANALYSIS

Spectral clustering (ISOCLS, section 3.3.2.2) was first applied to CZCS data (22/6/1981) for a narrow strip of water between Plymouth and Roscoff having a low-to-moderate phytoplankton count. The water-leaving radiances in channels 1, 2 and 3 were used and each pixel was assigned to one of four sub-classes; the number of which depends upon various clustering parameters, especially the maximum permitted standard deviation per class. By referring to the water-leaving radiance in channel 1, the sub-class numbers were allocated in such a way that they increase monotonically with increasing chlorophyll concentration. In order to reduce the effects of erroneous pixel classification, mean sub-class numbers were calculated from cells of 5 by 5 pixels. The mean sub-class number is compared with CPR data (23/6/1981) in Fig. 5.12, and does not appear to follow the diatom count, although it does track the CZCS spectral ratio in Fig. 5.2 (not shown). However, clustering of a strip five nautical miles East of the Plymouth-Roscoff route produced a good match with the diatom count; no doubt this improvement is attributable to the one day difference between datasets.

The application of clustering to a whole image involves a much larger number of pixels than the case above and the use of the hybrid (monocluster blocks) approach becomes imperative. Several small blocks (of perhaps 25 by 25 pixels) were selected from the CZCS image so as to cover the full range of chlorophyll concentration between them. These blocks were clustered to produce training statistics in the form of mean vectors and covariance matrices for each sub-class. These statistics were then used by a maximum likelihood classifier to classify each pixel in the image. Use of the more efficient and faster

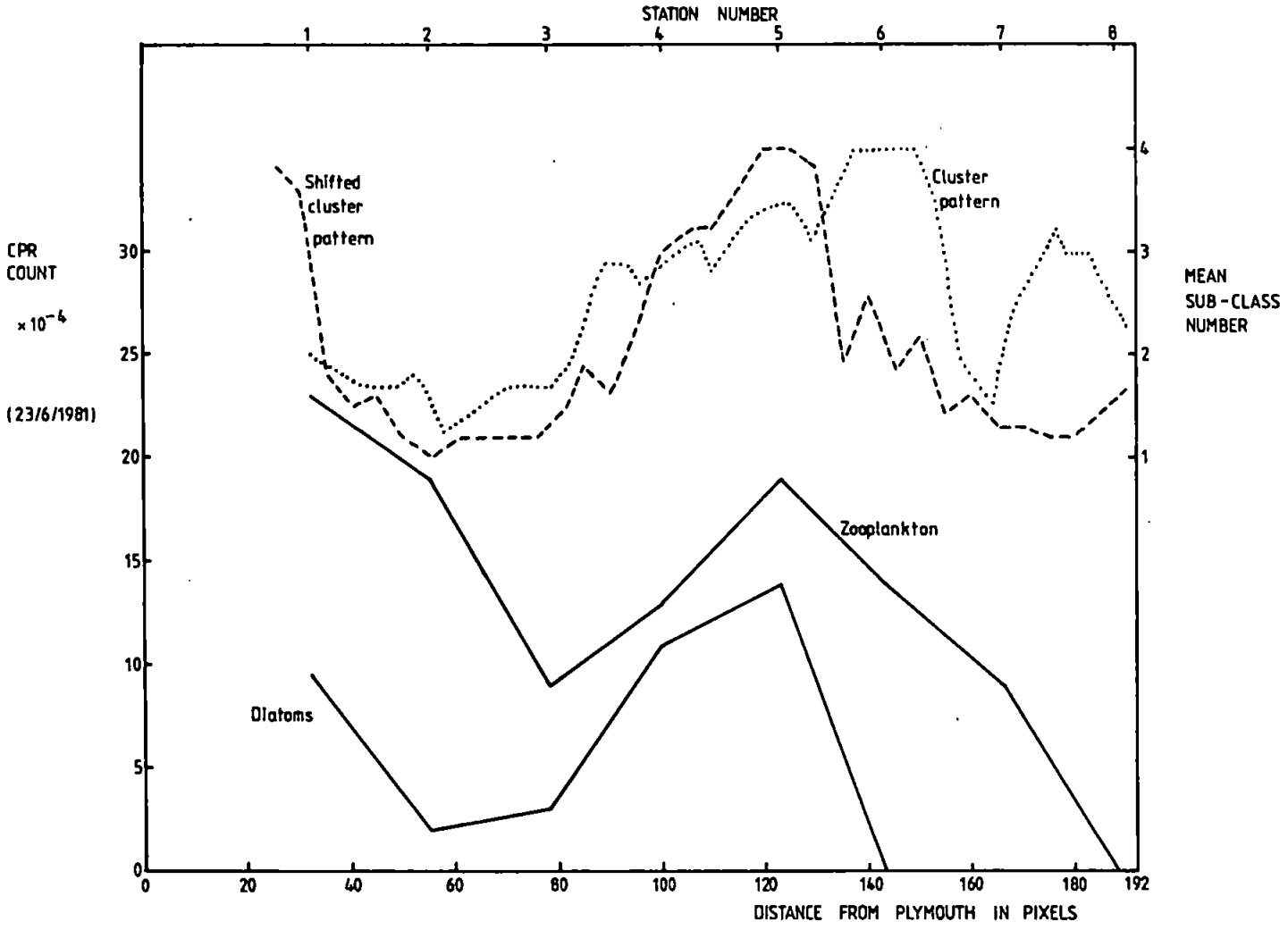

Figure 5.12 Plots of diatom count and cluster patterns for June 1981.

weighted-minimum-distance classifier produced very similar results shown in Plates 5.3 and 5.4 for 22/6/1981 and 29/7/1981 respectively. Each sub-class is displayed with a different colour.

Hybrid clustering of the 29/7/1981 image generated eight sub-classes (K=1,8) whose approximate locations in multispectral space (three channels) are shown in Fig. 5.13a. The variance of each sub-class is indicated roughly by each circle's diameter. Also shown is a dotted sub-class, produced by clustering pixels from coastal waters, which does not follow the trend of the other sub-classes. This sub-class represents areas contaminated by suspended sediments (Collins and Pattiaratchi 1984), land run-off etc., in which the water-leaving radiance in channel 4 (670 nm) may be non-zero, thus invalidating the atmospheric correction algorithm. Consequently, an accurate position for this coastal-water sub-class cannot be given in terms of absolute radiance values, although an equivalent sub-class for 22/6/1981 occupied virtually the same position.

The approximate chlorophyll concentration corresponding to each of these sub-classes is shown in Fig. 5.13b and the dotted line indicates that the relationship is non-linear.

Clustering is potentially a more powerful technique than conventional retrieval algorithms as it uses three channels (or more) rather than the usual two of the latter. Cluster analysis of low chlorophyll scenes (17/6/1984 and 3/7/1984) clearly indicated a distinct phytoplankton patch in the middle of the English Channel, despite chlorophyll concentrations of less than 1 $mg.m^{-2}$ with little variability. Conventional spectral ratios, in contrast, were barely

Plate 5.3 Colour cluster map for 22/6/1981. Red and blue represent high and low chlorophyll concentrations respectively. The large red patch in mid-Channel however, is due to a large sediment load which upsets the atmospheric correction algorithm.

Plate 5.4 Colour cluster map for 29/7/1981. Red and blue represent high and low chlorophyll concentrations respectively.

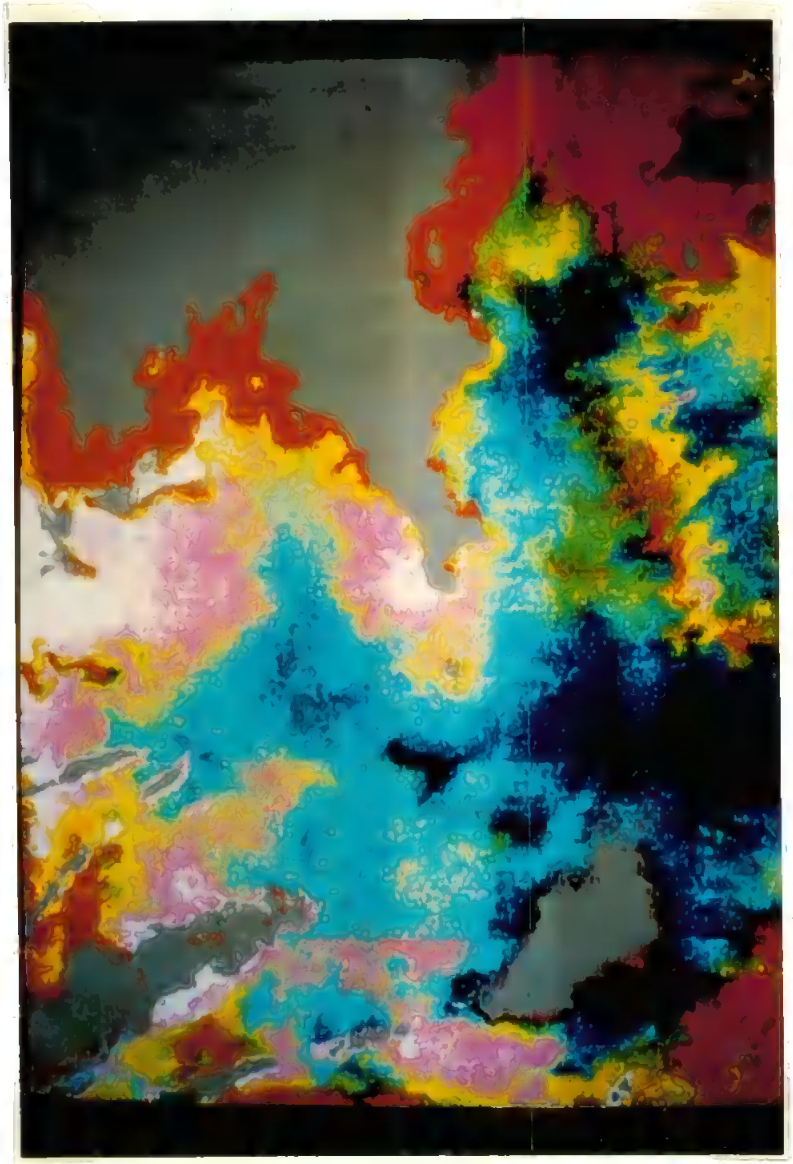

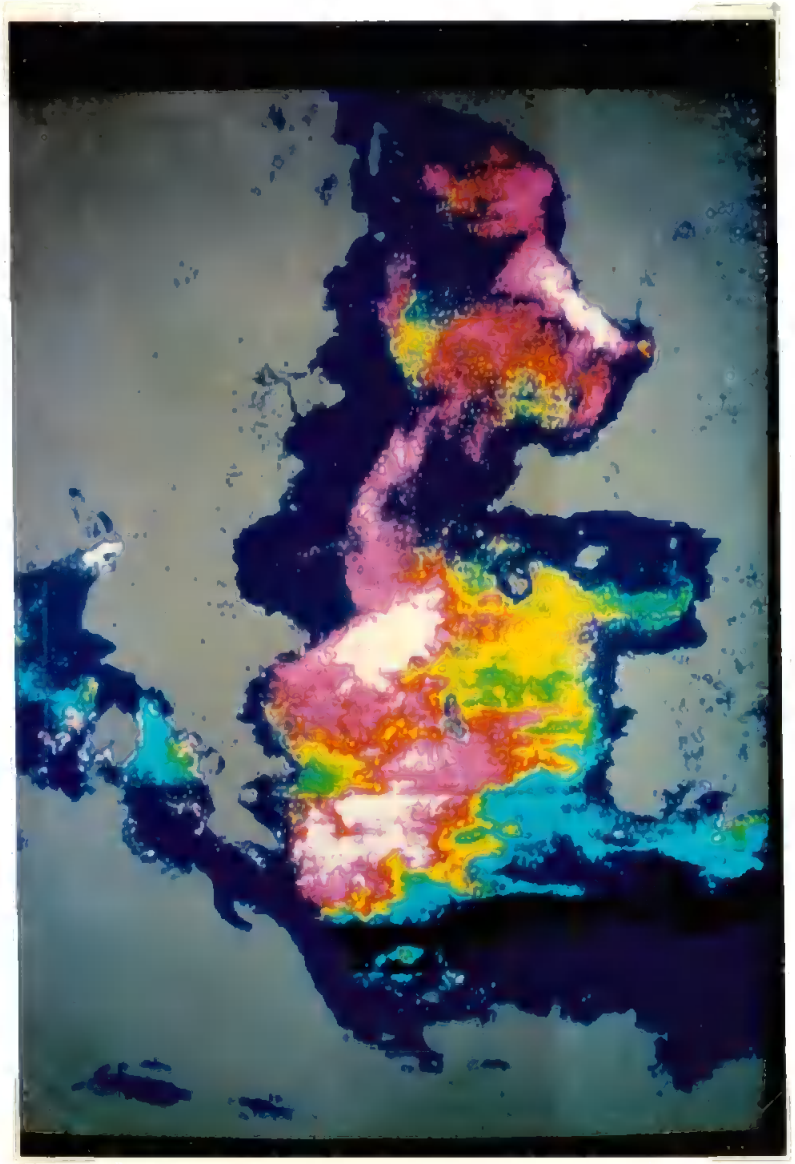

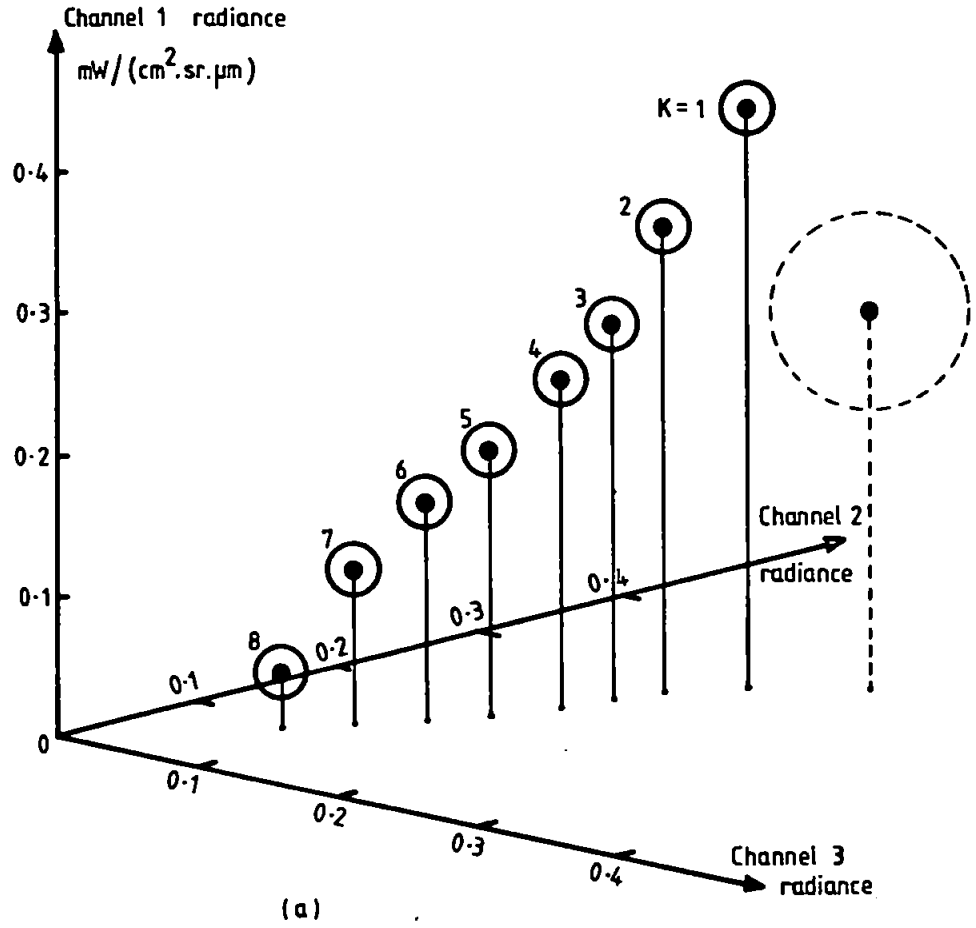

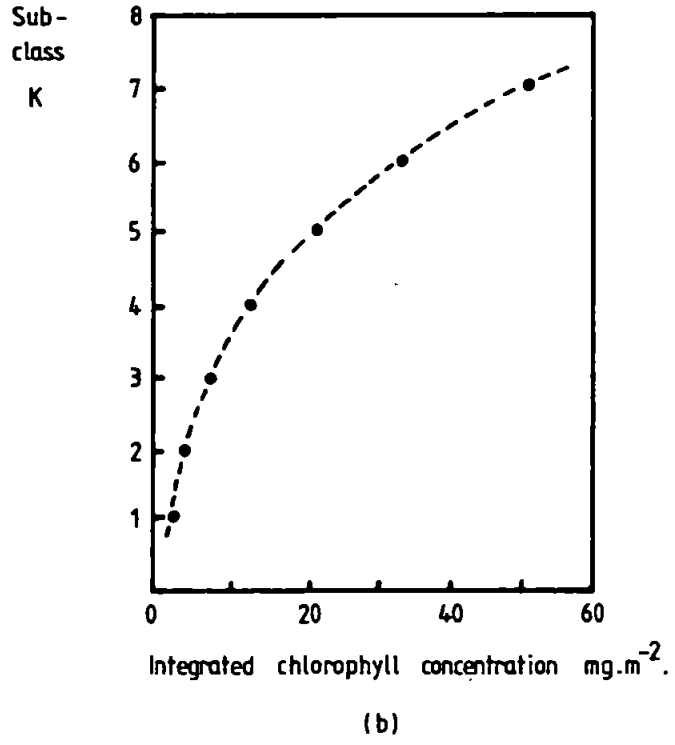

Figure 5.13 (a) Position of sub-classes in multispectral space.
(b) Relation between sub-classes and chlorophyll concentration.

able to discern these patches at all.

The determination of chlorophyll concentration by clustering assumes that both relationships in Fig. 5.13 are stable and valid under a variety of conditions. However, as the partitioning of the one chlorophyll class into several sub-classes is an inherently unpredictable process (Fig. 5.14) then clustering cannot determine absolute levels of chlorophyll concentration without sea truth. If, in the future, the stability of the overall chlorophyll class in multispectral space is established then it may become possible to relate chlorophyll sub-classes to a range of chlorophyll concentrations. This would be facilitated by constrained clustering which would ensure the production of the same set of sub-classes, i.e. the cluster centres are preset to match those for which there is supporting sea truth.

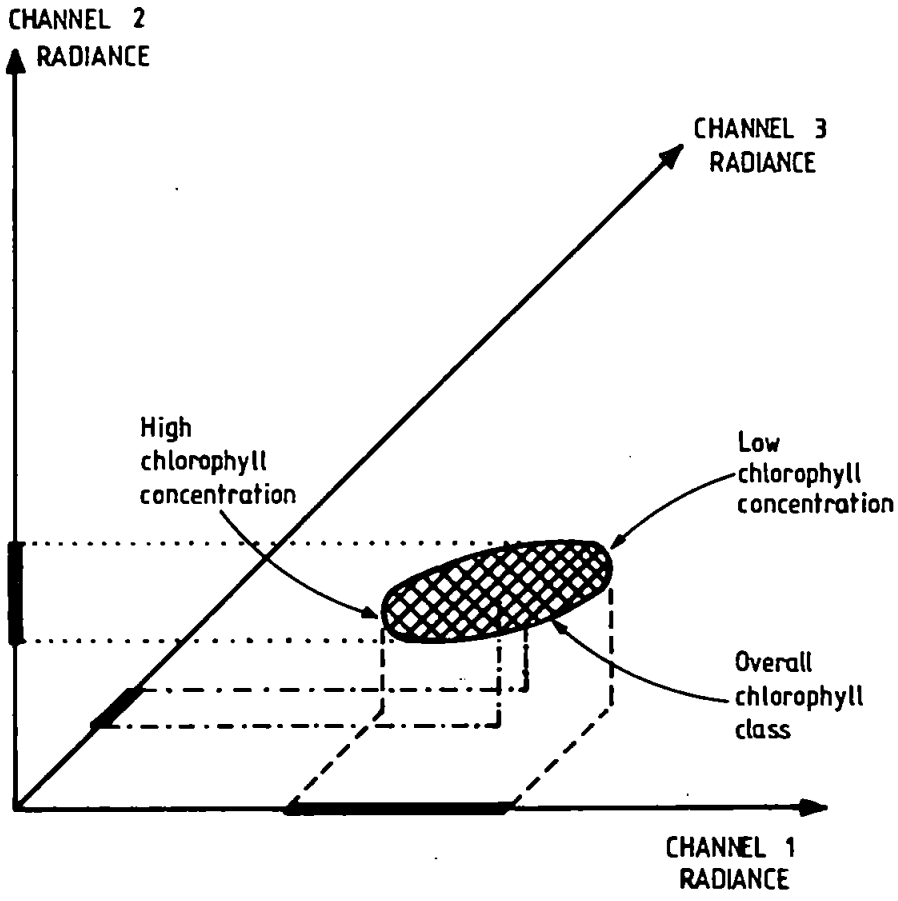

The three axes represent 3-dimensional multispectral space.

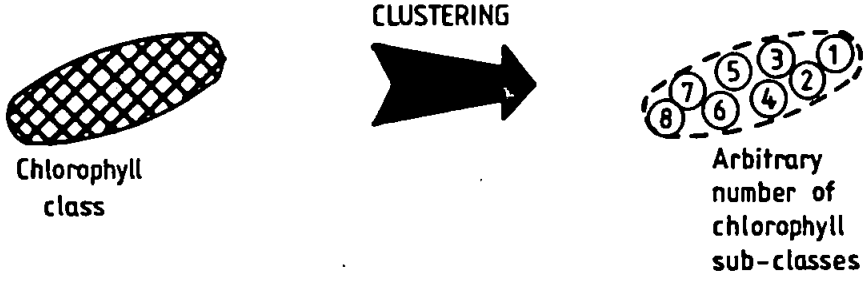

Figure 5.14 Partitioning of overall chlorophyll class into sub-classes as produced by clustering.

5.5 CONCLUSIONS

5.5.1 Objectives

All the objectives of this project have been successfully realised, that is the development of a low-cost image-processing system and software for the extraction and analysis of CZCS images. The image processor incorporates a 768x512x8 bit imagestore controlled by a suite of basic image processing programs. Software was also developed for the radiometric calibration, rectification and atmospheric correction of CZCS data. The last of these represented a particularly formidable problem.

5.5.2 Atmospheric correction

The development of an accurate and reliable atmospheric correction program was crucial in this work as the water-leaving radiance was, at times, less than 5% of the total radiance. In qualitative terms, the atmospheric correction program is very effective as it reveals sub-surface features which are not evident in the raw CZCS imagery. Moreover, the values of water-leaving radiance produced are reasonable and realistic, being less than 0.5 $mW/(cm^2.\mu m.sr)$. A further indication of its validity is provided by the striking similarity of chlorophyll distributions for 22/6/1981 and 29/7/1981 (Plates 5.1 and 5.2 respectively) when compared with those produced by Holligan et al. (1983) - see Figs. 1c and 1d respectively. This similarity is particularly convincing as the latter's algorithm is based upon the alternative approach of Viollier et al. (1980) which operates with reflectances rather than water-leaving radiances.

There is still, however, scope for improvement. The most pressing modification concerns the calculation of Sun-satellite geometry because the present partition of images into 24 (6x4) cells is too coarse resulting in vertical striping under some circumstances. Simply increasing the number of cells would reduce the cell size and consequently the error in Sun-satellite geometry without incurring a great increase in computer time. I recommend that the Sun-satellite geometry should be calculated in this way as image partition enables a good compromise to be made between accuracy and CPU time. As the algorithm stands, it is only applicable to waters which are not dominated by sediments; for extension to these waters the iterative technique of Smith and Wilson (1981) could be implemented, although this would increase the CPU time.

A further refinement would be to use the 'clear water radiance' concept (Gordon and Clark 1981) as this removes the uncertainty in determining the Ångström exponent, without requiring any simultaneous in-situ optical measurements.

This study clearly shows the direct influence of the Ångström exponent upon the correlation coefficient, which deteriorates dramatically with the onset of over-correction. This is confirmed by the assertion of Gordon and Clark (1980a) that an underestimate of the Ångström exponent is preferable to an overestimate as the latter causes larger errors.

5.5.3 Regression

Contrary to expectations, the well-established power law for chlorophyll retrieval algorithms was outperformed by the linear one. Polynomial regression produced the best correlation but only as a

consequence of tracking variations in homogeneous regions. This can result in spurious algorithms which are not valid in all cases, and so the polynomial form is not recommended. Consequently, the linear form is recommended for chlorophyll retrieval algorithms; the following two are suggested for low (< 5 $mg.m^{-2}$) and high (> 5 $mg.m^{-2}$) concentrations respectively:

Average chlorophyll concentration ($mg.m^{-3}$)

$$= 1.744 \left[\frac{L_w(550)}{L_w(443)}\right] - 0.836$$

Integrated chlorophyll concentration ($mg.m^{-2}$)

$$= 89.18 \left[\frac{L_w(550)}{L_w(520)}\right] - 36.53$$

The coefficients of the expression above for integrated chlorophyll differ from published ones because of the method used for determining the in-situ chlorophyll concentration of the water-column. Most studies simply use mean or surface values which are unlikely to correspond to the water-column depth sensed by the CZCS. The method used in this work represents a distinct improvement as it involves an assessment of the optical or penetration depth to which the CZCS can 'see'. Strictly speaking, these retrieval algorithms only apply to those waters in the English Channel in which sediments exert little influence. However, they may also be valid in other United Kingdom waters provided that they satisfy the conditions for Case 1 waters.

Apart from the inherent uncertainties in deriving chlorophyll retrieval algorithms, the situation is further compounded by the perennial lack of appropriate sea-truth; the most serious shortcoming being the large time differences between satellite pass and ship measurements.

5.5.4 Clustering

Both the K-means and ISOCLS clustering techniques were applied to CZCS data but only the latter was capable of discriminating regions with different concentrations of chlorophyll. The K-means algorithm only functions properly when distinct spectral classes are present, which is not the case with marine remote sensing. The hybrid or monocluster blocks method (Fleming and Hoffer 1977) was introduced when clustering whole images in order to reduce the computation time to an acceptable level. The statistics derived from the clustered blocks were used to classify the remaining pixels, by means of two classifiers namely: maximum likelihood and weighted minimum distance. The latter was found to be three times faster than the former and for only 5% or less of pixels was there any discrepancy between the two classifiers.

The patterns of phytoplankton distribution generated by clustering and by conventional retrieval algorithms are very similar - compare Plates 5.1 and 5.3 and Plates 5.2 and 5.4.

Clustering is useful for producing relative maps of phytoplankton distribution and is effective in identifying phytoplankton patches having low chlorophyll concentration. Clustering is suitable for many biological purposes which do not require absolute values. However, if the stability of the overall chlorophyll class in multispectral space is ever established then absolute values could be provided.

5.5.5 The future

The Nimbus-7 has now been in orbit for over seven years and although the CZCS has not suffered any mechanical or electrical breakdowns, the amount of data collected has dropped sharply during late 1985 and early 1986 due to diminishing power from the solar panels.

An improved CZCS sensor was suggested (Hovis 1981) as a candidate instrument for the American NOSS (National Oceanic Satellite System) but the whole program was scrapped due to budget cuts. It was proposed to equip the ERS-1 with an OCM (Ocean Colour Monitor), however the final design is based exclusively upon a microwave payload. The only sensor having appropriate spectral and radiometric characteristics for ocean colour studies is the MESSR on Japan's MOS-1 which is due for launch late 1986 or early 1987.

In the future we can look forward to sensors with much improved spectral resolutions as new technologies emerge, such as 'imaging spectrometry' (Goetz et al. 1985). This technique is already technically feasible and would provide 100 or more contiguous spectral channels in the visible and infra-red. The large number of channels (each 10 nm wide) creates a laboratory-like spectra which would enable ocean colour to be extensively studied, resulting in more reliable chlorophyll retrieval algorithms. Advances of this type would also act as a stimulus for obtaining more detailed knowledge of the optical properties of the sea and its many constituents. This data would further assist in the development of retrieval algorithms.

REFERENCES

Aiken, J., 1980, A marine environmental recorder. Marine Biology, 57, 237-240.

Aiken, J., 1981a, A chlorophyll sensor for automatic, remote, operation in the marine environment. Marine Ecology - Progress Series, 4, 235-239.

Aiken, J., 1981b, The undulating oceanographic recorder Mark 2. Journal of Plankton Research, 3, 551-560.

Alberotanza, L., and Zandonella, A., 1981, LANDSAT imagery of the Venetian Lagoon - a multitemporal analysis. In 'Oceanography from space', edited by J.F.R. Gower (New York: Plenum Press). pp. 421-428.

Alder, H.L., and Roessler, E.B., 1977, Introduction to probability and statistics, sixth edition (San Francisco: W.H. Freeman).

Allan, T.D., 1983, Oceanography from space. In 'Remote sensing applications in marine science and technology', edited by A.P. Cracknell (Dordrecht, Holland: Reidel). pp. 409-433.

Ångström, A., 1964, The parameters of atmospheric turbidity. Tellus, 16, 64-75.

Apel, J.R., 1983, Remote measurement of the ocean - an overview. In 'Remote sensing applications in marine science and technology', edited by A.P. Cracknell (Dordrecht, Holland: Reidel). pp. 1-16.

Arfken, G., 1970, Mathematical methods for physicists (New York: Academic Press).

Austin, R.W., 1980, Gulf of Mexico ocean-color surface-truth measurements. Boundary-Layer Meteorology, 18, 269-285.

Austin, R.W., 1982a, CZCS sensitivity loss study (preliminary results). EURASEP Secretariat Newsletter, No.7, Commission of the European Communities, Joint Research Centre, Ispra Establishment, 21020 Ispra, Varese, Italy. pp. 2, 7-8.

Austin, R.W., 1982b, Solar spectral irradiances for CZCS channels 1-4: revised values. EURASEP Secretariat Newsletter, No. 7, Commission of the European Communities, Joint Research Centre, Ispra Establishment, 21020 Ispra, Varese, Italy. pp. 17-28.

Ayres, F., 1954, Schaum's outline of theory and problems of plane and spherical trigonometry (New York: Schaum Publishing Company).

Bader, H., 1970, The hyperbolic distribution of particle sizes. Journal of Geophysical Research, 75, 2822-2830.

Ball Aerospace Systems Division, 1979a, Development of the Coastal Zone Color Scanner for Nimbus-7: Volume 1 - Mission objectives and instrument description. Final Report, F78-11, Rev. A. Ball Aerospace Systems Division, P.O. Box 1062, Boulder, CO 80306.

Ball Aerospace Systems Division, 1979b, Development of the Coastal Zone Color Scanner for Nimbus-7: Volume 2 - Test and performance data. Final Report, F78-11, Rev. A. Ball Aerospace Systems Division, P.O. Box 1062, Boulder, CO 80306.

Banahan, M., and Rutter, A., 1982, UNIX - The book (Wilmslow, Cheshire: Sigma Technical Press).

Bartolucci, L.A., Robinson, B.F., and Silva, L.F., 1977, Field measurements of the spectral response of natural waters. Photogrammetric Engineering and Remote Sensing, 43, 595-598.

Bauer, M.E., 1976, Technological basis and applications of remote sensing of the Earth's resources. I.E.E.E. Transactions on Geoscience Electronics, GE-14, 3-9.

Baylis, P.E., 1981, University of Dundee satellite image data acquisition and archiving facility. In 'Matching remote sensing technologies and their applications', Proceedings of the Annual Technical Conference, London (Reading: Remote Sensing Society). pp. 517-526.

Bohren, C.F., 1983, Simple experiments in atmospheric physics - colors of the sea. Weatherwise, 36, 256-259.

Boney, A.D., 1975, Phytoplankton (London: Arnold).

Brooks, D.J., 1975, LANDSAT measures of water clarity. Photogrammetric Engineering and Remote Sensing, 41, 1269-1271.

Brown, O.B., and Gordon, H.R., 1974, Size-refractive index distribution of clear coastal water particulates from light scattering. Applied Optics, 13, 2874-2881.

Castleman, K.R., 1979, Digital image processing (Englewood Cliffs, New Jersey: Prentice Hall).

Charlton, J.A., 1980, Sea truth measurements for remote sensing verification. In 'Coastal and marine applications of remote sensing', Proceedings of the Sixth Annual Conference of the Remote Sensing Society, Dundee (Reading: Remote Sensing Society). pp. 85-94.

Clark, D.K., 1981, Phytoplankton pigment algorithms for the Nimbus-7 CZCS. In 'Oceanography from space', edited by J.F.R. Gower (New York: Plenum Press). pp. 227-237.

Clarke, G.L., Ewing, G.C., and Lorenzen, C.J., 1970, Spectra of backscattered light from the sea obtained from aircraft as a measure of chlorophyll concentration. Science, 167, 1119-1121.

Collins, M., and Pattiaratchi, C., 1984, Identification of suspended sediment in coastal waters using airborne thematic mapper data. International Journal of Remote Sensing, 5, 635-657.

Colwell, R.N. (editor-in-chief), 1983, Manual of remote sensing, second edition (Falls Church, Virginia: American Society of Photogrammetry).

Computer (I.E.E.E), 1981, Special issue on pictorial information systems, 14.

Computer (I.E.E.E), 1983, Special issue on computer architectures for image processing, 16.

Cracknell, A.P., 1983, Data acquisition and quality. In 'Remote sensing applications in marine science and technology', edited by A.P. Cracknell (Dordrecht, Holland: Reidel). pp. 35-66.

Curran, P.J., 1981, Remote sensing: the role of small format light aircraft photography. Geographical Papers (Reading University, Geography Department).

Curran, P.J., 1985, Principles of remote sensing (London: Longman).

Daniel, C., and Wood, F.S., 1971, Fitting equations to data, second edition (New York: Wiley-Interscience).

Dave, J.V., 1978, Extensive datasets of the diffuse radiation in realistic atmospheric models with aerosols and common absorbing gases. Solar Energy, 21, 361-369.

DEC, 1979, Microcomputer processor handbook (Maynard, Massachusetts: Digital Equipment Corporation).

Deepak, A. (editor), 1980, Remote sensing of atmospheres and oceans (New York: Academic Press).

Deschamps, P.Y., Lecomte, P., and Viollier, M., 1977, Remote sensing of ocean colour and detection of chlorophyll content. Proceedings of the Eleventh International Symposium on Remote Sensing of Environment, Ann Arbor, Michigan. pp. 1021-1033.

Devijver, P.A., and Kittler, J., 1982, Pattern recognition: a statistical approach (Englewood Cliffs, New Jersey: Prentice-Hall).

Dorn, W.S., and Greenberg, H.J., 1967, Mathematics and computing with FORTRAN programming (New York: Wiley).

Duck, K.I., and King, J.C., 1983, Orbital mechanics for remote sensing. In 'Manual of remote sensing', second edition, editor-in-chief R.N. Colwell (Falls Church, Virginia: American Society of Photogrammetry). pp. 699-717.

Duff, M.J.B., and Levialdi, S. (editors), 1981, Languages and architectures for image processing (London: Academic Press).

Edwards, A.L., 1976, Introduction to linear regression and correlation (San Francisco: W.H. Freeman).

Einstein, A., 1910, Theorie der Opaleszenz von homogenen Flüssigkeiten und Flüssigkeitsgemischen in der Nähe des kritischen Zustandes. Annalen der Physik, 33, 1275-1298.

E.S.L. (Electromagnetic Systems Laboratory), 1976, IDIMS user's guide. Technical Memorandum ESL-TM 705, Sunnyvale, California.

Fleagle, R.G., and Businger, J.A., 1980, An introduction to atmospheric physics (New York: Academic Press).

Fleming, M.D., and Hoffer, R.M., 1977, Computer-aided analysis techniques for an operational system to map forest lands utilising Landsat MSS data. LARS Technical Report 112277, Laboratory for Applications of Remote Sensing, Purdue University, West Lafayette, Indiana.

Frei, W., and Chen, C.C., 1977, Fast boundary detection: a generalisation and a new algorithm. I.E.E.E. Transactions on Computers, 26, 988-998.

Freund, J.E., 1972, Mathematical statistics (Englewood Cliffs, New Jersey: Prentice-Hall).

Goetz, A.F.H., Vane, G., Solomon, J.E., and Rock, B.N., 1985, Imaging spectrometry for Earth remote sensing. Science, 228, 1147-1153.

Gonzalez, R.C., and Wintz, P., 1977, Digital image processing (Reading, Massachusetts: Addison-Wesley).

Gordon, H.R., 1973, Simple calculation of the diffuse reflectance of the ocean. Applied Optics, 12, 2803-2804.

Gordon, H.R., 1976a, Radiative transfer in the ocean: a method for the determination of absorption and scattering properties. Applied Optics, 15, 2611-2613.

Gordon, H.R., 1976b, Radiative transfer: a technique for simulating the ocean in satellite remote sensing calculations. Applied Optics, 15, 1974-1979.

Gordon, H.R., 1977, One parameter characterisation of the ocean's inherent optical properties for remote sensing. Applied Optics, 16, 2627.

Gordon, H.R., 1978a, Remote sensing of optical properties in continuously stratified waters. Applied Optics, 17, 1893-1897.

Gordon, H.R., 1978b, Removal of atmospheric effects from satellite imagery of the oceans. Applied Optics, 17, 1631-1636.

Gordon, H.R., 1980, Irradiance attenuation coefficient in a stratified ocean: a local property of the medium. Applied Optics, 19, 2092-2094.

Gordon, H.R., 1981a, A preliminary assessment of the Nimbus-7 CZCS atmospheric correction algorithm in a horizontally inhomogeneous atmosphere. In 'Oceanography from space', edited by J.F.R. Gower (New York: Plenum Press). pp. 257-265.

Gordon, H.R., 1981b, Reduction of error introduced in the processing of coastal zone color scanner-type imagery resulting from sensor calibration and solar irradiance uncertainty. Applied Optics, 20, 207-210.

Gordon, H.R., and Brown, O.B., 1973, Irradiance reflectivity of a flat ocean as a function of its optical properties. Applied Optics, 12, 1549-1551.

Gordon, H.R., and Brown, O.B., 1974, Influence of bottom depth and albedo on the diffuse reflectance of a flat homogeneous ocean. Applied Optics, 13, 2153-2159.

Gordon, H.R., Brown, J.W., Brown, O.B., Evans, R.H., and Clark, D.K., 1983a, Nimbus 7 CZCS: reduction of its radiometric sensitivity with time. Applied Optics, 22, 3929-3931.

Gordon, H.R., Brown, O.B., and Jacobs, M.M., 1975, Computed relationships between the inherent and apparent optical properties of a flat homogeneous ocean. Applied Optics, 14, 417-427.

Gordon, H.R., and Clark, D.K., 1980a, Atmospheric effects in the remote sensing of phytoplankton pigments. Boundary-Layer Meteorology, 18, 299-313.

Gordon, H.R., and Clark, D.K., 1980b, Remote sensing optical properties of a stratified ocean: an improved interpretation. Applied Optics, 19, 3428-3430.

Gordon, H.R., and Clark, D.K., 1981, Clear water radiances for atmospheric correction of coastal zone color scanner imagery. Applied Optics, 20, 4175-4180.

Gordon, H.R., Clark, D.K., Brown, J.W., Brown, O.B., and Evans, R.H., 1982, Satellite measurement of the phytoplankton pigment concentration in the surface waters of a warm core Gulf Stream ring. Journal of Marine Research, 40, 491-502.

Gordon, H.R., Clark, D.K., Brown, J.W., Brown, O.B., Evans, R.H., and Broenkow, W.W., 1983b, Phytoplankton pigment concentrations in the Middle Atlantic Bight: comparisons of ship determinations and CZCS estimates. Applied Optics, 22, 20-36.

Gordon, H.R., Clark, D.K., Mueller, J.L., and Hovis, W.A., 1980a, Phytoplankton pigments from the Nimbus-7 Coastal Zone Color Scanner: comparisons with surface measurements. Science, 210, 63-66.

Gordon, H.R., and McCluney, W.R., 1975, Estimation of the depth of sunlight penetration in the sea for remote sensing. Applied Optics, 14, 413-416.

Gordon, H.R., and Morel, A.Y., 1983, Remote assessment of ocean color for interpretation of satellite visible imagery (New York: Springer-Verlag).

Gordon, H.R., Mueller, J.L., and Wrigley, R.C., 1980b, Atmospheric correction of Nimbus-7 Coastal Zone Color Scanner imagery. In 'Remote sensing of atmospheres and oceans', edited by A. Deepak (New York: Academic Press). pp. 457-483.

Gower, J.F.R. (editor), 1980, Passive radiometry of the ocean (Dordrecht, Holland: Reidel).

Gower, J.F.R. (editor), 1981, Oceanography from space (New York: Plenum Press).

Gregory, R.L., 1979, Eye and brain, third edition (London: Weidenfeld and Nicolson).

Guberek, M.P., 1985, An interactive satellite data processing system for the earth sciences. In 'Advanced technology for monitoring and processing global environmental data', Proceedings of the International Conference of the Remote Sensing Society and the Center for Earth Resources Management, London (Reading: Remote Sensing Society). p. 288.

Hall, E.L., 1979, Computer image processing and recognition (New York: Academic Press).

Harvey, J.G., 1982, Atmosphere and ocean: our fluid environments (London: Vision Press).

Hibbs, A.R., and Wilson, W.S., 1983, Satellites map the oceans. I.E.E.E. Spectrum, 20, No.10, 46-53.

Højerslev, N.K., 1980, Water color and its relation to primary production. Boundary-Layer Meteorology, 18, 203-220.

Højerslev, N.K., 1981, Assessment of some suggested algorithms on sea colour and surface chlorophyll. In 'Oceanography from space', edited by J.F.R. Gower (New York: Plenum Press). pp. 347-353.

Holligan, P.M., Harris, R.P., Newell, R.C., Harbour, D.S., Head, R.N., Linley, E.A.S., Lucas, M.I., Tranter, P.R.G., and Weekley, C.M., 1984a, Vertical distribution and partitioning of organic carbon in mixed, frontal and stratified waters of the English Channel. Marine Ecology - Progress Series, 14, 111-127.

Holligan, P.M., Viollier, M., Dupouy, C., and Aiken, J., 1983, Satellite studies on the distributions of chlorophyll and dinoflagellate blooms in the western English Channel. Continental Shelf Research, 2, 81-96.

Holligan, P.M., Williams, P.J.leB., Purdie, D., and Harris, R.P., 1984b, Photosynthesis, respiration and nitrogen supply of plankton populations in stratified, frontal and tidally mixed shelf waters. Marine Ecology - Progress Series, 17, 201-213.

Holz, R.K., 1985, The surveillant science: remote sensing of the environment, second edition (New York: Wiley).

Hord, R.M., 1982, Digital image processing of remotely sensed data (New York: Academic Press).

Horstmann, U., and Hardtke, P.G., 1981, Transport processes of suspended matter, including phytoplankton, studied from LANDSAT images of the Southwestern Baltic Sea. In 'Oceanography from space', edited by J.F.R. Gower (New York: Plenum Press). pp. 429-438.

Hovis, W.A., 1981, The Nimbus-7 Coastal Zone Color Scanner (CZCS) program. In 'Oceanography from space', edited by J.F.R. Gower (New York: Plenum Press). pp. 213-225.

Hovis, W.A., 1982, Availability of Nimbus-7 Coastal Zone Color (CZCS) data. Deep-Sea Research (Part A - Oceanographic Research Papers), 29, 281-283.

Hovis, W.A., Clark, D.K., Anderson, F., Austin, R.W., Wilson, W.H., Baker, E.T., Ball, D., Gordon, H.R., Mueller, J.L., El-Sayed, S.Z., Sturm, B., Wrigley, R.C., and Yentsch, C.S., 1980, Nimbus-7 Coastal Zone Color Scanner: system description and initial imagery. Science, 210, 60-63.

Hovis, W.A., and Leung, K.C., 1977, Remote sensing of ocean color. Optical Engineering, 16, 158-166.

Ince, F., 1983, Digital image processing systems and remote sensing. International Journal of Remote Sensing, 4, 129-148.

Jerlov, N.G., 1968, Optical oceanography (Amsterdam: Elsevier Publishing Company).

Jerlov, N.G., 1976, Marine optics (Amsterdam: Elsevier Scientific Publishing Company).

Johnson, R.W., and Harriss, R.C., 1980, Remote sensing for water quality and biological measurements in coastal waters. Photogrammetric Engineering and Remote Sensing, 46, 77-85.

Johnson, R.W., and Munday, J.C., 1983, The marine environment. In 'Manual of remote sensing', second edition, editor-in-chief R.N. Colwell (Falls Church, Virginia: American Society of Photogrammetry). pp. 1371-1496.

Junge, C., 1955, The size distribution and aging of natural aerosols as determined from electrical and optical data on the atmosphere. Journal of Meteorology, 12, 13-25.

Junge, C.E., 1972, Our knowledge of the physico-chemistry of aerosols in the undisturbed marine environment. Journal of Geophysical Research, 77, 5183-5200.

Kane, G., 1981, 68000 microprocessor handbook (Berkeley, California: Osborne/McGraw-Hill).

Kattawar, G.W., and Humphreys, T.J., 1976, Remote sensing of chlorophyll in an atmosphere-ocean environment: a theoretical study. Applied Optics, 15, 273-282.

Kennedy, J.B., and Neville, A.M., 1986, Basic statistical methods for engineers and scientists, third edition (New York: Harper and Row).

Kernighan, B.W., and Mashey, J.R., 1979, The UNIX programming environment. Software- Practice and Experience, 9, 1-15.

Kernighan, B.W., and Ritchie, D.M., 1978, The C programming language (Englewood Cliffs, New Jersey: Prentice-Hall).

Khorram, S., 1981a, Use of ocean color scanner data in water quality mapping. Photogrammetric Engineering and Remote Sensing, 47, 667-676.

Khorram, S., 1981b, Water quality mapping from LANDSAT digital data. International Journal of Remote Sensing, 2, 145-153.

King-Hele, D.G., Pilkington, J.A., Walker, D.M.C., Hiller, H., and Winterbottom, A.N., 1983, The RAE table of earth satellites 1957-1982, second edition (London: Macmillan).

Kirk, J.T.O., 1983, Light and photosynthesis in aquatic ecosystems (Cambridge: Cambridge University Press).

Klooster, S.A., and Scherz, J.P., 1973, Water quality determination by photographic analysis. Proceedings of the Second Annual Remote Sensing of Earth Resources Conference, Tullahoma, Tennessee. pp. 1187-1200.

Kraus, J.D., 1966, Radio astronomy (New York: McGraw-Hill).

Kritikos, H., Yorinks, L., and Smith, H., 1974, Suspended solids analysis using ERTS-A data. Remote Sensing of Environment, 3, 69-78.

Landy, M.S., Cohen, Y., and Sperling, G., 1984, HIPS: A UNIX-based image processing system. Computer Vision, Graphics and Image Processing, 25, 331-347.

Le Fèvre, J., Viollier, M., Le Corre, P., Dupouy, C., and Grall, J-R., 1983, Remote sensing observations of biological material by LANDSAT along a tidal thermal front and their relevancy to the available field data. Estuarine, Coastal and Shelf Science, 16, 37-50.

Lillesand, T.M., and Kiefer, R.W., 1979, Remote sensing and image interpretation (New York: Wiley).

Lillesand, T.M., Scarpace, F.L., and Clapp, J.L., 1975, Water quality in mixing zones. Photogrammetric Engineering and Remote Sensing, 41, 285-298.

Logica, 1983, The INSIGHT image processing software package (London: Logica Ltd).

Lorenzen, C.J., 1966, A method for the continuous measurement of in vivo chlorophyll concentration. Deep-Sea Research, 13, 223-227.

Lorenzen, C.J., 1967, Determination of chlorophyll and pheo-pigments: spectrophotometric equations. Limnology and Oceanography, 12, 343-346.

Lucas, C., and Glover, R.S. (editors), 1975, Bulletins of Marine Ecology, Volume 8, Part 3.

McClain, E.P., 1980, Passive radiometry of the ocean from space - an overview. Boundary-Layer Meteorology, 18, 7-24.

Meyer-Arendt, J.R., 1972, Introduction to modern and classical optics (Englewood Cliffs, New Jersey: Prentice-Hall).

Michael, M., and Lin, W., 1973, Experimental study of information measure and inter-intra class distance ratios on feature selection and orderings. I.E.E.E. Transactions on Systems, Man and Cybernetics, 3, 172-181.

Mie, G., 1908, Beiträge zur Optik trüber Medien speziell kolloidaler Metallösungen. Annalen der Physik, 25, 377-445.

Miles, H. (editor), 1974, Artificial satellite observing and its applications (London: Faber and Faber).

Milgrom, L., 1984, Solar scientists go green with envy. New Scientist, Number 1395, 26-30.

Moore, G., 1986, Looking down on Nature. Electronics and Power (I.E.E.), 32, 369-372.

Morel, A., 1980, In-water and remote measurements of ocean color. Boundary-Layer Meteorology, 18, 177-201.

Morel, A., and Bricaud, A., 1981, Theoretical results concerning the optics of phytoplankton, with special reference to remote sensing applications. In 'Oceanography from space', edited by J.F.R. Gower (New York: Plenum Press). pp. 313-327.

Morel, A., and Gordon, H.R., 1980, Report of the working group on water color. Boundary-Layer Meteorology, 18, 343-355.

Morel, A., and Prieur, L., 1977, Analysis of variations in ocean colour. Limnology and Oceanography, 22, 709-722.

Mueller, J.L., and LaViolette, P.E., 1981, Color and temperature signatures of ocean fronts observed with the Nimbus-7 CZCS. In 'Oceanography from space', edited by J.F.R. Gower (New York: Plenum Press). pp. 295-302.

Paci, G., 1980, Results of studies on a coastal ocean monitoring satellite system. In 'Coastal and marine applications of remote sensing', Proceedings of the Sixth Annual Conference of the Remote Sensing Society, Dundee (Reading: Remote Sensing Society). pp. 105-119.

Pingree, R.D., Pugh, P.R., Holligan, P.M. and Forster, G.R., 1975, Summer phytoplankton blooms and red tides along tidal fronts in the approaches to the English Channel. Nature, 258, 672-677.

Plass, G.N., Kattawar, G.W., and Guinn, J.A., 1975, Radiative transfer in the earth's atmosphere and ocean: influence of ocean waves. Applied Optics, 14, 1924-1936.

Platt, T., and Herman, A.W., 1983, Remote sensing of phytoplankton in the sea: surface layer chlorophyll as an estimate of water-column chlorophyll and primary production. International Journal of Remote Sensing, 4, 343-351.

Potter, J.L., 1983, Image processing on the massively parallel processor. Computer (I.E.E.E.), 16, 62-67.

Rayleigh, Lord, 1871a, On the light from the sky, its polarisation and colour. Philosophical Magazine, 41, 107-120.

Rayleigh, Lord, 1871b, On the light from the sky, its polarisation and colour. Philosophical Magazine, 41, 274-279.

Rayleigh, Lord, 1871c, On the scattering of light by small particles. Philosophical Magazine, 41, 447-454.

Rosenfeld, A., and Kak, A.C., 1982, Digital picture processing, second edition (New York: Academic Press).

Rossi, B., 1967, Optics (Reading, Massachusetts: Addison-Wesley).

Sathyendranath, S., and Morel, A., 1983, Light emerging from the sea - interpretation and uses in remote sensing. In 'Remote sensing applications in marine science and technology', edited by A.P. Cracknell (Dordrecht, Holland: Reidel). pp. 323-357.

Schowengerdt, R.A., 1983, Techniques for image processing and classification in remote sensing (New York: Academic Press).

Sears, F.W., 1949, Optics (Reading: Massachusetts: Addison-Wesley).

Simpson, J.H., and Hunter, J.R., 1974, Fronts in the Irish Sea. Nature, 250, 404-406.

Singh, S.M., 1982, A procedure for atmospheric correction of coastal zone colour scanner (CZCS) data. In 'Remote sensing and the atmosphere', Proceedings of the Annual Technical Conference, Liverpool (Reading: Remote Sensing Society). pp. 169-176.

Singh, S.M., Cracknell, A.P., and Charlton, J.A., 1983, Comparison between CZCS data from 10 July 1979 and simultaneous in-situ measurements for south-eastern Scottish waters. International Journal of Remote Sensing, 4, 755-784.

Slater, P.N., 1980, Remote sensing: optics and optical systems (Reading, Massachusetts: Addison-Wesley).

Slater, P.N., 1983, Photographic systems for remote sensing. In 'Manual of remote sensing', second edition, editor-in-chief R.N. Colwell (Falls Church, Virginia: American Society of Photogrammetry). pp. 231-291.

Slater, P.N., 1986, Survey of multispectral imaging systems for Earth observations. In 'Remote sensing yearbook 1986', edited by A. Cracknell and L. Hayes (London: Taylor & Francis). pp. 141-163.

Smith, R.C., 1981, Remote sensing and depth distribution of ocean chlorophyll. Marine Ecology - Progress Series, 5, 359-361.

Smith, R.C., and Baker, K.S., 1983, Satellites for the study of ocean primary productivity. Advances in Space Research, 3, 123-133.

Smith, R.C., and Wilson, W.H., 1981, Ship and satellite bio-optical research in the California Bight. In 'Oceanography from space', edited by J.F.R. Gower (New York: Plenum Press). pp. 281-294.

Smoluchowski, M., 1908, Molekular-kinetische Theorie der Opaleszenz von Gasen im kritischen Zustande, sowie einiger verwandter Erscheinungen. Annalen der Physik, 25, 205-226.

Sørensen, B.M. (editor), 1981, Recommendations of the 2nd International Workshop on Atmospheric Correction of Satellite Observation of Sea Water Colour. Commission of the European Communities, Joint Research Centre, Ispra Establishment, 21020 Ispra, Varese, Italy.

Spitzer, D., Rappoldt, C., and Nykjaer, L., 1982, Optical remote sensing of turbid coastal waters. Proceedings of the First International Conference on Meteorology and Air/Sea Interaction of the Coastal Zone, The Hague (Boston, Massachusetts: American Meteorological Society). pp. 312-313.

Stewart, R.H., 1985, Methods of satellite oceanography (Berkeley: University of California Press).

Stone, J.M., 1963, Radiation and optics (New York: McGraw-Hill).

Stowe, K.S., 1979, Ocean science (New York: Wiley).

Sturm, B., 1981, The atmospheric correction of remotely sensed data and the quantitative determination of suspended matter in marine surface layers. In 'Remote sensing in meteorology, oceanography and hydrology', edited by A.P. Cracknell (Chichester: Ellis-Horwood). pp. 163-197.

Swain, P.H., and Davis, S.M. (editors), 1978, Remote sensing: the quantitative approach (New York: McGraw-Hill).

Swinbanks, D., 1986, Japan offers free data. Nature, 319, 438.

Tassan, S., 1981, The influence of wind in the remote sensing of chlorophyll in the sea. In 'Oceanography from space', edited by J.F.R. Gower (New York: Plenum Press). pp. 371-375.

Thomas, M.H.B., 1980, The physical basis of remote sensing measurements at sea (London: H.M.S.O.).

Tou, J.T., and Gonzalez, R.C., 1974, Pattern recognition principles (Reading, Massachusetts: Addison-Wesley).

Townshend, J.R.G., and Justice, C.O., 1980, Unsupervised classification of MSS Landsat data for mapping spatially complex vegetation. International Journal of Remote Sensing, 1, 105-120.

Trees, C., 1982, CZCS algorithm summary. EURASEP Secretariat Newsletter, No. 7, Commission of the European Communities, Joint Research Centre, 21020 Ispra, Varese, Italy. pp. 29-37.

Universal Encyclopedia of Mathematics, 1964, (London: Pan).

Vanselous, T.M., Kemmerer, A.J., Hovis, W.A., and Clark, D.K., 1978, Marine applications of the Nimbus-G Coastal Zone Color Scanner. Proceedings of the Twelfth International Symposium on Remote Sensing of Environment, Manilla, Phillipines. pp. 621-637.

Van Wie, P., and Stein, M., 1977, A LANDSAT digital image rectification system. I.E.E.E. Transactions on Geoscience Electronics, 15, 130-137.

Viollier, M., 1982, Radiometric calibration of the Coastal Zone Color Scanner on Nimbus 7: a proposed adjustment. Applied Optics, 21, 1142-1145.

Viollier, M., Deschamps, P.Y., and Lecomte, P., 1978, Airborne remote sensing of chlorophyll content under cloudy sky as applied to the tropical waters in the Gulf of Guinea. Remote Sensing of Environment, 7, 235-248.

Viollier, M., Tanré, D., and Deschamps, P.Y., 1980, An algorithm for remote sensing of water color from space. Boundary-Layer Meteorology, 18, 247-267.

Wade, J.G., Lawrence, D.H., and Rendle, M., 1984, Low-cost remote sensing experiments within an educational environment. Image and Vision Computing, 2, 3-12.

Waltuch, M., Fabos, J.G., and Gross, M., 1985, Workstations for landscape planning: the METLAND case study. In 'Advanced technology for monitoring and processing global environmental data', Proceedings of the International Conference of the Remote Sensing Society and the Center for Earth Resources Management, London (Reading: Remote Sensing Society). pp. 169-175.

Watson, D.J., Economou, D., and Grimsdale, R.L., 1983, Framestore systems for map displays. Image and Vision Computing, 1, 157-162.

Wilson, H.R., 1981, Elementary ideas of optical image processing. In 'Remote sensing in meteorology, oceanography and hydrology', edited by A.P. Cracknell (Chichester: Ellis-Horwood). pp. 114-123.

Wilson, W.H., Smith, R.C., and Nolten, J.W., 1981, The CZCS geolocation algorithms. SIO Ref. 81-32, Scripps Institution of Oceanography, Visibility Laboratory, La Jolla, California 92093.

Yarwood, J., 1973, Electricity and magnetism (London: University Tutorial Press).

Yentsch, C.S., 1983, Remote sensing of biological substances. In 'Remote sensing applications in marine science and technology', edited by A.P. Cracknell (Dordrecht, Holland: Reidel). pp. 263-297.

Yentsch, C.S., and Garfield, N., 1981, Principal areas of vertical mixing in the waters of the Gulf of Maine, with reference to the total productivity of the area. In 'Oceanography from space', edited by J.F.R. Gower (New York: Plenum Press). pp. 303-312.

APPENDICES 1 - 8

APPENDIX 1

IRRADIANCE AND RADIANCE

1) The term irradiance is used when radiation is incident upon a surface and is defined as the total radiant flux (from all directions) per unit area. Denoting irradiance by E:

$$E = \frac{d\Phi}{dA} \qquad \text{(A1.1)}$$

where dA is the area of a small region of the surface, upon which the flux (energy per unit time) is $d\Phi$. Typical units are $mW.cm^{-2}$. Spectral irradiance E_λ is the irradiance per unit wavelength:

$$E_\lambda = \frac{dE}{d\lambda} = \frac{d^2\Phi}{dAd\lambda} \qquad \text{(A1.2)}$$

Typical units are $mW.cm^{-2}.\mu m^{-1}$.

2) The term radiance describes the distribution of flux leaving a surface as a function of angle and is defined as the radiant flux emitted per unit area per unit solid angle. The radiance L is given by:-

IRRADIANCE AND RADIANCE (Continued)

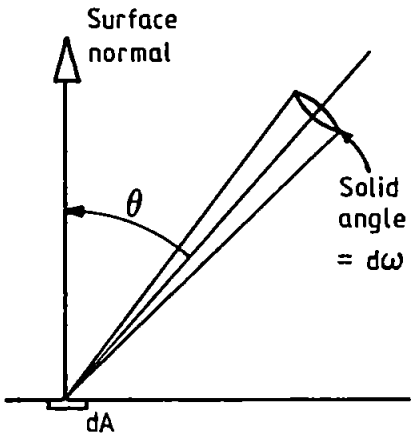

$$L = \frac{d^2\Phi}{dA \cos\theta . d\omega} \qquad (A1.3)$$

This is the radiance in the direction defined by θ. dω is the solid angle of a small cone centred on the specified direction. The term dA.cos θ represents the area of the surface element when viewed from the specified direction. The spectral radiance L_λ is the radiance per unit wavelength:

$$L_\lambda = \frac{dL}{d\lambda} = \frac{d^3\Phi}{dA \cos\theta . d\omega . d\lambda} \qquad (A1.4)$$

Typical units for L and L_λ are $mW.cm^{-2}.sr^{-1}$ and $mW.cm^{-2}.sr^{-1}.\mu m^{-1}$ respectively.

The presence of a cos θ term (in the form of μ) in the denominator of the expressions for Rayleigh and aerosol radiance accounts for the variation of L with θ.

As the CZCS operates in narrow bands within the visible spectrum, the measured quantity is spectral radiance. However the term 'spectral' has been dropped in the text, and both radiance and irradiance should be regarded as spectral quantities throughout.

APPENDIX 2

VOLUME SCATTERING FUNCTION AND SCATTERING COEFFICIENTS

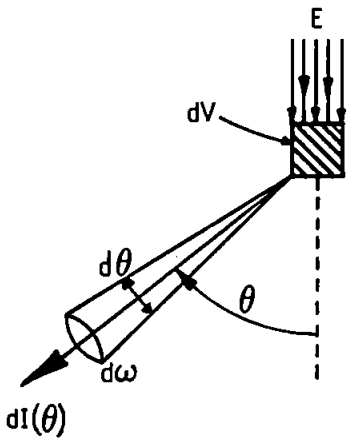

The angular distribution of light scattered from a scattering element is generally anisotropic and the variation with angle θ is specified by means of the volume scattering function β(θ). The intensity (power per unit solid angle) dI(θ) in the direction defined by θ is also directly proportional to the irradiance E and volume dV of the scattering region, that is:

$$dI(\theta) \propto E\, dV \qquad (A2.1)$$

Introducing β(θ) as the constant of proportionality compels it to account for the angular variation and provides a definition for the volume scattering function (Jerlov 1968):

$$\beta(\theta) = \frac{dI(\theta)}{E\,dV} \qquad (A2.2)$$

The units of β(θ) are $m^{-1}.sr^{-1}$. The total scattering coefficient b may be found by integrating β(θ) over all directions:

$$b = \int_{4\pi} \beta(\theta)\, d\omega \qquad (A2.3)$$

where $d\omega$ is the element of solid angle. Alternatively, the integration may be performed over θ, noting that an angular interval from θ to $\theta+d\theta$ represents a solid angle of $2\pi \sin\theta d\theta$. Therefore:

$$b = 2\pi \int_0^{\pi} \beta(\theta) \sin\theta \, d\theta \qquad \text{(A2.4)}$$

The forward and backward scattering coefficients, b_f and b_b respectively, may also be determined from $\beta(\theta)$:

$$b_f = 2\pi \int_0^{\pi/2} \beta(\theta) \sin\theta \, d\theta \qquad \text{(A2.5)}$$

$$b_b = 2\pi \int_{\pi/2}^{\pi} \beta(\theta) \sin\theta \, d\theta \qquad \text{(A2.6)}$$

Inspection of these two equations indicates that $b = b_f + b_b$. The units of b, b_f and b_b are all m^{-1}.

Finally, the scattering phase function $P(\theta)$ is also defined in terms of $\beta(\theta)$ (Gordon 1976a):

$$P(\theta) \equiv \frac{\beta(\theta)}{b} \qquad \text{(A2.7)}$$

$P(\theta)$ has units of sr^{-1}.

APPENDIX 3

DISPLACEMENT OF SUB-SATELLITE POINT FROM SCANLINE

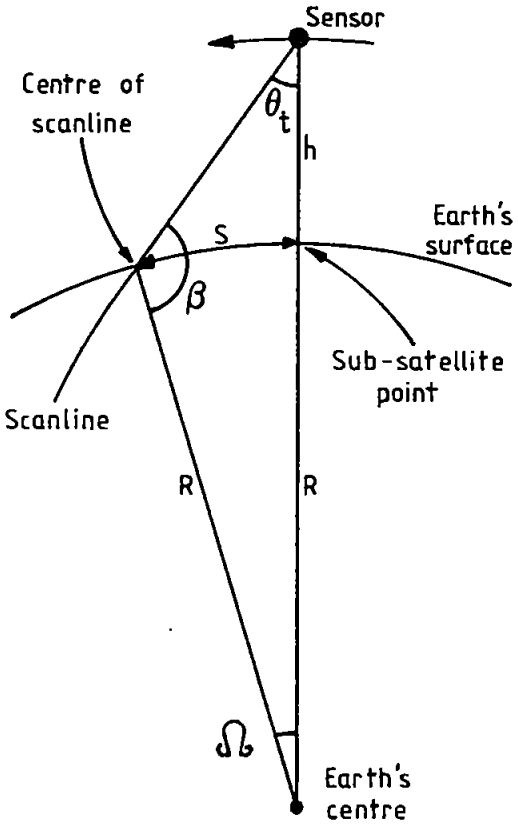

h is the sensor altitude (955 km).

R is the mean Earth radius (6371 km).

θ_t is the scan-mirror tiltangle.

Ω is the angle subtended by S at the Earth's centre.

S is the distance between the sub-satellite point and the centre of the scanline. S is required in the calculation of local time.

$$\beta = \pi - (\Omega + \theta_t)$$

$$R/\sin\theta_t = (R+h)/\sin\beta \qquad \text{(Using the sine rule for triangles)}$$

$$\therefore \sin\beta = (1 + h/R)\sin\theta_t$$

$$\sin\left[\pi - (\Omega + \theta_t)\right] = (1 + h/R)\sin\theta_t \qquad \text{(Substituting for } \beta\text{)}$$

$$\sin(\Omega + \theta_t) = (1 + h/R)\sin\theta_t \qquad (\sin[\pi - x] = \sin x)$$

$$\Omega = \sin^{-1}\left[(1 + h/R)\sin\theta_t\right] - \theta_t$$

DISPLACEMENT OF SUB-SATELLITE POINT FROM SCANLINE (Continued)

If the angle Ω is expressed in radians then:

$$S = \Omega R$$

$$S = R\left\{\sin^{-1}\left[(1+h/R)\sin\theta_t\right] - \theta_t\right\}$$

NOTE:

This expression may also be used to find the ground resolution as a function of scan-angle and to calculate the swath width by substituting the scan angle for θ_t.

APPENDIX 4

RECTIFICATION

Rectification, that is the identification of pixels corresponding to ship samples, requires the satisfaction of a least-squares criterion. Specifically, it requires that the following expression should be minimised (Eq. 3.35 of Section 3.3.1.3):

$$\sum_{i=1}^{n} (Z_i - c_o x_{oi} - c_1 x_{1i} - c_2 x_{2i} - c_3 x_{3i} - c_4 x_{4i} - c_5 x_{5i})^2 \qquad (A4.1)$$

This is achieved by partially differentiating Eq. A4.1 with respect to each coefficient and setting the result equal to zero in each case (Daniel and Wood 1971, Freund 1972):

$$\frac{\partial}{\partial c_k} \sum_{i=1}^{n} (Z_i - c_o x_{oi} - c_1 x_{1i} - c_2 x_{2i} - c_3 x_{3i} - c_4 x_{4i} - c_5 x_{5i})^2 = 0 \qquad (A4.2)$$

where c_k is the K^{th} polynomial coefficient and K = 0,...,5. Eq. A4.2 therefore represents a set of six equations. Substituting g_i for the expression within parentheses in Eq. A4.2:

$$\frac{\partial}{\partial c_k} \sum_{i=1}^{n} g_i^2 = 0$$

$$\sum_{i=1}^{n} \frac{\partial}{\partial c_k} (g_i)^2 = 0$$

$$2 \sum_{i=1}^{n} g_i \cdot \frac{\partial g_i}{\partial c_k} = 0 \qquad (A4.3)$$

$\frac{\partial g_i}{\partial c_k}$ is found by partially differentiating the expression within parentheses in Eq. A4.2:

$$\frac{\partial g_i}{\partial c_k} = \frac{\partial}{\partial c_k}\left(Z_i - c_o x_{oi} - c_1 x_{1i} - c_2 x_{2i} - c_3 x_{3i} - c_4 x_{4i} - c_5 x_{5i}\right)$$

$$= -x_{ki}$$

Eq. A4.3 now becomes:

$$2\sum_{i=1}^{n} g_i\left(-x_{ki}\right) = 0$$

$$\sum_{i=1}^{n} g_i . x_{ki} = 0 \qquad \text{(A4.4)}$$

Replacing g_i with the expression within parentheses in Eq. A4.2, Eq. A4.4 becomes:

$$\sum_{i=1}^{n}\left(Z_i - c_o x_{oi} - c_1 x_{1i} - c_2 x_{2i} - c_3 x_{3i} - c_4 x_{4i} - c_5 x_{5i}\right) . x_{ki} = 0$$

Rearranging:

$$\sum_{i=1}^{n} Z_i x_{ki} = \sum_{i=1}^{n}\left(c_o x_{oi} + c_1 x_{1i} + c_2 x_{2i} + c_3 x_{3i} + c_4 x_{4i} + c_5 x_{5i}\right) . x_{ki} \qquad \text{(A4.5)}$$

Eq. A4.5 may be expressed more concisely by dropping the 'i' subscripts and using Σ alone to represent the summation over i:

$$\Sigma Z x_k = c_o \Sigma x_o x_k + c_1 \Sigma x_1 x_k + c_2 \Sigma x_2 x_k + c_3 \Sigma x_3 x_k + c_4 \Sigma x_4 x_k + c_5 \Sigma x_5 x_k \qquad \text{(A4.6)}$$

Eq. A4.6 may be expanded to produce a set of six equations which are as follows (for K = 0,...,5 respectively):

$$c_0\Sigma x_0^2 + c_1\Sigma x_1x_0 + c_2\Sigma x_2x_0 + c_3\Sigma x_3x_0 + c_4\Sigma x_4x_0 + c_5\Sigma x_5x_0 = \Sigma Zx_0$$

$$c_0\Sigma x_0x_1 + c_1\Sigma x_1^2 + c_2\Sigma x_2x_1 + c_3\Sigma x_3x_1 + c_4\Sigma x_4x_1 + c_5\Sigma x_5x_1 = \Sigma Zx_1$$

$$c_0\Sigma x_0x_2 + c_1\Sigma x_1x_2 + c_2\Sigma x_2^2 + c_3\Sigma x_3x_2 + c_4\Sigma x_4x_2 + c_5\Sigma x_5x_2 = \Sigma Zx_2$$

$$c_0\Sigma x_0x_3 + c_1\Sigma x_1x_3 + c_2\Sigma x_2x_3 + c_3\Sigma x_3^2 + c_4\Sigma x_4x_3 + c_5\Sigma x_5x_3 = \Sigma Zx_3$$

$$c_0\Sigma x_0x_4 + c_1\Sigma x_1x_4 + c_2\Sigma x_2x_4 + c_3\Sigma x_3x_4 + c_4\Sigma x_4^2 + c_5\Sigma x_5x_4 = \Sigma Zx_4$$

$$c_0\Sigma x_0x_5 + c_1\Sigma x_1x_5 + c_2\Sigma x_2x_5 + c_3\Sigma x_3x_5 + c_4\Sigma x_4x_5 + c_5\Sigma x_5^2 = \Sigma Zx_5$$

These six equations may be converted into matrix form with $x_0,\ldots,x_5$ transformed back to their original forms of 1, E, N, E^2, EN and N^2 respectively:

$$\begin{bmatrix} \Sigma 1^2 & \Sigma E & \Sigma N & \Sigma E^2 & \Sigma EN & \Sigma N^2 \\ \Sigma E & \Sigma E^2 & \Sigma EN & \Sigma E^3 & \Sigma E^2N & \Sigma EN^2 \\ \Sigma N & \Sigma EN & \Sigma N^2 & \Sigma E^2N & \Sigma EN^2 & \Sigma N^3 \\ \Sigma E^2 & \Sigma E^3 & \Sigma E^2N & \Sigma E^4 & \Sigma E^3N & \Sigma E^2N^2 \\ \Sigma EN & \Sigma E^2N & \Sigma EN^2 & \Sigma E^3N & \Sigma E^2N^2 & \Sigma EN^3 \\ \Sigma N^2 & \Sigma EN^2 & \Sigma N^3 & \Sigma E^2N^2 & \Sigma EN^3 & \Sigma N^4 \end{bmatrix} \times \begin{bmatrix} c_0 \\ c_1 \\ c_2 \\ c_3 \\ c_4 \\ c_5 \end{bmatrix} = \begin{bmatrix} \Sigma Z \\ \Sigma ZE \\ \Sigma ZN \\ \Sigma ZE^2 \\ \Sigma ZEN \\ \Sigma ZN^2 \end{bmatrix}$$

This set of linear simultaneous equations is solved using the Gaussian Elimination technique (Dorn and Greenberg 1967) which converts the six by six matrix above into a triangular one, that is, one whose elements below the leading diagonal are all zero. The leading diagonal is the diagonal of matrix elements from the top left to the bottom right of the matrix. The technique is best explained by using a simple example of three simultaneous equations in matrix form:

$$\begin{bmatrix} a_{00} & a_{01} & a_{02} \\ a_{10} & a_{11} & a_{12} \\ a_{20} & a_{21} & a_{22} \end{bmatrix} \begin{bmatrix} x_0 \\ x_1 \\ x_2 \end{bmatrix} = \begin{bmatrix} y_0 \\ y_1 \\ y_2 \end{bmatrix}$$

For this three by three matrix to be triangular, elements a_{10}, a_{20} and a_{21} must be zero, i.e. eliminated. This is achieved by deriving a new row from two existing ones. For example, coefficient a_{10} is made zero in the following manner:

i) Calculate a multiplier $m = a_{10}/a_{00}$.

ii) Replace a_{10} by $a'_{10} = a_{10} - m a_{00} = 0$, as desired.

iii) Replace a_{11} by $a'_{11} = a_{11} - m a_{01}$.

iv) Replace a_{12} by $a'_{12} = a_{12} - m a_{02}$.

v) Replace y_1 by $y'_1 = y_1 - m y_0$.

In a similar way, a_{20} is eliminated by applying the same method to the third row with a multiplier m of a_{20}/a_{00}. The matrix equation then becomes:

RECTIFICATION (Continued)

$$\begin{bmatrix} a_{00} & a_{01} & a_{02} \\ 0 & a'_{11} & a'_{12} \\ 0 & a'_{21} & a'_{22} \end{bmatrix} \times \begin{bmatrix} x_0 \\ x_1 \\ x_2 \end{bmatrix} = \begin{bmatrix} y_0 \\ y'_1 \\ y'_2 \end{bmatrix}$$

All that remains is for a'_{21} to be eliminated. The same algorithm is applied once more with $m = a'_{21}/a'_{11}$:

i) Replace a'_{21} by $a''_{21} = a'_{21} - ma'_{11} = 0$, as desired.

ii) Replace a'_{22} by $a''_{22} = a'_{22} - ma'_{12}$.

iii Replace y'_2 by $y''_2 = y'_2 - my'_1$.

This results in the triangular form:

$$\begin{bmatrix} a_{00} & a_{01} & a_{02} \\ 0 & a'_{11} & a'_{12} \\ 0 & 0 & a''_{22} \end{bmatrix} \times \begin{bmatrix} x_0 \\ x_1 \\ x_2 \end{bmatrix} = \begin{bmatrix} y_0 \\ y'_1 \\ y''_2 \end{bmatrix}$$

The third row enables x_2 to be found. With this value, x_1 may be derived from the second row. Finally, knowing x_2 and x_1, the first row is used to find x_0. Exactly the same algorithm, but extended to a six by six matrix, is used to solve the rectification problem giving values for $c_0,\ldots,c_5$. This algorithm is easily implemented in a program, needing just eight lines.

The correlation coefficient r is given by (Alder and Roessler 1977):

$$r = \sqrt{\frac{SSR}{SS}} = \sqrt{\frac{\sum(Z_E - \bar{Z})^2}{\sum(Z - \bar{Z})^2}}$$

where $\overline{Z}$ is the mean value of Z. SS is the dispersion or spread of Z values about the mean and represents the total variation in Z. SSR (sum of squares for regression) is the dispersion of estimated Z values (Z_E) about the mean, and is a measure of the variation accounted for by the polynomial regression.

APPENDIX 5

RELATIONSHIPS BETWEEN ATTENUATION COEFFICIENT, OPTICAL DEPTH AND TRANSMITTANCE

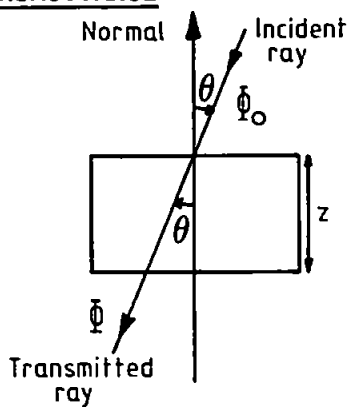

The intensity of light is reduced from Φ_0 to Φ on passing through an attenuating medium. Assuming that the medium is homogeneous with an attenuation coefficient c, then Φ is related to Φ_0 through:

$$\Phi = \Phi_0 e^{-cz/\cos\theta} \qquad (A5.1)$$

where z is the thickness of the medium and θ is the angle of incidence measured from the normal; this is the same as the zenith angle. The distance traversed by the ray is known as the pathlength and equals $z/\cos\theta$. As attenuation may be due to absorption and scattering then c = a + b where a and b are the absorption and scattering coefficients respectively.

Atmospheric composition and density vary with altitude and consequently a, b and hence c are all functions of altitude. In this case the cz term in the expression above is replaced by $\int c(z)dz$ with appropriate limits.

The overall attenuation of the whole atmosphere may be characterised by a single parameter, the optical depth or thickness τ, in the following way:

RELATIONSHIPS BETWEEN ATTENUATION COEFFICIENT, OPTICAL DEPTH AND TRANSMITTANCE (Continued)

$$\Phi = \Phi_0 e^{-\tau/\cos\theta} \tag{A5.2}$$

where $\tau = \int c(z)dz$.

The direct or beam transmittance T is defined by:

$$T = \frac{\text{Transmitted flux intensity}}{\text{Incident flux intensity}} = \frac{\Phi}{\Phi_0} \tag{A5.3}$$

$$= \exp\left(-\tau/\cos\theta\right) \tag{A5.4}$$

$$= \exp\left[-\int c(z)dz \Big/ \cos\theta\right] \tag{A5.5}$$

$$= \exp\left[-\int \left(a(z) + b(z)\right) \Big/ \cos\theta\right] \tag{A5.6}$$

The units of attenuation, absorption and scattering coefficients are m^{-1}; optical depth and transmittance are dimensionless quantities.

APPENDIX 6

RELATIONSHIP BETWEEN θ, θ_t and θ_v

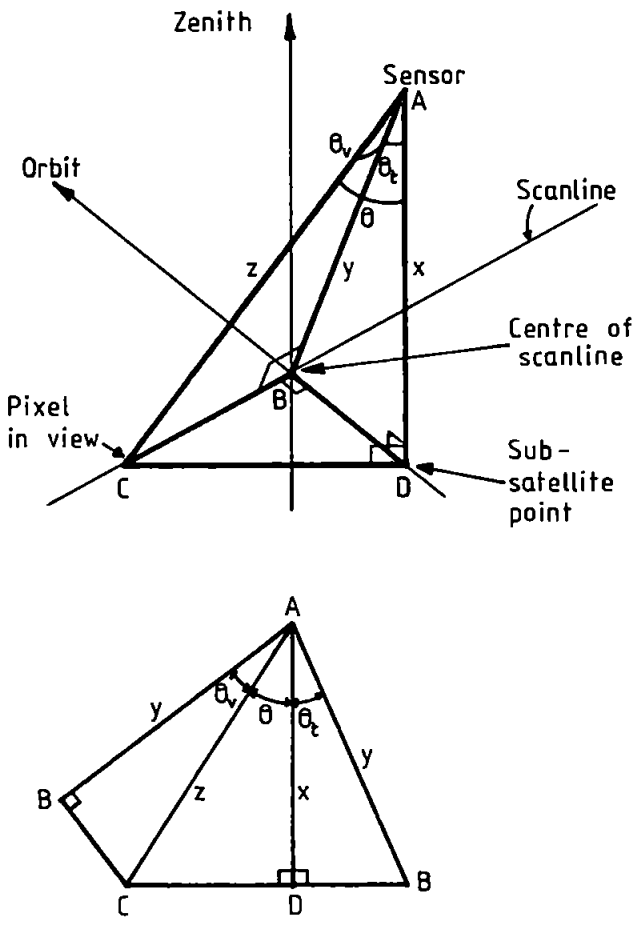

θ_t is the tiltangle; positive in this case.

θ_v is the view-angle; negative in this case.

θ is the zenith angle of the pixel-in-view to sensor direction. Also known as polar angle.

Sensor altitude is x.

1) Consider triangle ACD: $z \cos \theta = x$, $z = x/\cos\theta$.

2) Consider triangle ABD: $y \cos \theta_t = x$, $y = x/\cos\theta_t$.

3) Consider triangle ABC: $z \cos \theta_v = y$.

RELATIONSHIP BETWEEN θ, θ_t and θ_v (Continued)

Substituting for z and y in the third expression above:

$$\left(\frac{x}{\cos\theta}\right)\cos\theta_v = \left(\frac{x}{\cos\theta_t}\right)$$

$$\left(\frac{\cos\theta_v}{\cos\theta}\right) = \left(\frac{1}{\cos\theta_t}\right)$$

$$\cos\theta = \cos\theta_t . \cos\theta_v$$

$$\theta = \cos^{-1}\left[\cos\theta_t . \cos\theta_v\right]$$

APPENDIX 7

RELATIONSHIP BETWEEN ϕ', θ_t and θ_v

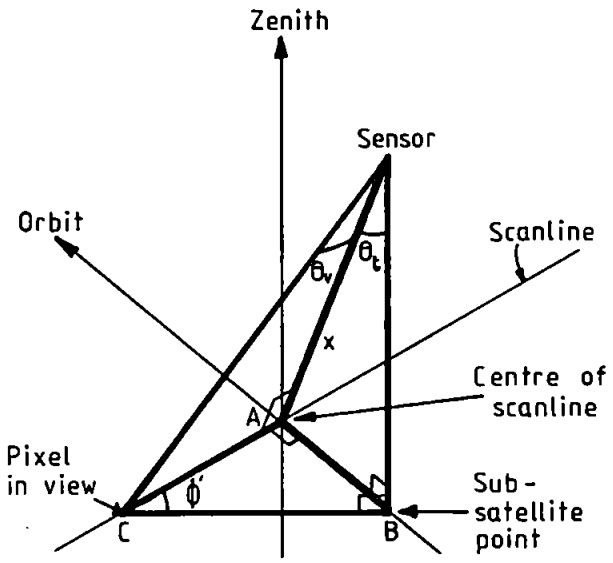

θ_t is the tiltangle; shown as positive.

θ_v is the view-angle; shown as negative.

ϕ' is required in the calculation of ϕ.

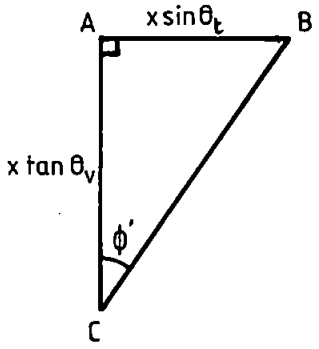

$$(x \tan\theta_v) \tan\phi' = x \sin\theta_t$$

$$\tan\phi' = \frac{\sin\theta_t}{\tan\theta_v}$$

$$\phi' = \left| \tan^{-1}\left(\frac{\sin\theta_t}{\tan\theta_v}\right) \right|$$

APPENDIX 8

DETERMINATION OF SCATTERING ANGLES

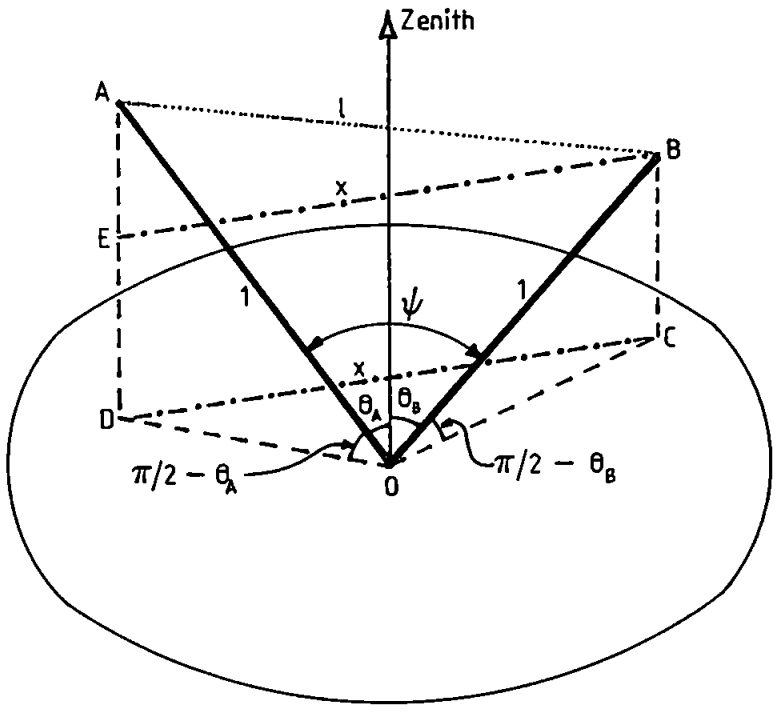

HEMISPHERE WITH RADIUS OF 1.

$\overline{BC} = \overline{DE}$

ORIGIN AT O.

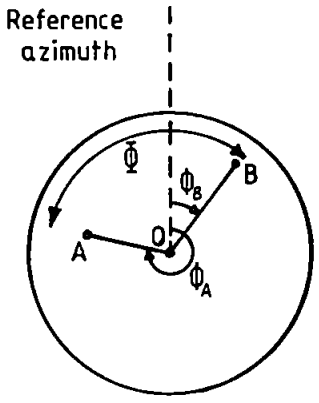

Plan view

The scattering angle ψ is the angle between the directions defined by OA and OB. The position of A, with respect to the origin O, is specified by its zenith angle θ_A and azimuth angle ϕ_A; likewise for B. Only the directions of A and B are important, so the lengths of OA and OB are set to one for simplicity.

The solution of ψ comprises three stages:

APPENDIX 8

DETERMINATION OF SCATTERING ANGLES (Continued)

1) Find x from the triangle OCD, using the cosine rule.

2) Find l from the triangle ABE, using Pythagoras's theorem.

3) Find ψ from the triangle ABO, using the cosine rule.

1) The length of OC is 1.cos $(\pi/2 - \theta_B)$ which equals $\sin\theta_B$. Similarly, the length of OD is $\sin\theta_A$. Therefore:

$$x^2 = \sin^2\theta_A + \sin^2\theta_B - 2\sin\theta_A \sin\theta_B \cos\Phi$$

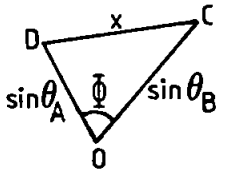

2) The length of BC and DE is 1.sin $(\pi/2 - \theta_B)$ which equals $\cos\theta_B$. Similarly, the length of AD is $\cos\theta_A$. The length of AE is $\overline{AD}$ - $\overline{DE}$ which equals $\cos\theta_A - \cos\theta_B$. Hence:

$$l^2 = x^2 + (\cos\theta_A - \cos\theta_B)^2$$

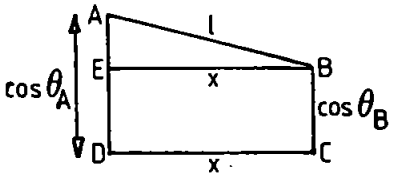

Substituting for x^2 gives:

$$l^2 = \sin^2\theta_A + \sin^2\theta_B - 2\sin\theta_A \sin\theta_B \cos\Phi + \cos^2\theta_A + \cos^2\theta_B - 2\cos\theta_A \cos\theta_B$$

$$l^2 = 2 - 2\left(\cos\theta_A \cos\theta_B + \sin\theta_A \sin\theta_B \cos\Phi\right)$$

3) The cosine rule gives the following for triangle ABO:

APPENDIX 8

DETERMINATION OF SCATTERING ANGLES (Continued)

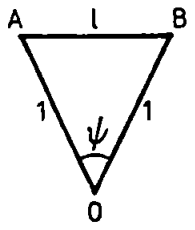

$$l^2 = 1^2 + 1^2 - 2.1.1\cos\psi$$

$$l^2 = 2 - 2\cos\psi$$

Substituting for l^2 gives:

$$2 - 2\cos\psi = 2 - 2\left(\cos\theta_A\cos\theta_B + \sin\theta_A\sin\theta_B\cos\Phi\right)$$

$$\cos\psi = \cos\theta_A\cos\theta_B + \sin\theta_A\sin\theta_B\cos\Phi$$

where Φ is the difference between ϕ_A and ϕ_B. Since cosine is an even function then either $(\phi_A - \phi_B)$ or $(\phi_B - \phi_A)$ may be used. It is possible for Φ to exceed π, in which case Φ should be replaced by $2\pi - \Phi$, however this is unnecessary because $\cos(2\pi - \Phi) = \cos\Phi$.

ψ, as given by the expression above, is simply the angle between two directions, measured in the plane in which the directions lie. The Sun-satellite geometry of the CZCS is not as straightforward and ψ represents neither the forward nor the backward scattering angle, but they both may be derived from it.

The forward scattering angle is associated with reflectance terms $\rho(\theta)$ and $\rho(\theta_0)$ and ψ_+ is the angle between the direction of the solar beam after reflection at the pixel-in-view and the pixel-in-view to sensor direction:

APPENDIX 8

DETERMINATION OF SCATTERING ANGLES (Continued)

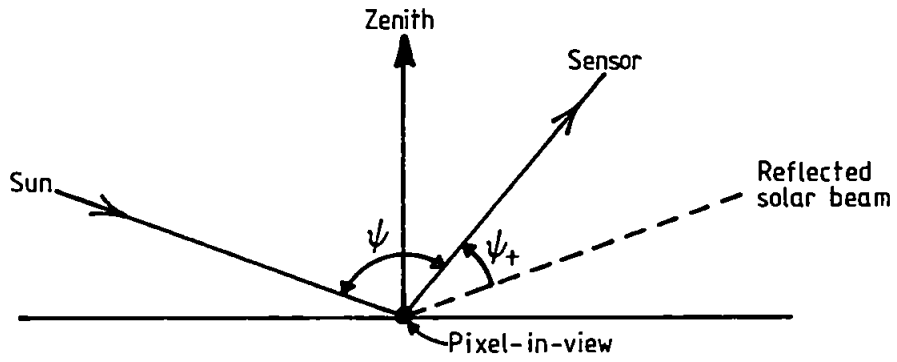

The angle ψ is given by the following expression (after changing θ_A, θ_B, ϕ_A and ϕ_B to those appropriate for the CZCS):

$$\cos\psi = \cos\theta\cos\theta_o + \sin\theta\sin\theta_o\cos\Phi$$

where Φ is $(\phi - \phi_o)$. The zenith angle of the solar beam and reflected solar beam are both θ_o, but the azimuth angles differ by π. By making an adjustment of π radians to Φ, ψ_+ may be determined thus:

$$\cos\psi_+ = \cos\theta\cos\theta_o + \sin\theta\sin\theta_o\cos(\Phi+\pi)$$

$$\cos\psi_+ = \cos\theta\cos\theta_o - \sin\theta\sin\theta_o\cos\Phi$$

since $\cos(\Phi + \pi) = -\cos\Phi$.

The backscattering angle is not associated with reflection of the solar beam and is the angle between the direction of the transmitted solar beam (when no scattering occurs) and the pixel-in-view to sensor direction:

APPENDIX 8

DETERMINATION OF SCATTERING ANGLES (Continued)

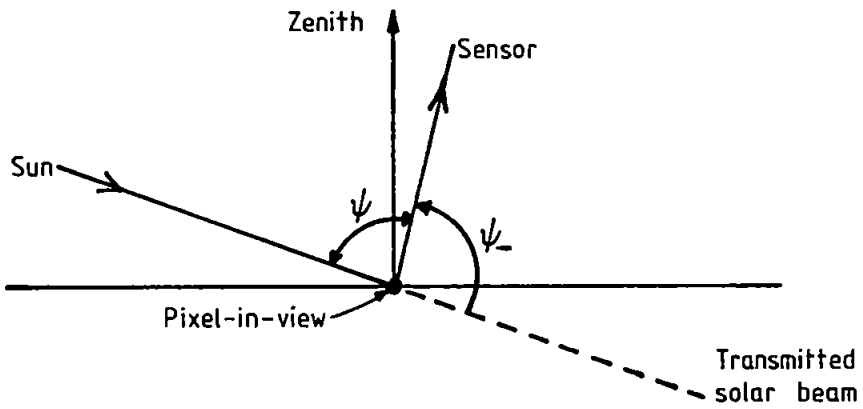

$\psi_- = \pi - \psi$ where ψ is found from:

$$\cos\psi = \cos\theta\cos\theta_o + \sin\theta\sin\theta_o\cos\Phi$$

A more elegant form can be produced by noting that:

$$\cos\psi_- = \cos(\pi - \psi) = -\cos\psi$$

Therefore:

$$\cos\psi_- = -(\cos\theta\cos\theta_o + \sin\theta\sin\theta_o\cos\Phi)$$

$$\cos\psi_- = -\cos\theta\cos\theta_o - \sin\theta\sin\theta_o\cos\Phi$$

The expressions for ψ_+ and ψ_- may be combined into one:

$$\cos\psi_\pm = \pm\cos\theta\cos\theta_o - \sin\theta\sin\theta_o\cos(\phi - \phi_o)$$

The sign of the $\cos\theta.\cos\theta_0$ term selects the forward or backward scattering angle. Φ has been replaced by $\phi - \phi_0$.

APPENDIX 9

LISTING OF THE ATMOSPHERIC CORRECTION PROGRAM

```
/*
        1         2         3         4         5         6         7         8
12345678901234567890123456789012345678901234567890123456789012345678901234567890

atmos.c         Performs atmospheric correction of CZCS images. See atmos.doc
-------         for further details.

Data for mean solar irradiances and Rayleigh and ozone optical thicknesses
obtained from 'Eurasep Secretariat Newsletter', February 1982, pages 18 and 37.
See also 'Recommendations of the 2nd International Workshop on Atmospheric
Correction of Satellite Observation of Sea Water Colour'.

D.H.Lawrence    8/6/84          Version 1

Department of Communication Engineering, Plymouth Polytechnic, Drake Circus,
Plymouth. PL4 8AA.

Variables       Brief description
---------       -----------------
alpha           Orbital inclination as a function of latitude
angsexp         Angstrom exponent
angsfact        waveratio raised to the power angsexp
bscatang        Array of back-scattering angles
cellat          Array of latitude values for centre of each cell (radians)
cellong         Array of longitude values for centre of each cell (radians)
channel         Channel number (1-3)
column          Column number
coordbuf        Input buffer for sample coordinates
correct1        Corrects picture-time to time at which pixel was viewed
correct2        Corrects time at which pixel was viewed to local time
cosalpha        Cosine of alpha
coscenlat       Cosine of scenelat or cosine of cellat
day             1 - 31 (for the date)
daynumber       1 - 365
day_tab         Table of number of days in each month
delta           Solar declination angle
deltacap        Capital delta, scanline azimuth angle (radians)
direct          Flag for West or East of Greenwich
dist1           Distance between pixel & receiving station (along a meridian)
dist2           Distance between pixel & sub-satellite point (along a meridian)
factor          Distance factor used to adjust solar irradiances
fildes1-3       File descriptors for filename1-3
fildes4         File descriptor for ...../dave/atmoscorr/coords (sample coords.)
filename1       Contains name of file to be corrected
filename2       Contains name of corresponding channel 4 file
filename3       Contains name of corrected output file
fscatang        Array of forward scattering angles
hour            1 - 24 (for the picture time)
i               Count used in 'for' loops etc
incid           Angle of incidence (above or below water) radians
initmnfr        Initial minor frame number (1-9) for left-hand edge of image
intrayx         Input line buffer (768 bytes) for channel 1,2 or 3
intray4         Input line buffer (768 bytes) for channel 4
intrcptx        Channel 1/2/3 intercept for radiometric conversion
intrcpt4        Channel 4 intercept for radiometric conversion
latcell         Radians of latitude subtended by 64 pixels (half cell)
latdegs         Degrees of latitude for centre of image
latmins         Minutes of latitude for centre of image
leap            Indicates leap year
line            Line number (0 - 511), used as array subscript
lines           Line number derived from line; used by atmos2 function
longcell        Radians of longitude subtended by 64 pixels (half cell)
longdegs        Degrees of longitude for centre of image
longmins        Minutes of longitude for centre of image
minute          0 - 59 (for the picture time)
month           1 - 12 (for the date)
negcount        Number of occurences of negative radiance in a line (768 pixels)
offset          Offset for lseek; used by atmos2 function
omega           Angle subtended at earth's centre by shift
outrayx         Output line buffer (768 bytes) for corrected channel 1,2 or 3
phi1            Used in determination of scanner azimuth
phi2            Used in determination of scanner azimuth
pictime         Picture time in hours G.M.T
pixelnum        Pixel number (114 - 2081), used to find viewangle
pixel           Pixel number (0 - 767), used as array subscript
phasefn1        Array of fwd. phase function values for Rayleigh scattering
```

```
phasefn2        Array of back phase function values for Rayleigh scattering
polang          Array of 6 'polar' angles (function of tilt & view angles)
printing        Indicates whether printing of intermediate values is required
radx            Aperture radiance for channel 1,2 or 3 for a single pixel
rad4            Aperture radiance for channel 4 for a single pixel
rayradx         Array of Rayleigh radiances for each cell centre for ch1/2/3
rayrad4         Array of Rayleigh radiances for each cell for channel 4
refindex        Refractive index of seawater
refract         Angle of refraction (above or below water) radians
row             Row number
scale           Radiance to pixel (byte) scaling factor
scanazim        Array of scanner azimuth angles for cell centres (radians)
scenelat        Latitude for centre of image
scenelong       Longitude for centre of image
season          Summer or winter; affects selection of optical thicknesses
shift           Distance between sub-satellite point & current scanline
sinalpha        Sine of alpha
sindelta        Sine of delta
sineterm        Used in the determination of Fresnel reflectance
slopex          Channel 1/2/3 slope for radiometric conversion
slope4          Channel 4 slope for radiometric conversion
solar_irrad     Array containing the seasonally adjusted solar irradiances
solazim         Array of solar azimuth angles for cell centres (radians)
solzen          Array of solar zenith angles for cell centres (radians)
status          Value returned by functions (0 or 1)
summer          Used to denote summer season
tanterm         Used in the determination of Fresnel reflectance
tauoz_tab       Table of ozone optical thicknesses
tauozx          Channel 1/2/3 ozone optical thickness
tauoz4          Channel 4 ozone optical thickness
taur_tab        Table of Rayleigh optical thicknesses
taurx           Channel 1/2/3 Rayleigh optical thickness
taur4           Channel 4 Rayleigh optical thickness
tilt            Scanner tilt angle in degrees (integer form)
tiltangle       Scanner tilt angle in radians (floating point form)
time_tab        Table of local times for each cell centre
totalneg        Total number of negative radiance pixels in a 768 by 512 image
transbmx        Channel 1/2/3 array of beam (direct) transmittances
transbm4        Channel 4 array of beam (direct) transmittances
transdfx        Array of 6 diffuse transmittances for channel 1, 2 or 3
viewangle       Array of 6 view angles; function of pixel numbers only
wavelens        Array of channel wavelength values
waveratio       [lambda0/lambda]
winter          Used to denote winter season
x,y,z           Used for intermediate float values
xcomp1          +xcomp1*sin(alpha) is 1 component of cell latitude
xcomp2          +xcomp2*cos(alpha) is 1 component of cell longitude
year            Year number (for the date)
yesorno         Decision flag
ycomp1          +ycomp1*cos(alpha) is 1 component of cell latitude
ycomp2          -ycomp2*sin(alpha) is 1 component of cell longitude
zone            Function of latitude, used to select optical thicknesses

Functions       Brief description
---------       -----------------
atmos1          Evaluates final correction algorithm for whole image
atmos2          Evaluates final correction algorithm for sample points
cellcent        Calculates latitude & longitude for cell centres
confirm         Confirms choice of parameters
day_of_year     Calculates days between Jan 1 & date
decline         Calculates solar declination angle
fresnel1        Calculates reflection coeff. for air --> water
fresnel2        Calculates reflection coeff. for water --> air
globalval       Determines global values
localval        Determines local values
optdepth        Selects appropriate Rayleigh & ozone optical thicknesses
params          Collects parameters from console
phasefuncs      Calculates forward & backward Rayleigh phase functions
polarang        Calculates the 6 'polar' or scanner zenith angles (in radians)
rayleigh        Calculates the Rayleigh radiance for each cell centre
scannerazim     Calculates scanner azimuth angle for each cell centre
solarazim       Calculates solar azimuth angle for each cell centre
solarirrad      Calculates adjusted solar irradiances
solarzen        Calculates solar zenith angle for each cell centre
times           Calculates local time for centre of each cell
transmit        Calculates diffuse and beam (direct) transmittances
*/
```

```
#include <math.h>

#define ALTITUDE      955.0       /* Kilometres */
#define CONVERSION    1.852       /* Number of Km in 1 Nautical Mile */
#define EARTHRADIUS 6371.0        /* Kilometres */
#define ECCENTRIC     0.0167      /* Eccentricity of earth's orbit */
#define EOF             0         /* End of file flag */
#define FIRSTPIXEL      114       /* Pixel number for left-hand end of scanline */
#define FRAMESIZE       136       /* Number of pixels in each minor frame */
#define GRESX         0.782       /* Ground resolution along CZCS track, Km */
#define GRESY         0.765       /* Ground resolution along scanline, Km */
#define IFOV      0.000698        /* Instantaneous field of view (radians) */
#define INCLINATION  23.44        /* Inclination of equator to ecliptic */
#define LATRXSTAT  56.4667        /* Latitude of receiving station (Dundee) */
#define LINES           512       /* Number of lines in image */
#define MID_AUTUMN      311       /* Daynumber for the middle of autumn */
#define MID_SPRING      126       /* Daynumber for the middle of spring */
#define NADIRPIX       1090       /* Nadir pixel number */
#define NOFILE           -1       /* No file flag */
#define PI    3.1415926536        /* PI/4 = Inverse tangent of 1 radian */
#define PIXELS           768      /* Number of pixels in one line */
#define SCANTIME   0.12375        /* Seconds */
#define SOLIRR1     186.42        /* Mean solar irradiance for channel 1 */
#define SOLIRR2     185.34        /* Mean solar irradiance for channel 2 */
#define SOLIRR3     184.76        /* Mean solar irradiance for channel 3 */
#define SOLIRR4     151.52        /* Mean solar irradiance for channel 4 */
#define TRACKINC      9.28        /* Trackline inclination at equator; degrees */
#define VELOCITY     6.416        /* Sub-satellite ground velocity, Km/second */
#define VERNALDAY    80.25        /* Approximately March 21 */

char direct,filename1[40],filename2[40],filename3[40],intrayx[PIXELS];
char intray4[PIXELS],outrayx[PIXELS],printing,yesorno;

int channel,day,daynumber,fildes1,fildes2,fildes3,hour,initmnfr,latdegs;
int latmins,londegs,lonmins,minute,month,scale,tilt,year;
int wavelens[5] = {0,443,520,550,670};

float angsexp,angsfact,cellat[4][6],cellons[4][6],intrptx,intrpt4;
float phasefn1[4][6],phasefn2[4][6],pictime,polang[6],rayradx[4][6];
float rayrad4[4][6],refindex,scanazim[4][6],scenelat,scenelons,slopex,slope4;
float solar_irrad[5],solazim[4][6],solzen[4][6],tauozx,tauoz4,taurx,taur4;
float tiltangle,time_tab[4][6],transbmx[4][6],transbm4[4][6],transdfx[6];
float viewangle[6];


main()
{
    int i;

    for (i=0; i<30; i++) {
        filename1[i] = '\0';
        filename2[i] = '\0';
        filename3[i] = '\0';
    }

    printf("\n\t\t\t ");
    system("date");                                   /* Print out the date */
    printf("\n");

    while(params());

    confirm();

    globalval();

    localval();

    printf("\nDo you wish to correct the whole image? (y/n): ");
    scanf("%*c %c",&yesorno);
    if (yesorno == 'Y' || yesorno == 'y')
        atmos1();

    printf("\nDo you wish to correct point samples only? (y/n): ");
    scanf("%*c %c",&yesorno);
    if (yesorno == 'Y' || yesorno == 'y')
        atmos2();
```

```
    close(fildes1);
    close(fildes2);
    close(fildes3);
}


atmos1()              /* Evaluates final correction algorithm for whole image */
{
    extern char intrayx[],intray4[],outrayx[];              /* See atmos.doc */
    extern int channel,fildes1,fildes2,fildes3,scale;
    extern float angsfact,intrcptx,intrcpt4,slopex,slope4,solar_irrad[];
    extern float transdfx[];

    int column,i,line,negcount,pixel,row;
    float radx,rad4,x,y,z;
    long int lseek(),totalneg;

    lseek(fildes1,0L,0);                  /* Place pointers at start of files */
    lseek(fildes2,0L,0);
    lseek(fildes3,0L,0);

    printf("\n\n\nLine          negative radiances\b\b\b\b\b\b\b\b\b\b\b\b\b");
    printf("\b\b\b\b\b\b\b\b\b\b\b\b\b");

    totalneg = 0L;

    for (line=0; line<LINES; line++) {
        row = 3 - line/128;       /* Select row, noting that file is reversed */

        read(fildes1,intrayx,PIXELS);       /* Read one line of channel 1/2/3 */
        read(fildes2,intray4,PIXELS);           /* Read one line of channel 4 */

        negcount = 0;                        /* Reset negative radiance counter */

        for (pixel=0; pixel<PIXELS; pixel++) {
            column = pixel/128;                                 /* Select column */

            x = (float) intrayx[pixel];
            y = (float) intray4[pixel];

            if (x<0.0)
                x += 256.0;                         /* Interpret sign bit as +128 */
            if (y<0.0)
                y += 256.0;                         /* Interpret sign bit as +128 */

            radx = slopex*x + intrcptx;             /* Channel 1, 2 or 3 radiance */
            rad4 = slope4*y + intrcpt4;                     /* Channel 4 radiance */

            z = -((rad4 - rayrad4[row][column])*angsfact);
            z *= (solar_irrad[channel])*(transbmx[row][column]);
            z /= (solar_irrad[4])*(transbm4[row][column]);
            z += (radx - rayradx[row][column]);
            z /= transdfx[column];          /* Convert to water leaving radiance */

            if (z<0.0) {
                i = 0;                       /* Force negative radiances to zero */
                negcount++;                   /* Count number of negative pixels */
            }

            else if (z==0.0)
                i = 0;

            else if (z>0.0)
                i = (int) scale*z + 0.5;           /* Scale & -> nearest integer */

            if (i>255)
                i = 255;                              /* Force values>255 to 255 */

            outrayx[pixel] = (char) i;       /* Place result in char o/p buffer */
        }

        write(fildes3,outrayx,PIXELS);        /* Write 1 line of corrected data */

        printf("%3d : %3d\b\b\b\b\b\b\b\b\b\b",line+1,negcount);

        totalneg += (long int) negcount;
    }
```

```
    printf("\n\nTotal number of negative radiance pixels = %ld\n",totalneg);
}


atmos2()            /* Evaluates final correction algorithm for sample points */
{
    extern char intrayx[],intray4[];                              /* See atmos.doc */
    extern int channel,fildes1,fildes2;
    extern float angsfact,intrcptx,intrcpt4,slopex,slope4,solar_irrad[];
    extern float transdfx[];

    int column,coordbuf[2],fildes4,line,lines,pixel,row;
    long int lseek(),offset;
    float radx,rad4,x,y,z;

    printf("\n\n\n");

    fildes4 = open("/prog1/dave/atmoscorr/coords",0);

    printf("\n\t L    P   R  C  OFFSET   CH%d   CH4   RADIANCE\n\t---  -",channel);
    printf("--  -  -  ------  ---  ---  --------\n");

    while((read(fildes4,coordbuf,4)) != EOF) {       /* Read coords until EOF */
        line = coordbuf[0];
        pixel = coordbuf[1];

        row = line/128;                                              /* Select row */
        column = pixel/128;                                       /* Select column */

        lines = LINES - line;                              /* Deal with line reversal */
        offset = (long) PIXELS*(lines - 1) + pixel;

        lseek(fildes1,offset,0);                                /* Position pointers */
        lseek(fildes2,offset,0);

        read(fildes1,intrayx,1);              /* Read 1 pixel from channel 1/2/3 */
        read(fildes2,intray4,1);                 /* Read 1 pixel from channel 4 */

        x = (float) intrayx[0];
        y = (float) intray4[0];

        if (x<0.0)
            x += 256.0;                              /* Interpret sign bit as +128 */
        if (y<0.0)
            y += 256.0;                              /* Interpret sign bit as +128 */

        radx = slopex*x + intrcptx;                  /* Channel 1, 2 or 3 radiance */
        rad4 = slope4*y + intrcpt4;                           /* Channel 4 radiance */

        z = -((rad4 - rayrad4[row][column])*angsfact);
        z *= (solar_irrad[channel])*(transbmx[row][column]);
        z /= (solar_irrad[4])*(transbm4[row][column]);
        z += (radx - rayradx[row][column]);
        z /= transdfx[column];                /* Convert to water-leaving radiance */

        printf("\t%3d  %3d  %d  %d  %6ld",line,pixel,row,column,offset);
        printf("  %3.0f  %3.0f  %7.4f\n",x,y,z);
    }

    close(fildes4);
}


cellcent()                  /* Calculates latitude & longitude for cell centres */
{
    extern char printing;
    extern float scenelat,scenelong;

    int column,row;
    float alpha,cosalpha,coscenlat,latcell,longcell,sinalpha,xcomp1,xcomp2;
    float ycomp1,ycomp2;

    coscenlat = cos(scenelat*PI/180.0);                    /* cosine of scenelat */
    alpha = asin((sin(TRACKINC*PI/180.0))/coscenlat);  /* alpha is not really */
    sinalpha = sin(alpha);                              /* a constant since it is a */
    cosalpha = cos(alpha);                             /* function of scene latitude */
```

```
    latcell = 64.0*GRESX/(CONVERSION*60.0);                    /* See atmos.doc */
    latcell *= PI/180.0;                                      /* Convert to radians */
    lonscell = 64.0*GRESY/(CONVERSION*coscenlat*60.0);         /* See atmos.doc */
    lonscell *= PI/180.0;                                     /* Convert to radians */

    /* Under rotation of alpha, a point [x,y] is mapped to
       [xcos(alpha) - ysin(alpha), ycos(alpha) + xsin(alpha)] */

    for (row=0; row<4; row++) {
        ycomp1 = latcell*((float) 3 - 2*row);
        ycomp2 = lonscell*((float) 3 - 2*row);
        for (column=0; column<6; column++) {
            cellat[row][column] = scenelat*PI/180.0 + ycomp1*cosalpha;
            cellons[row][column] = scenelons*PI/180.0 - ycomp2*sinalpha;
        }
    }

    for (column=0; column<6; column++) {
        xcomp1 = latcell*((float) 2*column - 5);
        xcomp2 = lonscell*((float) 2*column - 5);
        for (row=0; row<4; row++) {
            cellat[row][column] += xcomp1*sinalpha;
            cellons[row][column] += xcomp2*cosalpha;
        }
    }

    if (printing == 'Y' || printing == 'y') {
        printf("\tAlpha =%8.4f degrees\n", alpha*180.0/PI);

        printf("\n\tCell centre latitudes:\n\n");
        for (row=0; row<4; row++) {
            printf("\t");
            for (column=0; column<6; column++)
                printf("%10.5f", cellat[row][column]*180.0/PI);
            printf("\n");
        }

        printf("\n\tCell centre longitudes:\n\n");
        for (row=0; row<4; row++) {
            printf("\t");
            for (column=0; column<6; column++)
                printf("%10.5f", cellons[row][column]*180.0/PI);
            printf("\n");
        }
    }
}


confirm()                                          /* Confirms choice of parameters */
{
    extern char direct,filename1[],filename2[],filename3[];
    extern int channel,day,hour,initmnfr,latdegs,latmins,londegs,lonmins;
    extern int minute,month,scale,tilt,year;
    extern float angsexp,intrcptx,intrcpt4,refindex,slopex,slope4;

    printf("\n\n\t\t       PARAMETER  SUMMARY\n");
    printf("\t\t      ------------------\n");
    printf("Channel number:\t\t\t\t\t %d\n",channel);
    printf("Input file name:\t\t\t\t %s\n",filename1);
    printf("Corresponding channel 4 file name:\t\t %s\n",filename2);
    printf("Output file name:\t\t\t\t %s\n",filename3);
    printf("Date:\t\t\t\t\t\t %d %d %d\n",day,month,year);
    printf("Picture time (hrs, mins GMT):\t\t\t %d %d\n",hour,minute);
    printf("Latitude of image centre (degs,mins):\t\t ");
    printf("%d %d\n",latdegs,latmins);
    printf("Longitude of image centre (degs,mins,W/E):\t ");
    printf("%d %d %c\n",londegs,lonmins,direct);
    printf("Tilt angle (degrees):\t\t\t\t %d\n",tilt);
    printf("Initial minor frame number (1-9):\t\t %d\n",initmnfr);
    printf("Channel %d slope:\t\t\t\t %7.5f\n",channel,slopex);
    printf("Channel %d intercept:\t\t\t\t %7.5f\n",channel,intrcptx);
    printf("Channel 4 slope:\t\t\t\t %7.5f\n",slope4);
    printf("Channel 4 intercept:\t\t\t\t %7.5f\n",intrcpt4);
    printf("Angstrom exponent:\t\t\t\t%6.3f\n",angsexp);
    printf("Display scale factor:\t\t\t\t %d\n",scale);
    printf("Refractive index of seawater:\t\t\t%6.3f\n",refindex);
    printf("\n\t    ------------------||------------------\n");
}
```

```
day_of_year(day,month,year)          /* Calculates days between Jan 1 & date */
int day,month,year;
{
    int i,leap;
    static int day_tab[2][13] = {
        {0,31,28,31,30,31,30,31,31,30,31,30,31},
        {0,31,29,31,30,31,30,31,31,30,31,30,31}
    };

    leap = year%4 == 0 && year%100 != 0 || year%400 == 0;
    for (i=1; i<month; i++)
        day += day_tab[leap][i];
    return(day);
}


float decline(daynumber)                /* Calculates solar declination angle */
int daynumber;
{
    float delta,sindelta;

    sindelta=sin(INCLINATION*PI/180.0)*sin(2.0*PI*(daynumber-VERNALDAY)/365.0);
    delta = asin(sindelta);                 /* Inverse sine: no sign ambiguity */
    return(delta);
}


float fresnel1(incid)       /* Calculates reflection coeff. for air --> water */
float incid;
{
    extern float refindex;
    float refract,sineterm,tanterm,x;

    if (incid < 0.5*PI/180.0) {
        x = pow((refindex - 1.0)/(refindex + 1.0),2.0);
        return(x);
    }

    else {
        refract = asin((sin(incid))/refindex);
        sineterm = (sin(incid - refract))/(sin(incid + refract));
        sineterm = sineterm*sineterm;
        tanterm = (tan(incid - refract))/(tan(incid + refract));
        tanterm = tanterm*tanterm;
        return(0.5*(sineterm + tanterm));
    }
}


float fresnel2(incid)       /* Calculates reflection coeff. for water --> air */
float incid;
{
    extern float refindex;
    float refract,sineterm,tanterm,x;

    if (incid > asin(1.0/refindex))
        return(0.0);

    else if (incid < 0.5*PI/180.0) {
        x = pow((refindex - 1.0)/(refindex + 1.0),2.0);
        return(x);
    }

    else {
        refract = asin(refindex*sin(incid));
        sineterm = (sin(incid - refract))/(sin(incid + refract));
        sineterm = sineterm*sineterm;
        tanterm = (tan(incid - refract))/(tan(incid + refract));
        tanterm = tanterm*tanterm;
        return(0.5*(sineterm + tanterm));
    }
}
```

```
globalval()                                        /* Determines global values */
{
    extern char direct,printing;
    extern int channel,day,daynumber,hour,latdegs,latmins,londegs,lonmins;
    extern int month,tilt,wavelens[],year;
    extern float angsexp,angsfact,pictime,refindex,scenelat,scenelons;
    extern float tauozx,tauoz4,taurx,taur4,tiltangle;

    int i;
    float delta,decline(),waveratio;

    daynumber = day_of_year(day,month,year);
    delta = (decline(daynumber))*180.0/PI;
    pictime = (float) hour + minute/60.0;
    scenelat = (float) latdegs + latmins/60.0;
    scenelons = (float) londegs + lonmins/60.0;
    if (direct == 'W' || direct == 'w')
        scenelons = - scenelons;
    solarirrad(daynumber);
    tiltangle = ((float) tilt)*PI/180.0;
    waveratio = ((float) wavelens[4])/((float) wavelens[channel]);
    angsfact = pow(waveratio,angsexp);
    optdepth(channel,daynumber,scenelat);

    if (printing == 'Y' || printing == 'y') {
        printf("\n\n\n\nCalculating derived global values.....\n\n");
        printf("\tDaynumber = %d\n",daynumber);
        printf("\tSolar declination angle = %12.6f degrees\n",delta);
        printf("\tPicture time = %10.6f hours\n",pictime);
        printf("\tScene latitude = %10.6f degrees\n",scenelat);
        printf("\tScene longitude = %10.6f degrees\n",scenelons);
        printf("\tTiltangle = %8.2f degrees\n",tiltangle*180.0/PI);
        printf("\tAngstrom factor = %8.6f\n",angsfact);
        printf("\ttauozx = %6.4f\n\ttauoz4 = %6.4f\n",tauozx,tauoz4);
        printf("\ttaurx = %6.4f\n\ttaur4 = %6.4f\n",taurx,taur4);
        for (i=1; i<5; i++) {
            printf("\tAdjusted channel %d solar irradiance",i);
            printf(" = %8.3f\n",solar_irrad[i]);
        }
    }
}


localval()                                         /* Determines local values */
{
    extern char printing;

    if (printing == 'Y' || printing == 'y')
        printf("\n\n\n\nCalculating local values.....\n\n");

    cellcent();

    times();

    solarzen();

    solarazim();

    polarang();

    transmit();

    scannerazim();

    phasefunc();

    rayleigh();
}


optdepth(channel,daynumber,scenelat)          /* Selects appropriate Rayleigh & */
int channel,daynumber;                             /* ozone optical thicknesses */
float scenelat;
{
    int summer = 0;
    int winter = 1;
    int season,zone;
```

```
    extern float tauozx,tauoz4,taurx,taur4;

    static float tauoz_tab[5][6] = {
        {0.0, 0.0,    0.0,    0.0,    0.0,    0.0},
        {0.0, 0.0066, 0.0067, 0.0069, 0.0068, 0.0071},
        {0.0, 0.0166, 0.0200, 0.0237, 0.0213, 0.0275},
        {0.0, 0.0261, 0.0323, 0.0390, 0.0346, 0.0461},
        {0.0, 0.0158, 0.0191, 0.0226, 0.0202, 0.0264}
    };

    static float taur_tab[5][6] = {
        {0.0, 0.0,    0.0,    0.0,    0.0,    0.0},
        {0.0, 0.2329, 0.2311, 0.2316, 0.2300, 0.2303},
        {0.0, 0.1231, 0.1222, 0.1224, 0.1214, 0.1218},
        {0.0, 0.0969, 0.0962, 0.0964, 0.0956, 0.0959},
        {0.0, 0.0444, 0.0440, 0.0442, 0.0438, 0.0439}
    };


    if (daynumber >= MID_SPRING && daynumber < MID_AUTUMN)
        season = summer;
    else if (daynumber < MID_SPRING || daynumber >= MID_AUTUMN)
        season = winter;

    if (scenelat < 25.0)
        zone = 1;

    if (scenelat > 25.0 && scenelat < 55.0) {
        if (season == summer)
            zone = 2;
        else if (season == winter)
            zone = 3;
    }

    else if (scenelat > 55.0) {
        if (season == summer)
            zone = 4;
        else if (season == winter)
            zone = 5;
    }

    tauozx = tauoz_tab[channel][zone];
    tauoz4 = tauoz_tab[4][zone];
    taurx = taur_tab[channel][zone];
    taur4 = taur_tab[4][zone];
}


params()                                    /* Collects parameters from console */
{
    int status;
    extern char direct,filename1[],filename2[],filename3[],printing,yesorno;
    extern int channel,day,fildes1,fildes2,fildes3,hour,initmnfr,latdegs;
    extern int latmins,longdegs,longmins,minute,month,scale,tilt,year;
    extern float angsexp,intrcptx,intrcpt4,refindex,slopex,slope4;

    printf("\n ------------------------------------------------------------");
    printf("---------- \n");
    printf("|\t\t\t\t\t\t\t\t\t\t\t       |\n");
    printf("|    Program atmos.c. Performs atmospheric correction of CZCS ");
    printf("images. See       |\n|    atmos.doc for further details. Please ");
    printf("supply the following parameters:    |\n");
    printf("|\t\t\t\t\t\t\t\t\t\t\t       |");
    printf("\n ------------------------------------------------------------");
    printf("---------- \n\n\n");

    printf("\n 1) Do you require intermediate values to be displayed? (y/n): ");
    scanf("%c", &printing);

    printf("\n 2) Channel number (1 - 3) for the file to be corrected: ");
    scanf("%d", &channel);

    printf("\n 3) Full name of file to be corrected: ");
    scanf("%s", filename1);
    fildes1 = open(filename1,0);
```

```
if (fildes1 != NOFILE) {
    printf("\n 4) Full name of corresponding channel 4 image file: ");
    scanf("%s", filename2);
    fildes2 = open(filename2,0);
    if (fildes2 != NOFILE) {
        printf("\n 5) Full name for the corrected output file: ");
        scanf("%s",filename3);
        fildes3 = open(filename3,1);
        if (fildes3 != NOFILE) {
            printf("\n 6) Date (eg. 22 6 1981): ");
            scanf("%d %d %d", &day,&month,&year);

            printf("\n 7) Picture time in hours & minutes GMT, eg. 11 ");
            printf("20: ");
            scanf("%d %d", &hour,&minute);

            printf("\n 8) Latitude for centre of image (assumed to be in ");
            printf("the Northern hemisphere)\n    in degrees & minutes ");
            printf("(maximum value is 80 43), eg. 50 23: ");
            scanf("%d %d", &latdegs,&latmins);

            printf("\n 9) Longitude for centre of image in degrees & ");
            printf("minutes West or East of\n    Greenwich, eg. 4 10 W: ");
            scanf("%d %d %c", &longdegs,&longmins,&direct);

            printf("\n10) Tilt angle in degrees (even integer in the ");
            printf("range -20 to +20): ");
            scanf("%d", &tilt);

            printf("\n11) Initial minor frame number (1-9) for left-");
            printf("hand edge of image: ");
            scanf("%d", &initmnfr);

            printf("\n12) Channel %d slope (for radiometric conve",channel);
            printf("rsion): ");
            scanf("%f", &slopex);

            printf("\n13) Channel %d intercept (for radiometric c",channel);
            printf("onversion): ");
            scanf("%f", &intrcptx);

            printf("\n14) Channel 4 slope (for radiometric conversion): ");
            scanf("%f", &slope4);

            printf("\n15) Channel 4 intercept (for radiometric conversion");
            printf("): ");
            scanf("%f", &intrcpt4);

            printf("\n16) Value for the Angstrom exponent (range -2 to ");
            printf("+2): ");
            scanf("%f", &angsexp);

            printf("\n17) Scale factor (integer) for displaying image: ");
            scanf("%d",&scale);

            printf("\n18) Do you wish to use the default value (1.341) ");
            printf("for the refractive index of\n    seawater? (y/n): ");
            scanf("%*c %c", &yesorno);          /* The %*c absorbs a CR */

            if (yesorno == 'N' || yesorno == 'n') {
                printf("\n19) Enter desired refractive index: ");
                scanf("%f", &refindex);
            }
            else refindex = 1.341;

            status = 0;                                  /* Signals O.K. */
        }

        else {
            printf("\n\tERROR - Output file does not exist or cannot be ");
            printf("opened.\n");
            status = 1;                                  /* Signals an error */
        }
    }

    else {
        printf("\n\tERROR - Channel 4 file does not exist or cannot be ");
```

```
            printf("opened.\n");
            status = 1;                                    /* Signals an error */
        }
    }

    else {
        printf("\n\tERROR - Input file does not exist or cannot be opened.\n");
        status = 1;                                        /* Signals an error */
    }
    return(status);
}


phasefuncs()        /* Calculates forward & backward Rayleigh phase functions */
{
    extern char printing;
    extern float polang[];

    int column,row;
    float bscatang[4][6],fscatang[4][6],x,y;

    for (row=0; row<4; row++) {
        for (column=0; column<6; column++) {
            x = cos(polang[column])*cos(solzen[row][column]);
            y = sin(polang[column])*sin(solzen[row][column]);
            y *= cos(scanazim[row][column] - solazim[row][column]);
            fscatang[row][column] = acos(x - y);
            bscatang[row][column] = acos(-x - y);
            phasefn1[row][column] = 0.75*(1.0 + (x - y)*(x - y));
            phasefn2[row][column] = 0.75*(1.0 + (-x - y)*(-x - y));
        }
    }

    if (printing == 'Y' || printing == 'y') {
        printf("\n\tCell centre fwd. scatt. angles:\n\n");
        for (row=0; row<4; row++) {
            printf("\t");
            for (column=0; column<6; column++)
                printf("%10.5f",fscatang[row][column]*180.0/PI);
            printf("\n");
        }

        printf("\n\tCell centre back. scatt. angles:\n\n");
        for (row=0; row<4; row++) {
            printf("\t");
            for (column=0; column<6; column++)
                printf("%10.5f",bscatang[row][column]*180.0/PI);
            printf("\n");
        }

        printf("\n\tCell centre fwd. scatt. phase functions:\n\n");
        for (row=0; row<4; row++) {
            printf("\t");
            for (column=0; column<6; column++)
                printf("%10.5f",phasefn1[row][column]);
            printf("\n");
        }

        printf("\n\tCell centre back scatt. phase functions:\n\n");
        for (row=0; row<4; row++) {
            printf("\t");
            for (column=0; column<6; column++)
                printf("%10.5f",phasefn2[row][column]);
            printf("\n");
        }
    }
}


polarangs()                          /* Calculates the 6 'polar' angles in radians */
                                        /* Polar angle is equivalent to the */
{                                                  /* scanner zenith angle */
    extern char printing;
    extern int initmnfr;
    extern float polang[],tiltangle,viewangle[];

    int column,pixelnum;
```

```
    float x;

    for (column=0; column<6; column++) {
        pixelnum = (initmnfr - 1)*FRAMESIZE + FIRSTPIXEL + (64-1) + column*128;
        viewangle[column] = IFOV*((float) pixelnum - NADIRPIX);
        x = (cos(viewangle[column]))*(cos(tiltangle));
        polang[column] = acos(x);
    }

    if (printing == 'Y' || printing == 'y') {
        printf("\n\tView angles:\n\n\t");
        for (column=0; column<6; column++)
            printf("%10.5f",viewangle[column]*180.0/PI);
        printf("\n");

        printf("\n\tPolar angles (equiv. to scanner zenith angles):\n\n\t");
        for (column=0; column<6; column++)
            printf("%10.5f",polang[column]*180.0/PI);
        printf("\n");
    }
}


rayleigh()          /* Calculates the Rayleigh radiance for each cell centre */
{
    extern char printing;
    extern int channel;
    extern float polang[],solar_irrad[],taurx,taur4;

    int column,row;
    float fresnell(),x,y;

    for (row=0; row<4; row++) {
        for (column=0; column<6; column++) {
            x = fresnell(polang[column]) + fresnell(solzen[row][column]);
                                                        /* See atmos.doc */
            y = phasefn2[row][column] + x*phasefn1[row][column];
            y /= 4.0*PI*cos(polang[column]);
            rayradx[row][column] = y*taurx*solar_irrad[channel];
            rayradx[row][column] *= transbmx[row][column];
            rayrad4[row][column] = y*taur4*solar_irrad[4];
            rayrad4[row][column] *= transbm4[row][column];
        }
    }

    if (printing == 'Y' || printing == 'y') {
        printf("\n");
        printf("\tCell centre Rayleigh radiances for channel %d:\n\n",channel);
        for (row=0; row<4; row++) {
            printf("\t");
            for (column=0; column<6; column++)
                printf("%10.5f", rayradx[row][column]);
            printf("\n");
        }

        printf("\n\tCell centre Rayleigh radiances for channel 4:\n\n");
        for (row=0; row<4; row++) {
            printf("\t");
            for (column=0; column<6; column++)
                printf("%10.5f", rayrad4[row][column]);
            printf("\n");
        }
    }
}


scannerazim()       /* Calculates scanner azimuth angle for each cell centre */
{
    extern char printing;
    extern float tiltangle,viewangle[];

    int column,row;
    float deltacap,phi1,phi2,x;

    for (row=0; row<4; row++) {
        for (column=0; column<6; column++) {
```

```
            x = (sin(TRACKINC*PI/180.0))/(cos(cellat[row][column]));
            deltacap = acos(x);

            if (viewangle[column] == 0.0) {
                if (tiltangle > 0.0)
                    phi2 = PI/2.0;
                else if (tiltangle < 0.0)
                    phi2 = 3.0*PI/2.0;
                else if (tiltangle == 0.0)
                    phi2 = 0.0;
            }

            else {
                x = (sin(tiltangle))/(tan(viewangle[column]));
                phi1 = fabs(atan(x));

                if (viewangle[column] > 0.0) {
                    if (tiltangle > 0.0)
                        phi2 = PI - phi1;
                    else if (tiltangle < 0.0)
                        phi2 = PI + phi1;
                    else if (tiltangle == 0.0)
                        phi2 = PI;
                }

                else if (viewangle[column] < 0.0) {
                    if (tiltangle > 0.0)
                        phi2 = phi1;
                    else if (tiltangle < 0.0)
                        phi2 = 2.0*PI - phi1;
                    else if (tiltangle == 0.0)
                        phi2 = 0.0;
                }
            }
            scanazim[row][column] = (deltacap + phi2);
        }
    }

    if (printing == 'Y' || printing == 'y') {
        printf("\n\tCell centre scanner azimuth angles:\n\n");
        for (row=0; row<4; row++) {
            printf("\t");
            for (column=0; column<6; column++)
                printf("%10.5f",scanazim[row][column]*180.0/PI);
            printf("\n");
        }
    }
}


solarazim()             /* Calculates solar azimuth angle for each cell centre */
{
    extern char printing;
    extern int daynumber;
    extern float decline();

    int column,row;
    float delta,x;

    delta = decline(daynumber);

    for (row=0; row<4; row++) {
        for (column=0; column<6; column++) {
            x = - (sin(cellat[row][column]))*(cos(solzen[row][column]));
            x += sin(delta);
            x /= (cos(cellat[row][column]))*(sin(solzen[row][column]));
            solazim[row][column] = acos(x);
            if (time_tab[row][column] > 0.0)
                solazim[row][column] = 2.0*PI - solazim[row][column];
        }
    }

    if (printing == 'Y' || printing == 'y') {
        printf("\n\tCell centre solar azimuth angles:\n\n");
        for (row=0; row<4; row++) {
            printf("\t");
            for (column=0; column<6; column++)
```

```
                printf("%10.5f",solazim[row][column]*180.0/PI);
            printf("\n");
        }
    }
}


solarirrad(day)                         /* Calculates adjusted solar irradiances */
int day;
{
    extern float solar_irrad[];
    float factor;

    factor = 1.0 + ECCENTRIC*(cos((day - 3)*2.0*PI/365.0));
    factor = factor*factor;

    solar_irrad[1] = factor*SOLIRR1;
    solar_irrad[2] = factor*SOLIRR2;
    solar_irrad[3] = factor*SOLIRR3;
    solar_irrad[4] = factor*SOLIRR4;
}


solarzen()              /* Calculates solar zenith angle for each cell centre */
{
    extern char printing;
    extern int daynumber;
    extern float decline();

    int column,row;
    float delta,x;

    delta = decline(daynumber);

    for (row=0; row<4; row++) {
        for (column=0; column<6; column++) {
            x = (cos(cellat[row][column]))*cos(delta);
            x *= cos((time_tab[row][column])*PI/12.0);
            x += (sin(cellat[row][column]))*sin(delta);
            solzen[row][column] = acos(x);
        }
    }

    if (printing == 'Y' || printing == 'y') {
        printf("\n\tCell centre solar zenith angles:\n\n");
        for (row=0; row<4; row++) {
            printf("\t");
            for (column=0; column<6; column++)
                printf("%10.5f",solzen[row][column]*180.0/PI);
            printf("\n");
        }
    }
}


times()                         /* Calculates local time for centre of each cell */
{
    extern char printing;
    extern float pictime,tiltangle;

    int column,row;
    float alpha,correct1,correct2,dist1,dist2,omega,shift;

    omega = asin(sin(tiltangle)*(1.0 + ALTITUDE/EARTHRADIUS));
    omega -= tiltangle;
    shift = omega*EARTHRADIUS;

    for (row=0; row<4; row++) {
        for (column=0; column<6; column++) {
            alpha = asin((sin(TRACKINC*PI/180.0))/(cos(cellat[row][column])));

            dist1 = (cellat[row][column]*180.0/PI - LATRXSTAT)*60.0*CONVERSION;
            dist2 = -shift*cos(alpha);

            correct1 = (dist1 + dist2)/(VELOCITY*60.0*60.0);
            correct2 = (cellong[row][column])*12.0/PI;
```

```
            time_tab[row][column] = pictime + correct1 + correct2 - 12.0;
        }
    }

    if (printing == 'Y' || printing == 'y') {
        printf("\n\tCell centre local times:\n\n");
        for (row=0; row<4; row++) {
            printf("\t");
            for (column=0; column<6; column++)
                printf("%10.5f", time_tab[row][column]);
            printf("\n");
        }
    }
}


transmit()              /* Calculates diffuse and beam (direct) transmittances */
{
    extern char printing;                   /* These beam transmittances are the  */
    extern int channel;                     /* product of TO3[mu] and TO3[mu(0)]  */
    extern float tauozx,tauoz4,taurx;       /* and account for both the downwards */
                                            /* and upwards transmission of light. */
    int column,row;
    float x,y;

    for (column=0; column<6; column++) {
        x = 1.0/cos(polang[column]);
        transdfx[column] = exp(-0.5*taurx*x);

        for (row=0; row<4; row++) {
            y = 1.0/(cos(solzen[row][column]));
            transbmx[row][column] = exp(-tauozx*(x + y));
            transbm4[row][column] = exp(-tauoz4*(x + y));
        }
    }

    if (printing == 'Y' || printing == 'y') {
        printf("\n\tDiffuse transmittances for channel %d:\n\n\t",channel);
        for (column=0; column<6; column++)
            printf("%10.5f",transdfx[column]);
        printf("\n");

        printf("\n");
        printf("\tCell centre beam transmittances for channel %d:\n\n",channel);
        for (row=0; row<4; row++) {
            printf("\t");
            for (column=0; column<6; column++)
                printf("%10.5f",transbmx[row][column]);
            printf("\n");
        }

        printf("\n\tCell centre beam transmittances for channel 4:\n\n");
        for (row=0; row<4; row++) {
            printf("\t");
            for (column=0; column<6; column++)
                printf("%10.5f",transbm4[row][column]);
            printf("\n");
        }
    }
}
```

APPENDIX 10

PUBLISHED PAPERS

Low-cost remote sensing experiments within an educational environment

J G Wade, D H Lawrence and M Rendle

The results of a two-year preliminary investigation into the remote sensing field are described. Ways of investigating some of the major disciplines involved at low cost are shown. In particular a means of combining disciplines to yield topical experiments at graduate level is shown. Some of the many research possibilities within the field are also indicated. Based on experiments with data from a Nimbus-7 coastal zone colour scanner, multiband aerial photographs and an experimental low-cost image processor, an introduction is given to such aspects as atmospheric correction, data sources, typs of classification, fundamental hardware requirements and related image enhancement software.

Keywords: remote sensing, multiband photography, Nimbus-7 CZCS

Remote sensing is a multidisciplinary technology embracing, for example, geography, geology, marine science, atmospheric physics, pattern recognition, computer science, electronic engineering and satellite technology. The broad objective is to classify land and ocean areas into categories of interest using satellite and aerial platforms. This is often done using a remote, specialized commercial image processor. Since remote sensing is such a diverse field often involving high computing costs it can be difficult for an educational department to break into the field. The lack of low-cost local facilities for image input, output and processing is a particularly common problem[1,2]. Until low-cost remote sensing machines become readily available one solution is to add a tape drive and simple hardware to a readily available minicomputer. This was the approach adopted by the authors of this paper (Figure 1). The use of this system to gain experience in remote sensing is described with particular emphasis on a topical marine application and the use of data from a Nimbus-7 coastal zone colour scanner (CZCS). The overall objective of the paper is to provide an overview of the problems encountered by the authors, and to provide a practical guide for those with little or no experience of the subject.

Department of Communication Engineering, Plymouth Polytechnic, Plymouth, Devon, UK

FUNDAMENTAL CONSIDERATIONS

Data sources and atmospheric correction

Images are usually divided into classes such as urban, cropland, forest, bare soil and water using the fact that each class has a characteristic spectral signature. The data source therefore has to provide multispectral data. A well tried solution is to mount four carefully aligned 35 mm or 70 mm cameras with their associated blue, green, red and infrared filters in a light aircraft. This approach can give very high ground resolution, particularly from negative transparencies, and atmospheric effects (scattering and absorption) can be small at low altitudes[3], say below a few kilometres.

A disadvantage is that the images have to be input manually via a slide scanner. A vernier slide adjustment is required to minimize registration errors between bands. Moreover, since photographic film is used the multispectral analysis cannot go above the infrared wavelength and the optical filters have to be quite broad band relative to the bandwidths used in satellite multispectral scanners.

Most multispectral work is done using satellite data in computer-compatible tape (CCT) form, usually nine-track 63 bit/mm (1600 bit/in) phase encoded. The handling of such data is worth considering. We do this with reference to the Nimbus-7 CZCS which was designed primarily for ocean colour monitoring but also monitors suspended sediment, surface vegetation and sea surface temperature. With prior knowledge of the data format (not always a foregone conclusion) and with some software data demultiplexing, the raw digital count n of a CZCS image can be read using the tape drives of a conventional mainframe computer or, more conveniently, using a tape transport directly connected to the local image processor, as in Figure 1. Using radiometer calibration data on the tape the radiance at the sensor input can be expressed as

$$L_s = \frac{n}{a_S b_C} - \frac{a_C}{a_S b_C} \qquad 0 \le n \le 255 \qquad (1)$$

where the coefficients a_S, a_C and b_C can be found from a least-squares analysis. Assume that the sensor is viewing an ocean surface free of 'sun glitter'. Then L_S can be modelled as[4-6]

 0262-8856/84/01003-10$03.00

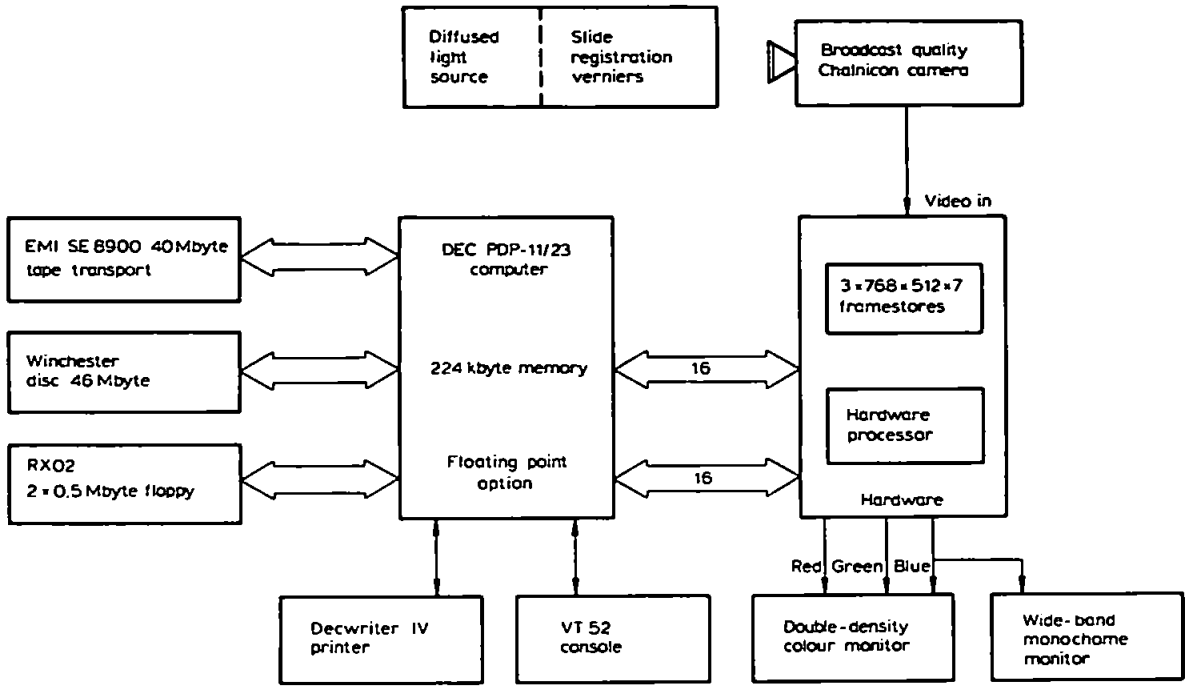

Figure 1. A low-cost image processor for remote sensing applications

$$L_S(\lambda) = L_R(\lambda) + L_A(\lambda) + L_W(\lambda) \quad (2)$$

where $L_R(\lambda)$ is the radiance at the sensor due to Rayleigh scattering, $L_A(\lambda)$ is the radiance at the sensor due to aerosol scattering, and $L_W(\lambda)$ is the radiance at the sensor due to diffuse water leaving radiance back-scattered from suspended manner. Only $L_W(\lambda)$ is of interest since this represents subsurface information. Unfortunately $L_W(\lambda)$ may be as little as 20% of $L_S(\lambda)$, and some atmospheric correction algorithm to remove other radiances is mandatory. These algorithms can be complex and are themselves subjects of much research activity.

Despite these drawbacks there are many advantages in using satellite data in CCT form. There are no image registration problems since digital data can be read precisely into framestores or computer memory. More importantly satellite radiometers are continuously being refined by provision of more spectral bands located at more suitable wavelengths (compare Landsat 1–3 with Landsat 4[7] and there is a vast database from which to choose.

Classification

If it is assumed that classification is to be based solely on multispectral data and if additional information such as image texture is neglected, the overall objective is to select a class for a pixel data vector $\mathbf{X}$; eg for the blue, green, red and infrared bands

$$\mathbf{X} = \begin{bmatrix} x_B \\ x_G \\ x_R \\ x_{IR} \end{bmatrix}$$

where x is the pixel grey-level value, usually in the range 0–255. Frequently the so-called supervised parametric approach is used where training vectors corresponding to known ground classes are used to estimate a conditional probability distribution function for class ω_i. This yields a conditional probability $p(\mathbf{X}|\omega_i)$ for vector $\mathbf{X}$ and the maximum-likelihood decision rule for m classes is invoked,[8] ie

$$\mathbf{X} \in \omega_i \quad \text{if} \quad p(\mathbf{X}|\omega_i) \geq p(\mathbf{X}|\omega_j) \quad j = 1, 2, \ldots, m$$

Such classification can be lengthy even on commercial image processing machines. In contrast, images can be 'classified' into a few classes by extracting useful features or retrieval algorithms from the dataset. Usually these algorithms are based on *a priori* knowledge of the spectral signature. An obvious class to detect on this basis is green vegetation, since it has a rapid increase in the reflectance (IR) in the infrared region compared with the low reflectance (R) in the red region due to a chlorophyll absorption maximum. Therefore the reflectance ratios

$$\frac{IR}{R} \text{ or } \frac{IR - R}{IR + R}$$

will classify green vegetation areas (see for example Curran's article[9]. The difference IR − R is seldom used because of its high sensitivity to variations in scene illumination. With care, these simple ratios can be used to detect not only green vegetation but water, bareland and snow (or clouds) as demonstrated in the space shuttle FILE experiment[10].

Retrieval algorithms are used extensively with CZCS data to give ocean chlorophyll concentration and total suspended sediment maps. In this case spectral separability is possible because a chlorophyll absorption maximum (low reflectance) occurs in the blue region at 480 nm and an absorption minimum or 'hinge point' occurs in the green region at approximately 550 nm. A

chlorophyll concentration map (in milligrams per litre) can then be derived as a ratio of pixel radiances[11, 12]

$$C = a_0 \left[\frac{L_W(\lambda_B)}{L_W(\lambda_G)} \right]^{a_1} \quad (3)$$

where a_0 and a_1 are constants found from regression analysis based on seatruth (physical measurements of chlorophyll) and $L_W(\lambda)$ is the water-leaving radiance (strictly this is not the same as $L_W(\lambda)$ at the satellite although ratioing partially cancels any atmospheric transmittance factors). A similar but less spectrally justifiable approach is to use linear combinations of images such as

$$C = a_0 + \Sigma a_i L_W(\lambda_i) \quad (4)$$

Expressions similar to equations (3) and (4) have been used for mapping total suspended sediment.

Unfortunately it appears that there is no universally applicable chlorophyll algorithm for all ocean areas[13] so the coefficients will vary and in general claims of high accuracy are questionable. On the other hand, such features can easily be evaluated at video rates using RAM look-up tables for log–antilog functions and an arithmetic logic unit (ALU), and this makes the processor interactive. A system implementing this approach is described below.

SIMPLE PROCESSOR

The processor has to store at least two images, apply some type of feature or retrieval algorithm, enhance the result and display it, preferably on a colour display. If photographic transparencies are to be used these have to be digitized, preferably at video rate ('frame grabbing'), and each narrow-band image has to be stored in a framestore. If satellite images are to be used a subimage has to be selected off disc since only a fraction of the original image can be displayed at any one time; eg only some 26% of the horizontal scan of a CZCS image can be accommodated on a conventional 512 × 512 pixel display and considerably more pixel data is available from newer satellites. As previously noted, the evaluation of retrieval algorithms can be hardware based at little extra cost and complexity, but the processor can also be used as a development system for more sophisticated classification, provided that relatively long software execution times are accepted. Simple image enhancement software is also useful.

Hardware

Figure 2 shows the video routing a for a processor built largely within the normal budget of an engineering department and using mostly readily available equipment. It provides interactive realtime feature evaluation plus image enhancement and has the following specifications

- realtime frame capture of System-I video signals (digitization and storage in 40 ms)
- up to three framestores, each 768 × 512 × 8 bits
- simple video-rate pipelined processor for ratios and linear combinations of images
- colour composite (false colour) facility
- display look-up tables for contrast stretching and pseudocolour (density slicing)
- two bidirectional 16-bit ports controlled under programmed I/O
- wide-band (7 MHz) RGB video outputs to a double-resolution colour monitor
- supervisory software and various image enhancement routines.

The engineering of this type of system is changing rapidly both at the chip level and at the system level, and design concepts rather than details are of benefit here. At the chip level the introduction of high-density dynamic and static RAMs has simplified framestore design to the point where input data demultiplexing is almost unnecessary. For example, in the system shown in Figure 2 the sampling frequency is 1024 times the line frequency or 16.0 MHz, giving a 62.5 ns clock period — a value significantly less than the cycle times of the 16 k dynamic RAMs used. This led to a complex 24-way multiplex scheme for data input and output to and from the RAMs. However, the use of 64 k RAMs would considerably ease the problem. The use of byte-wide pseudostatic 64 k RAMs is particularly attractive since this reduces multiplexing and power dissipation and simplifies addressing and refresh. An even more attractive scheme is to use 64 k byte-wide static RAMs in the configuration indicated in Figure 3. This requires only two-way I/O data multiplexing, and because there are no refresh requirements the address and data buses and all control lines can simply be switched to computer control for data transfer. There is also very little peripheral logic. At the system level the concept of standalone framestores is also changing. It is advantageous to include the framestore as part of the computer memory map if possible. Thus, rather than writing special handshaking routines to transfer image data between the CPU and framestore via programmed I/O there is a move to memory bus techniques where the CPU regards part of the framestore as part of its memory address space.

The 62.5 ns clock period means that the hardware processor for pointwise combination of images has to be pipelined by including latches at various points as indicated in Figure 2. This hardware facility is a standard feature on commercial image processors. For two images I_1 and I_2 the ALU and associated logic provide the following operations at video rate

arithmetic $\begin{cases} I_1 \text{ plus } I_2 \\ I_1 \text{ minus } I_2 \quad \text{(negative forced to zero)} \\ \lvert I_1 \text{ minus } I_2 \rvert \end{cases}$

logical $\begin{cases} I_1 \cdot I_2 \\ I_1 + I_2 \end{cases}$

The look-up RAMs LU1–LU3 would be linearly mapped by the computer for such pointwise equations, but they are mapped to log–antilog functions for ratios.

When ratioing it is necessary to use scaling factors to avoid severe quantizing and display problems since only 8-bit arithmetic is used. Consider how the hardware evaluates equation (3). After atmospheric correction, water-leaving radiances L_W are generally lower than 1 mW/cm^{2}sr μm with $L_W(\lambda_G) > L_W(\lambda_B)$ for significant chlorophyll concentration. These values must be scaled (say by a factor of 100) for representation in the framestores. Let the scaled values be x_G and x_B

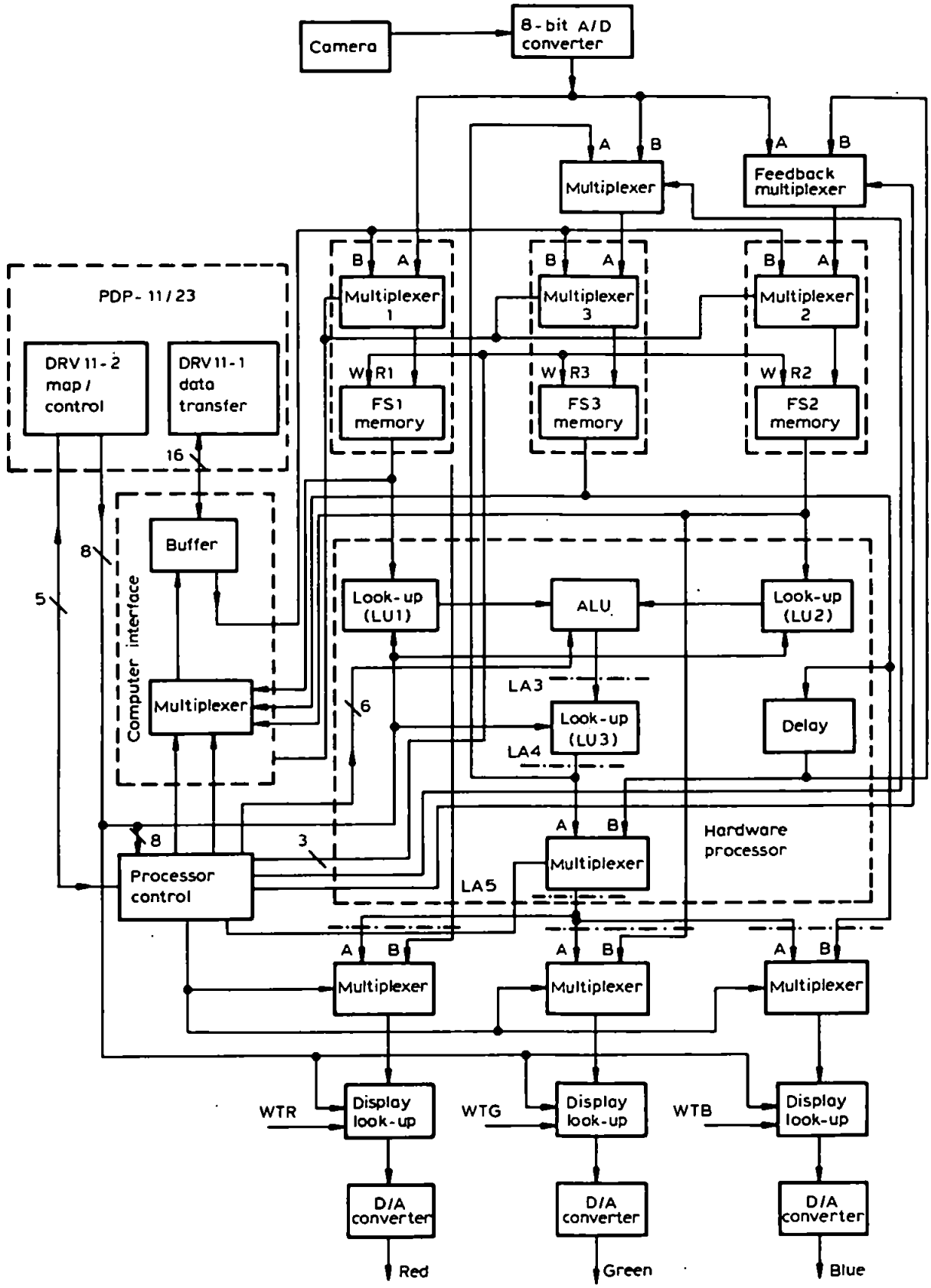

Figure 2. Processor video routing and control (— · —, pipelining latch)

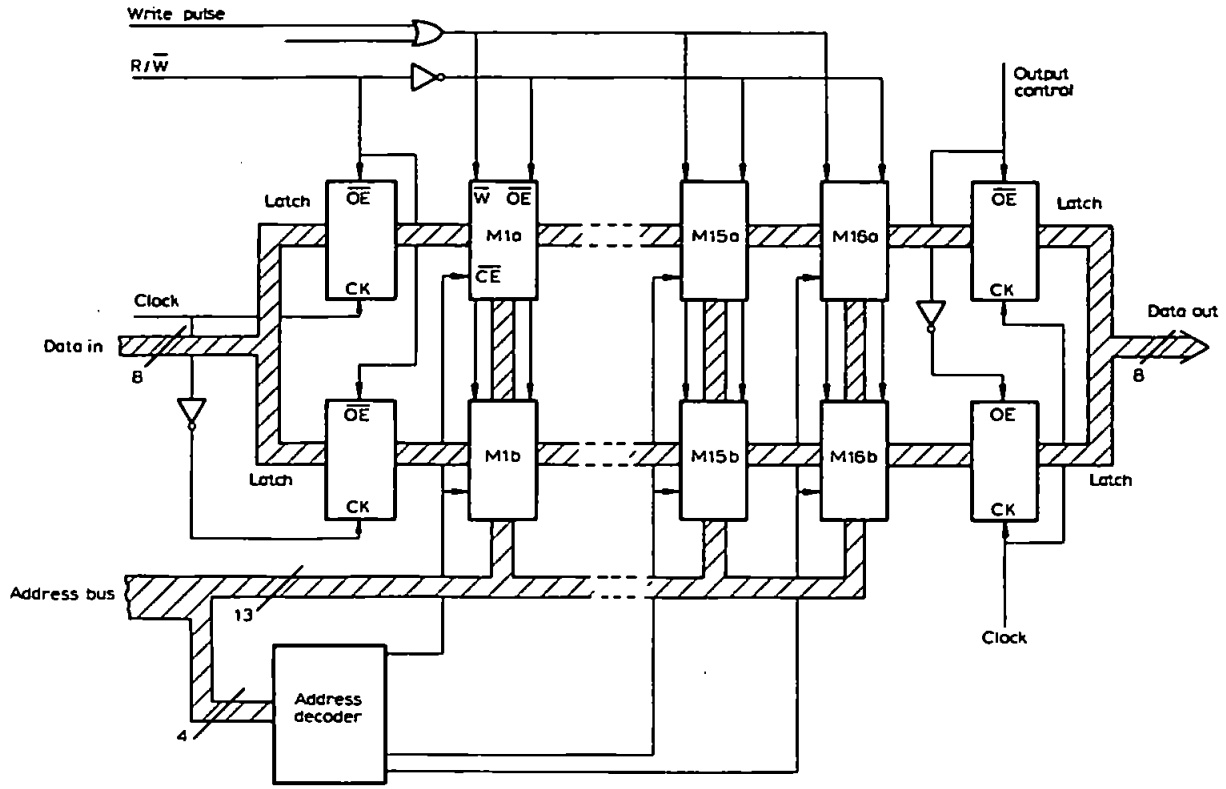

Figure 3. Memory organization for a 512 × 512 × 8-bit framestore (M1–M16 are 8 k × 8 CMOS static RAMs)

respectively. Scaling is also required to reduce quantizing effects associated with LU3 (antilogarithm) so scaling of equation (3) gives

$$C = \alpha a_0 \left(\frac{x_G}{x_B}\right)^{-a_1}$$

$$= b^{\{-a_1[\log x_G - \log x_B + \log(\alpha^{-1/a_1})]\ +\ \log a_0\}} \qquad (5)$$

where α is a scaling factor to reduce quantizing effects and b is the logarithm base. An optimum base is such that for an input of 255 to LU1–LU3 the output is also 255, ie $b = 1.021968271$. From equation (5) we see that C can be found by first computing $\log x_G - \log x_B$ using LU1, LU2 and the ALU. Then, with $\log x_G - \log x_B$ as input, LU3 can be programmed to provide exponentiation taking into account the fixed quantities a_0, a_1 and α. Changes in a_0 and a_1 can be accommodated simply by remapping LU3. With regard to scaling errors, if $\alpha = 1$ the error in the hardware-computed concentration can be of the order of 100% with respect to the value computed by floating point arithmetic. If $\alpha = 10$, the error after descaling can reduce to a few per cent and also the result is better suited for display.

To evaluate rapidly features involving linear combinations of many images, as in equation (4), a recursive loop was designed such that LU3 output can be fed back to framestore FS2 via the third framestore FS3. Data is read from FS1 and FS2, processed and then stored in FS3, all within the same 40 ms frame period. To do this the addressing and write pulses to FS3 must be delayed with respect to those for FS1 and FS2 and the extra logic complexity was not thought necessary at this stage.

Finally, Figure 2 shows the programmable display look-up tables found in most image processors. These fast bipolar RAMs can be programmed to a nonlinear transfer function for display enhancement and images can be pseudocoloured, eg by providing three different transfer functions for the red, green and blue outputs. Despite the fairly high clock rates, all the logic implied by Figure 2 was constructed using conventional wirewrap techniques and low-power Schottky TTL. The system was tested without the need for a logic analyser.

Software

Processor software has been written over a two-year period and divides into two main areas. Supervisory software is necessary to set the hardware up for various processing operations. In the simple system described this is done in the form of macros. For example a REG macro repeatedly writes to a framestore and alternately displays two framestore outputs to allow two photographic transparencies to be registered to within a pixel using vernier adjustments. A RATIO macro sets the hardware for writing data into two framestores, followed by video-rate log-antilog operations and linear display look-up tables. Different coefficients and scaling factors can be input into the macro. A SOFT macro sets the hardware for writing to a framestore, and for image data transfer to and from the framestore for software enhancement (software is then called using the system monitor). Ideally such macros and all software

enhancement should be incorporated into a higher-level command language capable of defining multiple processing operations by a one-line command string. Batchelor *et al.*[14] have described such a language for general image processing.

Image enhancement software has been written to outline coastal contours and pseudocolour images, for example. However, it should be noted that such algorithms also find application in advanced image classification schemes. FORTRAN enhancement programs for remote sensing applications are readily available[15] but since it is often necessary to tailor the program for the particular processor used it may well be better to write the software from first principles[16, 17].

To detect edges and to sharpen or smooth images we need a neighbourhood operator which generates a pixel value based on its nearest neighbours. Such an operator centred on a point (U, V) in an image $f(x, y)$ is conveniently defined by a weighting function $W(x - U, y \propto V)$ which is zero valued outside a small region. The inner product of the operator with the image is then

$$C(U, V) = \sum_x \sum_y W(x - U, y - V) f(x, y)$$

and for an $n \times n$ operator

$$C(U, V) = \sum_{i=1}^{n} \sum_{j=1}^{n} f_{ij} w_{ij} = (f, W)$$

This can be regarded as crosscorrelation. Where $C(U, V)$ is large it is assumed that the required function (eg an edge) is located.

The laplacian operator can be represented in generalized form by

$$W = \begin{array}{|c|c|c|} \hline 0 & -\gamma & 0 \\ \hline -\gamma & 1+4\gamma & -\gamma \\ \hline 0 & -\gamma & 0 \\ \hline \end{array}$$

where γ is a gain constant. If γ is too large random noise becomes objectionable but useful sharpening occurs for $\gamma \leq 2$. If used directly this means that point (x, y) in the original image $f(x, y)$ is output in the sharpened image as

$$\begin{aligned} C(x, y) &= (1 + 4\gamma) f(x, y) \\ &\quad - \gamma[f(x+1, y) + f(x-1, y) \\ &\quad + f(x, y+1) + f(x, y-1)] \\ &= f(x, y) + 5\gamma[f(x, y) - \overline{f(x, y)}] \end{aligned}$$

Often two or more operators are combined, as in edge detection. A point (x, y) in an edge-detected image $g(x, y)$ is generated by using an approximation to the image gradient at (x, y), ie

$$\begin{aligned} g(x, y) &\approx \left|\frac{\partial f}{\partial x}\right| + \left|\frac{\partial f}{\partial y}\right| \\ &= |(f, W_x)| + |(f, W_y)| \end{aligned}$$

where for the Sobel operator

$$W_x = \begin{array}{|c|c|c|} \hline 1 & 2 & 1 \\ \hline 0 & 0 & 0 \\ \hline -1 & -2 & -1 \\ \hline \end{array} \qquad W_y = \begin{array}{|c|c|c|} \hline 1 & 0 & -1 \\ \hline 2 & 0 & -2 \\ \hline 1 & 0 & -1 \\ \hline \end{array}$$

These and similar algorithms have been implemented in FORTRAN using a general 3×3 neighbourhood processing routine, and MACRO-11 assembly language is used to handle the programmed I/O. Since the appropriate operator has to be moved throughout the whole image the processing time can be lengthy but tolerable for a low-cost machine. Typically a 768×512 image takes several minutes even with a floating point CPU option although subimages can be selected under cursor control and processing time is reduced accordingly.

Pointwise software operations (where a pixel is modified independently of its neighbours) are usually faster. Here use is made of the display look-up RAMs in Figure 2. Besides pseudocolour and simple contrast stretching routines we have found that a 'histogram equalization' routine[16] is particularly useful. This computes the image grey-level histogram and redistributes the grey levels via the look-up RAMs to give an approximately flat histogram for the enhanced image. Redistribution is achieved by mapping each display look-up to the cumulative density function

$$S_k = \sum_{j=1}^{k} \frac{n_j}{N}$$

where S_k is the kth output grey level, n_j is the number of pixels at grey level j, and N is the total number of pixels in the image or subimage. A combination of histogram equalization and pseudocolour density slicing gives very effective enhancement of low-contrast ocean areas, for example.

Processing Examples

Figure 4a shows the result of applying the Roberts edge detection operator to a raw Nimbus-7 CZCS image of the English Channel (orbit 13437 22/06/81). In this figure an option has been used in which the variable gradient $g(x, y)$ is replaced by a constant level (black) provided that it exceeds a user-defined threshold; otherwise $g(x, y) = f(x, y)$. The effect is to outline the coast but retain some background information. Figure 4b shows how small subsurface effects in midchannel and high turbidity indications near peninsulas can be significantly enhanced using histogram equalization.

For remote sensing applications this particular orbit is useful since it represents a cloud-free pass at a time when sea truth (related to chlorophyll concentration) was measured across the channel between Plymouth, UK and Roscoff, France. It follows that if the raw image is atmospherically corrected it may be possible to obtain some correlation between these measurements and chlorophyll retrieval algorithms. A simple atmospheric correction algorithm relies on the assumption

$$\frac{L_A(\lambda)}{L_A(\lambda_R)} = \frac{L_{sun}(\lambda)}{L_{sun}(\lambda_R)}$$

where $L_{sun}(\lambda_R)$ is the solar radiance at the red wavelength λ_R. For images of ocean areas the aerosol radiance $L_A(\lambda_R)$ is then found by assuming that virtually all the sensor radiance at λ_R is due to aerosol and Rayleigh scattering, ie

$$L_A(\lambda_R) = L_S(\lambda_R) - L_R(\lambda_R)$$

giving, from equation (2), the result

Figure 4. Software enhancement of a Nimbus-7 CZCS image of the English Channel, showing (a) generation of a coastal outline while retaining tonal features and (b) histogram equalization used to enhance midchannel effects

$$L_W(\lambda) = L_S(\lambda) - L_R(\lambda) - [L_S(\lambda_R) - L_R(\lambda_R)] \frac{L_{sun}(\lambda)}{L_{sun}(\lambda_R)}$$

All parameters on the right-hand side of this equation are available from the satellite CCT, or can be calculated or are available from published data[8]. The algorithm was then applied to a narrow strip of water between Plymouth and Roscoff (north–south route) and estimates of $L_W(\lambda_B)$ and $L_W(\lambda_G)$ for the corresponding 20 nm CZCS channels along this strip were found. Finally, since coefficients a_0 and a_1 were unknown for this water area only the simple ratio $L_W(\lambda_G)/L_W(\lambda_B)$ was computed. This ratio is shown graphically in Figure 5a. The peak on the left-hand side of this graph corresponds to land near Plymouth whereas the small response in midchannel appears to correspond to the subsurface effect shown in Figure 4. There is a significant correlation coefficient (0.76) between the ratio and the diatom concentration measured by ship trawl although much more data is needed before an algorithm for this water area can be developed. However, the results do suggest a significant improvement in signal-to-noise ratio compared with the ratio derived from raw sensor radiance (Figure 5b).

Video-rate spectral ratioing has also been applied to multiband aerial photographs. Figure 6 shows how the IR/R reflectance ratio can be used to detect vegetation. Figure 6a shows a monochromatic print of a false colour image, formed by displaying the infrared image on the green channel and the red image on the red channel. It shows boats, paths and buildings (above the river) but these disappear on ratioing (see Figure 6b) since they have no significant IR/R response. To enhance the difference between vegetation types, selected grey levels were coloured (density slicing). This enhanced the visibility of trees.

More advanced processing

As previously intimated the processor can be used to examine more advanced pattern recognition concepts using software-based algorithms. For example, the use of spatial information, be it in the form of image structure, texture or context, is attractive because when it is combined with multispectral information the classification accuracy is significantly improved[7]. It is also possible to use texture alone (one spectral band) to classify images, and so a texture analysis program has been written based on the favoured technique of grey-tone spatial dependent matrices[18, 19]. Suppose a subimage comprises vertical stripes of grey level g_1 and g_2, ie

$$\text{subimage} = \begin{matrix} \overbrace{\begin{matrix} g_1 g_2 g_1 g_2 \cdots g_1 g_2 \\ g_1 g_2 g_1 g_2 \cdots g_1 g_2 \\ g_1 g_2 g_1 g_2 \cdots g_1 g_2 \\ \vdots \quad \vdots \quad \vdots \quad \vdots \qquad \vdots \quad \vdots \\ g_1 g_2 g_1 g_2 \cdots g_1 g_2 \end{matrix}}^{N_x \text{ columns (even)}} \end{matrix} \quad N_y \text{ rows}$$

An nth order probability distribution based on n pixels can be computed for this subimage and second-order statistics are often used. In this case we compute the joint probability density of pairs of grey levels that occur at two points separated by δ. This gives a grey-tone co-occurrence matrix **P**. The program considers only

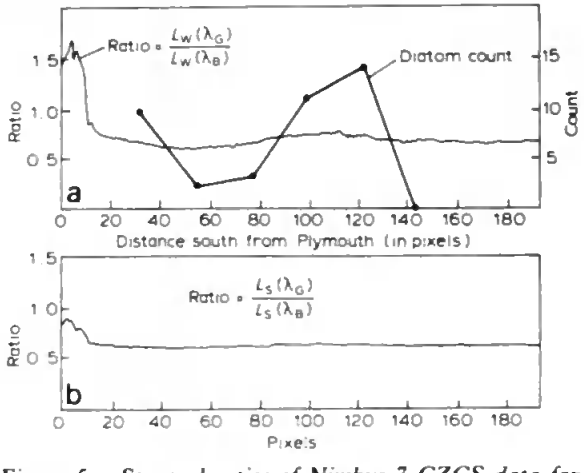

Figure 5. Spectral ratios of Nimbus-7 CZCS data for Plymouth to Roscoff: a, atmospherically corrected data; b, raw sensor data

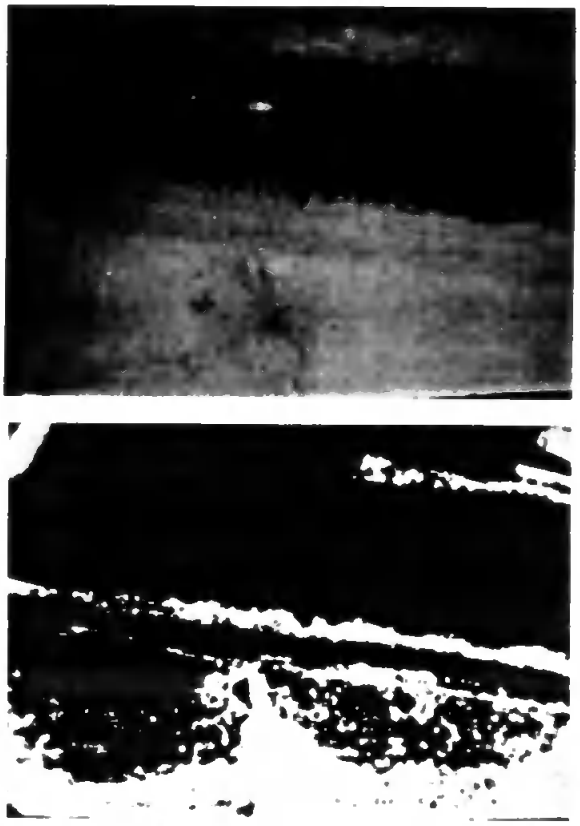

Figure 6. Spectral ratio from multiband aerial photographs: a, monochromatic print of a false colour image; b, IR/R reflectance ratio showing only vegetation classes

adjacent pixels ($\delta = 1$) and four directions, 0°, 45°, 90° and 135°. Considering horizontal spatial dependence (0°), for example, there are $(N_x - 1)N_y$ occurrences of a $g_1 g_2$(or $g_2 g_1$) transition and $2(N_x - 1)N_y$ possible pairs. Therefore the normalized horizontal matrix is

$$\mathbf{P}_0 = \begin{array}{c|cccccc} & j\rightarrow & & & & & \\ & 0 & 1 & 2 & \cdots & g_1 & \cdots & g_2 \\ \hline 0 & & & & & & & \\ 1 & & & & & & & \\ 2 & & & & & & & \\ \vdots & & & & & & & \\ i\downarrow\ g_1 & & & & & & & p(1,2) \\ \vdots & & & & & & & \\ g_2 & & & & & p(2,1) & & \end{array}$$

where

$$p(1,2) = \frac{N_y(N_x - 1)}{2N_y(N_x - 1)} = 0.5$$

For homogeneous subimages the matrix reduces to a single entry and for fine texture all the $p(i, j)$ could be similar. Haralick *et al.*[18] have proposed a number of features based on such matrices and the following have been tried on this processor

$$\text{ASM} = \Sigma p(i,j)^2$$
$$\text{ENT} = -\Sigma p(i,j) \log[p(i,j)]$$
$$\text{CON} = \Sigma (i-j)^2 p(i,j)$$

(The CON feature requires the subimage to be histogram equalized to minimize the effect of tonal variation between otherwise identical textures.)

By judicious choice of features and subimage size it is possible to discriminate certain ground classes. The results of preliminary experiments on aerial photographs taken at 0.5 km altitude are shown in Figure 7 (the 800 m resolution of the CZCS data precludes the use of texture measures over land areas but the 30 m resolution of Landsat-4, for example, should allow interesting texture measures to be carried out). Figure 7b indicates that simply taking the ratio of $\text{CON}_{\max}$ to $\text{CON}_{\min}$ for P_0, P_{45}, P_{90} and P_{135} allows a homogeneous area like a grass field to be distinguished from a semifilled car park. Figure 7a shows that measurements of mean(ENT) and mean(CON) allow grass fields to be distinguished from tree areas. This is a more useful result since tree areas and grass areas have similar spectral signatures. Similar clustering of data points occurs for ENT *versus* ASM although in both cases it was found necessary to select the subimage size carefully (a 40×40 subimage gave good clustering whereas a 20×20 subimage did not). Even so, since the subimages are still relatively small the run time of this program is less than 1 min and simple interactive experiments are quite feasible. A really useful application of such matrices seems to be where multispectral information is weak. A good example of this has been described by Shanmugan *et al.*[20] for the classification of geological rock formations.

The clustering concept also occurs in so-called unsupervised classification of multispectral data. Hybrid classifiers[8, 21] involving a mixture of unsupervised and supervised classification seem set to become prominent in the future. A clustering algorithm in this context clusters datapoints in multispectral space into spectral classes. It is a good starting point in a hybrid classifier since it shows natural patterns in the data and can be used to provide training statistics for the supervised process, should these be unavailable. A *K*-means clustering algorithm[22] for up to four spectral channels is

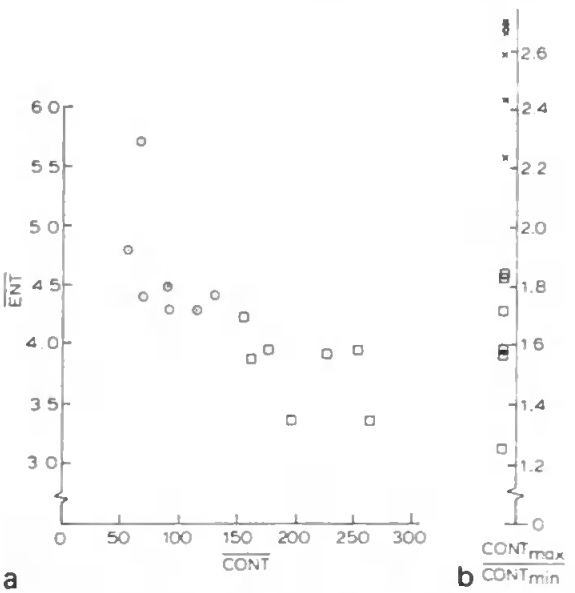

Figure 7. Results of simple classification experiments based on statistical measures of image texture (⊙, trees; ⊡, grass; ×, car park)

currently under investigation on this processor and the main procedures can be summarized as follows.

- Select a subimage and store in an array in memory. This array represents each pixel as a multispectral vector **X**.
- Decide on the number K of spectral classes and define initial cluster centres (arbitrarily).
- Use a distance measure to assign each pixel to the nearest cluster centre.
- Recalculate cluster centres (the mean vectors) and test for convergence (no move in the mean vector). If there is no convergence, go to the previous step again.
- Compute mean and standard deviation vectors for each class and also the intercluster distances. Print the results.

The limitations of a minicomputer for this type of analysis soon become apparent since effectively many iterations for each pixel are involved and CPU time can be high. Moreover, the 224k memory on this machine, including 160k of extended or virtual memory, is still a real limitation since even then the subimage array is limited to approximately 150×150 pixels. Much work is currently being carried out on specialized architectures for parallel image processing[23, 24] and no doubt interactive classifiers using special architectures will eventually be incorporated into low-cost remote sensing machines.

CONCLUSIONS

Remote sensing is a multidisciplinary field with high-cost implications. It can therefore be difficult to develop such work within the limited resources of an educational environment. A particular problem is often the lack of a local low-cost digital image processor with appropriate data I/O facilities. However, effective low-cost solutions can be designed within an engineering department using mostly readily available equipment and local engineering expertise. A system comprising three high-resolution framestores (possibly with image feedback between framestores), a pipelined hardware processor for fast pointwise combinations of images and fast display look-up RAMs allows simple classification (selected features) to be examined interactively and at low cost. The engineering of such a system is changing rapidly but the use of byte-wide high-density static RAMs for the framestores is particularly attractive. In addition to video-rate feature evaluation, software image enhancement, simple atmospheric correction and texture analysis can also be examined and here the execution times are still low enough for demonstrations. More advanced remote sensing concepts can be studied, such as the clustering of multispectral data, although problems arise as expected due to the lack of parallel processing and the speed and memory limitations of the minicomputer.

REFERENCES

1 **Lillesand, T** 'Trends and issues in remote sensing education' *Photogramm. Eng. Remote Sensing* Vol 48 No 2 (February 1982) pp 287–293

2 **Jensen, J** 'An interactive image processing system for remote sensing education' *Photogramm Eng. Remote Sensing* Vol 45 (1979) pp 1519–1527

3 **Hovis, W and Leung, K** 'Remote sensing of ocean colour' *Opt. Eng.* Vol 16 No 2 (1977) pp 158–166

4 'Atmospheric correction of satellite observation of sea water colour' *Recommendations of 2nd Int. Workshop Commission of the European Communities Joint Research Centre, Ispra Establishment 21020, Ispra (Va), Italy* (30th March–1st April, 1981)

5 **Viollier, M, Tanré, D and Deschamps, P** 'An algorithm for remote sensing of water colour from space' *Boundary-Layer Meteorol.* Vol 18 (1980) pp 247–267

6 **Sturm, B** 'The atmospheric correction of remotely sensed data and the quantitative determination of suspended matter in marine water surface layers' in **Cracknell, A P** (ed.) *Remote sensing in meteorology, oceanography and hydrology* Ellis Horwood, Chichester, UK (1981)

7 **Landgrebe, D A** 'Analysis technology for land remote sensing' *Proc. IEEE* Vol 69 No 5 (May 1981) pp 628–642

8 **Swain, P and Davis, S** (eds.) *Remote sensing: the quantitative approach* McGraw-Hill, New York, USA (1978)

9 **Curran, P** 'Multispectral remote sensing of vegetation amount' *Prog. Phys. Geogr.* Vol 4 (1980) pp 315–341

10 **Sivertson Jr, W E, Wilson, R G, Bullock, G S and Schappell, R T** 'Feature identification and location experiment' *Science* Vol 218 (3 December 1982)

11 **Gordon, H, Clark, D and Mueller, J** 'Phytoplankton pigments from the Nimbus-7 coastal zone colour scanner: comparisons with surface measurements' *Science* Vol 210 (October 1980) pp 63–66

12 *Eurasep Secretariat Newsletter* Vol 7, Commission of the European Communities Joint Research Centre, Ispra, Italy (February 1982)

13 **Singh, S and Cracknell, A** 'Comparison between CZCS data from 10th July, 1979 and simultaneous in-situ measurements for south eastern Scottish waters' *Int. J. Remote Sensing* Vol 4 No 4 (October 1983) pp 755–784

14 **Batchelor, B, Brumfitt, P and Smith, B** 'Command language for interactive image analysis' *Proc.* Vol 127 No 5 (1980) pp 203–218

15 **Cracknell, A P** (ed.) *Computer programs for image processing of remote sensing data* University of Dundee, UK (1982)

16 **Gonzalez, R and Wintz, P** *Digital image processing* Addison-Wesley, Reading, USA (1977)

17 **Frei, W and Chen, CC** 'Fast boundary detection: a generalisation and a new algorithm' *IEEE Trans. Comput.* Vol 26 No 10 (October 1977) pp 988–998

18 **Haralick, R M, Shanmugan, K and Dinstein, I**

'Textural features for image classification' *IEEE Trans. Syst., Man Cybern.* Vol 3 (November 1973) pp 610–621

19 **Haralick, R M** 'Statistical and structural approaches to texture' *Proc. IEEE* Vol 67, No 5 (May 1979) pp 786–803

20 **Shanmugan, K S, Narayanan, V, Frost, V S, Stiles, J A and Holtzman, J C** 'Textural features for radar image analysis' *IEEE Trans. Geosci. Remote Sensing* Vol 19 No 3 (July 1981) pp 153–156

21 **Justice, C and Townshend, J** 'A comparison of unsupervised classification procedures on Landsat MSS data for an area of complex surface conditions in Basilicata, southern Italy' *Remote Sensing Environ.* Vol 12 (1982) pp 407–420

22 **Tou, J T and Gonzalez, R C** *Pattern recognition principles* Addison-Wesley, Reading, MA, USA (1974)

23 **Danielsson, P and Levialdi, S** 'Computer architectures for pictorial information systems' *Computer* (November 1981) pp 53–67

24 **Duff, M** 'Parallel processors for digital image processing' in **Stucki, P** (ed.) *Advances in digital image processing* Plenum Press, New York, USA (1979)

INT. J. REMOTE SENSING, 1985, VOL. 6, NO. 11, 1749–1763

Analysis of CZCS data for the U.K. South-western Approaches

G. WADE, D. H. LAWRENCE and X. LING

Department of Communication Engineering, Faculty of Technology, Plymouth Polytechnic, Plymouth PL4 8AA, Devon, England

(Received 22 October 1983; in final form 6 March 1985)

Abstract. The implementation of a non-iterative atmospheric correction algorithm is described in detail and the performance of the algorithm is illustrated for several CZCS images. Chlorophyll retrieval is attempted using linear, power and polynomial regression for ratios of corrected images and the best correlation coefficients are in the region of 0·9. The same images are analysed in three spectral bands using the ISOCLS clustering algorithm and ocean areas are stratified into subclass patterns which correlate well with ratios and sea-truth. The monocluster blocks approach is used to extract training statistics for maximum likelihood classification of ocean areas and the results compare favourably with corresponding ratio images.

1. Introduction

This paper describes the analysis of multispectral data gathered from NIMBUS-7 CZCS passes over the U.K. South-western Approaches. The objective was to compare the synoptic mapping of subsurface chlorophyll using simple and more complex classification procedures based upon water leaving radiance L_W^λ measured in CZCS channels 1–3. The simple ratio L_W^3/L_W^1 for example (or the subsurface equivalent) is a useful chlorophyll retrieval feature because it exploits the chlorophyll absorption minimum near 550 nm (channel 3) and the absorption maximum near 443 nm (channel 1). On the other hand, the use of information in all three channels in a clustering algorithm for example may provide enhanced classification.

Prior to classification L_W^λ has to be separated from the total radiance L_T^λ measured by the satellite sensor and the major processes contributing to L_T^λ are modelled in figure 1. Processes 1–3 arising from Rayleigh and Mie scattering usually generate a dominant noise component, which could amount to more than 80 per cent of L_T^λ and only processes 4 and 5 provide useful subsurface information, and so contribute to L_W^λ. Since the extraction of L_W^λ is a significant computational problem the atmospheric correction procedure used is described in some detail.

2. Atmospheric correction

2.1. *Correction algorithm*

This section describes the basic algorithm which has been implemented and ancillary equations and a list of symbols are given in Appendices A and B. The atmospheric model in figure 1 assumes a flat sea surface so that any glitter contribution to L_T^λ is assumed zero. Processes 4 and 5 model radiation which penetrates the surface only to be partially backscattered, and then emerge as water leaving radiance L_W^λ. The contribution to L_W^λ from process 4 suffers attenuation due to scattering and ozone

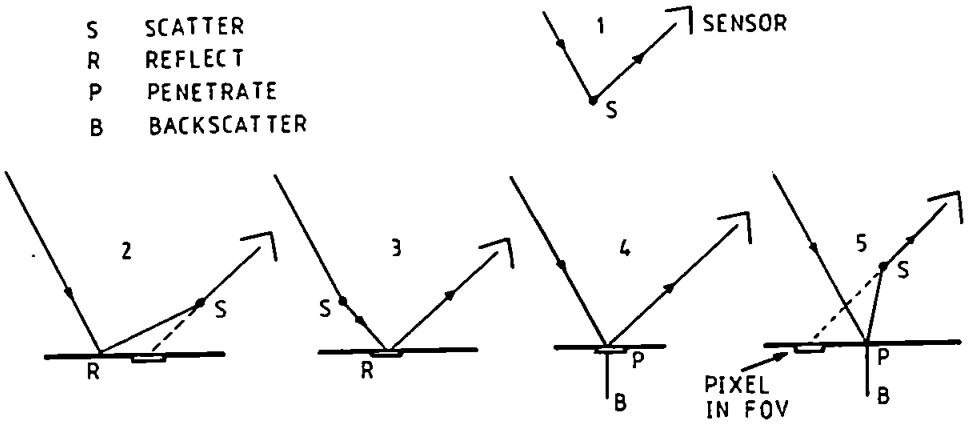

Figure 1. Contributions to sensor radiance.

absorption on its way to the sensor and this could be modelled with a direct transmittance T^{λ}. However, contributions to L_W^{λ} from adjacent pixels can occur due to forward scattering into the sensor FOV (process 5) so it is usual to associate a diffuse transmittance t_D^{λ} with L_W^{λ} where $T^{\lambda} < t_D^{\lambda} < 1$.

To a good approximation Rayleigh and aerosol scattering can be treated separately so L_T^{λ} can be expressed as (Sørensen 1981, Gordon *et al.* 1980)

$$L_T^{\lambda} = t_D^{\lambda} L_W^{\lambda} + L_R^{\lambda} + L_A^{\lambda} \tag{1}$$

where L_R^{λ} and L_A^{λ} correspond to Rayleigh and aerosol radiances, respectively. Since the Rayleigh optical thickness τ_R^{λ} is small (typically $\tau_R^{\lambda} \simeq 0{\cdot}1$ in the visible band) then a single scattering approximation can be used for L_R^{λ} (Viollier *et al.* 1980, Sørensen 1981) and this reduces to

$$L_R^{\lambda} = (\tau_R^{\lambda}/4\pi\mu)[P_R(\psi -) + (\rho(\theta) + \rho(\theta_0))P_R(\psi +)]E_0^{\lambda} T_{O_3}^{\lambda}(\mu) T_{O_3}^{\lambda}(\mu_0) \tag{2}$$

The Rayleigh phase function for backscattering into the sensor, $P_R(\psi -)$ is the dominant term and corresponds to the Rayleigh component of process 1. The term $[\rho(\theta) + \rho(\theta_0)]P_R(\psi +)$ represents a relatively small contribution due to specular reflection at the sea surface and corresponds to processes 2 and 3. Typically we have found $\rho(\theta)$ and $\rho(\theta_0)$ to be of the order of 0·02 and, since the phase functions are comparable to each other, we have neglected the transmittance loss associated with this reflectance term (B. Sturm, 1982, personal communication).

The aerosol optical thickness τ_A^{λ} is only small ($\tau_A \ll 1$) under very low aerosol conditions (see, for example, Viollier *et al.* 1980) but, under this assumption, L_A^{λ} can be expressed as a single scattering expression in the form of equation (2). In other words L_A^{λ} is assumed to be a linear function of the optical thickness τ_A^{λ} and the aerosol phase function is assumed to be independent of wavelength, an assumption found in more general, multiple scattering models (B. Sturm, 1982, personal communication, Gordon and Clark 1980). Taking the ratio of aerosol radiance for wavelengths λ and λ_0 (λ_0 = 670 nm, channel 4) gives

$$\frac{L_A^{\lambda}}{L_A^{\lambda_0}} = \frac{\tau_A^{\lambda}}{\tau_A^{\lambda_0}} \frac{E_0^{\lambda} T_{O_3}^{\lambda}(\mu) T_{O_3}^{\lambda}(\mu_0)}{E_0^{\lambda_0} T_{O_3}^{\lambda_0}(\mu) T_{O_3}^{\lambda_0}(\mu_0)} \tag{3}$$

B. Sturm (1982, personal communication) extends equation (3) to account for multiple

aerosol scattering but it has been shown that equation (3) is still approximately valid under multiple scattering conditions (Sørensen 1981). To enable L_A^λ to be estimated it is usual to assume

$$\frac{\tau_A^\lambda}{\tau_A^{\lambda_0}} = (\lambda_0/\lambda)^M \tag{4}$$

where M is the Ångström exponent. The fundamental idea of the algorithm is now invoked (Gordon 1978) whereby it is assumed that $L_W^{\lambda_0} = 0$. Hence, from equations (1), (3) and (4) it follows that

$$t_D^\lambda L_W^\lambda = L_T^\lambda - L_R^\lambda - (L_T^{\lambda_0} - L_R^{\lambda_0})\left(\frac{\lambda_0}{\lambda}\right)^M \frac{E_0^\lambda T_{O_3}^\lambda(\mu) T_{O_3}^\lambda(\mu_0)}{E_0^{\lambda_0} T_{O_3}^{\lambda_0}(\mu) T_{O_3}^{\lambda_0}(\mu_0)} \tag{5}$$

Should $L_W^{\lambda_0}$ be positive then the term $L_T^{\lambda_0} - L_R^{\lambda_0}$ could be replaced by $L_T^{\lambda_0} - L_R^{\lambda_0} - L_W^{\lambda_0}$ and the iterative technique of Smith and Wilson (1981) is then used to estimate $L_W^{\lambda_0}$. However, for the images analysed we found $(L_T^{\lambda_0} - L_R^{\lambda_0})$ to be typically an order of magnitude greater than a first estimate of $L_W^{\lambda_0}$ and the non-iterative algorithm was considered adequate.

2.2. *Implementation*

The atmospheric correction of three CZCS channels for a typical high-resolution display requires some 10^6 evaluations of equation (5). This can require considerable CPU time since L_R^λ, t_D^λ and $T_{O_3}^\lambda(\mu) T_{O_3}^\lambda(\mu_0)$ are all functions of the Sun–satellite geometry which varies with pixel number. This means that, in addition to the evaluation of (5), all the geometric relations in Appendix A (except equation (A 15)) have to be evaluated for each pixel unless some compromise is made to reduce computation time. A single geometric calculation at the scene centre was considered too coarse (a 768 pixel × 512 pixel scene subtends angles of approximately 30° × 20° at the satellite) and the results seem to support this conclusion.

The compromise adopted was to partition the scene into 24 square cells, each cell being 128 pixels × 128 pixels and subtending angles of approximately 5° × 5° at the satellite (figure 2 (*a*)). A single geometric calculation was then performed for the centre of each cell, yielding 24 values of L_R^λ, $L_R^{\lambda_0}$, $T_{O_3}^\lambda(\mu) T_{O_3}^\lambda(\mu_0)$ and $T_{O_3}^{\lambda_0}(\mu) T_{O_3}^{\lambda_0}(\mu_0)$, and six values of t_D^λ. These parameters were regarded as constant over the cell so that only equation (5) need be evaluated for each pixel.

Evaluation of the Sun–satellite geometric relations in Appendix A is straightforward except for parameters θ_1 and t. Considering the computation of cell centre latitude, θ_1, it is first necessary to align the satellite co-ordinate system (pixel and scan-line numbers) with terrestrial latitude and longitude by rotating the satellite scene through the orbital inclination angle α (figure 2 (*b*)). This angle is given by

$$\sin\alpha = \frac{\sin(\text{track-line inclination})}{\cos\Theta_1} \tag{6}$$

The track-line inclination is the angle between due north and the satellite track at the equator. Strictly α increases with increasing latitude but since the variation is small over the scene α is taken as constant, hence equation (6).

Rotation of a point (x, y) in the rectangular satellite co-ordinate system through an angle α about the origin maps the point to the co-ordinate $(x\cos\alpha - y\sin\alpha,\ y\cos\alpha + x\sin\alpha)$. This mapping leads to the following extrapolations for cell (j, k) assuming

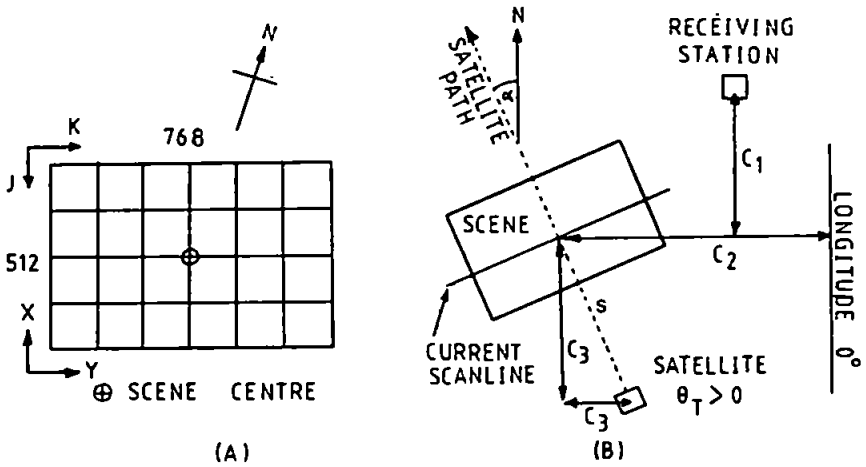

FIGURE 2. (*a*) Partitioning the image for geometric calculations. (*b*) Computing local time.

that the scene lies in a plane, i.e. neglecting Earth curvature

$$\theta_1(j,k)=\Theta_1+a[(3-2j)\cos\alpha+(2k-5)\sin\alpha] \tag{7}$$

$$\theta_2(j,k)=\Theta_2+b[-(3-2j)\sin\alpha+(2k-5)\cos\alpha] \tag{8}$$

where $j=0,\ldots,3$ and $k=0,\ldots,5$. Constants $2a$ and $2b$ define the angles subtended at Earth centre by the cells in the north–south and east–west directions, respectively, where

$$a=\frac{64\ (\text{ground resolution in } X \text{ direction (km)})}{60\times 1{\cdot}852}\ \text{degrees} \tag{9}$$

$$b=\frac{64\ (\text{ground resolution in } Y \text{ direction (km)})}{60\times 1{\cdot}852\cos\Theta_1}\ \text{degrees} \tag{10}$$

(1·852 is the conversion factor between nautical miles and kilometres.)

The local time t is required to compute the solar angles θ_0 and ϕ_0. It is the time relative to noon at the subsatellite point and is derived from the known picture time (the time of closest approach to the receiving station) by making the corrections indicated in figure 2 (*b*). Corrections C_1 and C_2 account for deviations in latitude and longitude from specified Earth points (figure 2) and C_3 corrects for scanner tilt which causes the subsatellite point to be displaced from the current scan line. The correction is

$$t=\text{picture time (G.M.T.)}+C_1+C_2+C_3-12\ \text{hours} \tag{11}$$

where

$$C_1=(\theta_1-\text{LAT})\left(\frac{1{\cdot}852\times\text{scan-line duration (s)}}{60\times\text{ground resolution in } X \text{ direction (km)}}\right) \tag{12}$$

$$C_2=\theta_2/15 \qquad (\theta_2 \text{ in degrees}) \tag{13}$$

$$C_3 = \frac{s \sin \alpha}{60 \times 15 \times 1{\cdot}852 \cos \theta_1} - \frac{s \cos \alpha \times \text{scan-line duration (s)}}{3600 \times \text{ground resolution in } X \text{ direction (km)}} \tag{14}$$

$$\frac{s}{R} = sin^{-1}\left[\left(1 + \frac{\text{satellite altitude}}{R}\right)\sin \theta_t\right] - \theta_t \tag{15}$$

The sign of s follows the sign of θ_t (radians) and LAT (degrees) is the latitude of the receiving station. Note that C_1, C_2 and C_3 are cell dependent so that there are 24 values for t.

The algorithm was written in *C* on a 68000 processor with a 1 Mbyte memory and operating under UNIX. The processor is backed up by a 40 Mbyte Winchester drive, 40 Mbyte 1600 bpi tape drive and floppy drives, and the display comprises several 768 pixel × 512 pixel image stores with look-up tables and a high-resolution monitor. The atmospheric correction of a single CZCS channel comprising 768 pixels × 512 pixels of raw digital data takes approximately 15 min without a floating point accelerator.

3. Processed images

3.1. *Atmospherically corrected images*

Low-cloud CZCS passes were selected for which some type of sea-truth was available, although even then sea-truth measurements rarely corresponded to the same day as the pass. Figures 3 and 4 illustrate the performance of the correction algorithm and it is apparent that correction removes haze and emphasizes subsurface effects such as high turbidity around headlands and mid-channel chlorophyll structures. It is also apparent that channel 1 correction is non-ideal. Correction is inherently more difficult at this wavelength due to greater uncertainty in the compensation for radiometer loss (Gordon *et al.* 1983, Austin 1982) and due to greater sensitivity to errors in the Ångström exponent. Even so, finer longitudinal partitioning of the scene seems advantageous and examination of L_R^λ indicates that a partitioning of 30 × 4 would more nearly match steps in L_R^λ in the horizontal and vertical directions.

The sensitivity of the correction to the Ångström exponent M was studied by examining the results of regression analysis for chlorophyll retrieval (§ 3.2). The correlation coefficients improved slightly as M increased from 0·3 but for $M = 1{\cdot}0$ there was a significant decrease and a significant increase in the proportion of negative radiances (suggesting overcorrection). All subsequent analysis was carried out for $M = 0{\cdot}5$.

3.2. *Spectral ratios*

Spectral ratios of atmospherically corrected images have been computed for CZCS passes on 22 June 1981, 29 July 1981 and 17 June 1984 and attempts have been made to correlate these ratios with available sea-truth. In each case image rectification was performed using the second-degree transformations

$$L = a_0 + a_1 E + a_2 N + a_3 E^2 + a_4 EN + a_5 N^2$$

$$P = b_0 + b_1 E + b_2 N + b_3 E^2 + b_4 EN + b_5 N^2$$

These equations enable pixel and line numbers P, L in the CZCS scan to be derived from the easting (longitude) and northing (latitude) co-ordinates E, N corresponding to sea-truth. The coefficients are derived by multiple linear regression and by using Gaussian elimination for the solution of six simultaneous equations derived from ground control points.

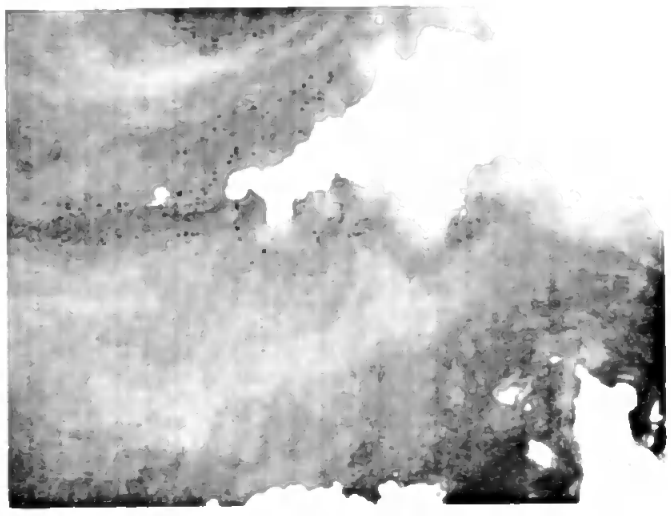

(*a*)

(*b*)

Figure 3. CZCS pass on 22 June 1981, channel 3: (*a*) raw digital count and (*b*) atmospherically corrected.

Figure 5 compares a plankton trawl between Plymouth and Roscoff on 23 June 1981 with the ratio L_w^{550}/L_w^{443} for 22 June 1981. A linear regression of this ratio with diatom count gave a correlation coefficient r of 0·78 although, clearly, there is a lack of data points and also a time discrepancy. More substantial sea-truth was available for the period 22 July 1981 to 2 August 1981 and various regressions have been tried for the

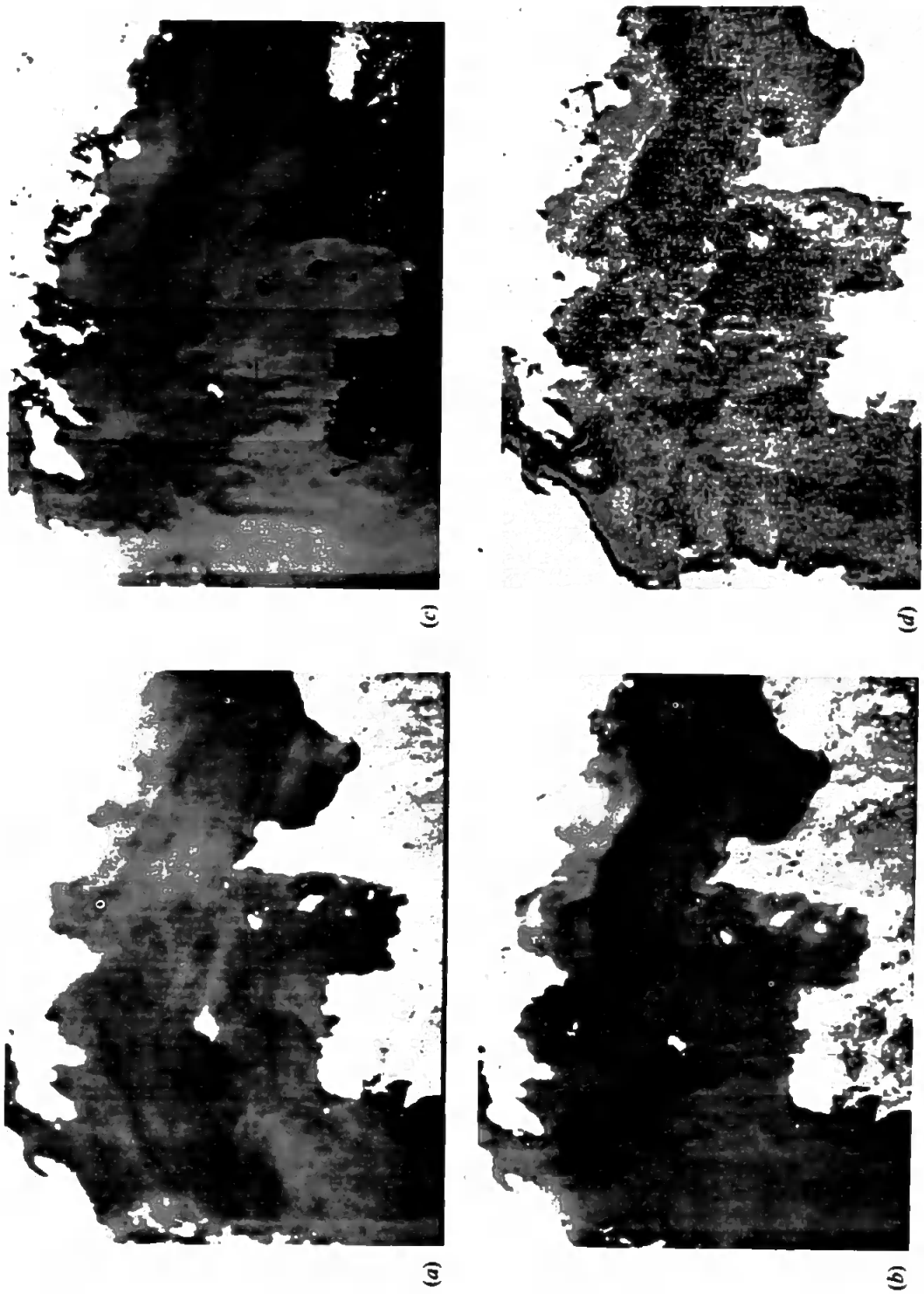

Figure 4. CZCS pass on 29 July 1981: (*a*) raw digital count, channel 3, (*b*) atmospherically corrected, channel 3, (*c*) atmospherically corrected, channel 1, showing cell striping and (*d*) ratio L_W^{550}/L_W^{520}.

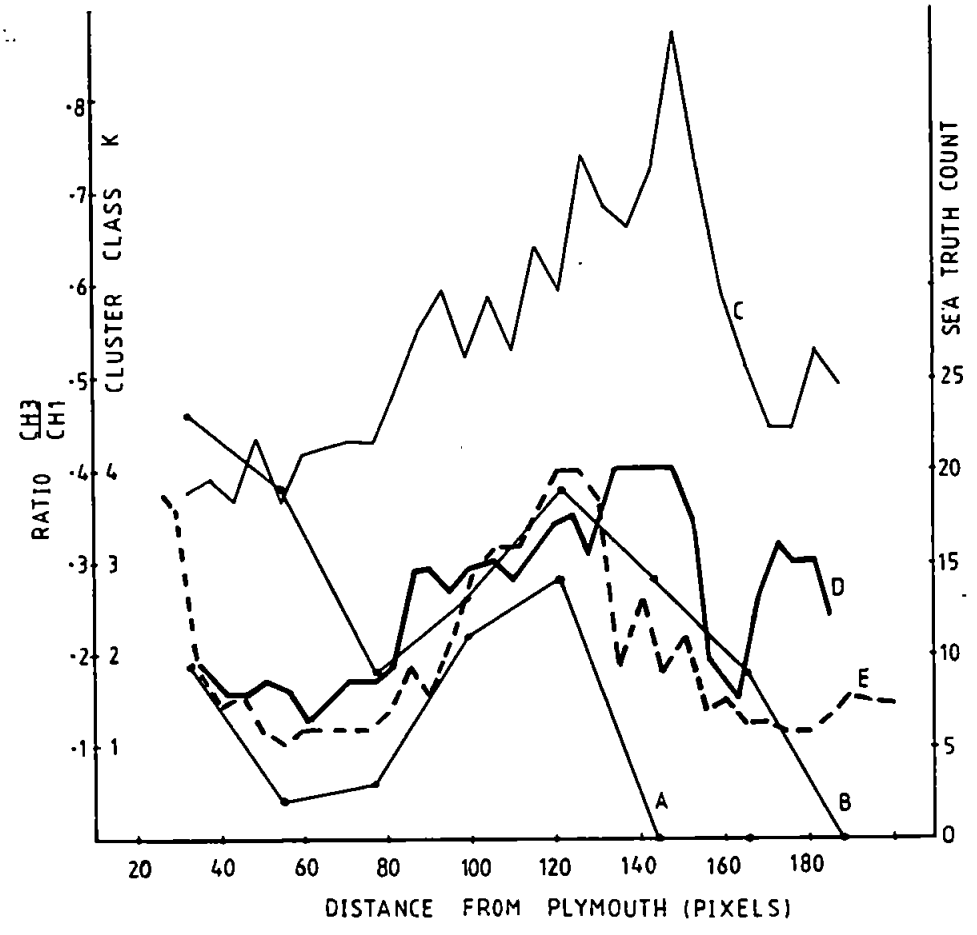

Figure 5. Comparison of ratio and cluster patterns with a plankton trawl: A, diatom count; B, zooplankton count; C, ratio of atmospherically corrected channels; D, cluster pattern, E, cluster pattern for 5 nautical mile shift.

29 July 1981 pass. The regressions were of the form

$$C = aR + b$$
$$C = aR^b$$
$$C = a + bR + cR^2 + dR^3$$

where C is the chlorophyll concentration (in mg m^{-2}) obtained by integration over one optical depth, and which includes phaeopigments, and R is the spectral ratio. Figure 6 shows that the chlorophyll concentrations were generally high so it was necessary to use the ratio L_w^{550}/L_w^{520} (see figure 4 (*d*)). The regression results are summarized in the table and they were computed from all data points gathered over the above dates, except for one data subset which appeared to be on a steep chlorophyll gradient and therefore was discarded. Integrated chlorophyll data was also available for the CZCS pass on 17 June 1984 although regression results were disappointing. The best correlation coefficient was 0·58 for a polynominal fit using the ratio L_w^{550}/L_w^{443}. The poor correlation is probably a result of low chlorophyll levels (typically < 1 mg m^{-2}) a 2 day measurement/pass discrepancy and uncertainties in the atmospheric correction,

specifically uncertainty in M and in the correction for radiometer sensitivity loss at such high orbit numbers.

Regression results

Linear			Power			Polynomial				
a	*b*	*r*	*a*	*b*	*r*	*a*	*b*	*c*	*d*	*r*
90·863	−39·358	0·88	52·278	2·664	0·86	176·6	−840·9	1295·5	−578·3	0·91

3.3. *Spectral clustering*

Cluster analysis and hybrid classification (Bauer and Davis 1976, Townshend and Justice 1980) have been applied to a number of CZCS passes. A form of the ISOCLS algorithm (ESL 1976, Justice and Townshend 1982) was implemented for clustering and a summary of results is given here. An exploratory cluster analysis of four separate CZCS atmospherically corrected passes for the South-western Approaches revealed a number of distinct classes in spectral space with typical mean vectors

$$\bar{x}\ (\text{thin cloud}) = \begin{bmatrix} 1{\cdot}6 \\ 1{\cdot}1 \\ 0{\cdot}6 \end{bmatrix}$$

$$\bar{x}\ (\text{thick cloud}) = \begin{bmatrix} 2{\cdot}4 \\ 1{\cdot}7 \\ 1{\cdot}3 \end{bmatrix}$$

$$\bar{x}\ (\text{coastal waters}) = \begin{bmatrix} 0{\cdot}5 \\ 0{\cdot}6 \\ 0{\cdot}5 \end{bmatrix}$$

$$\bar{x}\ (\text{ocean waters}) = \begin{bmatrix} L_W^{443} \\ L_W^{520} \\ L_W^{550} \end{bmatrix} = \begin{bmatrix} 0{\cdot}3 \\ 0{\cdot}7 \\ 0{\cdot}4 \end{bmatrix}$$

Similar distinctions in two-dimensional space have been found for LANDSAT images by Justice and Townshend (1982). Clearly, absolute radiance values (in mW/(cm^2 μm sr)) are only meaningful for ocean waters (since the correction algorithm computes L_W and assumes $L_W^{670} = 0$) although the identification of the above or similar regions in spectral space could aid classification.

The 22 June 1981 pass has been examined by straight clustering (unsupervised approach) of a narrow sea strip between Plymouth and Roscoff (figure 5). The ocean class was stratified into K subclasses where K depends upon the ISOCLS input parameters (particularly upon the maximum permitted standard deviation per class) and $K = 4$ for figure 5. The sea strip was then split into 5 pixel × 5 pixel cells and the mean class computed for each cell. Finally, class numbering was arranged to be proportional to sea-truth concentration using the reasonable assumption that the lowest radiance in channel 1 (or sometimes channel 2) corresponds to the highest chlorophyll concentration. The cluster pattern (D) correlates well with the spectral

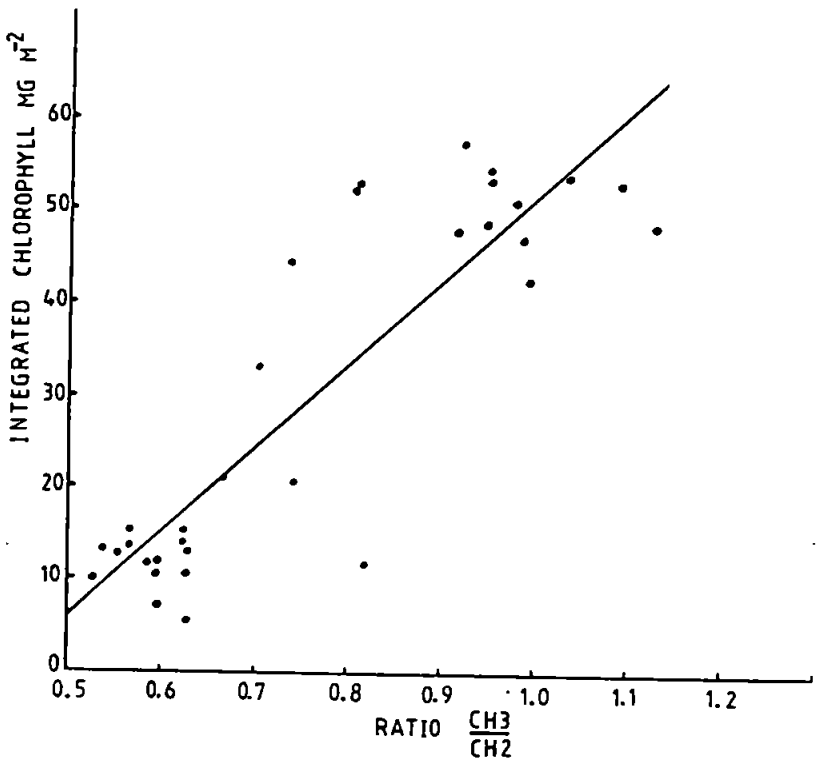

Figure 6. Linear regression for CZCS pass on 29 July 1981.

ratio (C). Also, when the sea strip is shifted 5 nautical miles east of the Plymouth–Roscoff route then the cluster pattern (E) correlates well with the diatom concentration, indicating that tidal flow has shifted the sea-truth.

Hybrid classification was used for the 29 July 1981 pass because a much larger data set (of the order of 10^5 pixels) had to be classified. Using the monocluster blocks approach (Fleming and Hoffer 1977), small heterogeneous blocks of data (typically 25 pixels × 25 pixels) were selected from cloud-free ocean areas and these data were collectively clustered to develop training statistics. The blocks were selected to give a data set representing virtually all significant cluster subclasses. The clustering programme developed a mean vector and a covariance matrix for each of the K classes and these statistics were used by a maximum likelihood classifier to extrapolate the classification over the whole image. This classifier used a multivariate normal distribution to estimate conditional probabilities on the reasonable assumption that each subclass is unimodal. Finally, the classifier ordered the class numbers as described above. It is worth noting that when a weighted minimum distance classifier (Michael and Lin 1973) was used for extrapolation it gave less than 5 per cent difference in pixel classification and took a third of the CPU time to classify the whole image. For the 29 July 1981 pass eight chlorophyll subclasses were generated leading to a 'pipelike' structure in spectral space (figure 7), and using integrated chlorophyll data it was possible to relate subclass K to chlorophyll concentration. The circles are an indication of class variance. Pixels from various coastal waters were also clustered to give a single class and figure 7 shows this to be located in a distinctly different region of spectral

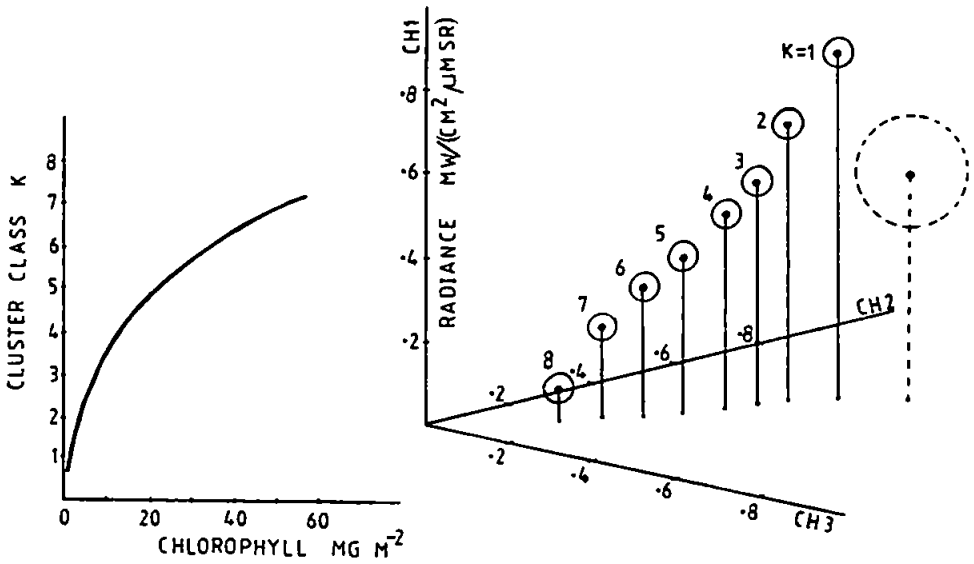

Figure 7. Chlorophyll signature in spectral space.

space. The class is shown dotted since the assumption of zero water leaving radiance at 670 nm is no longer valid, and therefore absolute radiance values will be in error. Figure 8 shows the maximum likelihood classification for 29 July 1981 and, as expected, the subsurface feature is similar to that in figure 4 (*d*). Clustering data for 22 June 1981 gives a similar but less elongated subclass structure (ellipsoidal) centred near subclasses 3 and 4 in figure 7; there is still significant channel 3 variation and the coastal class is in virtually the same position as that for 29 July 1981.

The advantages (if any) of clustering over the conventional and well-founded ratio methods for chlorophyll retrieval must stem from the simultaneous use of all the available information. For example, spectral ratios for the low chlorophyll images of 17 June 1984 and 3 July 1984, where the concentration was typically $< 1\ \mathrm{mg\,m^{-2}}$, resulted in weak, noisy features on a display whereas clustering and maximum likelihood extrapolation resulted in much stronger features. Also, it is widely recognized that the reflectivity in channel 3 does not vary strongly with changes in phytoplankton pigment concentration, although figure 7 suggests that channel 3 still contains some useful information since there is a significant radiance variation with concentration.

Conclusion

The atmospheric correction algorithm appears to perform reasonably well for ocean waters but in its non-iterative form it is not applicable to turbid coastal waters since then L_w^{670} is often non-zero. The major uncertainties in its application lie in the selection of the Ångström exponent and in the correction for radiometer losses, and the problem is worst for channel 1 and high orbit numbers. The cell striping effect on channel 1 images in particular can be reduced by a finer longitudinal partitioning of the scene for geometric calculations and a partitioning as high as 30×4 seems appropriate for the images analysed. This also supports the view that a single geometric calculation at scene centre is probably insufficient.

Figure 8. Maximum likelihood classification for CZCS pass on 29 July 1981.

Reasonable correlation has been found for linear, power and polynomial regression between spectral ratio and integrated chlorophyll concentration although sea-truth measurements are spread over a few days relative to the satellite pass. This may be due in part to the fact that most measurements were taken from several large fairly homogeneous areas of relatively high chlorophyll concentration thereby minimizing the effects of subsurface movement.

Cluster analysis of ocean areas is meaningful if the clustering procedure stratifies the ocean class into phytoplankton subclasses. Cluster patterns derived from clustering three-dimensional data show good agreement with ratio patterns and under certain assumptions it was possible to relate subclasses to chlorophyll concentration. Future satellites with more spectral bands in the visible region (e.g. one near 620 nm) may provide sufficient incentive to examine methods of chlorophyll retrieval using clustering. For certain water areas it may be possible to establish nominal mean vectors in spectral space each corresponding to a nominal chlorophyll density and classification could then be done by a single pass through a cluster algorithm.

Clearly it would be necessary to account for variations in solar illumination with zenith angle, e.g. by normalizing the axes in spectral space and the atmospheric correction algorithm must be reliable. Unfortunately, perhaps the major obstacle to formulating any type of classification procedure for the U.K. South-western Approaches is the lack of cloud-free CZCS passes with high chlorophyll and for which simultaneous sea-truth is available.

Acknowledgments

This work is supported by the U.K. Science and Engineering Research Council under grant no. GRC/29287. We also wish to thank Dr. P. M. Holligan, Marine Biological Association, Plymouth, and Dr. J. Aiken, Institute for Marine Environmental Research, Plymouth, for the provision of undulator ship-trawl measurements.

Appendix A

Sun–satellite geometry

The fundamental correction equation for L_W^λ requires the following relations

$$t_D^\lambda = \exp(-\tau_R^\lambda/2\mu) \tag{A 1}$$

$$L_T^\lambda = \text{slope}^\lambda \times \text{DN}^\lambda + \text{intercept}^\lambda \tag{A 2}$$

$$E_0^\lambda = \bar{E}_0^\lambda(1 + E\cos[2\pi(D-3)/365])^2 \tag{A 3}$$

$$T_{O_3}^\lambda(\mu)T_{O_3}^\lambda(\mu_0) = \exp[-\tau_{O_3}^\lambda(1/\mu + 1/\mu_0)] \tag{A 4}$$

$$\mu = \cos\theta \tag{A 5}$$

$$\mu_0 = \cos\theta_0 \tag{A 6}$$

where equations (A 2)–(A 4) also apply for λ_0. Relatively small attenuations from ozone, water vapour and aerosols have been ignored in the expression for diffuse transmittance t_D^λ (Sørensen 1981, Gordon and Clark 1980) and the slope and intercept follow from the satellite's voltage and active calibration data. Gordon's correction (Gordon *et al.* 1983) is used to correct for radiometer losses although this correction is suspect for high orbit numbers. To compute L_R^λ requires the Fresnel reflectance

$$\rho(i) = \frac{1}{2}\left[\frac{\sin^2(i-r)}{\sin^2(i+r)} + \frac{\tan^2(i-r)}{\tan^2(i+r)}\right] \qquad i = \theta, \theta_0 \tag{A 7}$$

$$N\sin r = \sin i \tag{A 8}$$

and the Rayleigh phase function

$$P_R(\psi\pm) = \tfrac{3}{4}(1 + \cos^2\psi\pm) \tag{A 9}$$

It is necessary to consider the Sun–satellite geometry to compute the scattering angles $\psi\pm$ and the final equations are

$$\cos\psi\pm = \pm\cos\theta\cos\theta_0 - \sin\theta\sin\theta_0\cos(\phi - \phi_0) \tag{A 10}$$

$$\cos\theta = \cos\theta_t\cos\theta_v \tag{A 11}$$

$$\theta_v = \text{IFOV}(\text{pixel number} - \text{nadir pixel}) \tag{A 12}$$

$$\cos\theta_0 = \sin\theta_1\sin\delta + \cos\theta_1\cos\delta\cos\omega t, (\omega = 2\pi/24) \tag{A 13}$$

$$\cos\phi_0 = (\sin\delta - \sin\theta_1\cos\theta_0)/\cos\theta_1\sin\theta_0 \qquad (\text{if } t > 0,\ \phi_0 \to 2\pi - \phi_0) \tag{A 14}$$

$$\sin\delta = \sin 23{\cdot}44^\circ \sin[2\pi(D - 80{\cdot}25)/365] \tag{A 15}$$

The nadir pixel is 1090 and pixel numbers range from 114 to 2081. Derivation of cell latitude, θ_1, and local time, t, is described in the text. Finally, the scanner azimuth angle ϕ is computed as follows, (following Singh 1982 and private communication),

$$\phi = \Delta + \phi'' \tag{A 16}$$

$$\cos\Delta = \frac{\sin(\text{track-line inclination})}{\cos\theta_1} \tag{A 17}$$

where ϕ'' is derived from the following table

	$\theta_v > 0$	$\theta_v = 0$	$\theta_v < 0$
$\theta_t > 0$	$\pi - \phi'$	$\pi/2$	ϕ'
$\theta_t = 0$	π	0	0
$\theta_t < 0$	$\pi + \phi'$	$3\pi/2$	$2\pi - \phi'$

and ϕ' is computed from

$$\phi' = |\tan^{-1}(\sin\theta_t / \tan\theta_v)| \tag{A 18}$$

Appendix B

List of symbols used

$2a$	Latitude subtended by 128 pixel × 128 pixel cell.
α	Orbital inclination (function of latitude).
$2b$	Longitude subtended by 128 pixel × 128 pixel cell.
C_1	Correction to local time due to difference in latitude.
C_2	Correction to local time due to difference in longitude.
C_3	Correction to local time due to non-zero tilt.
D	Day number from 1 January (1–365).
DN	Raw digital count from satellite data.
δ	Solar declination angle.
Δ	Scan-line azimuth angle.
E	Eccentricity of Earth's orbit.
E_0^λ	Seasonally adjusted solar irradiance.
$\bar{E}_0^\lambda$	Mean solar irradiance.
i	Angle of incidence.
IFOV	Instantaneous field of view of the sensor (0·04°).
L_A	Radiance due to aerosol scattering.
L_R	Radiance due to Rayleigh scattering.
L_T	Total radiance at satellite.
L_W	Water leaving radiance.
λ	Wavelength.
λ_0	670 nm, channel 4.
M	Ångström exponent.
μ	$\cos\theta$.
μ_0	$\cos\theta_0$.
N	Refractive index of sea-water.
P_A	Phase function for aerosol scattering.
$P_R(\psi+)$	Phase function for Rayleigh scattering (forward).
$P_R(\psi-)$	Phase function for Rayleigh scattering (backward).
ϕ	Scanner azimuth angle.
ϕ_0	Solar azimuth angle.
$\psi+$	Forward scattering angle.
$\psi-$	Backward scattering angle.
r	Angle of refraction.
R	Earth radius.
ρ	Fresnel reflectance.
s	Normal distance between subsatellite point and current scan line.

t Local time.
t_D Diffuse transmittance.
T_{O_3} Beam or direct transmittance due to ozone.
τ_A Optical thickness due to aerosols.
τ_{O_3} Optical thickness due to ozone.
τ_R Optical thickness due to Rayleigh materials.
θ Polar angle (scanner zenith angle).
θ_0 Solar zenith angle.
θ_1 Latitude of centre of a 128 pixel × 128 pixel cell.
θ_2 Longitude of centre of a 128 pixel × 128 pixel cell.
θ_t Sensor tilt angle.
θ_v View angle (function of pixel number only).
Θ_1 Latitude for centre of 768 pixel × 512 pixel scene.
Θ_2 Longitude for centre of 768 pixel × 512 pixel scene.

References

AUSTIN, R. W., 1982, *Eurasep Secretariat Newsletter*, No. 7. Commission of the European Communities, Joint Research Centre, Ispra Establishment, 21020 Ispra, Varese, p. 2.

BAUER, M. E., and DAVIS, B. J., 1976, Stratification of LANDSAT data by clustering. *Proceedings of the Symposium on Machine Processing of Remotely Sensed Data*, West Lafayette, Indiana.

E.S.L. (ELECTROMAGNETIC SYSTEMS LABORATORY INC.), 1976, IDIMS user's guide. Technical Memorandum ESL-TM 705, Sunnyvale, California.

FLEMING, M. D., and HOFFER, R. M., 1977, Computer-aided analysis techniques for an operational system to map forest lands utilizing Landsat MSS data. LARS Technical Report 112277 Laboratory for Applications of Remote Sensing, Purdue University, West Lafayette, Indiana.

GORDON, H. R., 1978, Removal of atmospheric effects from satellite imagery of the oceans. *Appl. Optics*, **17**, 1631.

GORDON, H. R., and CLARK, D. K., 1980, Atmospheric effects in the remote sensing of phytoplankton pigments. *Boundary-Layer Met.*, **18**, 299.

GORDON, H. R., CLARK, D. K., MUELLER, J. L., and HOVIS, W. A., 1980, Phytoplankton pigments from the Nimbus 7 Coastal Zone Color Scanner: comparisons with surface measurements. *Science*, **210**, 63.

GORDON, H. R., BROWN, J. W., BROWN, O. B., EVANS, R. H., and CLARK, D. K., 1983, Nimbus 7 CZCS: reduction of its radiometric sensitivity with time. *Appl. Optics*, **22**, 3929.

JUSTICE, C. O., and TOWNSHEND, J. R., 1982, A comparison of unsupervised classification procedures on Landsat MSS data for an area of complex surface conditions in Basilicata, Southern Italy. *Remote Sensing Environ.*, **12**, 407.

MICHAEL, M., and LIN, W., 1973, Experimental study of information measure and inter–intra class distance ratios on feature selection and orderings. *I.E.E.E. Trans. Syst. Man Cybernet.*, **3**, 172.

SINGH, S. M., 1982, A procedure for atmospheric correction of coastal zone colour scanner (CZCS) data. In *Remote Sensing and the Atmosphere. Proceedings of the Annual Technical Conference*, Liverpool, December (Reading: Remote Sensing Society), p. 169.

SMITH, R. C., and WILSON, W. H., 1981, Ship and satellite bio-optical research in the California BIGHT. In *Oceanography from Space*, edited by J. F. R. Gower, (New York: Plenum), p. 281.

SØRENSEN, B. M. (editor), 1981, *Recommendations of the Second International Workshop on Atmospheric Correction of Satellite Observation of Sea Water Colour*, Commission of the European Communities, Joint Research Centre, Ispra Establishment, 21020 Ispra, Varese.

TOWNSHEND, J. R., and JUSTICE, C. O., 1980, Unsupervised classification of MSS Landsat data for mapping spatially complex vegetation. *Int. J. remote Sensing*, **1**, 105.

VIOLLIER, M., TANRÉ, D., and DESCHAMPS, P. Y., 1980, An algorithm for remote sensing of water color from space. *Boundary-Layer Met.*, **18**, 247.